FACULTY OF ENGINEERING SCIENCE
DEPARTMENT OF ELECTRICAL ENGINEERING (ESAT)
Kasteelpark Arenberg 10
BE-3001 LEUVEN, Belgium
+3216321130
gofran.chowdhury@kuleuven.be
https://www.esat.kuleuven.be/



Gofran Chowdhury

Beyond uniformity: Physics informed advanced thermal modeling for photovoltaic systems

September 2025

KU LEUVEN

Arenberg Doctoral School
Department of Electrical Engineering (ESAT)

Beyond uniformity: Physics informed advanced thermal modeling for photovoltaic systems



Supervisors:
Prof. Francky Catthoor
Prof. Jef Poortmans

Gofran Chowdhury

Dissertation presented in partial fulfillment of
the requirements for the degree of
Doctor of Engineering Science(Ph.D.):
Electrical Engineering

September 2025

BEYOND UNIFORMITY: PHYSICS INFORMED ADVANCED THERMAL MODELLING FOR PHOTOVOLTAIC SYSTEMS

Gofran CHOWDHURY

Chairperson:
Prof. Paul Sas

Supervisors:
Prof. Jef Poortmans
Prof. Francky Catthoor

Additional members:
Prof. Michaël Daenen
Prof. Geert Deconinck
Prof. Jan Cappelle
Asst Prof. Elham Shirazi

Dissertation presented in partial fulfilment of the requirements for the degree of Doctor of Engineering Science (Ph. D.): Electrical Engineering
In collaboration with:

imec

September 2025

© 2025 GOFRAN CHOWDHURY
Uitgegeven in eigen beheer, GOFRAN CHOWDHURY, MECHELEN, BELGIUM

Alle rechten voorbehouden. Niets uit deze uitgave mag worden vermenigvuldigd en/of openbaar gemaakt worden door middel van druk, fotokopie, microfilm, elektronisch of op welke andere wijze ook zonder voorafgaandelijke schriftelijke toestemming van de uitgever.

All rights reserved. No part of the publication may be reproduced in any form by print, photoprint, microfilm, electronic or any other means without written permission from the publisher.

Acknowledgements

Where do I even start! Life takes you in winding paths. Very often, while walking that path, it feels visionless, directionless sometimes, perhaps, hopeless. And yet, when you zoom out and look back, all those directionless brushstrokes turn into a painting that makes sense. The journey of a PhD is almost always like that.

This is the only page in the whole thesis where I get to say a formal thank you to the many people who invested their time and energy to carry me through. There are so many I have to thank. Whatever I managed to see, I saw because others lifted me.

Let me begin with the examination committee. Jef, thank you for being smart and kind at the same time. You always made sure to listen and provide full attention to students like me. Dirk, thank you for your patience and mentorship. Hans, for those overlapping years of work you were steady. Geert, your calendar is always full with work, yet I have never seen you without a smile. Michael, thank you for being approachable; beyond imec we kept working projects, conferences. Eli, thank you for being colleague and friend at the same time; there is more to build together. Jan, without your open door and active support, this PhD would not exist. Prof. Jan Degrève, thank you for removing the administrative thorns so the walk of my PhD could continue. And Francky whatever I write here will be too small. You changed the course of my life, and my wife's, beyond this PhD. Saying "thank you" is not large enough.

Bert, when we first met, I didn't imagine we would build such a close relationship. I know I can share anything with you, and you will be there.

Anastasios, not only my student my friend. I crossed the finishing line because Jan, Bert, and you stood with me.

There are so many imec and KU Leuven colleagues with whom I have shared and created memories. A simple “thank you” feels small. I hope in the years to come we keep close over coffee, and the small activities that make the days feel human. Thank you, Rik, Arnaud, Imre, Patrizio, Wenya, Bart, Santhosh, Jonathan, Tom, Apostolis, Arvid, and many more.

Gauthier and Mohammed yes, I supervised both your master’s theses. But I received more than I gave. Thank you.

Thank you, Murad bhai and Tipu mama. You taught me how to read and how to reflect. You may not know it, but both of you shaped how I read, how I think about life. Nanu, Fatima aunty, Nazim mama, Hujur mama thank you for seeing the little me you once knew, and giving your time so that I could stand here today.

To my brothers, Jhumon and Adnan we might not talk every day, but know that you are heart; you live in my heart. I would have been so happy to see you both here. Maha, thank you for joining this sometimes a bit crazy family.

Ammu and Abbu you are here to celebrate this occasion with me. Many days I wondered if this day would ever come. It was not always evident. Whatever I am right now, whatever roads I have walked, it is because of you. You are my north star.

Lastly, Asia. By now, we have known each other for a third of our lives. Truth be told, I barely remember life before you. You have been there for me and for us so gracefully; you are a force of nature. I still don’t know why you chose me. I am glad and lucky you did. I look forward to celebrating all of it your success, our sadness, our happiness together, as we always have.

I pray that Almighty rewards you many many more times than what you have kindly gifted me.

Abstract

This PhD thesis investigates the thermal modelling of photovoltaic (PV) systems with a focus on spatial temperature variability and its influence on energy yield estimation. While irradiance modelling has matured to high levels of precision, the treatment of thermal effects in PV performance simulations often remains simplistic. Conventional approaches typically rely on steady-state formulations and assume spatially uniform temperatures, even though empirical observations and experimental studies suggest otherwise. The consequence is a systemic underestimation of real-world temperature-induced losses, particularly in large-scale and micro grid installations.

The work is structured around a sequence of interconnected questions. First, it examines to what extent different PV cell technologies respond to temperature, both in controlled simulations and under real operational conditions. A sensitivity analysis reveals that minor variations in temperature assumptions can shift the relative performance ranking between technologies, underscoring the need for accurate modelling in climate-specific system design. Subsequently, widely used temperature estimation models, spanning steady-state and transient formulations are evaluated using long-term outdoor measurements. The results show that model performance deteriorates at finer spatial and time resolutions and under fluctuating irradiance, conditions common in operational settings yet rarely captured in validation studies.

To address these limitations, the thesis develops a coupled computational fluid dynamics (CFD) and heat transfer model capable of resolving fine-grained spatial temperature distributions across PV module surfaces. This modelling approach incorporates volumetric heat generation within individual layers of

the module and accounts for wind driven forced convection. Experimental wind tunnel tests and outdoor measurements are used to validate the model. Particular attention is paid to the role of module geometry and airflow revealing that localized cooling patterns, driven by both module framing and environmental exposure, can lead to intra-module temperature difference exceeding 15°C.

In later chapters, this CFD model is extended to simulate hypothetical configurations and emerging applications. Based on all the learning CFD modelling, and outdoor measurement, an empirical over temperature correction model is proposed that integrates wind direction as a calibratable parameter. This model proves transferable between sites with similar wind regimes and offers a calibratable method to improve yield simulations.

A separate case study is devoted to floating PV systems. Contrary to common expectations, the study finds that wind exposure, rather than water adjacency, remains the dominant factor in determining module temperature. These findings reinforce the central claim of the thesis: that temperature variability in PV systems is driven primarily by site-specific airflow and requires tailored modelling strategies.

Taken together, the contributions of this thesis provide a pathway towards more physically representative and location-sensitive thermal models for PV energy yield simulation. The work does not argue for universal all in one modelling but instead highlights where simplified approaches fall short and what more advanced but still pragmatic alternatives should be applied. The implications span from improved bankability assessments to informed technology selection and long-term asset reliability.

Keywords
Photovoltaic (PV) Systems, Thermal Modelling, PV Cell Temperature, Energy Yield Estimation, Computational Fluid Dynamics (CFD), Forced Convection, Spatial Temperature Distribution, Temperature Sensitivity Analysis, Floating PV

Abstract

Dit proefschrift onderzoekt de thermische modellering van fotovoltaïsche (PV) systemen, met bijzondere aandacht voor ruimtelijke temperatuurvariaties en hun invloed op de inschatting van de energieopbrengst. Terwijl de modellering van instraling inmiddels een hoge graad van nauwkeurigheid bereikt heeft, blijft de behandeling van thermische effecten in PV-prestatiemodellen vaak simplistisch. Traditionele benaderingen steunen doorgaans op stationaire modellen en gaan uit van een uniforme temperatuurverdeling over het moduleoppervlak, hoewel empirische observaties en experimentele studies het tegendeel aantonen. Dit leidt tot een structurele onderschatting van temperatuurgeïnduceerde verliezen, vooral bij grootschalige installaties en microgridtoepassingen.

De opbouw van dit werk volgt een reeks onderling verbonden onderzoeksvragen. In eerste instantie wordt nagegaan in welke mate verschillende PV-celtechnologieën reageren op temperatuur, zowel in gesimuleerde scenario's als onder reële operationele omstandigheden. Uit gevoeligheidsanalyses blijkt dat kleine ruimtelijke en temporele variaties in temperatuurveronderstellingen de relatieve prestatievolgorde tussen technologieën al sterk kunnen beïnvloeden, wat het belang onderstreept van nauwkeurige modellering binnen klimaatspecifieke systeemontwerpen. Vervolgens worden gangbare temperatuurmodellen zowel stationair als transiënt geëvalueerd aan de hand van langdurige metingen in de buitenomgeving. De resultaten tonen aan dat de modelprestaties verslechteren bij fijnere tijdsresoluties en wisselende instralingsomstandigheden, situaties die in de praktijk veel voorkomen, maar zelden worden meegenomen in validatiestudies.

Om deze beperkingen te verhelpen, wordt in dit proefschrift een gekoppeld model ontwikkeld op basis van computationele stromingsleer (CFD) en warmtetransport, waarmee gedetailleerde ruimtelijke temperatuurverdelingen op het oppervlak van PV-modules gesimuleerd kunnen worden. Dit model houdt rekening met volumetrische warmteopwekking in de afzonderlijke materiaallagen van het paneel en met door wind aangedreven geforceerde convectie. Validatie vindt plaats via windtunnelproeven en metingen in de buitenlucht. Er wordt specifiek aandacht besteed aan de invloed van modulegeometrie en luchtstroming. Het onderzoek toont aan dat lokale afkoelpatronen, gestuurd door zowel de module-inkadering als blootstelling aan de omgeving, kunnen leiden tot temperatuurgradiënten binnen een module van meer dan 15°C.

In latere hoofdstukken wordt het CFD-model uitgebreid om gecontrolleerde testconfiguraties en realistische nieuwe toepassingen te simuleren. Op basis van de inzichten uit zowel modellering als veldmetingen wordt een empirisch correctiemodel ontwikkeld dat oververhitting inschat op basis van windrichting als kalibreerbare parameter. Dit model blijkt overdraagbaar tussen locaties met gelijkaardige windregimes en biedt een praktische methode om opbrengstvoorspellingen te verbeteren.

Een afzonderlijke studie richt zich op drijvende PV-systemen. In tegenstelling tot gangbare veronderstellingen blijkt niet de nabijheid van water, maar de blootstelling aan wind de overheersende factor te zijn die de moduletemperatuur bepaalt. Deze bevindingen versterken de centrale stelling van dit proefschrift: dat temperatuurvariatie in PV-systemen hoofdzakelijk wordt gestuurd door lokale luchtstroming en vraagt om plaatsgebonden modellering.

Samengenomen bieden de bijdragen in dit proefschrift een weg naar meer accurate fysisch realistischere en locatiegevoelige thermische modellen voor het simuleren van de energieopbrengst van PV-systemen. Het werk pleit niet voor één universeel model, maar toont aan waar vereenvoudigde benaderingen tekortschieten en welke pragmatische alternatieven in de plaats moeten komen. De implicaties reiken van verbeterde rendabiliteitsanalyses tot onderbouwde technologiekeuzes en verhoogde betrouwbaarheid op lange termijn.

List of publications

Journal publications

1. Chowdhury, G., Goossens, D., Goverde, H., Catthoor. (2018). Experimentally validated CFD simulations predicting wind effects on photovoltaic modules mounted on inclined surfaces. Sustainable Energy Technologies and Assessments, 30(March 2017), 201–208. https://doi.org/10.1016/j.seta.2018.10.005

2. Chowdhury Gofran, Haggag Mohamed, & Poortmans Jef. (2023). How cool is floating PV? A state-of-the-art review of floating PV's potential gain and computational fluid dynamics modelling to find its root cause. EPJ Photovolt., 14, 24. https://doi.org/10.1051/epjpv/2023015

3. Chowdhury, G., Kladas, A., Herteleer, B., Cappelle, J., & Catthoor, F., "A calibratable PV temperature model that integrates Wind Direction in a realistic way: Insights from Long-Term Outdoor Measurements" (Currently in review in Progress in Photovoltaic Journal)

4. Chowdhury, G., Kladas, A., Herteleer, B., Cappelle, J., & Catthoor, F., "Performance Analysis of Highly Cited Silicon Photovoltaic Module Temperature Estimation Methods: A Critical Review," SSRN: https://ssrn.com/abstract=4212108 " (Currently in review in Solar RRL)

5. Chowdhury Gofran, Du Boullay Gauthier, & Poortmans Jef., "Investigating the temperature distribution of a PV module under various environmental

factors and exploring novel module geometries for the reduction of thermal losses". " (Currently in review in Solar RRL)

6. Herteleer, B., Kladas, A., Chowdhury, G., Catthoor, F., & Cappelle, J. (2023). Investigating methods to improve photovoltaic thermal models at second-to-minute timescales. Solar Energy, 263, 111889. https://doi.org/10.1016/j.solener.2023.111889

7. Manganiello, P., Govaerts, J., Horvath, I. T., Chowdhury, M. G., Yordanov, G. H., Goverde, H., Aldalali, B., Beausoleil-Morrison, I., Valkealahti, S., Lappalainen, K., & Poortmans, J. (2020). Tuning electricity generation throughout the year with PV module technology. Renewable Energy, 160, 418–427. https://doi.org/10.1016/j.renene.2020.06.106

Patents:

1. Bourisli, R., Aldalali, B. S. H. M., Tuomiranta, A., Chowdhury, G., & Poortmans, J. (2025). System comprising photovoltaic modules with multiple vanes and corresponding arranging method, US2025023503A1.

2. Bourisli, R., Aldalali, B. S. H. M., Tuomiranta, A., Chowdhury, G., & Poortmans, J. (2025). System comprising photovoltaic modules with multiple vanes and corresponding arranging method, EP4199120A1.

Conference publications:

1. Chowdhury, G., Kladas, A., Herteleer, B., Cappelle, J., & Catthoor, F. (2021). Sensitivity analysis of the state of the art silicon photovoltaic temperature estimation methods over different time resolution. 2021 IEEE 48th Photovoltaic Specialists Conference (PVSC), 1340–1343. https://doi.org/10.1109/PVSC43889.2021.9519068

2. Chowdhury, G., Somma, L., Goossens, D., Goverde, H., Horvath, I., Voroshazi, E., Poortmans, J., Catthoor, F. (2018). Novel computational fluid dynamics modelling of spatial convective heat transfer over PV-modules mounted on an inclined surface with an underlying air gap. 35th European Photovoltaic Solar Energy Conference and Exhibition - EUPVSEC, 1182–1185. https://doi.org/10.4229/35thEUPVSEC20182018-5CV.1.15

3. Chowdhury, G., Goverde, H., Manganiello, P., Voroshazi, E., Poortmans, J., & Catthoor, F. (2019). Sensitivity analysis of the effect of forced convection on photovoltaic module temperature and energy yield. 2019 IEEE 46th Photovoltaic Specialists Conference (PVSC), 1237–1241. https://doi.org/10.1109/PVSC40753.2019.8980517

4. Yordanov, G., Chowdhury, M. G., Moschner, J. D., & van der Heide, A. S. H. (2021). Beyond-Standard Equivalent Cell Temperature (ECT) Evaluation. Proc. 38th European Photovoltaic Solar Energy Conference, 820–824. https://doi.org/10.4229/EUPVSEC20212021-4AV.2.15

5. R. Lundholm, D. Goossens, H. Goverde, J. Poortmans, M.G. Chowdhury, J. G. (2018, November 7). Investigating the Effect of Soiling on the Power Production of PV Panels Exposed to Wind: Wind Tunnel Approach. 35th European Photovoltaic Solar Energy Conference and Exhibition. https://doi.org/10.4229/35thEUPVSEC20182018-5CV.3.30

6. Shirazi, E., Lemmens, J., Gofran Chowdhury, M., Tuomiranta, A., Catthoor, F., Voroshazi, E., & Gordon, I. (2021). Cloud Detection for PV Power Forecast based on Colour Components of Sky Images. 2021 IEEE 48th Photovoltaic Specialists Conference (PVSC), 2389–2391. https://doi.org/10.1109/PVSC43889.2021.9518667

List of Abbreviations and Symbols

PV:	Photovoltaic
GHI:	Global Horizontal Irradiance
DHI:	Diffuse Horizontal Irradiance
DNI:	Direct Normal Irradiance
G_{poa}/ G	Plane of Array Irradiance
WS	Wind Speed
WD	Wind Direction
RH	Relative Humidity
T_{amb}/ T_a	Ambient temperature
MPPT	Maximum power point tracking
CFD	Computational Fluid Dynamics
DNS	Direct Numerical Simulation
EVA	Ethyl Vinyl Acetate
FF	Fill Factor
FEM	Finite Element Method
FPV	Floating Photovoltaic
GCI	Grid Convergence Index
GPV	Ground-mounted Photovoltaic
HTC	Heat Transfer Coefficient

HDPE	High Density Polyethylene
LES	Large Eddies Simulation
NS	Navier-Stokes
PV	Photovoltaic
PVT	Photovoltaic/Thermal
PID	Potential Induced Degradation
RH	Relative Humidity
RANS	Reynolds Averaged Navier Stokes
SST	Shear Stress Transport
TI	Turbulence Intensity
WVC	Water Veil Cooling
KUL	KU Leuven
EV	Energyville
A	Module's surface area (m^2)
c	Concentration (mol/m^3)
Cp	Specific heat capacity at constant pressure ($J/(kg\cdot K)$)
D	Diffusion coefficient (m^2/s)
F	Buoyancy force (N/m^3)
fo	Extrapolated solution
g_{evap}	Evaporation flux ($kg/(m^2 \cdot s)$)
Hb	Characteristic height (m)
I	Diode current (A)
I_L	Photo-generated current (A)
I_o	Reverse/Dark saturation current (A)
I_{sc}	Short circuit current (A)
K	Evaporation rate (m/s)
k	Turbulence kinetic energy (m^2/s^2)
	Thermal conductivity ($W/(m\cdot K)$)

L	Length scale (m)
Lvap	Latent heat of vaporization (J/kg)
Mv	Molar mass (kg/mol)
Pmax	Maximum output power (W)
p	Absolute pressure (Pa) Rate of convergence
Q	Heat source (W/m^2)
qevap	Heat flux during evaporation or condensation ($J/m2 \cdot s$)
R	Specific gas constant ($J/(kg * k)$)
Re	Reynolds number
r	Grid refinement ratio
T	Absolute temperature (◦C)
Tmod	Module temperature (◦C)
U	Instantaneous velocity (m/s)
u	Velocity vector (m/s)
u+	Velocity vector in viscous units
uI	Fluctuation velocity (m/s)
uτ	Frictional velocity (m/s)
Voc	Open circuit voltage (V)
y	Distance to wall (m)
y+	Distance to wall in viscous units
zo	Aerodynamics roughness length (m)
α	Wind Direction (◦)
αabs	Absorption coefficient
μ	Turbulent dissipation rate (m^2/s^3)
η	Conversion efficiency (%)
θ	Tilt angle (◦)
μ	Dynamic viscosity ($Pa \cdot s$)
μT	Turbulent viscosity ($Pa \cdot s$)

ν	Kinematic viscosity (m^2/s)
ρ	density (kg/m^3)
τw	Wall shear stress (Pa)
φ	Relative humidity level
ω	Specific dissipation rate (s^{-1})

Contents

List of Figures 9
List of Tables 15
1 Introduction 17
1.1 Primary Motivation of The PhD and Its Boundary 17
1.2 State of Art and Related Work Overview 20
1.2.1 Overview of Photovoltaic Energy Yield Simulation Models 20
1.2.2 Different Modelling Approaches for PV Energy Yield Modelling 20
1.2.3 Temporal Resolution and Input Data Requirements 21
1.2.4 Performance Modelling and Output Metrics 22
1.2.5 Strengths and Limitations of Different Models 22
1.2.6 Broader Research Gap Focusing on Physics Based Models 24
1.3 PhD Thesis Scope 25
1.4 PhD Thesis Core Contribution 26
1.4.1 Technology Choice and Temperature Sensitivity (Chapter 2) 26
1.4.2 State of Art on Modelling Limitations and the Need for Resolution (Chapter 3) 27
1.4.3 Wind and Geometry: Spatial Modelling Through CFD (Chapter 4) 28
1.4.4 Coupled CFD Thermal Modelling of Spatial Temperature Distribution in PV Modules Chapter 5) 28
1.4.5 Calibratable Thermal Modelling: Integrating Wind Directional Effects into PV Temperature Estimation (Chapter 6) 29
1.4.6 How A Detailed PV Thermal Model Can Help Identify Root Cause of Difference in Thermal Behaviour Like Floating PV (Chapter 7) 31
1.5 Structure of the Dissertation 32
2 Impact of Accurate Thermal Modelling on PV Technology Choices 33
2.1 Motivation and Organisation 33
2.2 Chapter Specific Introduction and State of Art 35

2.3 Description of Different Cell Technologies 36
2.4 Climatic Datasets 37
2.4.1 Canada (Ottawa) 39
2.4.2 Belgium (Genk) 39
2.4.3 Italy (Catania) 39
2.4.4 Kuwait (Kuwait City) 39
2.5 Energy Yield Simulation Framework 40
2.6 Results and Discussion 41
2.6.1 Energy Yield Analysis 41
2.6.2 Suitable Zones for Technology Deployment 46
2.7 Chapter Summary 47
3 Evaluating the Role of Forced Convection in PV Temperature and Yield Modelling 49
3.1 Motivation and Organisation 49
3.2 Chapter Specific Introduction and State of Art 51
3.3 Sensitivity Analysis of the Effect of Forced Convection on Photovoltaic Module Temperature and Energy Yield 53
3.3.1 Simulation Framework: Electrical Optical and Thermal Model 54
3.3.2 Sensitivity of PV Module Energy Yield and Temperature to Forced Convection Over a Different Period 54
3.4 Performance Analysis of Highly Cited Silicon Photovoltaic Module Temperature Estimation Methods 57
3.5 Experimental Setup Description 58
3.6 Climatic Dataset Selection 61
3.7 Results and Discussion 62
3.7.1 Long Term Performance Analysis 63
3.7.2 Performance in a Shorter Period 65
3.7.3 Model Performance on A Matrix of Irradiance, Ambient Temperature, Wind Speed, and Time Resolution 67
3.7.4 Time Resolution 69
3.7.5 Steady State Models Transient Moving Average Model 71
3.8 Chapter Summary 74
4 Capturing Wind Effect in PV Systems 77
4.1 Motivation and Organisation 77

4.2 Chapter Specific Introduction and State Of Art 78
4.3 CFD Model 81
4.4 Validation of CFD Model 82
4.4.1 Wind Tunnel Setup 83
4.4.2 CFD Model Setup 84
4.4.3 Validation Metrics 87
4.5 Results and Discussion 88
4.5.1 Comparison of Experimental and CFD Simulated Results 88
4.5.2 Effect of the Air Gap 91
4.5.3 Effect of the Wall Cavity 93
4.6 Chapter Summary 96
5 High Resolution Thermal Simulation of PV Modules 99
5.1 Motivation and Organisation 99
5.2 Chapter Specific Introduction and State Of Art 100
5.2.1 Experimental Wind Tunnel Setup 102
5.2.2 CFD Model Description 104
5.2.3 Experimental Validation 105
5.2.4 Section Summary 107
5.3 Simulation of Full Scale PV Module 107
5.3.1 Physics Assumptions for Models 108
5.3.2 CFD Model Setup 111
5.3.3 Results and Discussion 119
5.4 Chapter Summary 121
6 A Calibratable PV Temperature Model that Integrates Wind Direction 125
6.1 Motivation and Organisation 125
6.2 Chapter Specific Introduction and State of the Art 126
6.3 Indoor Experimental Result 127
6.4 Experimental Set Ups 128
6.5 Data Analysis 130
6.5.1 The Influence of Gpoa On iΔT and Its Relationship With Wind Direction 132
6.5.2 Analysis Between iΔT and OT Relative to Wind Direction 134
6.5.3 Method Development 136
6.6 Schematic of Over Temperature Model 137
6.7 Experimental Validation 140

6.8 Result Discussion 143
6.9 Chapter Summary 144
7 How Cool is Floating PV? 146
7.1 Motivation and Organization 146
7.2 Chapter Specific Introduction and State of the Art 148
7.3 Chapter Specific Introduction of FPV 149
7.4 CFD Model Description 152
7.4.1 Geometry and Finite Element Model Assumptions 152
7.4.2 Air and Water Domains 153
7.4.3 Multiphysics Settings 154
7.4.4 Mesh Creation and Grid Independency Test 157
7.4.5 Finite Element Model Grid Independence Test 158
7.4.6 Model Validation With Experimental Results From The Literature 161
7.5 Results and Discussion 161
7.5.1 Comparing FPV with GPV 161
7.5.2 Relative Humidity Impact 163
7.5.3 Ambient Temperature Impact 165
7.5.4 Wind Speed Impact 166
7.5.5 Water Temperature Impact 167
7.5.6 Tilt Angle Impact 169
7.5.7 Wind Direction Impact 170
7.5.8 Solar Irradiance Impact 172
7.5.9 Water Proximity Impact 174
7.5.10 Evaporation Rate Impact 175
7.5.11 Water Depth 176
7.5.12 Power Plant Characteristics 178
7.5.13 Summary of the finite element modelling results 179
7.5.14 Modelling summary 181
7.6 Chapter Summary 183
8 Conclusion 185
8.1 Summary of PhD contributions 185
8.2 Future Work 190
8.2.1 Theme 1: CFD Based Modelling Framework 190
8.2.2 Theme 2: Adapting PV Thermal Models for Operational Efficiency 191
8.2.3 Theme 3: Going beyond the thermal topic 192
9 References 194

List of Figures

Figure 1-1: Technology with the lowest LCOEssc by year and E3ME region. Each map shows the 70 E3ME regions: in 2020 (a), 2023 (b), 2027 (c) and 2030 (d). The biggest [2] 18

Figure 1-2: Sructure of the Dissertation 32

Figure 2-1: Illustration of SHJ-IBC cell structure 37

Figure 2-2: Schematic overview of IMEC's PV energy yield simulations framework 40

Figure 2-3: Module cross section layout 41

Figure 2-4: Energy yield simulated for SHJ-IBC, n-PERT, p-PERC and Full-AL-BSF for four different locations, Kuwait, Italy, Belgium and Canada. 42

Figure 2-6: Cell technology performance with daily total irradiance and average ambient temperature 43

Figure 2-5: Seasonal variation in energy yield of n-PERT, p-PERC and Full-AL-BSF with respect to SHJ-IBC for A) Kuwait, B) Italy, C) Belgium, and D) Canada. The Table under each graph gives the average ambient temperature and average insolation for that location in a season. 43

Figure 2-7: a) Variation of normalised peak power with module temperature for different cell technologies. The graph is obtained by using simulated data points of different technologies at various instances of 1000 W/m^2 and fit with linear regression. The inset table quotes the V_{oc} temperature coefficient of

different cell technologies. b) Cell technology in low illumination conditions - conversion efficiency at 25°C c) SHJ-IBC shunt resistance sensitivity..... 45

Figure 2-8: World map overlap of different cell technology performance with daily average insolation and ambient temperature..... 46

Figure 3-1: Experimental setup in Oldenburg University..... 53

Figure 3-2: (a). Relative energy yield rmse for wind and no wind effect across different temporal resolutions (b). Absolute temperature RMSE for wind and no wind condition 55

Figure 3-3: Simulated Vs Measured solar cell temperature for 11th Aug 2014. (a) Wind effect is included (b) wind effect is not included 56

Figure 3-4: PV cell temperature and power output for incremental forced convection 57

Figure 3-5: Experimental setup and temperature sensor location on PV module 60

Figure 3-6: Sample Day type of cloudy, semi-cloudy, sunny days with standard deviation of G_{PoA} of all the selected days..... 61

Figure 3-7: Long period analysis (May-December) with 1Hz resolution..... 62

Figure 3-8: Distribution plots of $T_{predicted}$ - $T_{measured}$ 64

Figure 3-9: Short period analysis (May-September) with 1 Hz resolution 66

Figure 3-10: Demonstration of the wind speed cooling reaction of every steady state model, along with the measured PV temperature values for each G_{PoA} and T_{amb} level segment..... 69

Figure 3-11: Prediction model accuracy dependency over different time resolution..... 70

Figure 3-12: Absolute error of classified days (May-September) with 1Hz resolution.....71

Figure 3-13: Outlier improvement with WMA 72

Figure 3-14: Four specific day evaluation, Best Vs Worst, Steady State Vs WMA 73

Figure 4-1: Computational model. (a) Model geometry for 9.0 cm cavity; (b) Model geometry for 4.5 cm cavity; (c) Model geometry for 0.0 cm cavity; (d)

Definition of H; (e) Computational grid of the CFD environment with the 4 subdomains; (f) Cross section of sub domain 82

Figure 4-2: Grid Independency test. The figure shows the calculated wind speed at 1.5 mm above and below the module for a 3.5 cm air gap setup and a freestream approaching wind speed of 5 m s-1 for 3 domains: G1 (20.7 106 elements), G2 (13.9 106 elements), and G3 (7.7 106 elements). The differences are very small. For the final calculations in this study domain G2 was used. .. 85

Figure 4-3: Inlet wind profile information. (a) Wind velocity profiles. Dots represent the experimental data; solid lines are the CFD profiles used in the calculations. (b) Turbulence intensity profiles. 86

Figure 4-4: CFD-calculated versus experimentally measured wind velocities. 89

Figure 4-5: Air flow field along the central axis of the experimental setup. All data are for a 9.0 cm cavity, identical to the wind tunnel setup. 89

Figure 4-6: Turbulent kinetic energy for 5 m s-1 inlet wind velocity. 92

Figure 4-7: Average calculated wind velocity at 1.5 mm above the top surface (left) and below the back surface (right) of the module, for the 3 wall cavities investigated. Data are for the central line of the module and a freestream wind velocity of 5 m s-1. 94

Figure 4-8: Average wind velocity vector field perpendicular to the module, for the 3 wall cavities investigated. The vector field is shown for the 4 positions where wind speeds were measured in the wind tunnel (4.0 cm, 19.5 cm, 35.3 cm and 50.9 cm from the leadin edge). 95

Figure 5-1: (a) 3D surface mesh of the wind tunnel test section (b) Wind velocity vector and magnitude for a 3.5 cm air gap and 5 ms-1 inlet wind speed. 103

Figure 5-2: Richardson numbers for different inlet wind speed conditions, for 3.5 and 5.5 cm air gaps. 104

Figure 5-3: Simulated versus measured surface temperature, for a 3.5 and a 5.5 cm air gap 104

Figure 5-4: Surface temperature on the module's top surface, for a 5.5 cm air gap. 105

Figure 5-5: Temperature profile along the central line of the module 106

Figure 5-6: PV module properties 108

Figure 5-7: Energy balance over a ground-mounted PV module 109

Figure 5-8: a) Computational domain, b) symmetry for wind direction $\alpha = 0°$ 111

Figure 5-9: Inlet wind profiles: a) wind velocity magnitude; b) turbulence intensity. 112

Figure 5-10: Contribution to the total yearly insolation (%) of different irradiance levels at different ambient temperatures, collected at Genk (Belgium). 113

Figure 5-11: a) Hybrid Mesh. b) Zoom on inner block: different mesh element shapes: blue = hexahedra, yellow = pyramids, pink: tetrahedra. c) Meshing of the PV module: blue = PV cells, yellow = EVA. d) 3D view of the mesh: blue = air, orange= solid. 114

Figure 5-12: Mesh convergence plot. 117

Figure 5-13: : Temperature of the centre point in the PV cell. 118

Figure 5-14: Temperature profile of full scale module under test condition. ..119

Figure 5-15: Airflow of the reference modules: cross-sectional profile view at the middle of the right windwise. 120

Figure 5-16: Simulation results from parametric studies. 121

Figure 6-1: Experimental setup description 128

Figure 6-3: Spatial temperature distribution and cooling analysis from experiment 1 132

Figure 6-4: Spatial temperature distribution and cooling analysis from experiment 2 133

Figure 6-5: This figure demonstrates the correlation between PoA, over temperature and ΔTintra-module. The plots are from 07/06/2021 with one second resolution. 134

Figure 6-2: PV spatial temperature as function of both G_{poa} and W_s .....**Error! Bookmark not defined.**

Figure 6-6: Scatter plot between the $\Delta T_{intra\text{-}module}$ and over temperature. The data used for this graph are from April 2021-June 2021 in five-minute resolution..... 135

Figure 6-7: This figure demonstrates the linear relationship between the extreme over temperatures and the middle cell's over temperature. The data used for this graph are from April 2021-June 2021 in five-minute resolution. 137

Figure 6-8: Schematic of over temperature model formulation 137

Figure 6-9: Demonstration of the wind direction bins used for coefficient calculation. Below the bin title, the percentage of the data coming from that direction is visible. Below the direction title in each polar plot, the percentage of data that this bin contain..... 138

Figure 6-10: Wind direction coefficients from 12 bin method: The counter clock-wise stands from West wind direction coefficients and the clock-wise for East. 139

Figure 6-11: Demonstration of the approach behind the coefficient dataset splitting. The counter clock-wise stands from West wind direction coefficients and the clock-wise for East..... 140

Figure 6-12: T measured vs T predicted comparison.....141

Figure 6-13: Over temperature model performance on clear sky and semi cloudy day from experiment 1 and 2..... 142

Figure 7-1: a) Wind tunnel (shown only half) and the water domain of the model. b) FPV system, showing the frame and floating structure dimensions. c) The PV module's layers..... 152

Figure 7-2: a) Elements used to construct mesh, blue=hexahedrons, orange = pyramids and green = tetrahedrons. b) Zoom in demonstrating boundary layer meshing. c) and d) Results of y+ on top and bottom module faces respectively. 156

Figure 7-3: Plots of temperature, velocity and pressure from left to right respectively..... 159

Figure 7-4: Plots of a) Relative Humidity and b) Air temperature directly underneath the module at various altitudes from water level..... 160

Figure 7-5: Plots of air density at different humidity levels..... 162

Figure 7-6: a) Air temperature at different humidity levels. b) Close up plot. 163

Figure 7-7: Module operating temperature versus wind velocity. Dotted lines are linear and logarithmic forecasts..... 165

Figure 7-8: Evolution of air temperature with elevation from water for different water body temperatures. 166

Figure 7-9: Streamlines of wind velocity for different module tilt angles..... 168

Figure 7-10: Top view of FPV temperature profiles for various values of the wind direction (α). 169

Figure 7-11: Temperatures simulated for different wind directions. 171

Figure 7-12: Wind flow from bottom to top. a) Temperature contours for the reference panel. b) Temperature difference between Q = 200W/m² and Q = 600W/m². c) Temperature difference between Q = 1000W/m2 and Q = 600W/m2. 171

Figure 7-13: FPV temperature vs clearing distance..... 173

Figure 7-14: Temperature distributions and wind flow for three different clearings (height from the water level is changed)..... 173

Figure 7-15: Approaching wind velocity for 1 m and 6 m deep waters. Movement to the left on x-axis means approaching module..... 176

Figure 7-16: The four studied power plant configurations. a) Both modules facing wind inlet. 176

Figure 7-18: Wind and temperature profiles for all configurations. Modules and frame are colored red for clarity. In the velocity temperature plots, P1 is on the left. 177

Figure 7-17: Average PV temperature per panel for the four power plant installation types. 178

List of Tables

Table 1-1: Strengths and Limitations of Physical, Empirical, Machine Learning, and Hybrid Models 23

Table 2-1: Summary of modelled solar cell parameters..... 36

Table 2-2 Overview of different climatic location 38

Table 3-1: Selected models 59

Table 4-1: Statistical analysis of experimental and simulation data. RMSE = root-mean-square deviation; R = correlation coefficient; FB = fractional bias 88

Table 5-1: Optical properties used for the absorption coefficient. 111

Table 5-2: Number of mesh elements for the different grids. 115

Table 5-3: Results for different discretization orders. 115

Table 5-4: GCI computation for different physical quantities..... 116

Table 6-1: RMSE of over temperature model performance with 2, 12, and 24 segments of wind direction 140

Table 7-1: The thermal properties of the materials used throughout the paper (∗ Indicates values obtained from COMSOL material library)..... 153

Table 7-2: The reference parameter values used in the simulations..... 155

Table 7-3: GCI computation across three grids for different physical quantities. Temperature measurements are averages..... 157

Table 7-4: Change in module temperature with ambient temperature setting. 164

Table 7-5: Average panel temperature for different amounts of irradiance. Bold indicates reference FPV settings. 172

Table 7-6: Sensitivity analysis of ambient temperature and wind speed variations on FPV module temperature. 180

1 Introduction

1.1 Primary Motivation of The PhD and Its Boundary

At the turn of the millennium, the global installed capacity of photovoltaic (PV) systems stood at just 1 gigawatt. By 2004, we had reached a pace of adding 1 GW per year. That rate accelerated to 1 GW per month by 2010, and by 2022, the world was installing the same amount on a daily basis. Now, forecasts suggest that by 2030, more than 10 GW of PV could be added each day [1]. This staggering growth can't be explained only by cheaper modules or favourable policies. It points to a deeper transformation in how societies are reorganizing their energy systems driven by a mix of economic pragmatism and long-term sustainability goals. In Figure 1-1, a range of published projections makes clear that the rise of PV is not a temporary surge but a structural shift. In such a scenario, where PV systems are no longer niche but central, the importance of reliable, site-aware performance modelling becomes both a technical and financial necessity [2].

This thesis begins with that premise. While hardware and deployment capacity have scaled at unprecedented speed, our ability to predict how these systems will perform, especially under variable thermal conditions, has not evolved at the same pace. The intention here is not to construct a model that captures every imaginable condition. Instead, the focus is on examining some of the inherited assumptions in widely used modelling approaches, and proposing a shift in how we frame the problem. The core contribution lies in thermal modelling, not just as an academic curiosity, but as a necessary layer of realism for future PV planning. It is also recognised that such advanced models are not needed everywhere. For small-scale rooftop or lightly loaded ground-mounted systems,

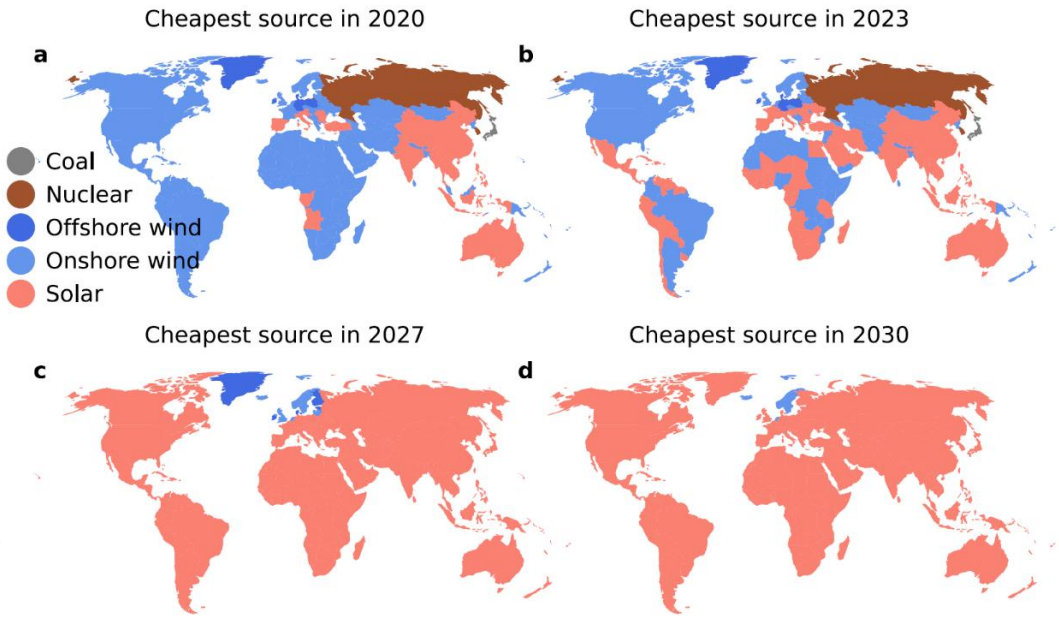

Figure 1-1: Technology with the lowest LCOEssc by year and E3ME region. Each map shows the 70 E3ME regions: in 2020 (a), 2023 (b), 2027 (c) and 2030 (d). The biggest [2]

the cost and effort of detailed parameterization may not be justifiable. But the equation changes when dealing with larger deployments, whether it is a single site hosting a multi-megawatt or gigawatt-scale plant, or a network of distributed systems in a microgrid setting.

Take the example of a large utility-scale PV plant built on a single site. These systems can involve thousands of rows of modules spread across several hectares. Across such a site, irradiance may remain relatively consistent. Wind, however, does not. The presence of PV arrays alters local airflow. Rows near the perimeter behave differently than those in the interior. Wind slows down, changes direction, or becomes turbulent depending on obstructions and layout. These differences in wind flow have led to differences in convective cooling. As a result, operating temperature is not uniform even under identical solar input. What looks like a small deviation in thermal conditions may cause uneven current generation between strings, especially at high irradiance.

The same concern applies to systems that are not in a single location, rather segments of PV plants connected to same micro grid. One system might face open wind exposure, another might be partially shielded by trees or buildings. On their own, these systems seem too small to warrant detailed thermal modelling. But taken together, when they feed into a shared inverter, storage system, or local grid, the variation in performance becomes important. Slight

differences in temperature affect when modules reach their maximum power point, how much they degrade, or how consistently they contribute to local supply. In such contexts, assuming thermal uniformity across the system introduces error, that accumulates over time.

In both cases, the aggregated capacity and spatial extent introduce variability across terrain and microclimates that cannot be overlooked. Assuming uniform temperature performance in such contexts is not just naïve; it will be costly because the relative changes are in the about 10% and potentially even more. Even small thermal estimation errors, when multiplied across millions of modules and years of operation, add up quickly.

In earlier decades, the thermal simplifications used in modelling were often good enough. Most systems were small, computational resources were expensive, and the stakes were low. PV's role in the energy mix was marginal, so errors had limited impact. Today, things look different. PV is on track to deliver a large share of global electricity, and high-resolution computing is no longer a barrier. What was once acceptable as an engineering trade-off has become a performance risk. If the industry continues to rely on outdated models, it risks either underestimating losses or overdesigning systems both with financial consequences.

This research addresses one such blind spot: the interplay between wind patterns and thermal behaviour in PV fields. While the experiments are constrained, as all physical investigations are, the approach offers a framework that others can replicate, adapt, and scale. It's not just about adding another layer of complexity. It's about offering an actionable method that bridges modelling with reality. With PV now delivering the world's lowest LCOE and that figure still declining operators are under pressure to optimise at every level. Oversizing a plant to absorb inefficiencies might sound practical, but it's becoming harder to justify, especially where grid permissions, land use, and capital efficiency are tightly managed. The better path is to sharpen the models. Every relative improvement, even in the range of a few percentage points, in operation and modelling accuracy can materially influence the long-term economic viability of large-scale PV installations. This thesis therefore examines the role of detailed thermal and wind interactions, which have often been oversimplified or treated as uniform. The findings suggest that these seemingly minor variations are not just peripheral but may play a decisive role in shaping the next generation of PV system design and operational strategies. Its relevance is most pronounced for commercial and industrial deployments, microgrids,

and utility-scale sites where thermal effects are no longer just noise, but part of the signal.

1.2 State of Art and Related Work Overview

1.2.1 Overview of Photovoltaic Energy Yield Simulation Models

The accurate simulation of photovoltaic (PV) energy yield is critical for the design, operation, and economic assessment of solar energy systems. While solar irradiance is the primary driver of PV performance, various environmental, structural, and electrical factors influence the actual energy yield. Over the past decades, numerous models have been developed to estimate PV energy yield under diverse conditions. These models differ in their underlying assumptions, computational complexity, temporal resolution, and data requirements. This section provides an overview of the major classes of general-purpose PV energy yield simulation models, highlighting their respective strengths and limitations.

PV energy yield models can broadly be categorized into four types: physical (first-principles), empirical, machine learning (ML), and hybrid approaches. These models are designed for general-purpose applications, aiming to simulate PV performance across various system sizes, geographical regions, and configurations [3].

1.2.2 Different Modelling Approaches for PV Energy Yield Modelling

Physical models, also known as deterministic or analytical models, are grounded in energy balance equations that incorporate radiation, convection, and conduction mechanisms, along with electrical performance modelling. Notable examples include the Sandia Performance Model [4], [5] and the heat balance equations developed by Duffie and Beckman [6]. These models require detailed knowledge of system parameters (e.g., tilt, azimuth, module properties, mounting configuration) and meteorological inputs such as global horizontal irradiance (GHI), ambient temperature, and wind speed. The strength of physical models lies in their generalizability, interpretability, and foundation in thermodynamic principles. Most importantly a crucial aspect for nowcasting is their “extrapolation potential”! However, they often entail a relatively high computational burden and may oversimplify certain dynamic processes such as thermal inertia or partial shading effects.

Empirical models derive predictive relationships between environmental inputs and energy yield using statistical regression. These models typically rely on

linear or nonlinear equations fitted to historical data, often under the assumption of steady-state operation. Their advantage lies in simplicity and minimal input data requirements. However, their accuracy is inherently limited outside the calibration conditions, and they are ill-suited to simulate transients or system-level interactions. However, a fundamental limitation especially for nowcasting is that they can at most be used for interpolation within the bounds of the training data, and not for extrapolation into future or unseen scenarios. Widely used empirical models include the Ross [7], King model [4], [8] and Faiman's [5] back sheet based temperature correction formulation.

Machine learning models represent a growing domain in PV performance modelling. Algorithms such as support vector regression (SVR), random forests (RF), and deep learning methods like long short-term memory (LSTM) networks have been employed to capture complex, nonlinear relationships between input variables and energy yield [9], [10], [11], [12]. These models require large amounts of training data but often outperform analytical models in terms of accuracy when data is abundant. Nevertheless, they lack physical transparency, are sensitive to overfitting, and typically require model re-training when deployed to new locations. While often accurate within well-sampled datasets, purely data-driven models lack transparency, are vulnerable to overfitting, and typically cannot generalize well to conditions that deviate from those seen during training.

Hybrid models seek to combine the benefits of physical interpretability with the flexibility of data-driven approaches. This includes physics-informed neural networks [13], [14], ensemble models blending empirical and deterministic outputs, or data assimilation techniques that dynamically update physical model predictions using real-time measurements. While hybrid approaches are promising, they remain relatively underexplored in peer-reviewed literature compared to the three categories above.

1.2.3 Temporal Resolution and Input Data Requirements

Temporal resolution plays a crucial role in determining both the applicability and computational demands of PV simulation and forecasting models. Models may operate at sub-hourly (e.g., 1–15 min), hourly, or daily timescales. Sub-hourly models are especially important for forecasting, grid integration studies, or systems with storage and dynamic load profiles. However, they require high-quality, high-frequency input data, which may not be readily available in many

regions. Conversely, daily models are computationally efficient but can miss intra-day variations and misrepresent peak mismatch losses or cloud transients.

In terms of input data, most models require at minimum GHI and ambient temperature. More sophisticated implementations further include wind speed, plane-of-array irradiance (POA), relative humidity, tilt angle, module temperature coefficients, and electrical configuration details. Data quality and resolution heavily influence simulation accuracy, with missing or low-resolution inputs introducing notable uncertainty. While many simulation tools incorporate transposition and decomposition models to estimate missing irradiance components (e.g., beam and diffuse), these steps add further layers of assumption [15], [16], [17].

1.2.4 Performance Modelling and Output Metrics

The primary output of an energy yield simulation model is typically the energy produced (kWh) over a defined period, along with derived metrics such as capacity factor or performance ratio (PR). More advanced models decompose energy losses into categories such as optical, thermal, mismatch, wiring, and inverter losses. These breakdowns are valuable for diagnostics and system optimization [15], [16], [17].

Physical and hybrid models tend to offer the most comprehensive performance loss breakdowns, whereas empirical and ML models often focus solely on output prediction without intermediate stages. Notably, the incorporation of thermal performance models accounting for heat exchange via convection and radiation has improved model fidelity, particularly in regions with large temperature fluctuations or low wind speeds. Still, many models continue to assume uniform module temperature, ignoring spatial temperature difference which can affect localized cell degradation and power conversion efficiency.

1.2.5 Strengths and Limitations of Different Models

Each type of these energy yield model offers trade-offs between accuracy, interpretability, data requirements, and generalizability: While several commercial tools (e.g., PVsyst, SAM) and open-source libraries (i.e., pvlib-python [18], [19], [20]) integrate many of these modelling approaches, they often rely on default assumptions which must be critically assessed. Benchmark studies show that inter-model variation in predicted yield can exceed 5–10% [15], [16], especially in systems with bifacial modules, non-standard tilts, or floating PV installations. A closer examination of benchmark studies conducted

by Sandia Lab, USA, offers clarification grounded in empirical data. In this multiyear benchmark study, leading PV modelling universities and commercial software providers were invited to participate in blind testing. They showed that overall yearly PV energy yield estimation can be ±5% under controlled conditions with system-specific data but can exceed ±7–8% if relying on generic specification sheet inputs and steady-state models. How do you translate that to real life PV operation [15], [16]. On a simplified calculation for a 500 MW PV plant: A 4.5% overestimation due to poor temperature and input modelling accuracy could result in a $1.68 million/year overprediction in expected revenues (based on $0.05/kWh and 1500 kWh/kWp/y) [16]. This underscores the importance of model selection in decision-making for PV system design and performance evaluation.

Table 1-1: Strengths and Limitations of Physical, Empirical, Machine Learning, and Hybrid Models

Model Type	**Strengths**	**Limitations**
Physical	Transparent, generalizable, loss breakdown, modular	Input-intensive, slow, may oversimplify transients
Empirical	Simple, fast, requires minimal data	Limited to training context, lacks transparency, poor extrapolation
Machine Learning	High predictive accuracy (with enough data), handles nonlinearities	Data-hungry, lacks interpretability, low generalization to unseen contexts
Hybrid	Balanced accuracy and interpretability, adaptive to system changes	Complex to implement, still under development in the literature

The comparison in Table 1-1 makes clear that no single approach is universally optimal; however, the limitations of empirical and machine learning models become particularly evident when conditions deviate from those represented in their training data. These methods tend to perform well in familiar settings but often fall short when applied to unseen scenarios or when rapid environmental changes occur. In contrast, models built on physical principles either alone or as

part of hybrid structures retain a degree of reliability and explanatory power that others lack. In particular, when properly calibrated for a subrange, they allow extrapolation outside that range to the full usage range potentially. When the goal is to achieve accurate yield estimation across diverse and evolving contexts, physically grounded models improved by additional data based approach to perform that accurate subrange calibration have the potential to have the desired overall accuracy in conditions where the initial training was not applied for.

1.2.6 Broader Research Gap Focusing on Physics Based Models

Operational forecasting and system planning for solar installations rely heavily on performance modelling tools, some of which still depend on simplified assumptions about irradiance, temperature, and their effects on module output. Among the key factors, irradiance of course is the dominant factor of PV's electrical generation. Therefore, irradiance's impact on PV is as well as studied in details. In the current state of art there is high level of confidence on such relationships. While irradiance has long been recognized as the dominant input variable, it is now widely accepted that the thermal behaviour of PV modules contributes non-negligibly to performance variation, particularly in geometries and installations with strong convective dynamics or high ambient temperatures due to climatic condition. For crystalline silicon modules, which represent the vast majority of installations, cell efficiency declines linearly with temperature on the order of 0.28–0.65% per °C rise above standard test conditions [21], [22], [23] . This effect, although straightforward in theory, is complicated in practice by the spatial variability of wind and heat exchange conditions across real installations.

Existing empirical temperature models, while convenient and computationally efficient, often rely on averaged or quasi-steady-state assumptions that neglect the spatial and temporal heterogeneity of PV operating conditions. These models typically assume uniform module temperatures or apply simplified energy balances that fail to resolve localized convective effects. Generally in state of art PV modelling approaches these were not considered either because it was assumed to not have significant effect or there was not effective and efficient approach to model those yet. However, measurements taken under outdoor conditions regularly reveal temperature differences across the surface of a single module, sometimes exceeding 15–20°C depending on wind direction, air gap configuration, and module tilt [24], [25], [26], [27], [28]. In dense array configurations or in novel applications such as floating PV (FPV) and building-

integrated PV (BIPV), these differences can become even more significant, introducing systematic errors into energy yield estimates.

In recent years, universities and industries both begun to explore more detailed physical modelling approaches, particularly those grounded in computational fluid dynamics (CFD), to better characterize heat exchange processes around PV modules. CFD models are capable of resolving fine-scale turbulence, localized flow separation, and wall-surface interactions that govern forced convection a dominant heat transfer mode in many outdoor PV scenarios. When calibrated against controlled experimental data, these models can provide insight not just into average thermal behaviour but into the distribution of temperatures across the module surface and support structure. While CFD modelling provides a lot of insight into understanding the thermal behaviour of PV module it remains to be computationally expensive and time consuming still for instantaneous application [29], [30], [31], [32], [33], [34], [35], [36], [37], [38], [39], [40].

1.3 PhD Thesis Scope

This thesis is situated at the intersection of that modelling gap, in particular of the promising physics-based class. Its objective is to assess, model, and explain the spatial variability of PV module temperature under a range of operational conditions, with particular attention to the coupling between wind flow and thermal differences. The investigation proceeds in three main stages. First, a critical review is conducted of existing PV cell temperature estimation models, including those widely used in simulation software and technical assessments. Their assumptions and limitations are evaluated in light of outdoor measurement data. Second, controlled wind tunnel experiments and field measurements are used to examine how wind speed, module configuration, and installation geometry influence spatial temperature profiles. Third, experimentally validated CFD models are developed to simulate these effects under varying boundary conditions, enabling a detailed sensitivity analysis of key parameters.

In doing so, this work contributes to a more physically informed understanding of PV thermal dynamics, which has implications for both the short-term accuracy of performance models and the long-term reliability of system components. The inclusion of spatial thermal and airflow effects is not merely an academic concern; it affects inverter loading, degradation rates, and the identification of fault conditions in large-scale solar plants. Moreover, in design scenarios where technology selection is based on simulated yield over multiple

decades, unmodeled temperature effects may provide skewed view of the perceived cost-benefit ratio of different module types or mounting strategies.

In addition to the standard ground mounted installations, special attention is given to floating PV systems. These systems, deployed on reservoirs or artificial basins, are often marketed with the assumption of superior cooling due to water proximity. However, literature reviews and thermal modelling have shown that this cooling is not universal and is heavily modulated by site-specific airflow conditions, relative humidity, and panel spacing [Chowdhury et al., 2023]. By applying validated CFD models, this thesis aims to separate plausible cooling effects from marketing assumptions and to identify the physical mechanisms underlying observed performance gains.

Ultimately, the contribution of this work lies in proposing a modelling framework that can move beyond generalized temperature assumptions and toward a representation of thermal behaviour that accounts for spatial, and environmental variation. Such models, if integrated into yield prediction tools or monitoring systems, will enhance operational accuracy, reduce uncertainty in long-term planning, and support more rational decision-making in PV system design particularly in emerging configurations where conventional empirical models fall short.

1.4 PhD Thesis Core Contribution

1.4.1 Technology Choice and Temperature Sensitivity (Chapter 2)

Temperature has a direct, inverse impact on PV module efficiency. Commercial crystalline silicon technologies, which currently dominate the market, typically lose between 0.28% to 0.65% efficiency per degree Celsius increase in cell temperature [21], [22], [23]. Despite this well-established relationship, temperature is still often treated as a secondary consideration during system design and energy yield prediction. This oversight can result in sub-optimal technology selection, particularly in climates with high ambient temperatures or complex meteorological profiles. Moreover recently published state of art benchmarking studies by Sandia Lab, USA shows how the state of art PV modelling falls short and can have error of 5-10% due to either wrong or simplified assumptions of operational scenarios [15], [16].

This PhD responds to this by conducting a comparative analysis of four representative mainstream silicon-based PV technologies (BSF, PERC, PERT, and SHJ-IBC) using a state-of-the-art simulation platform with steady state

temperature models. From the results this can be clearly seen that due to small changes in temperature modelling parameters, the PV technology choices can be widely different. This paves the necessity to verify and propose more accurate temperature models that corresponds to real life situations.

1.4.2 State of Art on Modelling Limitations and the Need for Resolution (Chapter 3)

The next layer of complexity lies in the estimation of PV module temperature. The field is dominated by steady-state models, which are computationally efficient but built on simplified assumptions. The core discrepancies come from three perspectives. First PV modules response to irradiation is almost instant. Which means when you block sunlight you see the impact of it right away on the current and voltage. However, just because sunlight is blocked doesn't mean that a PV module loses it thermal inertia right away. It takes some time to equalize. Most importantly the time to equalize is never constant and widely depends on the continuous influence of the corresponding meteo input. Second perspective is that PV module temperature quickly equilibrates to ambient conditions, with negligible transient or spatial variability. In this case, the core assumption is within PV module or even within one array the temperature must be close enough to be considered uniform. Lastly, such models with these assumptions are widely used in simulation tools due to their low input requirements and ease of implementation.

However, this assumption often fails under real-world operating conditions. For instance, rapid shifts in cloud cover, intermittent shading, and wind dynamics can create short-term and localized temperature deviations that steady-state models are unequipped to capture. Transient models offer a potential improvement, accounting for the module's thermal capacitance and short-term dynamics. Yet even these are rarely validated comprehensively across different temporal resolutions.

This PhD addresses this gap by evaluating both steady-state and transient models on a range of timescales and under varying climatic conditions. This not only provides a clearer picture of model accuracy but also introduces a new layer of nuance into the selection of temperature models. Importantly, our results challenge the conventional wisdom that a single model can be broadly applied, and instead propose a more adaptive approach based on available meteorological data and application requirements.

Another often-overlooked aspect is intra-module temperature variation. Though some studies claim this variation is minimal, others have observed differences as high as 8°C between cells in the same module. In this study we highlight the absence of model validation in this area and suggest that these temperature differences, though small, may still have measurable impacts on performance and degradation over time.

1.4.3 Wind and Geometry: Spatial Modelling Through CFD (Chapter 4)

Environmental heat exchange particularly convective cooling due to wind is another area where simplifications dominate. Conventional models either ignore wind effects altogether or treat them as uniform boundary conditions. This approach fails to account for localized turbulence, eddy formation, and the interaction between wind and structural geometry.

This PhD tackles this limitation using Computational Fluid Dynamics (CFD), developing a detailed 3D model of airflow over PV modules mounted on inclined surfaces. The proposed model incorporates irregular geometries, including variations in air gaps and wall cavities, often neglected in previous work. Through wind tunnel validation, we demonstrate that these seemingly minor details can significantly alter airflow patterns and, in turn, the module's thermal profile.

A key insight from our CFD analysis is that even small structural features such as cavity depth or module mounting configurations can introduce lateral wind deflection and turbulence, resulting in temperature heterogeneity across the module. These effects are particularly pronounced in urban or rooftop environments where airflow is heavily disturbed and becomes turbulent. Our work not only models these effects with high spatial resolution but also ties them back to energy yield outcomes, emphasizing their practical relevance.

1.4.4 Coupled CFD Thermal Modelling of Spatial Temperature Distribution in PV Modules Chapter 5)

Next, we extend the previous investigations by developing a computational model to examine the spatial temperature distribution on photovoltaic (PV) modules. While many energy yield models rely on simplified or averaged thermal behaviour, this chapter focuses on a more detailed approach that links surface temperature variations to airflow conditions and module construction features.

The work centres on a coupled simulation method combining Computational Fluid Dynamics (CFD) with heat transfer modelling. The model represents the layers of a PV module glass, encapsulant (EVA), silicon cells, and the back sheet using thin thermal layers that generate heat internally, corresponding to the unconverted portion of solar irradiance. Wind flow over and beneath the inclined modules is resolved using a standard turbulence model with mesh settings optimized to capture near-wall behaviour.

To validate the simulation results, measurements were taken in a controlled wind tunnel environment. PV modules with 3.5 cm and 5.5 cm air gaps were tested under three wind speeds (3, 4, and 5 m/s). The model reproduced the observed surface temperatures with reasonable accuracy, especially along the centreline of the module. Differences between simulated and measured temperatures were mostly associated with areas of flow separation or reattachment, which are sensitive to local turbulence.

The results point to a clear spatial pattern in temperature distribution: the leading edge of the module is typically better cooled due to direct exposure to airflow, while the rear and central section's experience less convective removal of heat. These patterns are consistent across different air gap sizes and are influenced by both module inclination and wind speed. The findings suggest that even small changes in mounting configuration or environmental conditions can lead to significant temperature differences across the module surface.

This modelling framework also provides a basis for comparative analysis. For example, the model can be adapted to simulate different wind directions and ambient conditions, offering insights into how design choices affect temperature profiles and, by extension, module efficiency and potential degradation.

In summary, this chapter introduces a validated method for capturing localized thermal effects in PV modules. The approach addresses some of the limitations of commonly used empirical models and supports the development of more accurate energy yield estimates, particularly in conditions where convective cooling plays a significant role.

1.4.5 Calibratable Thermal Modelling: Integrating Wind Directional Effects into PV Temperature Estimation (Chapter 6)

This study focuses on a critical yet often overlooked assumption in PV system modelling: the uniformity of module surface temperature. Conventional models generally predict a single, spatially averaged temperature for a PV module based on irradiance, ambient temperature, and wind speed. This simplification has

practical value but can introduce significant inaccuracies particularly under high irradiance and low wind conditions where internal module temperature differences can become substantial.

To evaluate this, long term outdoor measurements were conducted across two geographically distinct sites with differing module layouts. Detailed thermal data was collected using embedded sensors distributed across the surface of each module. The results show that under high irradiation (G_{POA}) conditions, intra module temperature differences can reach up to 10°C in densely packed arrays and up to 15°C in isolated module configurations. The assumption of uniform temperature thus holds only under limited meteorological conditions primarily during periods of low irradiance or sustained high wind speeds.

A key finding of the study is that both wind speed and wind direction strongly influence the spatial distribution of temperature across a module. While wind speed is often included in existing temperature estimation models, wind direction is rarely considered in an explicit or calibrated form. To address this gap, a directional over temperature model is proposed. This model introduces a set of coefficients that adjust the predicted temperature based on wind direction segments. The coefficients can either be adopted as is or calibrated with site-specific measurements. Importantly, the calibration process does not require long-term data; even a few months of high frequency measurements are sufficient to achieve reliable accuracy.

The model was developed using data from one test site and validated on a second, 137 km away, demonstrating robustness across varying array configurations and ambient conditions provided the regional wind patterns are broadly similar. This suggests that the proposed method has potential for wider application, especially when supported by regional wind profiling.

The study concludes by identifying several avenues for future refinement. Among them is the integration of finite element modelling to simulate airflow and heat exchange across modules under controlled boundary conditions. Such an approach could improve model generalization, compensate for uneven wind direction sampling in outdoor datasets, and contribute toward establishing universal directional coefficients for thermal prediction in PV systems.

In summary, the inclusion of wind direction into PV temperature modelling represents a step forward in reducing error in yield prediction particularly under conditions where energy production is highest and modelling accuracy matters most.

1.4.6 How A Detailed PV Thermal Model Can Help Identify Root Cause of Difference in Thermal Behaviour Like Floating PV (Chapter 7)

This study builds on earlier investigations into convective thermal behavior by examining the reported cooling advantage of floating photovoltaic (FPV) systems. While it is widely believed that FPVs operate at lower temperatures than their ground-mounted counterparts, the physical explanation for this effect remains disputed. Reported performance gains vary significantly across studies, and proposed mechanisms including evaporative cooling, water-as-heat-sink effects, and enhanced wind exposure have not been systematically validated.

To address this gap, a detailed modelling framework was developed using coupled Computational Fluid Dynamics and heat transfer simulation. The model accounts for multiple interacting parameters, including wind speed, direction, ambient and water temperatures, panel tilt, humidity, and proximity to the water surface. The PV module is represented as a layered structure consisting of glass, encapsulant (EVA), silicon, and backsheet materials, with internal heat generation determined from absorbed solar irradiance. The surrounding airflow and water body are simulated using validated boundary conditions and grid convergence techniques.

A comprehensive sensitivity analysis was conducted to isolate the influence of each parameter. Results showed that the presence of water alone does not significantly lower module temperature. The cooling effect from evaporative processes was found to be spatially limited confined to a narrow "vapor blanket" extending only a few centimetres above the water surface. In contrast, wind driven convection emerged as the primary factor influencing temperature reduction. FPV modules positioned with adequate clearance and exposure to wind exhibited surface temperatures up to 2 °C lower than obstructed configurations. Changes in ambient air temperature also contributed to cooling but with a weaker effect than airflow velocity. The model also allowed for comparative testing of different plant layouts and installation geometries. Scenarios with parallel module rows, variations in tilt, and different module spacings were simulated to assess the interaction between flow behaviour and thermal response. It was observed that thermal performance is highly sensitive to wind obstruction and circulation patterns around the module surfaces. Modules shielded from airflow showed higher operating temperatures, regardless of proximity to water.

In summary, the modelling confirms that enhanced convective cooling primarily due to wind is the dominant factor behind the observed temperature advantage

of FPV systems. While water bodies can contribute marginally through local microclimate effects, their role appears secondary. This insight clarifies longstanding ambiguities in the literature and provides a validated, physics based explanation that supports more reliable prediction of FPV energy yield.

1.5 Structure of the Dissertation

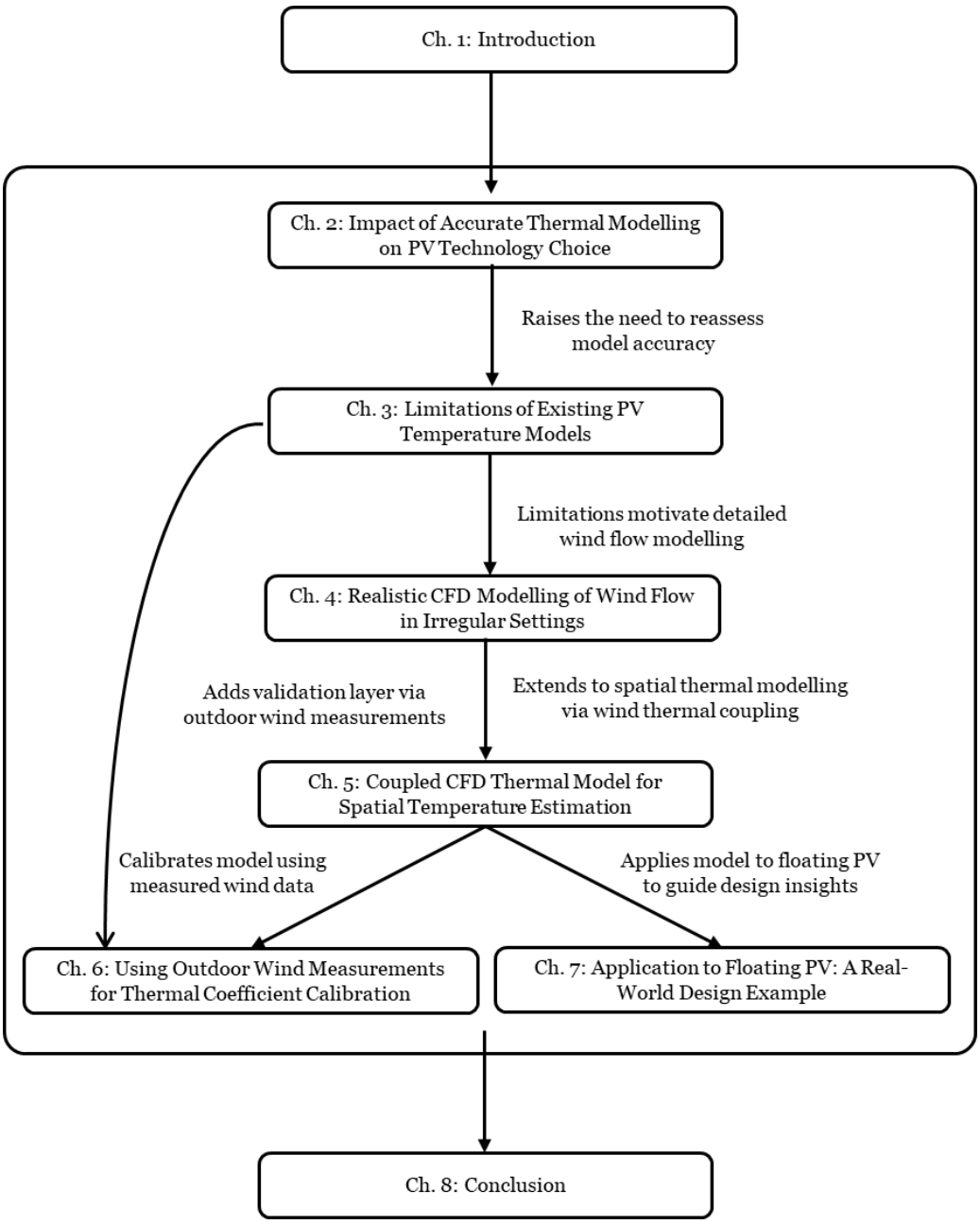

Figure 1-2: Sructure of the Dissertation

2 Impact of Accurate Thermal Modelling on PV Technology Choices

2.1 Motivation and Organisation

This chapter focusses on one specific question: how much do temperature coefficients matter when comparing photovoltaic (PV) technologies under identical modelling conditions? The broader motivation, already introduced in Chapter 1, is that thermal behaviour though often secondary in modelling tools has direct consequences for energy yield. Here, we isolate that effect by holding the simulation framework constant and varying only the cell parameters.

The study uses a fixed modelling environment, already validated in prior work, where all inputs irradiance, ambient temperature, wind speed are uniform across different cases and across the entire PV cell [22]. Only the cell parameters of the PV cells differ. Four representative of mainstream silicon-based cell types are selected: three commonly used (BSF, PERC, PERT), and one state-of-the-art variant (SHJ-IBC). All comparisons are performed at the cell level, not the module level, to remove packaging effects from the analysis.

At this point, a question naturally arises. Why restrict the selection to just these four? There are, after all, many more technologies available commercial and experimental. The answer is deliberate. This chapter does not seek to define an optimal technology. Nor does it intend to suggest that these four are exhaustive or superior. The goal is different. It is to show that even small differences in cell parameters, particularly the thermal coefficients, can produce large shifts in simulated performance. And more importantly, to highlight what this means for modelling practice.

The implications are not subtle. Across different climatic conditions, a cell that performs well under one set of assumptions may fall behind when thermal sensitivity is accounted for. A technology with a 0.30%/°C loss may seem similar to one with 0.36%/°C in isolation. But over a multi-year simulation in a hot climate, the gap becomes material. In terms of financial modelling, site selection, and long term yield estimation, this difference can shift design priorities.

One could assume that improving cell temperature coefficients is the natural solution. And to some extent, it is. But that's only part of the story. The other part the one less often addressed is how we model those coefficients in the first place. Most energy yield simulations apply steady-state approximations. These ignore transient thermal effects. They assume temperature is uniform across a module. They assume wind acts in predictable, scalar ways. These simplifications, while convenient, will obscure the real thermal dynamics of a system in operation.

In this chapter, none of those complexities are introduced yet. That is intentional. Here, the thermal model is treated as reliable. This is a controlled case. We test what happens when you change only the input parameters the cell data while leaving everything else untouched. What follows is a set of results that serve less as a final answer and more as a provocation. If such differences arise under stable modelling conditions, what happens when the model itself is unstable? That latter equally important question becomes central in the next chapter.

In summary, this chapter does not claim that SHJ-IBC is best. Nor does it argue against any other mainstream conventional technologies. It makes a simpler point, but one that carries weight: the choice of technology cannot be separated from the assumptions embedded in how we simulate it. If thermal effects are poorly captured, even the most advanced cells may underperform. Conversely, modest technologies may be overestimated if their limitations are masked by overly simplistic models. Both modelling and material science must be developed together.

Apart from this, the summary we derive is purely based on cell parameter differences: Our results show that the better temperature coefficient of technologies like SHJ-IBC plays a significant role in energy yield output especially in climates with higher insolation and higher temperature conditions. In colder climates however, cell technologies with higher temperature coefficients and lower shunt resistance perform better due to a better response

at low illumination and the lower ambient temperature. However, these trends are affected by seasonal variations and the best performing technology can therefore be dependent on the season for certain climates. Our simulations show that a single technology can be the most suited for some climates, whereas in other geographical locations a combination of different technologies which leads to a balanced seasonal energy yield is the best. We conclude our study by presenting a global map with suggestions of which cell technology is best from an energy yield perspective depending on the local climate's average daily insolation and temperature. This map clearly shows the large potential of the high temperature coefficient technologies like SHJ-IBC over a significant portion of the globe.

2.2 Chapter Specific Introduction and State of Art

Photovoltaic energy is intermittent. It depends on widely fluctuating meteorological conditions like irradiation, ambient temperature, wind speed, wind direction, and other technical specifications. Apart from irradiance, PV performance is also highly influenced by cell operation temperature [41]. Hence, research is being conducted to reduce the influence of operating temperature on PV performance. One of the most promising upcoming PV technologies in that respect is the SHJ IBC cell technology. Therefore, it is necessary to investigate the potential increase in energy yield of this state of the art SHJ IBC cell technology for various geographical locations and climates in comparison to the other major silicon-based cell technologies. Among the commercially available cell technologies BSF, PERC, PERT cells are expected to dominate in the coming decade and hence we have selected these technologies for comparison [42]. One way to evaluate cell technologies is through field measurements. These experiments take a long time and extensive resources. Moreover, it is challenging to explore novel cell technologies like SHJ-IBC in outdoor conditions, mainly because commercial modules of these technologies are not available yet or hard to get. Therefore, even though SHJ-IBC modules are still not commercially available, this study aims to explore its potential through use of a state-of-the-art energy yield analysis model, developed by imec and already used and validated in earlier works [22], [23], [24], [26], [27], [28], [43], [44], [45], [46]. This chapter compares all major silicon-based PV technologies with SHJ IBC at the cell level through imec's simulation platform. Our results will guide global utility PV companies in making better decisions on which technology to use where and will support PV power plant optimisation with different cell technologies tuned to both seasonal and regional changes. Finally,

this chapter identifies the regions where SHJ-IBC is the best suited technology from an energy yield perspective and presents this information in the form of a global map.

2.3 Description of Different Cell Technologies

SHJ-IBC combines the advantage of both heterojunction and back-contacted cells. The amorphous silicon heterojunction solar cell was patented, developed and commercialised by Sanyo (later transferred to Panasonic) already a long time ago. Thanks to its high quality surface passivation, surface recombination can be minimised and a high V_{oc} can be realised, especially for very thin cells [48]. The IBC structure on the other hand allows to remove the front side metallisation, thus allowing maximal light transmission into the cell and maximising current generation. This back-contact cell concept was also already developed and commercialised into modules in the past, and has been delivering the highest performance for commercial PV modules in the market since quite some time [49]. Combining the heterojunction-based surface passivation with the typical IBC back-contact structure recently led to SHJ-IBC cells exhibiting a world record energy conversion efficiency for crystalline silicon single-junction solar cells at 26.6 % [50]. For the current chapter SHJ-IBC cell data came from the published literature [51]. An illustration of the cell architecture is shown in Figure 2-1. As for BSF, PERT and PERC, cell data parameters were taken from reference [44]. All the cell parameter details used in the simulation are provided in Table 2-1.

Table 2-1: Summary of modelled solar cell parameters

	J_L (mA·cm^{-2})	J_o (fA.cm^{-2})	n	R_s (Ω.cm^2)	R_{sh} (Ω.cm^2)	β_t (mV. °C^{-1})
SHJ-IBC	41.18	8.16	0.99	0.376	2305	-1.79
n-PERT [47]	39.41	25.33	0.95	0.662	1449	-1.81
p-PERC [47]	38.57	57.04	0.93	0.786	913	-1.85
Al-BSF [47]	37.06	135.02	0.94	0.824	702	-1.94

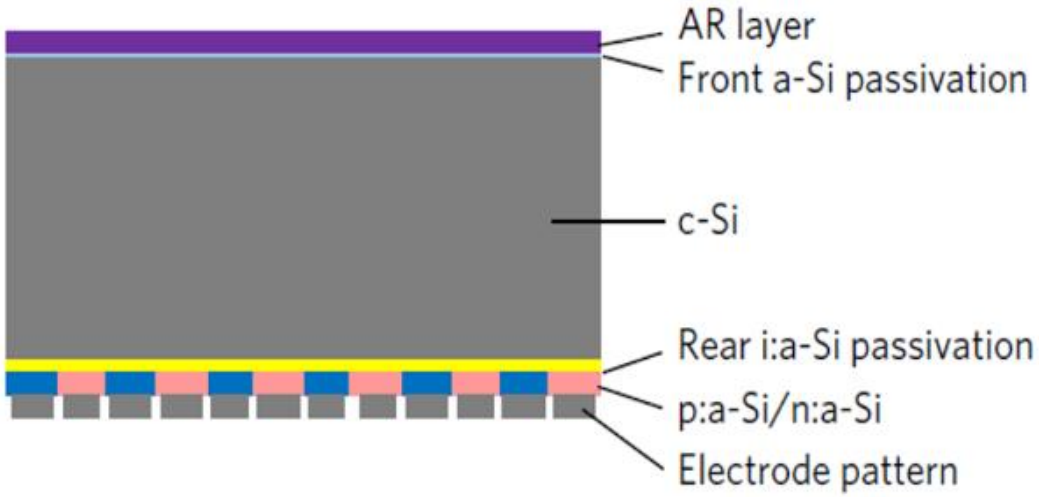

Figure 2-1: Illustration of SHJ-IBC cell structure

2.4 Climatic Datasets

For this comparative study, we had access to four high-resolution climatic datasets to represent the hot, sunny and cold climatic region selected [52]. These databases provide a basis to compare the cell technologies ranging from hot & dry to cold & wet conditions. As SHJ-IBC has an improved temperature coefficient performance, it is necessary to test its energy yield performance where cells are expected to have high, moderate, and low temperatures. Details of the selected weather profiles are provided in [52]. The POA irradiance was generated using GHI and DHI. All four of the chosen locations had comparable elevation over sea level. However, all four of them have different climatic profiles. Ottawa (Canada) had a 14% higher annual insolation compared to Genk (Belgium) but lower average ambient temperature (GHI weighted), as calculated via equation 1. The effect of such variations in climate on cell technology performance will be described in the latter part of the text.

$$GHI\ weighted\ T_{amb} = \frac{\Sigma_{i=1}^{N}(T_{amb,i} \times GHI_i)}{\Sigma_{i=1}^{N} GHI_i} \qquad \text{Eq 1}$$

In some climatic datasets WS, WD, and ambient temperature were recorded with 15 minutes averaged resolution. To generate correct interpolation, the dynamics of the thermal system was studied. It was concluded that temperature of the PV module is not sensitive to any variation to the thermal circuit lower than 13 minutes 20 seconds. Therefore, highly varying wind conditions below 13 minutes 20 seconds for the thermal model in the energy yield modelling framework would provide the same result if the average value between that

interval was taken. For a more detailed explanation of the process, we refer to [53]. This method was implemented only on Italy (Catania) wind data. For the rest of the climatic datasets, higher resolution dataset was interpolated to one minute.

Table 2-2 Overview of different climatic location

Location	Tilt angle [°] [54]	Köppen-Geiger climate classification [55]	Altitude over sea level [m]
Canada (Ottawa)	37	Dfb (Cold, no dry season, warm summer)	62
Belgium (Genk)	35	Cfb (Temperate, no dry season, warm summer)	78
Italy (Catania)	27	Csa (Temperate, dry summer, hot summer)	20
Kuwait (Jahra)	26	BWh (Arid, desert, hot)	237

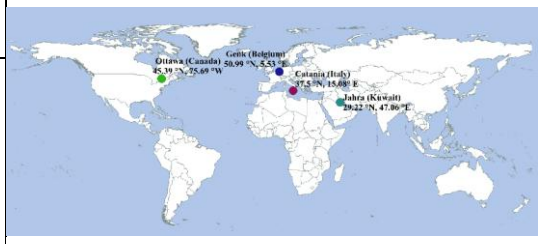

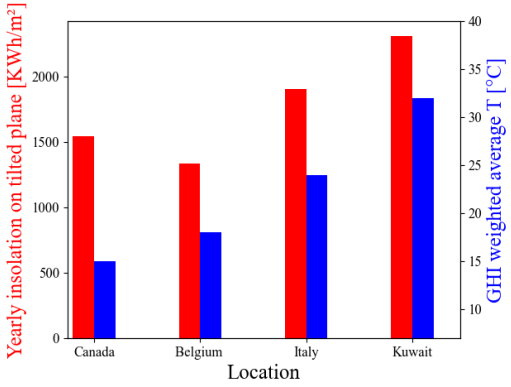

2.4.1 Canada (Ottawa)

Canada dataset was from Carleton University, Ottawa. The dataset used in this study was from 20th August 2017 to 19th August 2018. The dataset contained a minute resolution of GHI, DHI, DNI, WS, WD, and ambient temperature [56].

2.4.2 Belgium (Genk)

Belgium dataset was from the EnergyVille-1 campus located in Genk. The test setup is monitored by KU Leuven and imec. This dataset contains GHI, DHI, WS, WD, ambient temperature. The dataset is from 2nd July 2018 to 1st July 2019. All the properties were measured with a temporal resolution of 1 minute.

2.4.3 Italy (Catania)

The Italy dataset was provided by Enel Green Power from a site in Catania (Passo Martino, Zona Industriale). It contains GHI, DHI, DNI, WS, WD, RH, and ambient temperature. The dataset is from 18th May 2017 to 15th May 2018, which is three days short of one full year. Therefore, the missing data 15-18th May 2018 was generated assuming weighted persistence. The assumption was that the weather for those three days was equal to the previous days. The GHI, DHI, and DNI were recorded with a temporal resolution of one min. However, the WS, WD, and ambient temperature were recorded with 15 min temporal resolution. Therefore, the dataset was homogenised and synchronised to obtain a dataset of one-minute resolution.

2.4.4 Kuwait (Kuwait City)

The Kuwait dataset was from the Shagaya renewable energy park provided by Kuwait Institute for Scientific Research (KISR). This dataset contains GHI, DHI, DNI, WS, WD, ambient temperature, relative pressure, relative humidity. The dataset is from 1st January 2014 to 31st December 2014. All the properties were measured with a temporal resolution of 1 min. [44]

2.5 Energy Yield Simulation Framework

In this study, imec's advanced energy yield simulation framework was used to compare the performance of different PV cell technologies under different climates. This approach is used firstly to compare the impact of cell technologies in an unclouded manner, and lastly, it is significantly faster than outdoor tests. The simulation framework is an Electrical, Optical, and Thermal (EOT) model based on meteorological inputs like irradiance, ambient temperature, wind speed and wind direction. PV cell and module properties are defined within the EOT framework. Cell technology parameters (Table 2-1) were used as input to evaluate performance in a hypothetical PV installation in four different climates.

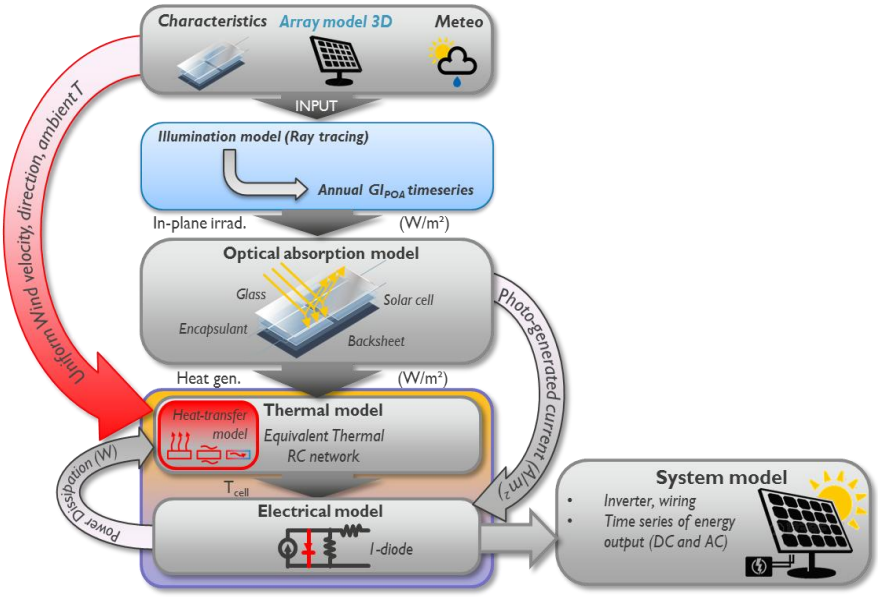

Figure 2-2: Schematic overview of IMEC's PV energy yield simulations framework

In Figure 2-2, the high-level overview of the EOT modelling framework is shown. Combined with high-resolution meteorological input and the physics-based model provides increased accuracy for different cell technology simulations. For the experimental validation of this model and detailed explanation, we would refer to [22], [23], [24], [25], [26], [27], [28], [44], [45], [46], [57], [58]. SHJ IBC cell technology is still not available in a commercial PV module format; therefore, to analyse the advantage of a different generation of silicon cell technology, PV module and system-level power loss were not considered. Instead, we studied hypothetical ground-mounted glass back sheet PV modules of 60 cells. They are composed of glass, an encapsulant (EVA), solar cells, an encapsulant (EVA) and glass. The layup and the thickness of the different layers are provided in Figure 2-2 and Figure 2-3. All the thermal

properties of these layers are kept constant for different technology simulations to compare cell technologies objectively. The simulation is done for monofacial configuration. Therefore, no light coming from the rear side is considered. The PV module orientation was south (180°). The optimal tilt angle was selected based on the location-specific optimised annual energy yield [54]. The compared power output throughout the study is the available power at MPPT.

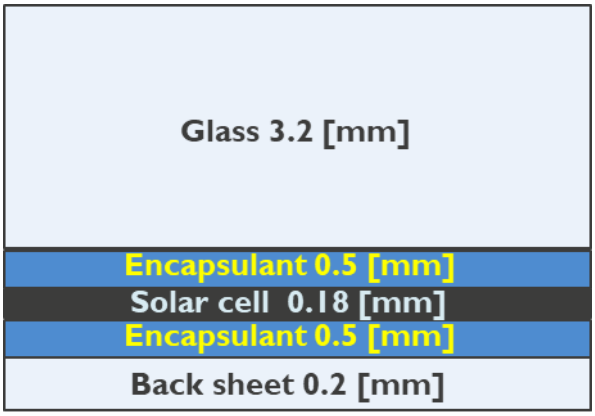

Figure 2-3: Module cross section layout

2.6 Results and Discussion

This section analyses the energy yield simulated for SHJ-IBC cells at different climatic conditions and compares it with other Si PV technologies available in the market. With these results, we emphasize the need for climate-based technology deployment for better energy yield and identify a suitable deployment zone for SHJ-IBC PV technology worldwide.

2.6.1 Energy Yield Analysis

Figure 2-4 shows the energy yield simulated for the four different Si cell technologies at four different climatic conditions. We can see that the SHJ-IBC cell performs much better than other technologies in Kuwait, Italy, and Belgium, whereas, in Canada, n-PERT performs on par with SHJ-IBC. This clearly shows the general superiority of SHJ-IBC over other technologies. To identify the reasons for the better performance of the SHJ-IBC cell technology, we will analyse the yield data in-depth to understand the variation in behavior of different cell technologies at various operating conditions. The energy yield difference with respect to the SHJ-IBC technology is plotted in Figure 2-6 for the three other cell types as a function of the different seasons and the different locations.

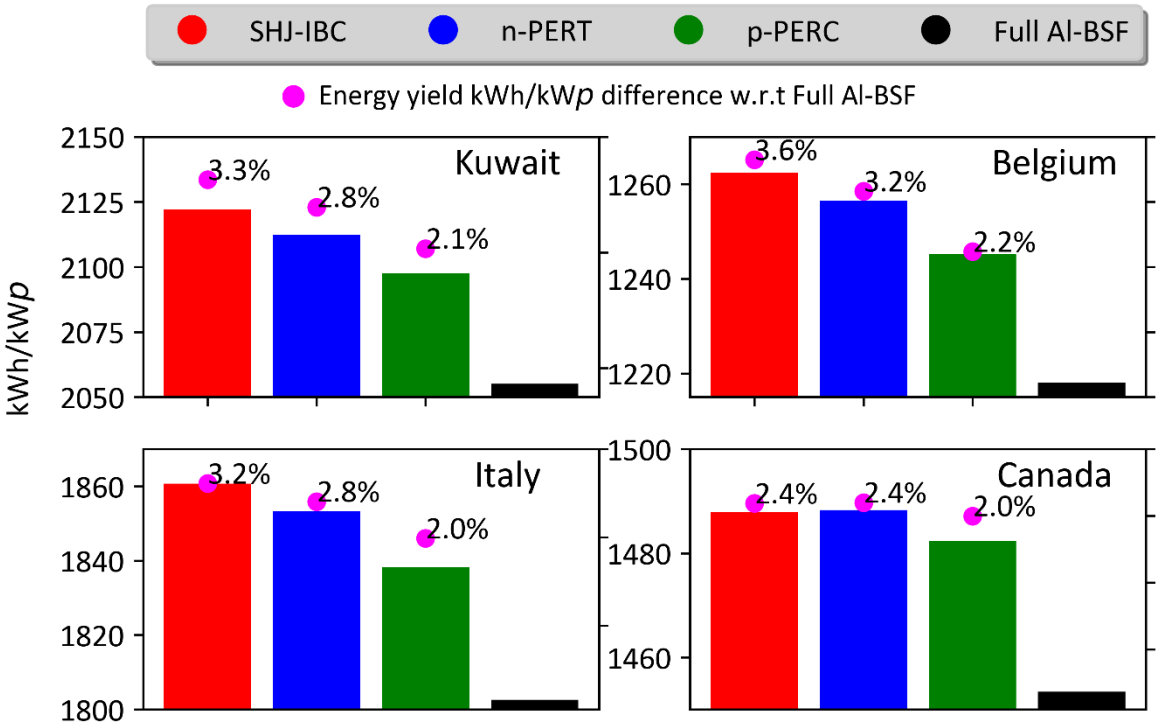

Figure 2-4: Energy yield simulated for SHJ-IBC, n-PERT, p-PERC and Full-AL-BSF for four different locations, Kuwait, Italy, Belgium and Canada.

Figure 2-6 a shows that in Kuwait, SHJ-IBC outperforms all the other technologies throughout the year. The primary factor that comes into play here is the low temperature coefficient of the SHJ-IBC solar cells. In the spring, summer, and autumn months, where the average temperature is high, the energy yield performance of the various solar cell technologies is in line with the difference in their temperature coefficients (see Table 2-1). The same trend is also seen in Spring, Summer and Autumn of Italy (Figure 2-6b) and Belgium (Figure 2-6c), while the trend slightly changes in Canada (Figure 2-6d).

In Winter, the performance of SHJ-IBC to other technologies) improves with decreasing insolation for Kuwait (5.49 kWh/m^2), Italy (3.93 kWh/m^2) and Belgium (1.61 kWh/m^2). However, in Canada (2.59 kWh/m^2) during Winter, n-PERT and p-PERC cells produce a higher kWh/kW$_p$ energy yield compared to SHJ-IBC.

To gain additional insights from the yield data, we plotted the best-performing cells in a day against the average operating conditions on that day in Figure 2-5. A day is identified by the plane of array insolation and average ambient temperature.

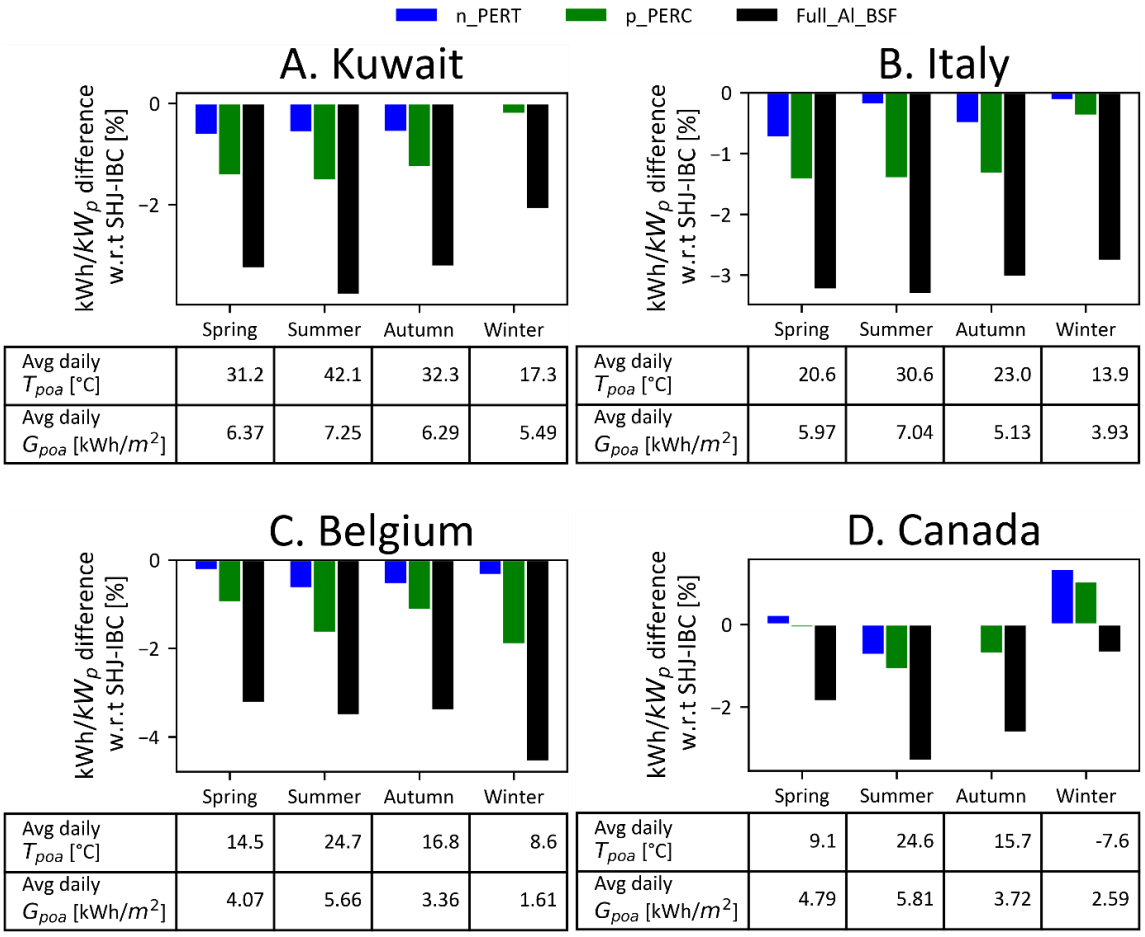

A. Kuwait	Spring	Summer	Autumn	Winter
Avg daily T_{poa} [°C]	31.2	42.1	32.3	17.3
Avg daily G_{poa} [kWh/m^2]	6.37	7.25	6.29	5.49

B. Italy	Spring	Summer	Autumn	Winter
Avg daily T_{poa} [°C]	20.6	30.6	23.0	13.9
Avg daily G_{poa} [kWh/m^2]	5.97	7.04	5.13	3.93

C. Belgium	Spring	Summer	Autumn	Winter
Avg daily T_{poa} [°C]	14.5	24.7	16.8	8.6
Avg daily G_{poa} [kWh/m^2]	4.07	5.66	3.36	1.61

D. Canada	Spring	Summer	Autumn	Winter
Avg daily T_{poa} [°C]	9.1	24.6	15.7	-7.6
Avg daily G_{poa} [kWh/m^2]	4.79	5.81	3.72	2.59

Figure 2-6: Seasonal variation in energy yield of n-PERT, p-PERC and Full-AL-BSF with respect to SHJ-IBC for A) Kuwait, B) Italy, C) Belgium, and D) Canada. The Table under each graph gives the average ambient temperature and average insolation for that location in a season.

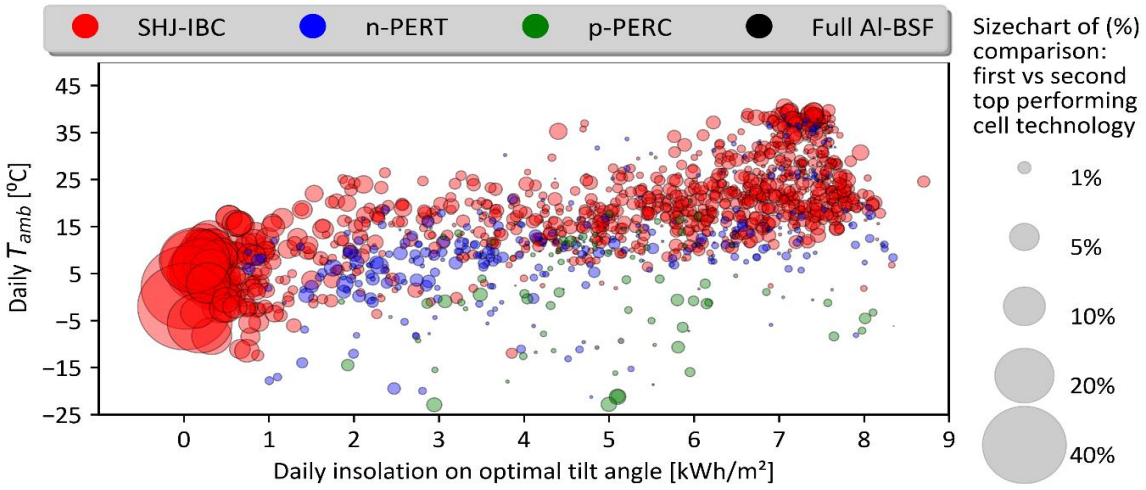

Figure 2-5: Cell technology performance with daily total irradiance and average ambient

The magnitude of a cell's performance compared to the second-best on the same day is represented by the size of the data point and it can be read with the area of the circle indicated in the legend. The figure offers clear zones of operation for the different technologies. The SHJ-IBC dominates the region in two segments, namely where daily insolation is between 0-1 kWh/m^2, and where daily T_{amb} is higher than 15°C at 1-8 kWh/m^2. The n-PERT on the other hand performs the best where the average daily insolation is in the range of 1 - 5 kWh/m^2 and average ambient temperatures are within 5 and 15°C. Besides that, p-PERC exhibits a unique behaviour too. It performs best when there is comparatively higher insolation and very low daily T_{amb}. This kind of day type is common in high-altitude mountains, on continental North American plains and in northern Russia. Out of the entire dataset, the Full Al-BSF extremely rarely performs as the best among all the four technologies. There are two parameters that correlate with the observed behaviour of each technologies: The temperature coefficient of V_{oc} (β_t) and the shunt resistance (R_{sh}).

The temperature coefficient of V_{oc} is an essential factor for deciding the energy yield as it has a significant effect on the power. Figure 2-7 (a) shows the variation in the peak power for other technologies at 1000 W/m^2 over a wide range of module temperatures. The data in the graph is normalized peak power for different operating instances at 1000 W/m^2 across all four locations simulated. The normalized peak power used here is the ratio of power simulated to power at STC. We observe that the lower the temperature coefficient, the higher the performance above module temperature of 25°C. Thus SHJ-IBC technology with the lowest temperature coefficient dominates at high temperature regions. Whereas for the module temperatures below 25°C, the trend reverses and modules with high temp coefficient have the upper edge. This explains the advantage of n-PERT and p-PERC over SHJ-IBC during winter in Canada. So, the temperature coefficient of Voc explains the trend seen in Figure 6 across the y-axis.

To understand the higher performance of the SHJ-IBC solar cells at days with very low irradiation (<1kWh/m^2), we plotted the conversion efficiency of different technologies at 25 °C against the irradiance in Figure 7b. The graph also contains an additional data for SHJ-IBC but with a low shunt resistance of 1000 Ω.cm^2 for comparison. At low irradiance, the conversion efficiency increases with increase in shunt resistance.

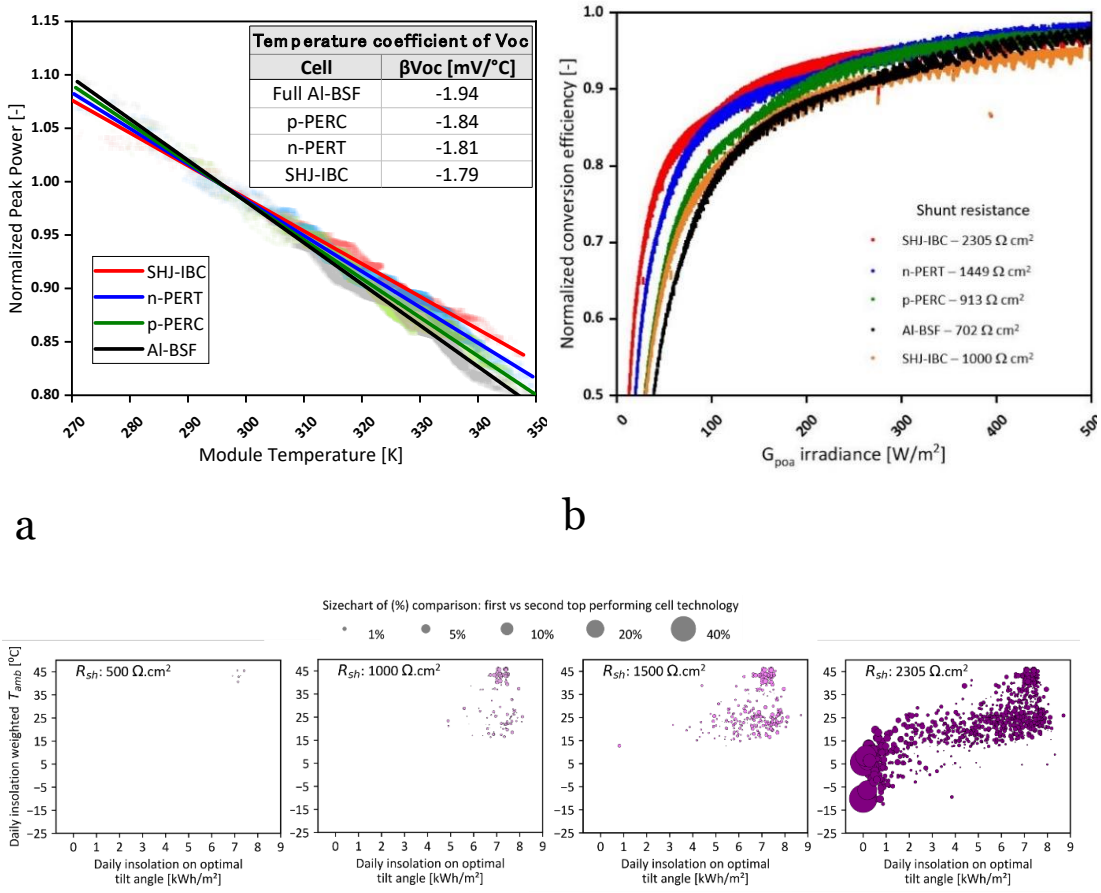

Figure 2-7: a) Variation of normalised peak power with module temperature for different cell technologies. The graph is obtained by using simulated data points of different technologies at various instances of 1000 W/m² and fit with linear regression. The inset table quotes the V_{oc} temperature coefficient of different cell technologies. b) Cell technology in low illumination conditions - conversion efficiency at 25°C c) SHJ-IBC shunt resistance sensitivity

We can also observe that as the irradiance increases, the conversion efficiency of the n-PERT, n-PERC are in par with SHJ-IBC. As the shunt resistance increases, the shunt leakage reduces at low illumination. This leads to a higher rate of efficiency drop in a cell with low shunt resistance. SHJ-IBC cells with high conversion efficiency have less thermalization heat compared to other technologies, and therefore they always exhibit lower module temperatures than other technologies. In SHJ-IBC with low shunt resistance (1000 Ω.cm²), conversion efficiency drops faster at low illumination. The drop in conversion efficiency increases the thermal losses, which is the major contributor to module temperature. This effect reduces module temperature differences among the cell technologies, thus reducing the advantage that SHJ-IBC had over other

technologies. Thus, the combined impact of high temperature coefficient and low shunt resistance causes other technologies to perform better than SHJ-IBC (1000 Ω.cm²) at low temperature and illumination regions. Figure 7c show the results of the sensitivity analysis of SHJ-IBC technology. As the shunt resistance improved, the energy yield performance of the technology improved considerably at low insolation regions. Figure 7b and c confirms the significance of shunt resistance at low irradiance conditions.

2.6.2 Suitable Zones for Technology Deployment

There are two general conclusions that be drawn from Figure 2-5. Firstly, the cell technologies perform in a predictable and yet in a variable magnitude. They do not have a constant or linear performance throughout a different matrix of day types. Secondly, cell parameters determine how a specific cell technology performs on days with different weather conditions. These two insights can be used to tune cell parameters and a combination of technology types for seasonal or yearly performance objectives.

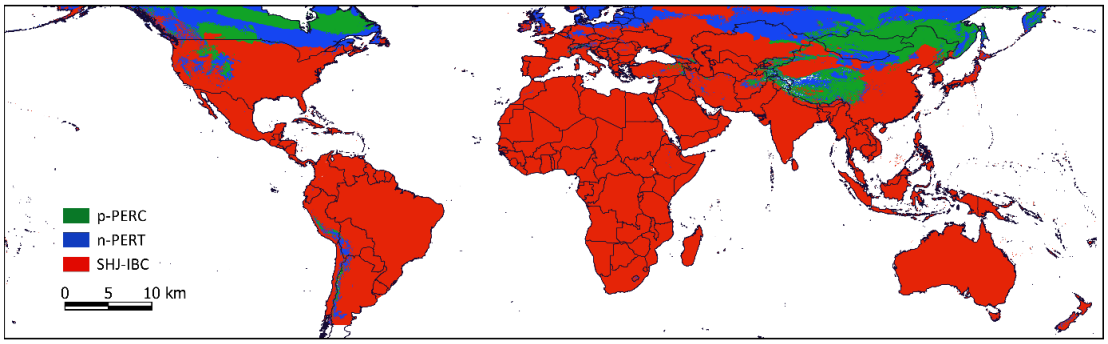

Figure 2-8: World map overlap of different cell technology performance with daily average insolation and ambient temperature

To have a broader perspective on the suitability of deployment of different technologies, a world map portraying climatic zones was made in Figure 2-8. However, some caution is suggested to interpret the results portrayed in this figure. The map is based on two data sets from Solaris, containing average daily ambient temperature and average daily insolation on optimal tilt angle [59]. Figure 2-5 data points are translated on a global scale in Figure 2-8. The different colors indicate different zones where a specific cell technology is performing best for a yearly average. It can be noticed that SHJ-IBC is best suited for deployment on an annual scale in a significant part of the world. From the earlier analysis, SHJ-IBC performs the best high insolation and high ambient temperature zones. In contrast, n-PERT performs well in most

insolation zones, which also have a moderately colder climate. However, p-PERC takes over n-PERT in day types with much lower ambient temperature zones. This analysis is conducted on yearly averaged data, which means this pattern would change for seasonally averaged insolation and ambient temperature maps. In summer, SHJ-IBC would increase its zones. Whereas in the wintertime, n-PERT and p-PERC would increase their shares. However, such seasonal data was not available in open source to explore these scenarios on a map. From the yearly averaged data, this study concludes that SHJ-IBC technology can be deployed to a significant part of the world and is clearly the future technology in regard to better energy yield performance.

2.7 Chapter Summary

This chapter has examined how thermal sensitivity at the cell level specifically temperature coefficients influences energy yield across climates. The exercise was not intended to produce final rankings of specific photovoltaic (PV) technologies, nor to recommend a specific cell architecture. Rather, by holding the modelling environment constant and focusing only on four silicon-based technologies, the aim was to understand how small differences in thermal behaviour can scale into larger yield variations when considered over time and across geography. In addition, the impact of the temperature coefficient value on selecting a technology for a given climate is studied.

The results, drawn from simulation across Kuwait, Italy, Belgium, and Canada, revealed patterns that were at once consistent and conditional. In warm and irradiance-rich regions, particularly Kuwait, high temperature coefficient technologies like SHJ-IBC consistently performed better. This advantage extended to Italy as well, regardless of season. The performance gain in these locations can be traced, mostly, to the superior temperature coefficient. Consequently, its output declines more slowly as the module heats. But that is only part of the explanation. Secondary conclusion from this study is that cell technologies response to low light condition regulated by shunt resistance can also be a driving force for optimal choice of technology.

Belgium presented a different case. The low annual insolation and high frequency of overcast days did not penalize SHJ-IBC. Quite the opposite. Here, it outperformed the others, even though irradiance levels were modest. This cannot be attributed to temperature coefficient alone. The likely contributor is improved shunt resistance and the device's ability to function more stably under diffuse or highly variable light. In contrast, the Canadian dataset produced no

dominant outcome. Despite higher annual irradiance than Belgium and lower ambient temperatures, SHJ-IBC did not consistently outperform the technologies with lower temperature coefficients. On some days, n-PERT and p-PERC showed better results. The deciding factor appeared to be the daily interplay between temperature, irradiance intensity, and its stability across hours.

Seasonal transitions were not abrupt. There was no clear boundary where one cell type ceased to perform and another took over. Rather, there was a difference. Below an average daily temperature of 15°C, and with daily insolation between 1–8 kWh/m², the PERT and PERC cells gained ground. As temperatures rose above that mark, especially under strong, consistent sun SHJ-IBC began to show a clearer margin.

From this, one general conclusion can be drawn. PV technology selection should not be decoupled from climatic conditions. Nor should it rely solely on nameplate efficiency or nominal coefficients. Even within a single climate zone, seasonal shifts can tilt performance in favour of one cell structure over another. And while high temperature coefficients may offer advantage in hot climates, the yield implications in colder regions depend more on other cell parameters.

A global suitability map was presented as part of this work. It is not prescriptive. It does not state that SHJ-IBC must be used in certain regions. What it does show is where this particular technology has a higher likelihood of delivering better energy yield, assuming the modelled conditions reflect reality. The map is illustrative of a broader point: performance differences cannot be meaningfully assessed without reference to context. Climate, not only efficiency metrics, defines technological advantage.

The underlying argument of this chapter is methodological. Cell parameters matter. But how we model cell parameters matter too. Inaccurate or overly simplified thermal modelling may flatten differences that in reality are decisive. In this chapter, we assumed the model was sound. The variations in yield were attributed solely to the cell coefficients. But in practice, these coefficients interact with wind, irradiance quality, tilt, mounting, and more. Their influence is conditional, not absolute.

The next chapter will take this premise further. If even in a controlled model, small differences in cell thermal behaviour produce significant shifts in energy yield, then what happens when the thermal model itself is put under scrutiny? That is the question ahead.

3 Evaluating the Role of Forced Convection in PV Temperature and Yield Modelling

3.1 Motivation and Organisation

Previous chapters established the dependency of accurate thermal modelling perspective for PV energy yield simulation. Chapter 2 in particular demonstrated that small deviations in thermal assumptions can shift the ranking between technologies, potentially altering design decisions. Yet, in practice, temperature modelling remains a secondary concern in most forecasting tools, often reduced to fixed formulations with minimal input demand. These simplifications persist not due to ignorance, but for reasons of legacy, convenience, and computational cost. However, the margins of tolerance are now narrower. On a simplified calculation for a 500 MW PV plant: A 4.5% overestimation due to poor temperature and input modelling accuracy could result in a $1.68 million/year overprediction in expected revenues (based on $0.05/kWh and 1500 kWh/kWp/y) [11]. Therefore, in the context of modern PV development as stated in the introduction, such reductions can no longer be sustained.

This chapter examines one of the most overlooked elements in PV temperature modelling: the effect of forced convection, i.e. wind. Although its presence in energy balance equations is acknowledged, its treatment is usually largely simplified. Empirical constant coefficients are assigned, sometimes based on measurement campaigns, more often copied from earlier literature. The nature of wind, its fluctuations across time and terrain, and its ability to create localized cooling, all these are either ignored or merged into a single constant parameter.

Whether this treatment is sufficient was not obvious. In this chapter we will show a motivated answer to this important question.

To assess the magnitude of the omission, we begin with a direct comparison between simulations and outdoor measurement campaign. The setup was straightforward. Two simulation runs were performed using the validated imec's energy yield model [28], [60]. In the first, the heat transfer coefficient was modelled as a function of wind speed. In the second, it was held constant. Both cases were evaluated against long-term outdoor data collected over 176 days, with high-resolution logging. The results were clear. When wind was neglected, the energy yield simulations produced a daily energy yield relative error exceeding 50%. Including wind reduced that to under 3%. And as the temporal resolution increased, hourly, sub-hourly, down to 10-second intervals, the discrepancy widened. It became clear that wind does not only matter, it matters most when one wants to resolve yield at lower granular timescale.

But precision is not only a matter of whether wind is included. It is also a matter of how it is included. The second section of this chapter evaluates that question in depth. A total of ten highly cited and implemented PV temperature models were selected, and one transient formulation using a weighted moving average (WMA) which is implemented in PVLib python package by Sandia. These were benchmarked across a range of timescales, from yearly aggregates to sub-minute intervals. The outcome of this evaluation was more complex. All models showed sensitivity to time resolution. In many cases, the error in predicted module temperature ranged from less than a degree to over 30°C. Such variation is not a statistical detail. It directly influences energy yield prediction.

What explains these deviations? The issue is not merely the structure of the models but also the assumptions they embed. Most steady-state formulations rely on average irradiance and ambient temperature, treating wind as either a fixed input or a secondary correction. Some include wind speed explicitly, yet fail to resolve its temporal character. The WMA model, by contrast, incorporates thermal history and allows recent past values to shape the current estimate. It showed improved performance, especially on semi-cloudy days where irradiance and wind vary sharply. But this improvement was not universal. On clear days with stable conditions, some of the simpler models performed just as well.

A further layer of insight came from disaggregating the error by meteorological regime. Days were manually classified into sunny, semi-cloudy, and overcast. Here, it became evident that model performance is highly context-specific. Some

models such as Faiman's calibrated version, performs well on sunny days but degraded under variable sky conditions. Others, such as Skoplaki or Mattei, display higher resilience across different day types, though none shows uniform accuracy. Across all models, the magnitude of deviation is larger during periods of lower wind speed. This suggests a structural underestimation of forced convection, particularly when its effects are subtle but persistent.

The practical implication is that most commonly used temperature estimation methods are tuned to ideal or static scenarios. Few have been stress-tested under transient or fluctuating inputs. And yet, these are precisely the conditions that define real PV operation. The effect is cumulative: under-predict cell temperature, and one overestimates power. Do this systematically, and long-term yield assessments become heavily skewed.

At this point in the thesis, the rationale for more physically grounded models becomes unavoidable. It is not simply a matter of improving accuracy; it is about exposing the assumptions that currently shape design tools and performance guarantees. Most existing models, while useful in certain contexts, fail to account for the spatial and temporal heterogeneity of convective effects. The consequence is not just thermal deviation, but financial risk.

The work here does not claim final results. It does, however, make one assertion clearly that the modelling of PV module temperature, particularly in the presence of wind, cannot remain as it is. The systems are changing, the environments are more variable, and the performance expectations are sharper. Our models must follow.

3.2 Chapter Specific Introduction and State of Art

The cell temperature of the PV module depends on a combination of heat conduction, convection and radiation from within the module towards the environment. Many studies already showed the significant effect of wind on solar cell temperature [22], [24]. Wind removes heat from the top and bottom of the solar PV module by forced and natural convection. The type of convection that dominates also varies in function of wind speed and direction. Several published studies describe heat transfer characteristics from the module towards the environment in scenarios with varying wind flow condition and mounting structure [24], [34], [39], [61], [62]. Moreover, that heat transfer characteristic is spatially variable over the PV module subjected to wind [27].

Although extensive research has been carried out on the effect of wind on PV, there is a lack of understanding on how sensitive PV module's temperature and energy yield estimation are to changes in wind conditions [22], [24]. That is also directly related to the sensitivity to potential errors, which provides essential insights to develop accurate energy yield simulation. Therefore, this study focuses on the sensitivity of the PV module's temperature and energy yield to forced convection.

Secondly, as PV temperature is one of the primary variables to determine PV energy systems performance, this is necessary to have an accurate temperature estimation model. There is an increasing interest in tuning PV energy systems to seasonal variation, load profile, landscape, and building space availability [63]. In such scenarios, short-term energy yield prediction is of crucial importance. Hence, to determine which temperature estimation models provide the best accuracy in different time resolutions is necessary. Equation-based temperature estimation models for PV can be broadly categorized into steady-state and transient, moving average models. Within the steady-state model, the core assumption is that PV module temperature is regulated primarily by the fluctuating weather condition, and the transient thermal capacitance is assumed to be negligible. Steady-state models are valuable and popular due to their lower demand for input variables and simplicity of implementation. Transient models promise to address the thermal capacitance and consider some specific temporal resolution. However, there are always some uncertainties if this temporal resolution must be kept constant or not. To our existing knowledge, no published research tested this hypothesis. Another common assumption is intra-module temperature uniformity or non-uniformity with negligible intra-module temperature variation. Faiman et al. suggested that the intra-module temperature variation from the middle cell to the corner can be limited to 2K [5]. Goverde et al. indicated that the intra-module temperature could be as high as 8K [26]. However, as no steady-state PV temperature models tested in this chapter provide to inspect intra-module temperature variability, therefore for this chapter we will only test the existing PV temperature models assuming that its only one temperature per PV module.

Moreover, steady-state models can be broadly categorized into explicit and implicit models. Explicit models determine PV cell temperature directly, and implicit models that bootstrap on back-sheet temperature determine cell temperature. Multiple review papers have tested the validity of various PV temperature estimation models. However, there is a clear gap in testing PV

temperature estimation models' validity of both steady-state and transient models on different temporal resolutions and day types. This is critical to test any model's extreme limit and range of accuracy. This will support future exploration on which models can be selected to determine PV temperature models adapted to your requirement and computational resources

3.3 Sensitivity Analysis of the Effect of Forced Convection on Photovoltaic Module Temperature and Energy Yield

First, we present our Electrical Optical and Thermal (EOT) PV system Modelling framework, and the experimental setup is described briefly. Secondly, we extract the difference between simulated and measured PV energy yield and cell temperature at different timescale, either considering wind or no wind conditions. Finally, considering wind effects on PV module, further investigation is done to study at which wind conditions PV module's power output and cell temperature are most sensitive to changes. In this case, the PV module's power output and temperature are simulated in steady-state conditions with incremental changes of forced convection. The finding of this latter simulation will be used to understand what degree of accuracy for the heat transfer coefficient induced by forced convection is required for an accurate simulation of the energy yield.



Figure 3-1: Experimental setup in Oldenburg University

3.3.1 Simulation Framework: Electrical Optical and Thermal Model

Imec's Electrical-Optical-Thermal simulation framework allows estimation of the energy yield of silicon solar PV module [22]. The inputs of this model are irradiance, ambient temperature, wind speed and wind direction, next to module material and cell properties. The EOT model simulates electrical output and solar cell temperature as a function of illumination, sky temperature, ambient temperature, wind speed, wind direction, thermal state and electrical operation point with a fine spatial and temporal resolution. We simulated the output of a 72-cell multi-crystalline silicon module for 176 days and compared this to measurement results from the experimental setup installed in the Oldenburg University, located at latitude 53.1523°N and longitude 8.166°E at an inclination 54° facing south [22]. The wind speed and direction were measured with an anemometer installed next to the PV module. This measurement setup is shown in Figure 3-1.

3.3.2 Sensitivity of PV Module Energy Yield and Temperature to Forced Convection Over a Different Period

The EOT model was adapted to simulate two conditions. In Scenario one, simulation includes heat transfer coefficient as a function of wind speed and direction. In Scenario two, constant heat transfer (10 $Wm^{-2}K^{-1}$) over the PV module is simulated, based on the assumption that wind speed and direction do not affect the heat transfer. The measured PV module back sheet temperature and energy yield were compared with simulated solar cell temperature and energy yield.

There were significant differences observed between scenario one and scenario two for the whole data set of 176 days especially when compared in different time resolution, from daily (24 hours) to 10 sec. Root Mean Square Error (RMSE) (1) was used to calculate the deviation where Mi and Si mean measured and simulated values respectively. In Figure 3-2(a). For scenario one with complete EOT where wind effects are considered the relative RMSE of energy yield was 2.8%, which is, to best of our knowledge, currently the most precise energy yield estimation for PV. While for scenario two where no wind effect is considered it can be seen that daily energy yield RMSE is 50%. Such a vast difference between the two scenarios indicate that if the wind is not considered, there is going to be a significant error on energy yield estimation. Moreover, this deviation of energy

yield increases with smaller time resolution, which suggests wind dynamics are important for higher accuracy.

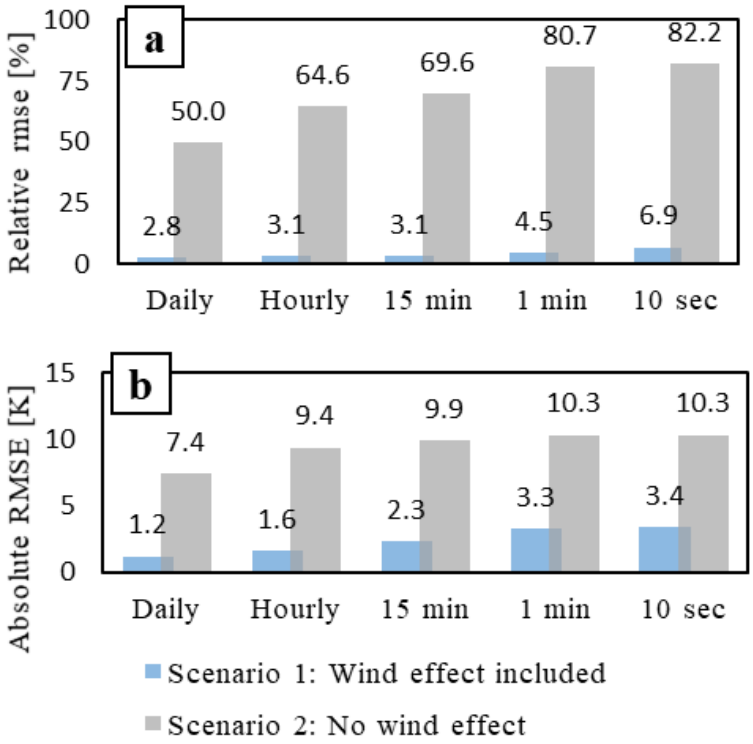

Figure 3-2: (a). Relative energy yield rmse for wind and no wind effect across different temporal resolutions (b). Absolute temperature RMSE for wind and no wind condition

This variation in energy yield estimation can be explained by incorrect cell temperature estimation. From Figure 3-2(b), solar cell temperature daily absolute RMSE was 1.2 K for scenario one. Whereas, for scenario two, with no wind effect included, the deviation is 7.4 K and the deviation increases in smaller time resolution. For 10 sec resolution, the absolute deviation is 10.3 K. This deviation of cell temperature is much more visible when seen for a whole day period. For such daily temperature comparison, measurements during one highly varying day (11th August 2014) were compared with simulated temperature. In Figure 3-3 (a), for scenario one, where wind effects are taken into consideration, the simulated solar cell temperature follows the trend of the measured PV module back sheet temperature quite well. In contrast to that, in Figure 3-3 (b), where no wind effect is considered, there is a considerable difference of simulated and measured temperature.

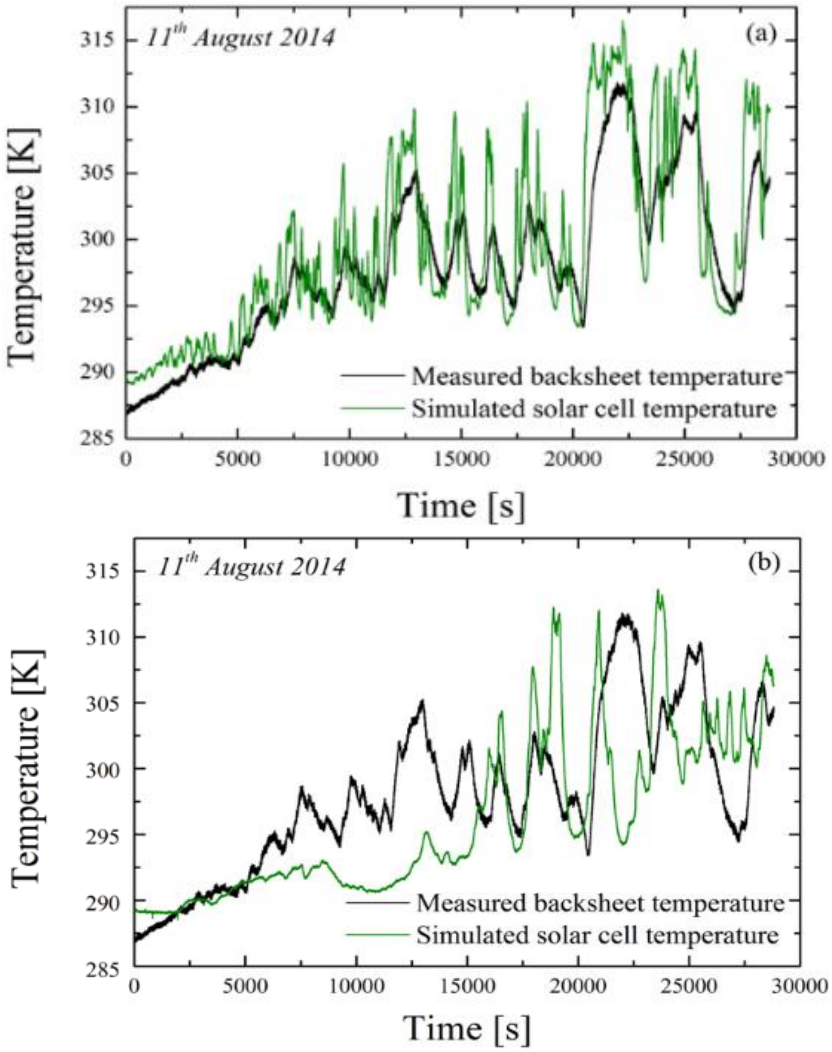

Figure 3-3: Simulated Vs Measured solar cell temperature for 11th Aug 2014. (a) Wind effect is included (b) wind effect is not included

For a further understanding of the PV module's sensitivities to different forced convection scenarios, a 60 cell glass-back sheet PV module's power output and cell temperature were simulated by the EOT model for different forced convection scenarios. To reduce complexities of different variable and to purely study the effect of forced convection on PV performance, few assumptions were made. In the case presented in this Section, it is assumed that there is negligible heat transfer from the back side of the module. So heat transfer by forced convection will occur only from the front side of the module. The ambient temperature and illumination were 25°C and 1000 W/m2 respectively and simulations were performed in steady state condition. The effect of forced convection is translated as heat transfer coefficient. Hence, the power output of

the module is simulated for the incremental heat transfer coefficient. The relationship between the heat transfer coefficient and wind flow near the surface of the PV module was estimated from wind tunnel measurements [24].

In Figure 3-4, it is visible that for higher wind speed region, the changes in cell temperature with increasing heat transfer coefficient is quite small. Hence the power output in higher wind speed region is less sensitive to varying heat transfer coefficient. Whereas, in the low wind speed region, the cell temperature is quite sensitive to changes in the heat transfer coefficient. Hence, the power output is highly sensitive too. This indicates that, for lower wind speed region, a small error in modelling heat transfer coefficient would lead to large error in PV module power output estimation.

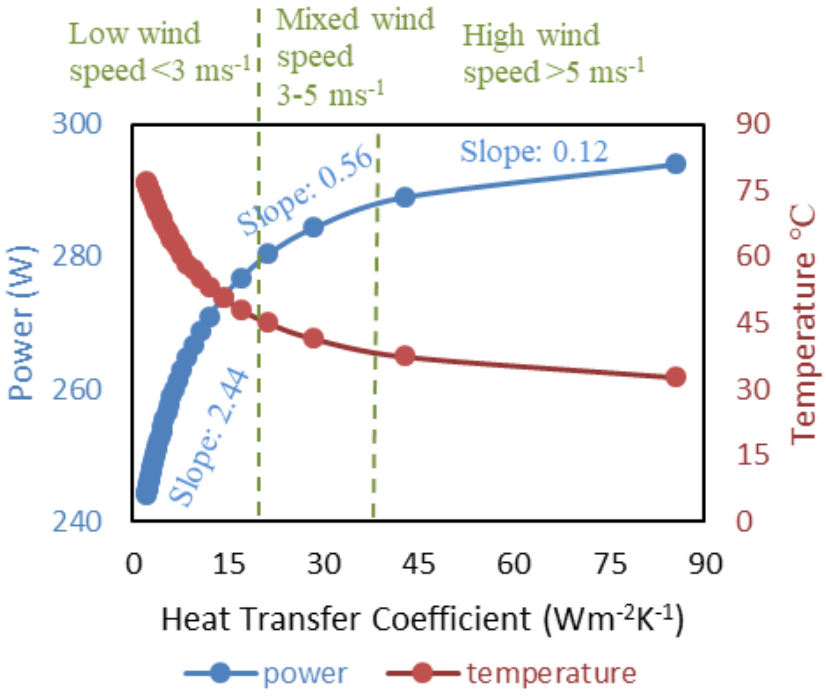

Figure 3-4: PV cell temperature and power output for incremental forced convection

3.4 Performance Analysis of Highly Cited Silicon Photovoltaic Module Temperature Estimation Methods

This study selected ten steady-state and one transient model to analyze the sensitivity. The steady-state models were in the top ten highly cited models by researchers, and one transient model has been published in recent times. Another transient model was published but was not selected due to particular meteorological variable requirements [64]. It required short and long-wave

radiation data, which we do not have. Therefore, we proceeded with ten unique steady-state models and one transient model. The objective of this study is to test all the models with the published standard state (i.e. using the equation with the given coefficients). Most of the models selected in this study didn't provide the option to calibrate their coefficients.

Nevertheless, some models suggested that, for the best performance, the coefficient should be calibrated with the available measurement data. Therefore we presented results with both standard formulation and calibrated formulation wherever it was possible. All the selected models are provided with the equation and necessary coefficients in Table 3-1. All these models will follow the naming convention stated in the table for ease of reading and continual flow.

3.5 Experimental Setup Description

To test temperature estimation method's sensitvity, an innovative experimental test setup is prepared. PV module temperature analysis is usually conducted with temperature sensors on the surface of the module. The most popular choice of placement is on the back sheet. This placement is done primarily because of two reasons. Firstly, it is difficult and costly to laminate temperature sensors inside the module. Secondly, the widespread assumption that the back sheet and temperature relationship is linear. Hence, you can estimate cell temperature if you know the back sheet temperature. For this study, it was decided to integrate temperature sensors inside the module for two reasons. First, PV energy yield analysis cell temperature is input to any such equations. So, it is best to acquire cell temperature as accurately as possible. Lastly, outdoor weather conditions might not impact thermal paste/ glue for the back sheet temperature sensor for a shorter period. However, this will introduce uncertainties for an extended period of outdoor weather monitoring, where outdoor meteorological variables will influence the back-sheet temperature monitoring.

Table 3-1: Selected models

	Models	Equation	Coeff values
Steady-state model			
1.	Ross Model [7]	$T\_c = T\_amb + k * G\_T$	$k = 0.030\ ^{K}/_{\frac{W}{m2}}$
2.	Faiman Model [5]	$〖T\_c = T〗\_amb + G\_T/((U\_o + U\_1 * WS))$	$U\_o = 25$ $U\_1 = 6.84$
3.	Faiman Model_calibrated [5] (Calibrated Coefficient)	$〖T\_c = T〗\_amb + G\_T/((U\_o + U\_1 * WS))$	$U\_o = 34.22$ $U\_1 = 6.26$
4.	King [4]	$T\_BS = G\_T * (e\^(a + b * WS)) + T\_amb$ $T_c = T_BS + G_T/G_STC * \Delta$T_CBS	$a = -3.56$ $b = -0.75$ $\Delta T\_CBS = 0.003$
5.	King_calibrated [4] (Calibrated Coefficient)	$T\_BS = G\_T * (e\^(a + b * WS)) + T\_amb$ $T_c = T_BS + G_T/G_STC * \Delta$T	$a = -3.54$ $b = -0.16$ $\Delta T\_CBS = 0.003$
6.	TamizhMani [65]	$T\_m = 0.943 * T\_amb + 0.028 * G\_T - 1.528 * WS + 4.3$	
7.	Mattei [66]	$T = (U\_PV \times T\_amb + G\_T \times A)/(U\_PV - B \times G\_T)$	$Upv = 20.9 + 3.32 * WS$ $A = 0.59$ $B = 0.05 * 10\^(-2)$
8.	Skoplaki [67]	$T\_c = T\_a + \omega * (0.32/(8.91 + 2 * V\_f)) * G\_T$	$\omega = 1$ $V\_f = WS/0.67$
9.	King2 [8]	$T\_c = T\_amb + G\_T/G\_ref * (0.0712 * V\_w\^2 - 2.411 * V\_w + 32.96)$	
10.	Tselepis & Trianagnostopoulos [68]	$T\_c = 30 + 0.0175 * (G\_T - 150) + 1.14 * (T\_amb - 25)$	
11.	Chenni [69]	$T\_c = T\_amb + 0.0138 * G\_T * (1 + 0.031 * T\_amb) * (1 - 0.042 * WS)$	
12.	Mondol [70]	$T\_c = T\_amb + 0.031 * G\_T - 0.058$	
Transient moving average model			

13.	Prilliman (WMA) [71]	$T\_(MA,i) = (\sum\_(i=2)\hat{}(t\_i \leq 1200)\text{▒}(T\_(ss,i) \times e\hat{}(-P * t\_i)))/(\sum\_(i = 2)\hat{}(t\_i \leq 1200)\text{▒}(e\hat{}(-P * t\_i)))$ $"P = "\ a\_0\ " + "\ a\_1 * WS + a\_2 * m\_u + a\_3 * WS * m\_u$	$a\_0 = 0.0046$ $a\_1 = 0.00046$ $a\_2 = -0.00023$ $a\_3 = -1.6E\text{-}05$

For this module, 9 Pt_{100} sensors of 4 mm^2 of accuracy class ISO AA were soldered with a four-wire cable and packaged inside the purpose-built module. The location of these sensors is close to the centre of the cell. These sensors can capture rapid temperature fluctuations due to their low thermal constant. Most importantly, they are relatively immune to outdoor transient thermal fluctuations and corrosion as they are packaged inside the module. Moreover, two back-sheet temperature sensors were also installed too. The location of all these sensors is given in Figure 3-5. The module uses monocrystalline cells with a standard 60 cell configuration.



Figure 3-5: Experimental setup and temperature sensor location on PV module

The outdoor experimental site is located on the KU Leuven campus in Ghent. The geolocation is 51°03'12N, 3°43'49E. The array is installed with azimuth at 180° (South). In Figure 3-5, a full view of the setup can be seen. The data logging is conducted by National Instruments 9074 compact Rio and LabVIEW. Data is logged in four primary segments: Meteorological input, PV temperature sensors, I-V measurements, and inverter power and energy logging. Meteorological inputs contain pyranometers (horizontal and plane of the array at 18°), ambient temperature, wind speed and wind direction. A first class advanced anemometer acquires wind speed data from Thies Clima. The range of measurement is from 0.3 ms^{-1} to 75 ms^{-1}. An Ekopower wind vane is used to measure wind direction, with an uncertainty of 3°. All the data from this experimental campaign was logged at 1 Hz [72].

3.6 Climatic Dataset Selection

For the current study, the climatic data logging starts from 1st May 2015 to 31st December 2015. Most importantly, to explore where the highest mismatch is coming from, it was necessary to funnel downtime periods from a top-down approach. It started with an extended period towards a shorter period of error analysis. Due to that, emphasis was given to the study of the May to September timeline. The higher absolute error of temperature prediction correlates with higher insolation because insolation has the highest weightage within any temperature prediction model. So, these five months cover the entire summer period of Belgium with the highest insolation. The overall error evolution of these five months will be discussed in the latter part of the chapter.

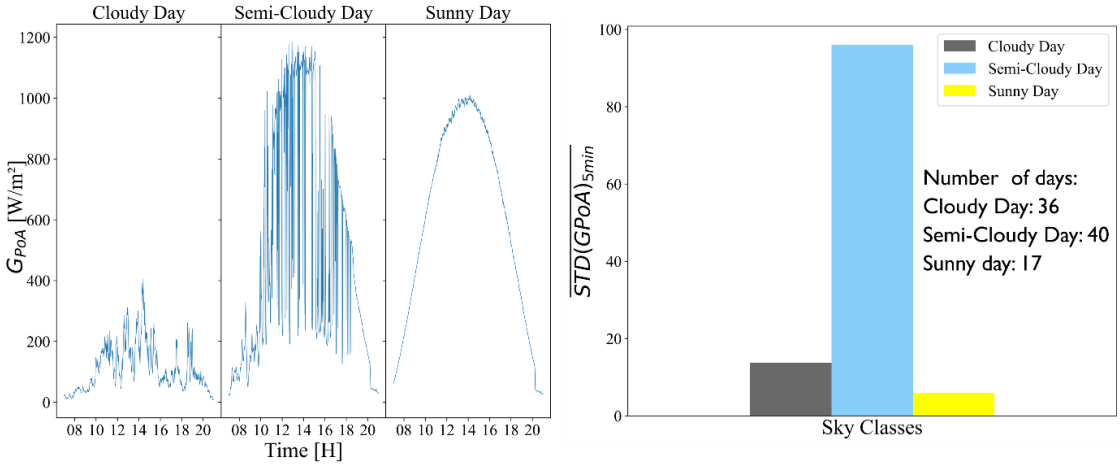

Figure 3-6: Sample Day type of cloudy, semi-cloudy, sunny days with standard deviation of G_{PoA} of all the selected days

Moreover, to focus and find out categorically where the errors are coming from, it was necessary to manually classify days with distinctive characteristics of cloudy, semi-cloudy, and clear sky days. We first used sky classification methods, but those methods could not distinguish mixed days both with clear sky and semi cloudy status. Therefore it was necessary to select the days based on a qualitative approach. Four sample days of these types are shown in Figure 3-6. Within the period of May-September, 62 days had mixed irradiance type, which was not taken into account for this day type analysis. The number of three other kinds of days is shown in Figure 3-6. The standard deviation of PoA of all these selected day classifications provides insight into the chosen day types. Within the days, the period selected is between 10:00-17:00 because 74% of the daily insolation is concentrated within this period. It's easier to investigate the error matrix quantitatively in the high insolation hours.

3.7 Results and Discussion

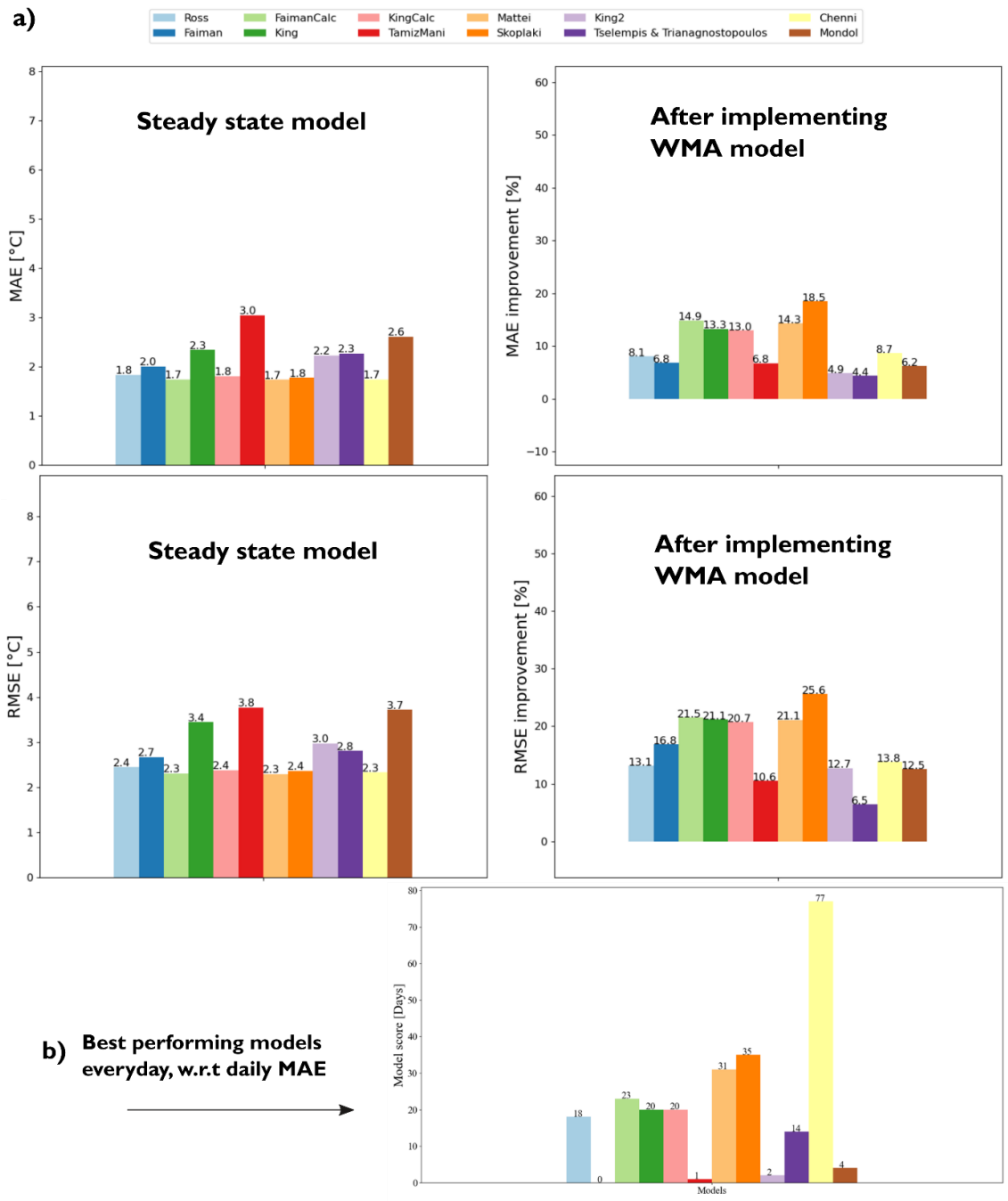

Figure 3-7: Long period analysis (May-December) with 1Hz resolution

The results analysis will follow the top down approach from a long to a short period, followed by a matrix analysis of the inherent dependencies of these models. It will help evaluate the sensitivity of different models with variable time

resolution. All the RMSEs and MAEs are calculated with 1Hz resolution dataset. The models are compared with the standard steady state model and then with the WMA implementation. This will also help to identify possible improvement pathways too. Moreover, the impact of different meteorological variables and time resolution dependency will be presented too.

3.7.1 Long Term Performance Analysis

In Figure 3-7, the RMSE and MAE are compared throughout May-December on the left side. On the right side, the impact of the WMA method is seen with a percentage dimension. The RMSE values are similar to reported literature from the same climatic region [73]. Therefore, just based on RMSE and MAE alone, from a long-term perspective, most of these models can be chosen for temperature prediction. In contrast, Mondol, Tamizmani, and King are the least-performing models. Compared to RMSE values, MAE values indicate that Faiman and King, compared to Tamizmani, have more outliers. Moreover, King2 and Tselempis exhibit some sensitivity towards outliers, but these are not statistically significant to be conclusive at this point. The WMA method is implemented on these steady-state models as a next step. As shown on the right side of Figure 3-7, they all have improved prediction but not in a similar range.

Skoplaki was one of the best-performing models in steady-state formulation, and it stands out with the most significant improvement after the transient averaged effect is taken into account. Tselempis seems to have the most negligible impact even after WMA. Skoplaki considers the effects of wind, and Tselempis doesn't. Therefore, Tselempis improved to a lesser magnitude. The general conclusion is that the best-performing steady-state models have statistically insignificant error differences based on RMSE and MAE alone. Therefore, we tried a different matrix to distinguish. The best performing method according to MAE is chosen per day. In that category, it can be seen that Chenni's model was the best performing model over 70 days, whereas with a similar overall RMSE and MAE, Mattei was best performing only for 30 days. There is two takeaway from this long-term analysis. First, WMA methods improve the performance of all the steady-state models. Two, it is challenging to select the best and least performing models just with RMSE and MAE alone over such a long time resolution as a lot of absolute errors are averaged out in the process.

Moreover, the distribution plot of error comparison of different models in Figure 3-8 reveals some interesting aspects. It is clear from the distribution plots that all the models compared in this chapter overestimate PV temperature. Here these models can be segmented into two groups. The first group, which considers the G_T and T_amb. The second group incorporates WS along with G_T and T_amb.

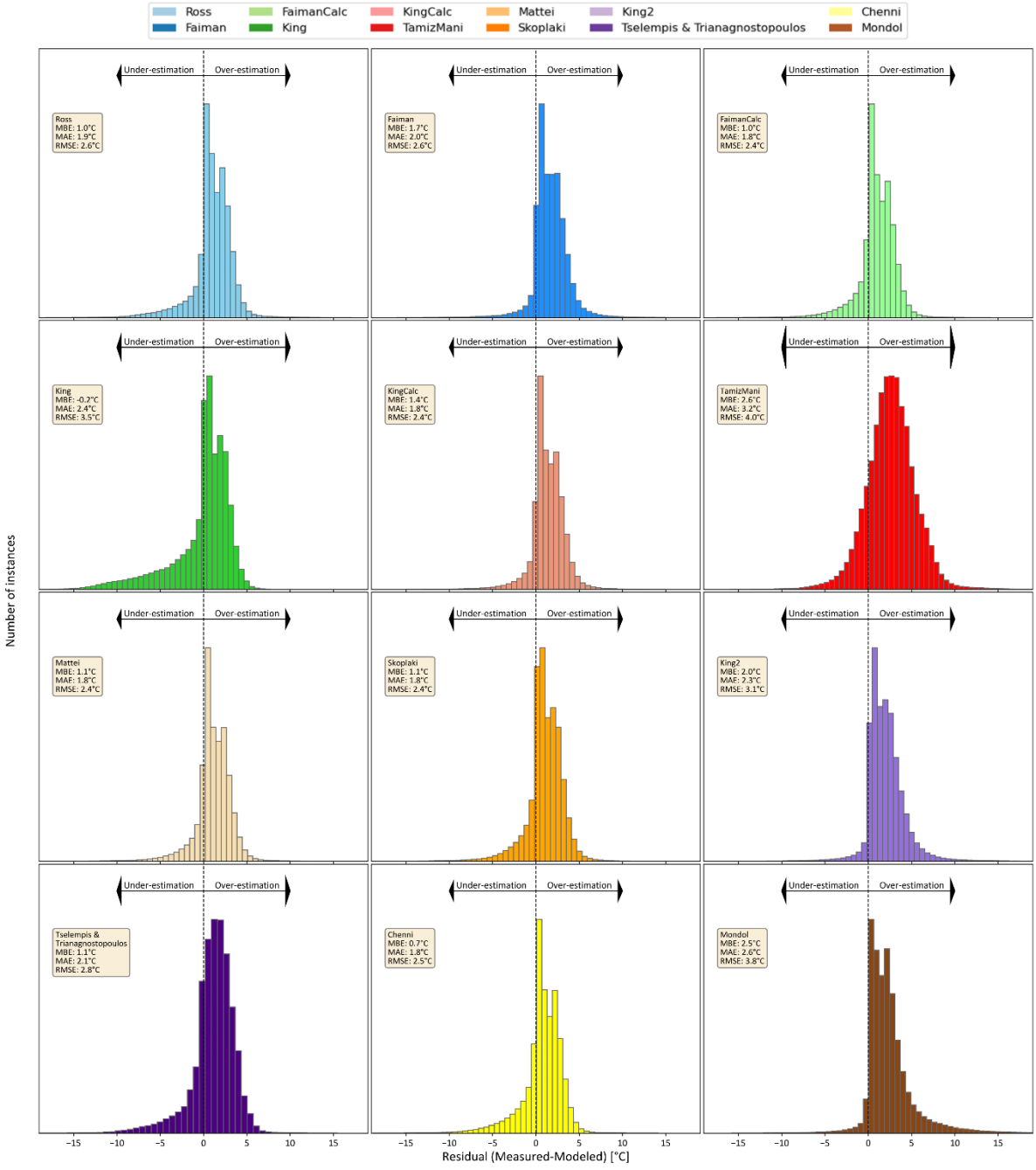

Figure 3-8: Distribution plots of $T_{predicted}$ - $T_{measured}$

The first group consisted of Ross, Mondol, and Tselepis model. Mondol is almost like a mirror of the Ross model where a constant was inserted. Ross model has some underestimation, and Mondol wanted to improve it by inserting a negative constant. It did improve on the underestimation but again increased the overestimation resulting in gross RMSE/ MAE mismatch for the longer term. Tselepis also attempted to fix the mismatch by introducing constants within the equation, but in the end, it also had a higher RMSE/ MAE mismatch than the Ross model. Even after WMA implementation, these three models don't improve significantly, where Tselepis has the most negligible improvement compared to all the 12 models. Therefore it indicates that the mismatch/ overestimation of these models cannot be improved by introducing constants within the equation. It just comes from some other meteorological parameters/ variables. Thus, the second model group comes into effect to improve this mismatch. All these models used WS in various formats. However, all of them overestimates much more than the first group. One might conclude that perhaps the first group of models have better performance. Still, in the overall performance comparison, it is clear that by integrating WS into the equation, accuracy improves for most models. In the latter part of the chapter, the improvement in the short term by implementing WS will become more evident. A hypothesis for the gross overestimation can be attributed to the fact that all the models' assumptions on the effect of wind must have an inherent issue. These models underestimate the impact of wind and predict a higher PV temperature than in reality. Consequently, they overestimate in different magnitudes. When WMA is implemented in this second group, most of these models improve higher than the first group. This indicates that the transient effect of WS was a source of error for these models.

3.7.2 Performance in a Shorter Period

A quick conclusion from the longer period analysis would be that Chenni is the best performing model over the longer period, but this doesn't necessarily translate into overall performance right away, mainly because we need to be careful of what type of days are. Maximum energy from PV is extracted during high insolation days. All these models exhibit higher errors during that time. Hence it is crucial to know how these models perform during that period. The analysis would focus on how they perform in different day types within that period. From May to September, days were classified as cloudy, semi-cloudy and sunny. The selection method is described in the earlier segment.

On the left side of Figure 3-9[a], the first thing to see is that Chenni is not the best-performing model for this period. Mattei has the overall best performance. Still, the magnitude difference between all good performing models is small to distinguish by RMSE and MAE alone. It is also crucial to compare Figure 3-9 [a] and Figure 3-9 [b] because Tamizmani is not the least performing model either; now it's King. The magnitude of error difference is statistically significant here for this case too. When these plots are expanded into cloudy, semi-cloudy and sunny day classifications, the RMSE and MAE error for some models can be higher than 7°C. One trend is clear: for all the models, the error-wise, semi-cloudy day has higher errors. This is primarily because steady-state equations cannot solve fluctuating irradiance in fast-moving cloud conditions.

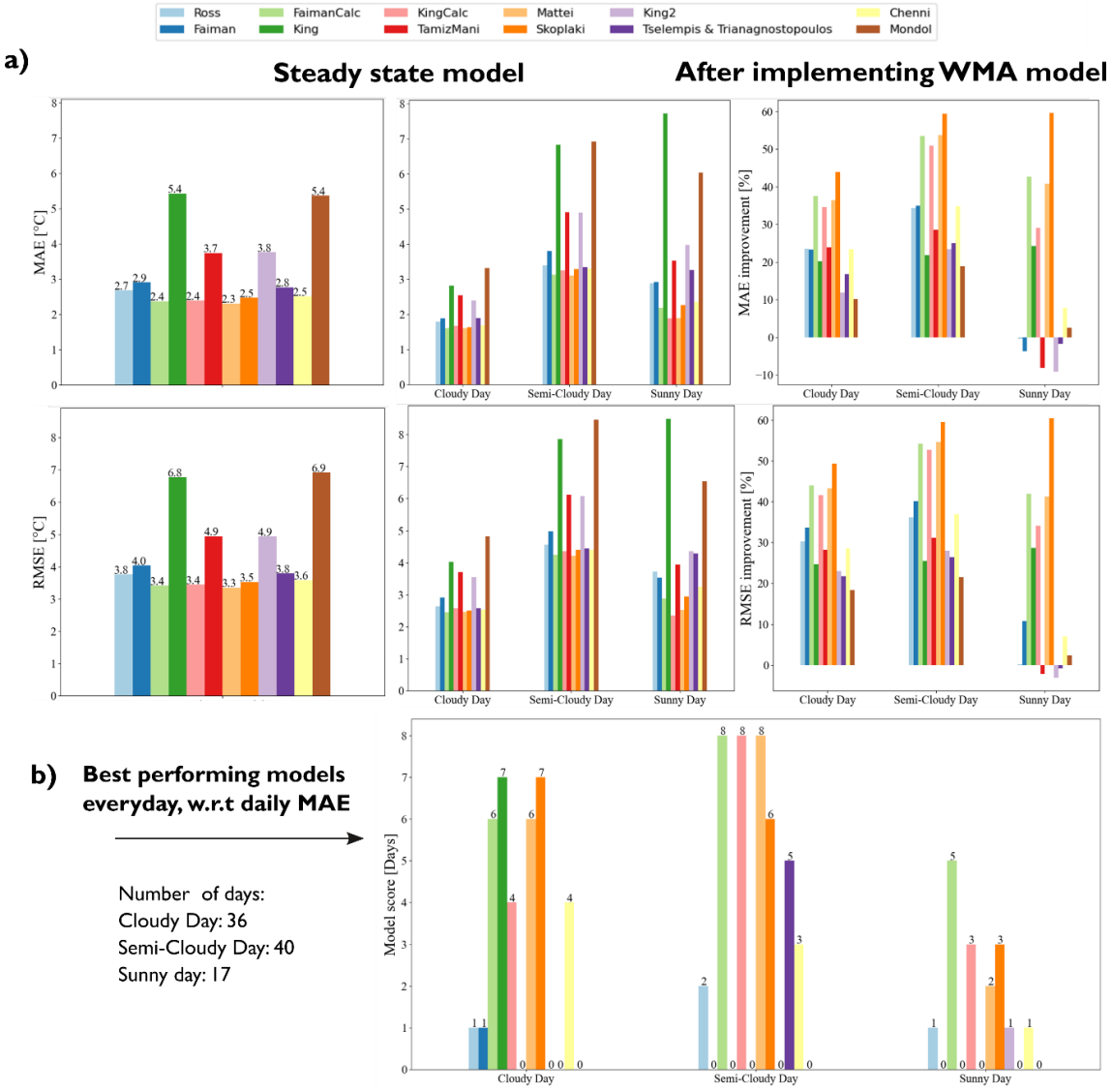

Figure 3-9: Short period analysis (May-September) with 1 Hz resolution

Moreover, after implementing the WMA method, the expectation would be to improve all the models. We can see significant improvement in most of the models' error values. Especially on semi-cloudy days, Mattei and Skoplaki show almost 60% improvement in errors. However, the surprising result is that Ross, Faiman, Tamizmani, King2, and Tselepis errors are increased on sunny days instead of reducing errors. This indicates that some of these models provide high weightage to irradiance, which doesn't necessarily correspond to reality because absorbed heat is also dynamically removed from the module through convection.

The overall RMSE or MAE value can also be misleading if you want to select the best-performing models in these daily classifications. To assess this, in Figure 3-9[b], the best-performing models per day were plotted. It shows how many days each model was the lead performer compared to others. From Figure 3-9[a], even though King has higher errors, in the cloudy day segment, it stands out as the daily best number of times as Skoplaki. FaimanCalc, KingCalc, and Mattei have an equal number of days on a semi-cloudy day where they are the best models. For sunny days FaimanCalc is the lead model. A takeaway from this part of the analysis would be that FaimanCalc seems to have an overall advantage in absolute RMSE/ MAE and the best-performing model in different day types for a higher insolation period. Chenni, on the other hand, even though they were the best performer for the entire period, fails to stand out in the higher insolation period. It also shows some sensitivity with increasing irradiance conditions.

3.7.3 Model Performance on A Matrix of Irradiance, Ambient Temperature, Wind Speed, and Time Resolution

Irrespective of the development process, the steady-state equation assumes the impact of wind speed is the same frequency as irradiance. Therefore, these approaches were developed in higher time resolutions(i.e. minutes/ hours). In the end, it is assumed that they should operate with similar accuracy, even in the second resolution. Hence, the available one-second data have been resampled to one-hour averages to compare with steady-state model performance in an hourly time resolution. Moreover, the data have been matrixed into several irradiances, ambient temperature, and wind speed segments. This will provide insight into the performance status of steady-state models in these segments.

Intending to evaluate the response of a steady-state model to the wind speed, ambient temperature and plane of array irradiance should remain constant. In contrast, meteorological parameters in an outdoor experiment cannot be controlled. To tackle this, the data will be analyzed separately into segments of specific ambient temperature and wind speed levels. To increase the amount of data on each segment, measured PV temperatures will be included for ±50 Wm-2 around the set irradiance value of 200, 500, 1000 Wm-2 and ±4℃ around the set ambient temperature set values of 20 and 30℃. Along with the examined models, a fitted 1st order equation will be calculated for each segment, as shown in equation 1.

$$a * WindSpeed^2 + b * WindSpeed + c \qquad (1)$$

It has been stated by several authors that with the increase in wind speed, the rate of change of cooling decreases. On the other hand, models such as TamizMani, a linear regression product, consider that wind speed cooling increases linearly with increased wind speed. Considering the above, the α coefficient of the fitted equation has been set to be either zero (colling decreasing linearly) or positive (the rate of change of wind speed colling is decreasing linearly).

As is visible from Figure 3-10, there is an apparent decrease in PV temperature as the wind speed increases. Some cases indicate a linear reduction according to the fitted equation line, while some others are logarithmic. Faiman, King Calc, Mattei & Skoplaki show the best accuracy in all cases. Between those models, Faiman and KingCalc appear to be more stable. On the other hand, the fitted equation relies only on wind speed, which is a limit factor for its accuracy.

Two general conclusions from Figure 3-10 that can be made here are the following: firstly, not all the models perform at the same level at various irradiance, wind speed, or ambient temperature conditions. These models are closer to reality in low ambient temperature and lower irradiance. In contrast, they tend to perform least in higher ambient temperature and irradiance conditions. Secondly, not all models are equally correct/wrong all the time. Sometimes they are closer to experimental values and sometimes far off. Our hypothesis is, that further improvement of these equation-based models requires conditional modifications. Simply introducing static constants is not a

way forward. Studies can continue in the direction of how to make these models robust enough to adapt to variable meteorological parameters.

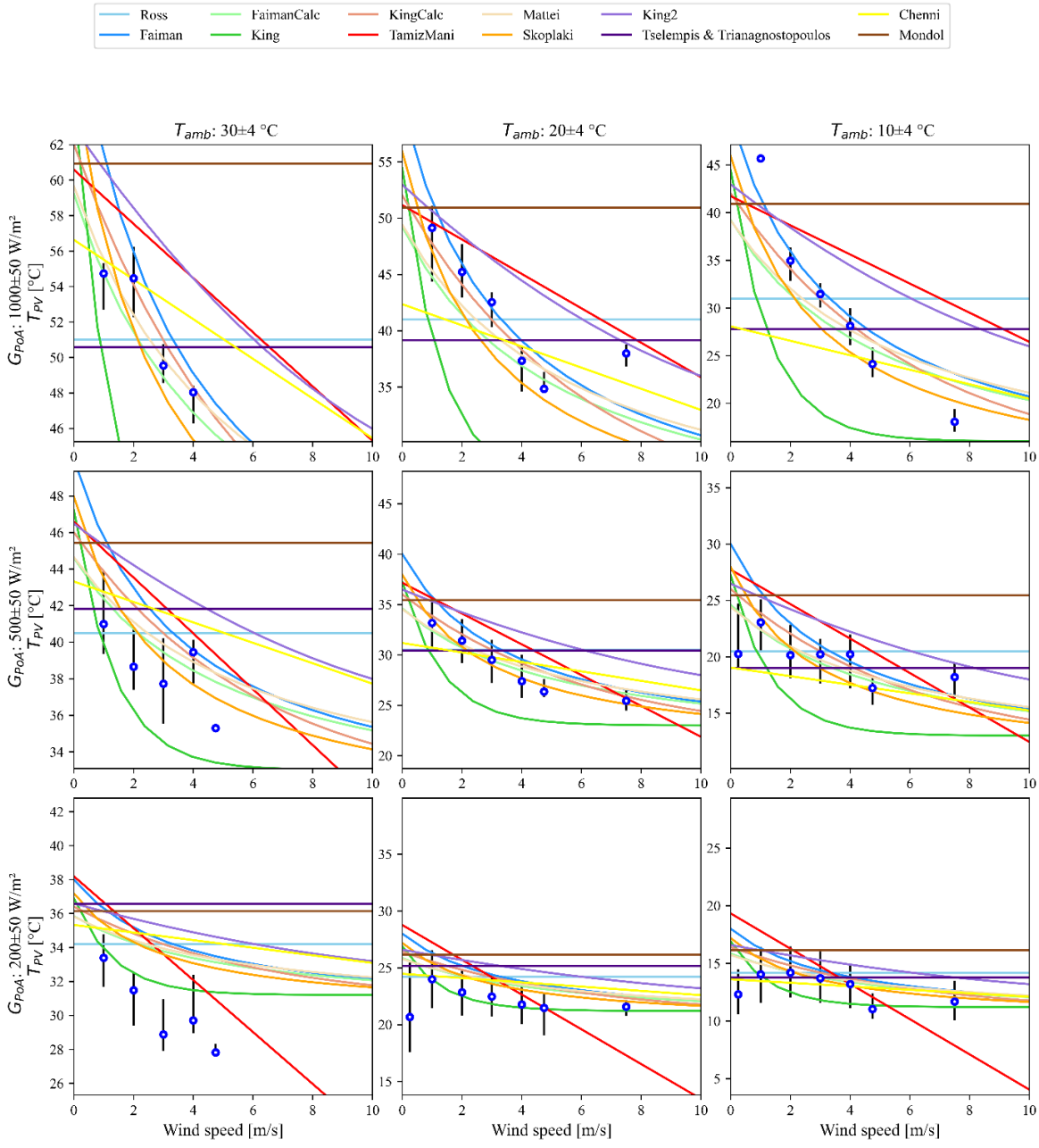

Figure 3-10: Demonstration of the wind speed cooling reaction of every steady state model, along with the measured PV temperature values for each G_{PoA} and T_{amb} level segment.

3.7.4 Time Resolution

A day with variable irradiance and wind speed is selected to display the impact of time resolution on PV temperature model accuracy. According to previous short period analysis, variable days are when you can expect the highest

mismatches. For model comparison, we selected the most simple model, i.e. Ross model, vs the most adaptable one, i.e. Faiman Calc and King Calc. Because Faiman Calc and King calc uses calibrated co-efficient based on the experimental setup. As calibrated coefficients require preliminary experimental data, it is sophisticated to acquire and implement.

Figure 3-11 exhibits the time-series performance of these models in 1s, 5 min, and 1-hour time resolution, both with standard and WMA implementation. Ross has the least accuracy, and Faiman Calc has the best accuracy in all three resolutions. Some general observations can be made here. Firstly, with standard implementation, the more time is averaged out, the better the models perform. Improvement after WMA implementation increases with increasing time resolution. This means it performs the best in 1s resolution, and in 1-hour resolution, the accuracy can flip to standard implementation too.

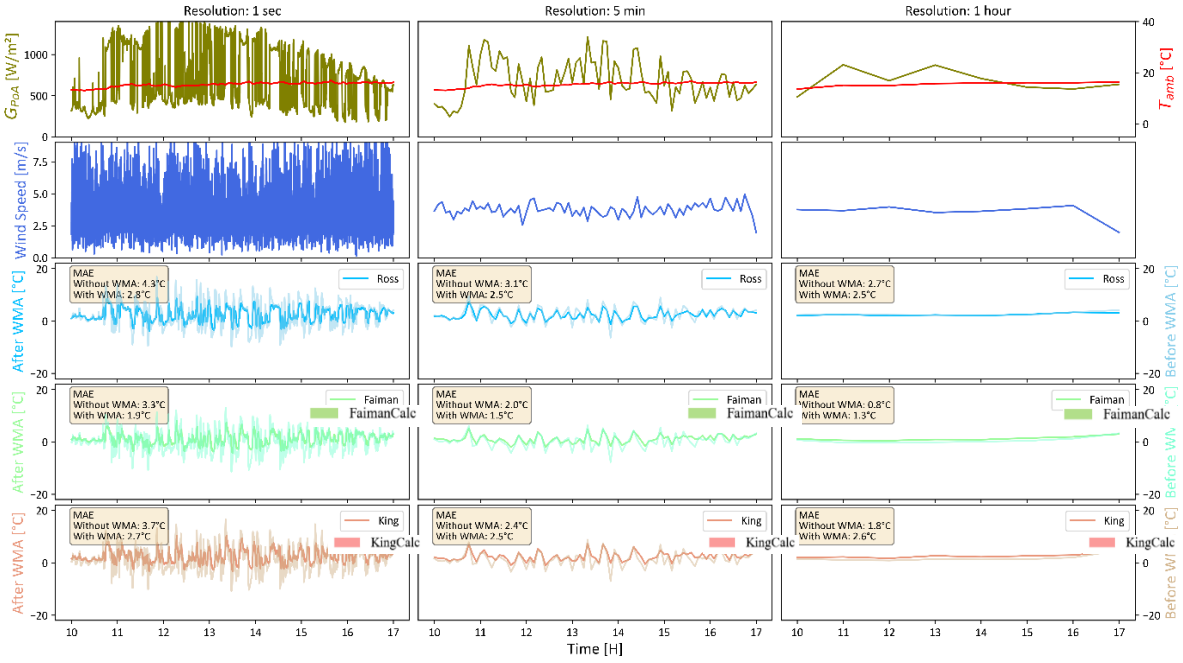

Figure 3-11: Prediction model accuracy dependency over different time resolution

Depending on the user's requirement, these models must be selected carefully. If the requirement is hourly resolution, then standard Faiman Calc (also used in PVSyst) can be a good choice. However, if the requirement is higher time resolution than even Faiman Calc exhibits a mismatch of 15°C and 10°C (with WMA) during midday when PV's highest power generation capacity resides. This means that energy yield estimation mismatch due to incorrect temperature

estimation in that period of time would have a higher impact than the morning or afternoon period.

3.7.5 Steady State Models Transient Moving Average Model

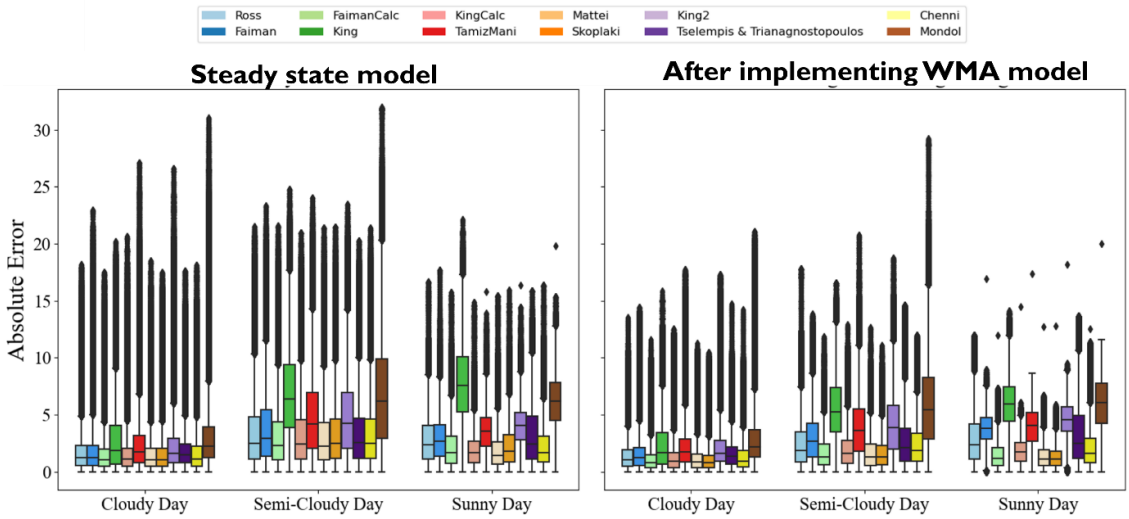

Figure 3-12: Absolute error of classified days (May-September) with 1Hz resolution

It is evident from Figure 3-7, and Figure 3-9 is that WMA models improve all the best-performing models. From RMSE and MAE, it is clear. This is the case if the target is to achieve accuracy in an extended period over a daily improvement. To check further robustness of the steady state and transient model, it is essential to look into the absolute error range. For this purpose, in Figure 3-12, in May-September in classified days, absolute errors are plotted. As presented earlier, semi-cloudy days will have higher errors, but what is interesting is that even the median absolute error of best-performing models is around 3°C. FaimanCalc, Skoplaki, and Mattei, from the previous discussion, which were suggested as models of choice for higher insolation periods for 25% of the time, have an absolute error of temperature prediction between 5-10°C. Even if the outliers of 25°C are not taken into account, having an absolute 5-10°C mistake for 25% of the time is a significant mismatch for energy yield prediction. Once the transient models are implemented, the range of outliers visibly improves on cloudy, semi-cloudy and sunny days. The medians also slightly enhance all the models. But as presented in Figure 3-7 and Figure 3-9, the improvement percentage is not always in the same range. Then again, what is curious to look at is, that even after transient model implementation for semi-cloudy day FaimanCalc, Skoplaki, and Mattei, 25% of the time absolute error range is within 2.5-7.5 °C.

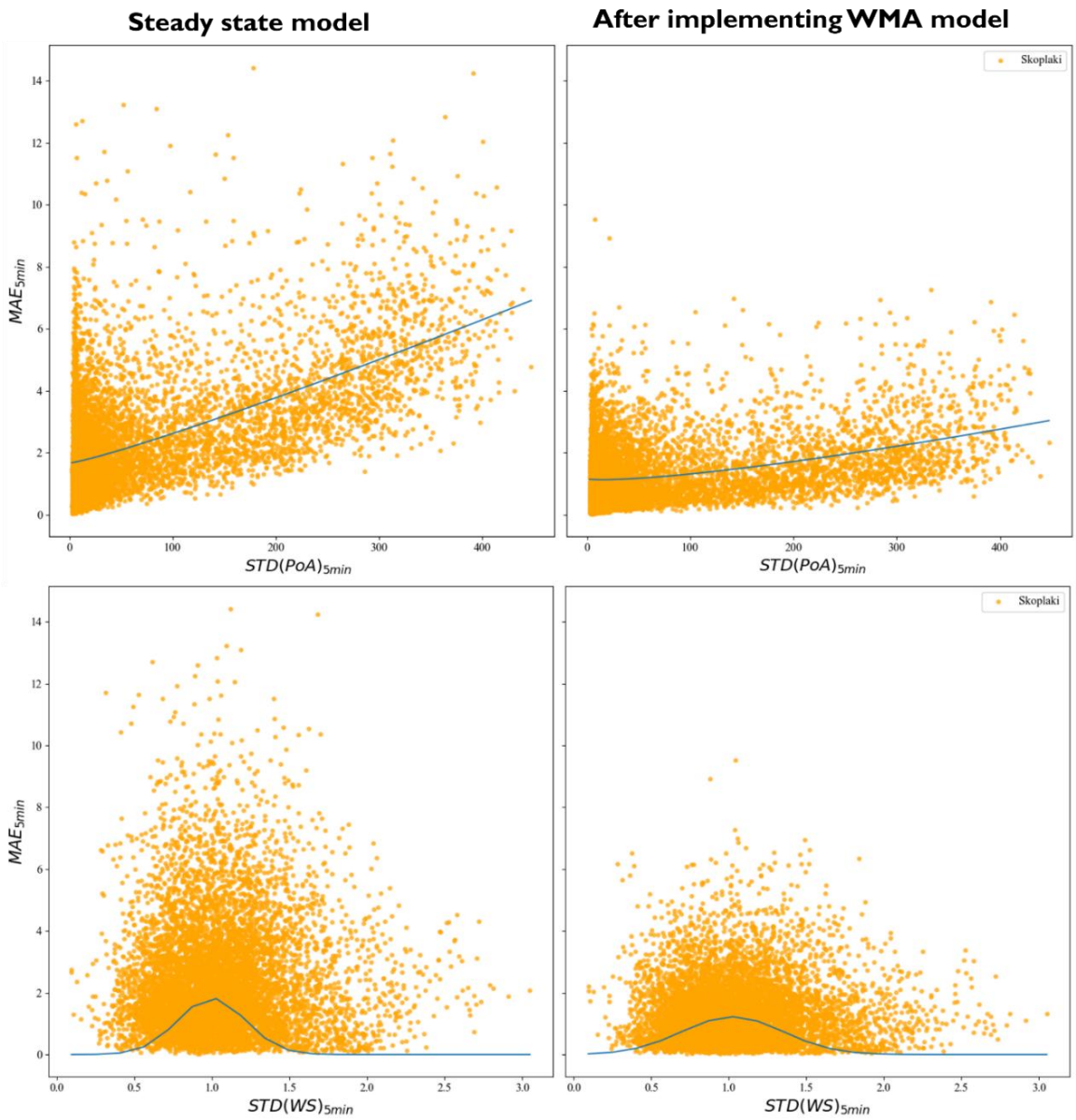

Figure 3-13: Outlier improvement with WMA

The transient model improves by not taking the instantaneous assumptions instead of averaging the response. This can be seen in Figure 3-13 for Skoplaki, which had the best improvement after implementing WMA. In all the plots, you can observe that many outliers are improved based on the frequency of PoA and wind speed. But from the PoA plots, there are two observations one with an increase of fluctuation of PoA, the MAE increases. Two which are even more surprising is that with a stable PoA, you can expect to increase MAE as high as the highly fluctuating ones. This indicates that even with stable PoA, there are still uncertainties inherent to the models. From the wind speed plot, the

observation is that the MAE error range increases with the increase of wind speed fluctuations, but there is also a tipping point. When wind speed fluctuations cross that point, the MAE starts to decrease. It indicates that the weightage on wind speed is not also constant. We would refer to [19], and [20] for a detailed explanation of this process.

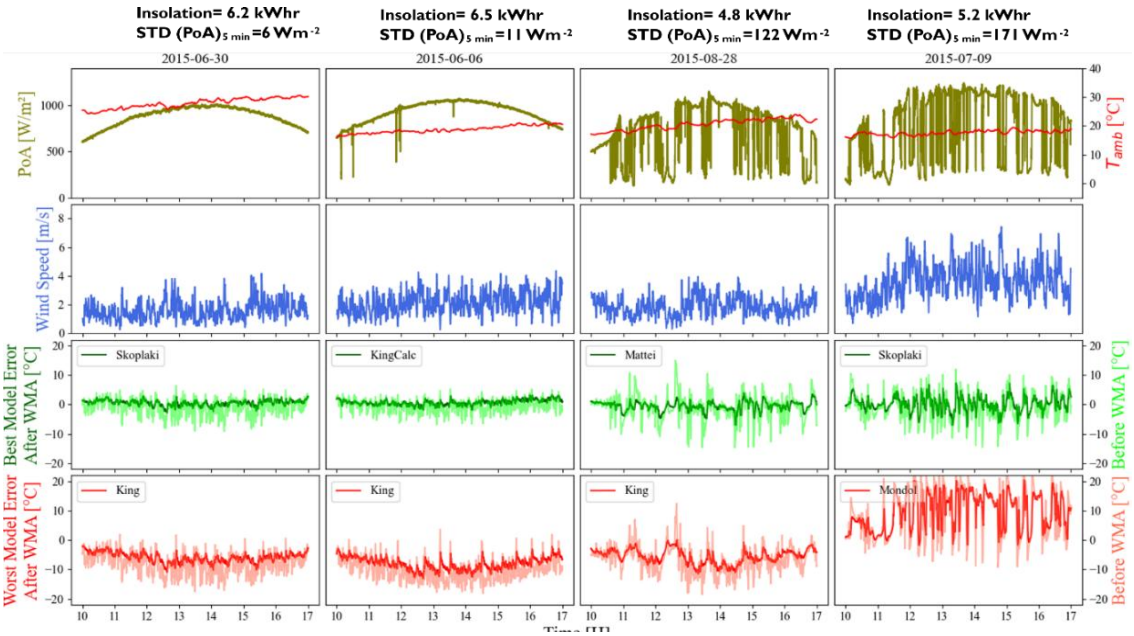

Figure 3-14: Four specific day evaluation, Best Vs Worst, Steady State Vs WMA

To demonstrate the impact of fluctuating variables like PoA and wind speed on temperature prediction, we picked four days from May to September with similar insolation profiles with different fluctuations and mean wind speed. Just from the insolation values, the common assumption would be that the temperature prediction error range would be similar too. However, in **Error! Reference source not found.**, it is shown that is not the case, and to explain this, the temperature prediction profile over the entire day period is plotted. Both the best and least performing models from those days were picked, too, to exhibit the impact of WMA on different models that are not in the same frequency. King and Mondol were the least performing ones, which was expected from Figure 3-9[a] as they were also the least performing for this period. The best performing model was a mixture of different models, as shown in Figure 3-9[b]. One thing is sure from **Error! Reference source not found.** is that WMA improves all these models and takes it much closer to the absolute zero error line, especially in the first two days with a sunny

classification. On the other side, on semi-cloudy days, especially with higher wind speed, the errors oscillate between +7°C to -7°C.

3.8 Chapter Summary

The objective of this chapter was to interrogate the treatment of wind, specifically, forced convection in PV temperature and energy yield models. Two distinct investigations were conducted: one assessing the sensitivity of energy yield to convective heat transfer, and the other evaluating the robustness of widely cited temperature estimation models against high-resolution, long-term measurements.

The first part, grounded in combined simulation and experimental work, made the consequences of neglecting wind explicit. When wind was omitted from the thermal model, daily energy yield predictions deviated sharply from observed values. The relative RMSE approached 50%. When wind was properly integrated, this dropped below 3%. The disparity grew further as temporal resolution increased, indicating that thermal dynamics, notably wind-induced cooling, exert a stronger influence in high-resolution contexts. Moreover, in low wind speed, small variations in convective input resulted in disproportionately large shifts in predicted temperature and output. This finding is operationally significant. It suggests that PV arrays enveloped between other arrays are vulnerable to errors from oversimplified thermal modelling.

The second segment turned to the models themselves. Eleven highly cited and used temperature estimation methods ten steady-state, one transient were systematically benchmarked. No model proved universally reliable. Chenni's formulation performed best in long-term aggregate terms. Yet, during periods of high irradiance (May to September), other models, particularly the calibrated variants of Faiman and King, as well as Mattei and Skoplaki, emerged as more effective, depending on day type. FaimanCalc consistently stood out in terms of balance across scenarios, but only when calibration data were available. In its absence, Skoplaki presented a viable alternative.

A broader theme emerged: none of the models could be assumed to incorporate the crucial time-variant aspects. While often treated as such, their accuracy proved highly sensitive to both temporal resolution and meteorological variability. The implementation of the WMA (Weighted Moving Average) method helped mitigate these issues, improving performance by 6% to 25% depending on the model and condition. For Skoplaki, the gain was particularly notable up to 60% improvement on semi-cloudy days. However, even with

WMA applied, absolute temperature prediction errors of up to 7.5°C remained, especially under mixed sky or fluctuating wind conditions.

The implication is twofold. First, the assumption that these models can be applied blindly across timescales or site conditions is no longer tenable. Second, thermal inertia, rarely accounted for in steady-state formulations, appears to be a critical missing link. The persistent mismatch between predicted and observed values, even after calibration, hints at structural limitations in the underlying formulations. These models were never designed for sub-hourly dynamics. Their use in that context, without adaptation, introduces hidden but significant error.

A further limitation resides in their implicit assumption of temperature uniformity across module types and designs. That assumption, while convenient, fails to account for the growing heterogeneity in module architecture, encapsulation, and mounting formats particularly as utility-scale projects. The inability of current models to distinguish between thermal profiles of different designs raises a larger concern.

This chapter, therefore, concludes on a cautious but clear note. The role of wind, especially in low-speed conditions, cannot be treated marginally. Nor can PV temperature models continue to assume universal validity across time and configuration. If temperature is to be used correctly, as a predictive input for energy yield, then its modelling requires re-examination. Not just in terms of equations and coefficients, but in assumptions, structure, and resolution.

These findings lead directly to the work in Chapter 4, where the spatial and fluid-dynamic basis of PV thermal behaviour is addressed. Rather than refining empirical models further, the next step is to construct a physically resolved representation of airflow, heat exchange, and surface temperature distribution. Only then can the root of these modelling inconsistencies be understood and improved.

4 Capturing Wind Effect in PV Systems

4.1 Motivation and Organisation

In chapter 3, the limitations of steady-state and transient models were examined with respect to their ability to capture the thermal behaviour of photovoltaic (PV) modules under real-world conditions. While these models serve as practical tools for many applications, they are built on simplifications that do not hold when temperature dynamics vary sharply over time or across the surface of a module. One of the most overlooked sources of such variation is convective cooling, specifically, how wind interacts with the physical geometry of PV array and systems.

The influence of wind is not uniform, neither in space nor in time. It is shaped by the geometry of the mounting structure, the depth of the air gap beneath the module, the presence of cavities at its edges, and the surrounding architectural context. These interactions produce highly non-linear effects: flow detachment, reattachment, turbulence, and eddy formation. Together, these create spatial and temporal differences in surface temperature that can no longer be dismissed as second-order phenomena. The challenge lies in how to model these effects with enough fidelity to matter, and with enough validation to trust the outcome.

Computational Fluid Dynamics (CFD) provides the necessary framework. It allows us to simulate airflow with spatial resolution far beyond what is possible using empirical correlations or bulk convective coefficients. However, CFD simulations cannot be accepted on theoretical strength alone. They require experimental validation under controlled conditions, and this is where practical limitations begin to appear.

A typical commercial PV module measures roughly two metres by one. Moreover, a representative PV systems consist of multiple arrays with many modules. However, such a setup is costly to run CFD simulations and setting up controlled wind tunnel experiments at this scale is, in most cases, unfeasible. The equipment required is rare, costly, and beyond the reach of most academic environments. Outdoor measurements, while useful, offer limited control over boundary conditions and are not easily replicable. As a result, we have adopted a pragmatic approach. Custom mini-modules were constructed, sized specifically to fit within a medium-scale wind tunnel. These are not reduced-scale replicas designed to mimic full-module behaviour in all respects; rather, they are instruments, configured to allow direct observation of how wind interacts with features such as air gaps and cavity walls.

This chapter presents the outcome of that decision. A series of wind tunnel experiments were conducted under varying freestream wind speeds, ranging from 1 to 5 m/s. Wind velocity was measured at multiple locations across both the front and rear surfaces of the test module. Two air gap configurations 3.5 cm and 5.5 cm were tested, along with three cavity depths at the base of the module: 0 cm, 6 cm, and 9 cm.

The findings demonstrate that narrower air gaps result in lower near-surface wind speeds and, consequently, reduced convective heat removal. This effect was observed not only on the module's top surface but also within the air gap and along the rear. Cavity structures, although not significantly altering the wind speed magnitude, produced noticeable lateral deflection and the formation of clockwise and anti-clockwise vortices adjacent to the module. These flow structures, while confined to local regions, influence the thermal environment in measurable ways. So, it demonstrates how quite small details of the overall cell and module structure still influence the results in a non-negligible way.

4.2 Chapter Specific Introduction and State Of Art

The actual cell temperature is the result of an interplay of a complicated set of heat flows, combining conduction, convection and radiation effects both within the module and between the module and its environment. As part of this complex interplay, the operating temperature of the cell is (among other factors) affected by the discharge of heat caused by forced convection generated by wind [74], [75]. Air blowing over a PV module will, therefore, affect the performance of the module. Studies have shown that the temperature difference between the top and back surface of a PV module can mount to 20 °C and more, depending

on the location on the module and the approaching wind speed [27]. These spatial differences in temperature affect the energy production by the module [26]. Consequently, for accurate energy yield predictions, it is imperative to understand better the effects of wind blowing over PV installations. Since Computational Fluid Dynamics (CFD) models are capable of simulating airflow over and around objects [29], [30], [34], [35], [76], [77], it has become a promising tool in PV research. Adequate validation of the predicted results remains necessary, however, especially when the objects under investigation are simplified in the model to reduce computational effort or because of scaling reasons.

Nowadays, PV modules attached to buildings are not only installed on the roof but also on other integral parts such as façades, walls and window replacements. The specific geometry of these installations can vary greatly, with different shapes and sizes of air gaps between the module and the building itself, irregular cavities in the building wall, etc. These irregularities have a strong impact on the local wind field and, therefore, on the electrical performance of the PV modules. Although many studies have investigated the installation of PV modules on the roof of buildings, the details in the local roof and building geometry have often been overlooked. In the simulations, simplified, regular shapes have been used that do not include many of the local details such as small-scale cavities, the correct rounding of corners, protrusions, or other irregularities. The scale of such irregularities, often in the order of centimetres, complicates their inclusion in CFD models and may also substantially increase the computational time.

Extensive research has been conducted on wind effects on both roof-mounted [29], [30], [31], [32], [33] and ground-mounted PV modules [34], [35], [36], [37]. In these studies, multi-module PV systems were investigated, but no detailed, fine-grained analyses were done of the wind flow field. One reason is that for multi-module setups, an excessive amount of grid cells is required in 3D CFD models to correctly simulate the details in the air flow field that are observed in the field experiments.

Wilson and Paul [78] have studied the effect of mounting geometry on forced convection underneath solar modules for different inclination angles (0-90°), air gap thicknesses (10-500 mm) and wind velocities (0-3 ms^{-1}). A Boussinesq assumption with a 2D steady state, laminar, pressure-based solver was used. In their study, they looked at the laminar wind flow characteristics, but only in the air gap underneath the module. Xing et al. [79] used the same assumptions and inlet wind velocities as in Wilson and Paul's [78] model and compared the

results of their CFD calculations to experimental data from Trinuruk [80]. Wu et al. [81] performed a numerical study in which they investigated the heat transfer from an inclined PV panel for different wind conditions. Roeleveld et al. [82] conducted CFD simulations for BIPV/T systems with an air gap underneath the module, but their analysis was done with a 2D $k-\omega$ turbulence model (k = turbulent kinetic energy, ω = specific rate of dissipation) and only considered the region in the air gap itself.

Karava et al. [30] used R $k-\epsilon$ (ϵ = turbulent energy dissipation rate) and SST $k-\omega$ turbulence models to perform 1:50 scale 3D modellings of roof-mounted PV/T systems with a closed cavity underneath the PV module. Subsequently, Karava et al. [29] studied the wind flow field of low-rise, building-mounted PV/T applications without an air gap under the module The role of air gaps on the performance of BIPV panels was investigated by Mirzaei et al. [83]. In their study, measurements were conducted in a vertical plane along the centerline of a 1:20 scale model in a wind tunnel. A 2D mean flow was assumed through the air gap underneath the module. The results clearly demonstrated the effect air gaps underneath PV modules have on temperature profiles over the module surface. In [38], a 3D CFD model was used to calculate the effect of temperature variations caused by wind flow over a PV module with an air gap underneath it. The results were tested in wind tunnel measurements with a 1:20 scale model. However, the study did not provide details about the effect of turbulence. In a subsequent study [39] they used CFD to simulate the wind velocity field, the temperature field, the turbulence field and the convective heat transfer over the same scale model. In [40], another CFD model was used to calculate the effect of air gap thickness on convective cooling.

So far, no studies have been conducted where 3D CFD modelling of air flow over building-attached PV modules that explicitly includes the (often very small-scale) details in the mounting construction and/or the building underneath it, has been validated with full-scale measurements. Previous studies used more or less idealised, regular shapes where the details were removed for practical, modelling and/or computational reasons. Especially for local cavities and other irregularities, a denser, finer-grained grid is required than in custom 2D models. In this work we study the importance of including these finer-grained details in CFD models, test the effect of grid density on the results, and compare the calculations with experimental measurements in a wind tunnel. This information is necessary to select and develop an accurate CFD model that, at a later stage, can be integrated into thermal models that calculate the energy yield

of BIPV installations with different configurations. We also propose a realistic path towards a CFD model that is both capable and fast enough to accurately simulate even very small irregularities in buildings or other PV supporting structures.

4.3 CFD Model

In this study, a commercial multi-physics modelling software package including CFD models (COMSOL Multiphysics, version 5.2a) was used to calculate the steady-state wind flow over setup with an inclined roof in a wind tunnel. Reynolds-Averaged Navier-Stokes (RANS) equations were used. As the maximum inlet wind speed in the simulations is 5 m s-1 (Mach number: 0.015) the air flow in the test section of the tunnel can be considered incompressible [84]. The standard $k-\epsilon$ model was used for the numerical modelling of turbulent flow. This model is invalid for the domain very close to the wall because in this region, viscosity dominates the flow. Therefore, standard wall functions are defined to bridge the logarithmic layer and the viscous sublayer. In the CFD space the floor of the wind tunnel's test section, the surfaces of the experimental setup, the side walls and the ceiling are all described by a wall function.

For Newtonian incompressible flow, the $k-\epsilon$ model uses the following equations for velocity (u) and pressure (p):

$$\rho(u.\nabla)k = \nabla\left[\left(\mu + \frac{\mu_T}{\sigma_k}\right)\nabla k\right] + P_k - \rho\epsilon \quad (1)$$

$$\rho(u.\nabla)\epsilon = \nabla\left[\left(\mu + \frac{\mu_T}{\sigma_\epsilon}\right)\nabla\epsilon\right] + C_{\epsilon 1}\frac{\epsilon}{k}P_k - C_{\epsilon 2}\rho\frac{\epsilon^2}{k} \quad (2)$$

Turbulent viscosity (μ_T) is equal to:

$$\mu_T = \rho C_\mu \frac{k^2}{\epsilon} \quad (3)$$

with C_μ a constant.

The production factor P_k is equal to:

$$P_k = \mu_T[\nabla u: (\nabla u + (\nabla u)^T)] \qquad (4)$$

In the equations (1)-(4), the values that were plugged into the $k-\epsilon$ model are: $C_\mu = 0.09$, $\sigma_k = 1$, $\sigma_\epsilon = 1.30$, $C_{\epsilon 1} = 1.44$ and $C_{\epsilon 2} = 1.92$. These values were acquired from a turbulent flow conditions data fitting [78], [85].

4.4 Validation of CFD Model

The CFD model described in the previous section was validated with experiments performed in a wind tunnel.

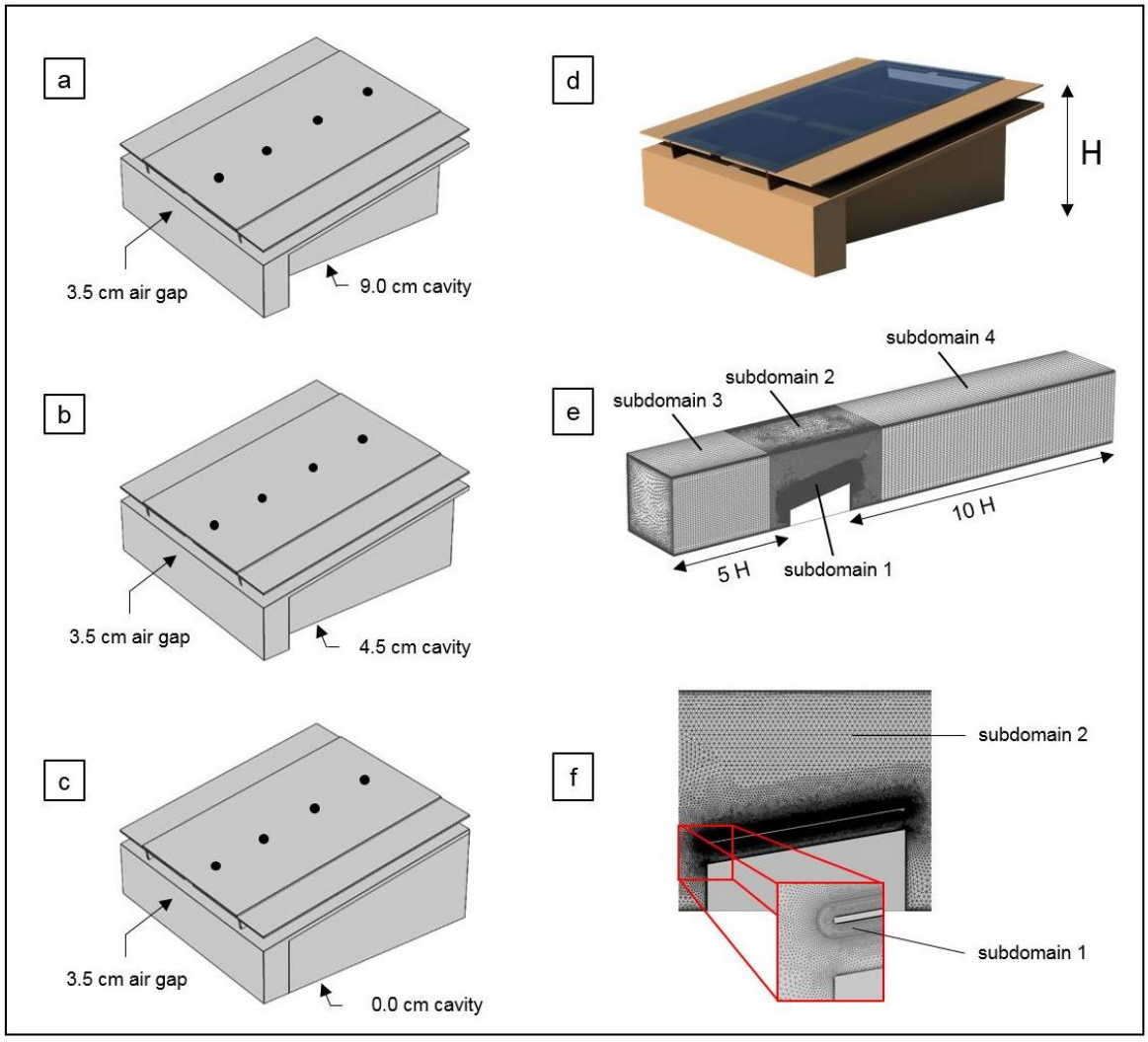

Figure 4-1: Computational model. (a) Model geometry for 9.0 cm cavity; (b) Model geometry for 4.5 cm cavity; (c) Model geometry for 0.0 cm cavity; (d) Definition of H; (e) Computational grid of the CFD environment with the 4 subdomains; (f) Cross section of sub domain

4.4.1 Wind Tunnel Setup

The structure that was tested in the wind tunnel is shown in Figure 4-1(a). It is made of Styrofoam and is 54.5 cm long and 52.7 cm wide, with an inclined roof. The upwind façade is 12 cm high whereas the downwind façade is 20.5 cm high, Don't we have to mention somewhere especially what is the height of H, resulting in an inclination angle of 10 degrees. The roof is made of cardboard 0.4 cm thick. On the roof is a PV module 54.5 cm long, 34.6 cm wide and 0.4 cm thick. The module is extended on two sides by a 54.5 cm long, 9.0 cm wide and 0.4 cm thick cardboard plate. The cardboard plates create a cavity of 9.0 cm wide on both side walls of the construction, as shown in Figure 4-1(a).

To investigate the effect of the presence of an air gap underneath the PV module, the module (with the two cardboard plates attached to it) was installed at two vertical positions above the cardboard roof during the experiments: 3.5 cm and 5.5 cm.

All experiments were conducted in the subsonic closed-loop atmospheric wind tunnel at KU Leuven [86]. The dimensions of the test section are 760 cm (length) × 120 cm (width) × 60 cm (height) and the experimental setup was installed at 5.5 m from the inlet of the test section. In the CFD domain, we modelled 362 cm of the test section, whereby the experimental setup was placed at 102 cm downwind from the model inlet.

Experiments were performed under five aerodynamic conditions, with freestream wind velocities of 1, 2, 3, 4 and 5 m s-1. This adequately spans the range of annual average wind speeds that are recorded near the Earth's continental surfaces [87], [88] . Wind speed was measured with a standard mini pitot tube connected to a digital Furness FC016 manometer with a 0.01 m s-1 precision. For each aerodynamic condition, we measured the near-surface wind speed at 4 points on the centerline of the PV module, on the upper (illuminated) as well as on the lower (shaded) side (Figure 4-1(a-c)). The downwind distances from the leading edge of the PV module were: 4.0 cm, 19.5 cm, 35.3 cm and 50.9 cm. All measurements were done at 1.5 mm above the surface of the module to avoid disruption of the wind flow field in the near-surface region. Wind speeds were measured for a total time of 9 min. The average value was then used for testing the steady numerical model. Apart from average wind speeds, turbulence intensity was also measured for the five aerodynamic conditions with a hotwire anemometer.

4.4.2 CFD Model Setup

A 3D CFD model was created for Figure 4-1(e). Following [89] the experimental setup was placed at 5H from the inlet (Figure 4-1(d-e)) and at 10H from the outlet. To reduce the computational time we divided the domain into four subdomains (see Figure 4-1(e)). Subdomains 1 and 2 were covered with an unstructured tetrahedral mesh. Especially subdomain 1 (the subdomain surrounding the module) was given a high-density mesh. On the surfaces of the module and the experimental setup, fine prismatic cells were constructed on the walls to capture the variations in the flow appropriately. The other two subdomains 3 and 4 had a structured mesh.

Grid sensitivity analysis was carried out according to the guidelines described in [90]. The relative tolerance was set to 10-3 for the solver. To check grid independence, we used the following three domains: G1 (20,693,577 elements), G2 (13,945,903 elements), and G3 (7,664,067 elements). Results are shown in Figure 4-2. The refinement ratio between G1 and G2 was 1.14, and between G2 and G3, 1.60. The deviation of the average wind velocity (measured at 1.5 mm above and below the module) between G1 and G2 is 1.06%, and between G2 and G3, 1.27%. The grid convergence index (GCI) proposed by Roache [90] was calculated for this average wind velocity using equation (24) in [89]. First order discretisation was used in the solver. The GCI21 was 9.46%, and the GCI32 was 2.67%. Based on the average deviation in wind velocity, the GCI index and the available computational resources, grid G2 was retained in the further calculations. In this study, the term "air gap" is used for the open space between the roof and the PV module whereas the space under the inclined cardboard plates will be referred to as a "wall cavity". Figure 4-1(a-c) shows the geometry and position of the air gap and the wall cavities in the experimental setup (one cavity on each side of the setup). In this study, the CFD model was tested for two thicknesses of air gap: 3.5 cm and 5.5 cm.

To test the importance of including wall cavities in a CFD simulation, we calculated the airflow pattern for three cavity depths: 9 cm, 4.5 cm, and 0 cm (no cavity in the wall).

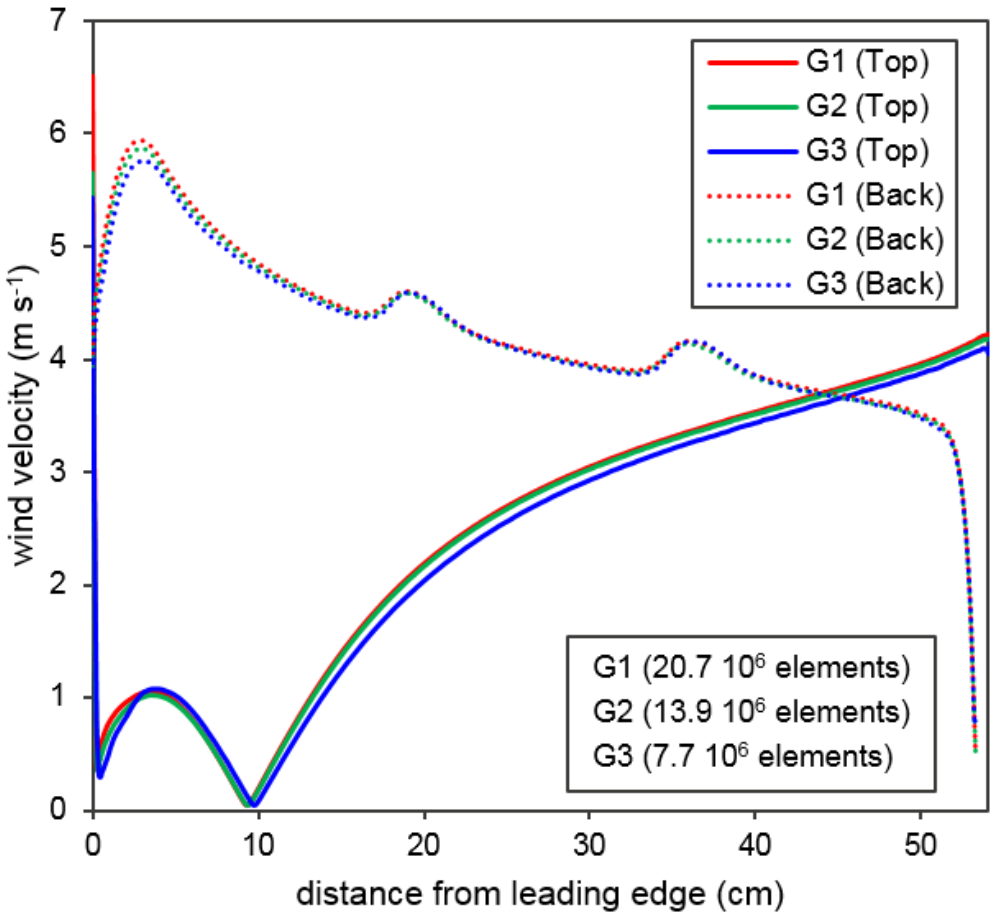

Figure 4-2: Grid Independency test. The figure shows the calculated wind speed at 1.5 mm above and below the module for a 3.5 cm air gap setup and a freestream approaching wind speed of 5 m s-1 for 3 domains: G1 (20.7 106 elements), G2 (13.9 106 elements), and G3 (7.7 106 elements). The differences are very small. For the final calculations in this study domain G2 was used.

Figure 4-3 shows the inlet wind conditions used in this study. The following parameters were used for the inlet: freestream wind velocity: 1, 2, 3, 4 and 5 m s-1; corresponding turbulence intensity: 8.7, 7.6, 6.5, 6.3 and 6.1% (at 20 cm height; see Figure 4-3 for more details); corresponding ambient temperature: 295.15, 293.35, 294.85, 296.15 and 296.55 K; atmospheric pressure: 1 atm. All these values were obtained from the wind tunnel measurements.

To simulate the flow behaviour in the boundary layer while keeping the computational effort low, a growth factor of 1.2 was used to create the viscous

sublayer. A dimensionless wall distance y^+ was used to characterize grid resolution in the viscous layer. The expression for y^+ is:

$$y^+ = \frac{\rho \mu_\tau y_p}{\mu} \qquad (5)$$

with

$$\mu_\tau = C_\mu^{\frac{1}{4}} \sqrt{k_p} \qquad (6)$$

where y_p = distance from point P, k_p = turbulent kinetic energy at point P, and $C_\mu = 0.09$ [76], [91].

Keeping y^+ close to 11.06 in the region of interest allows one to adequately generate the effect of turbulence in the near-wall region. Especially at the top surface of the module where flow separation occurs, y^+ was kept exactly at 11.06. Elsewhere in the model y^+ was maximum 17.7.

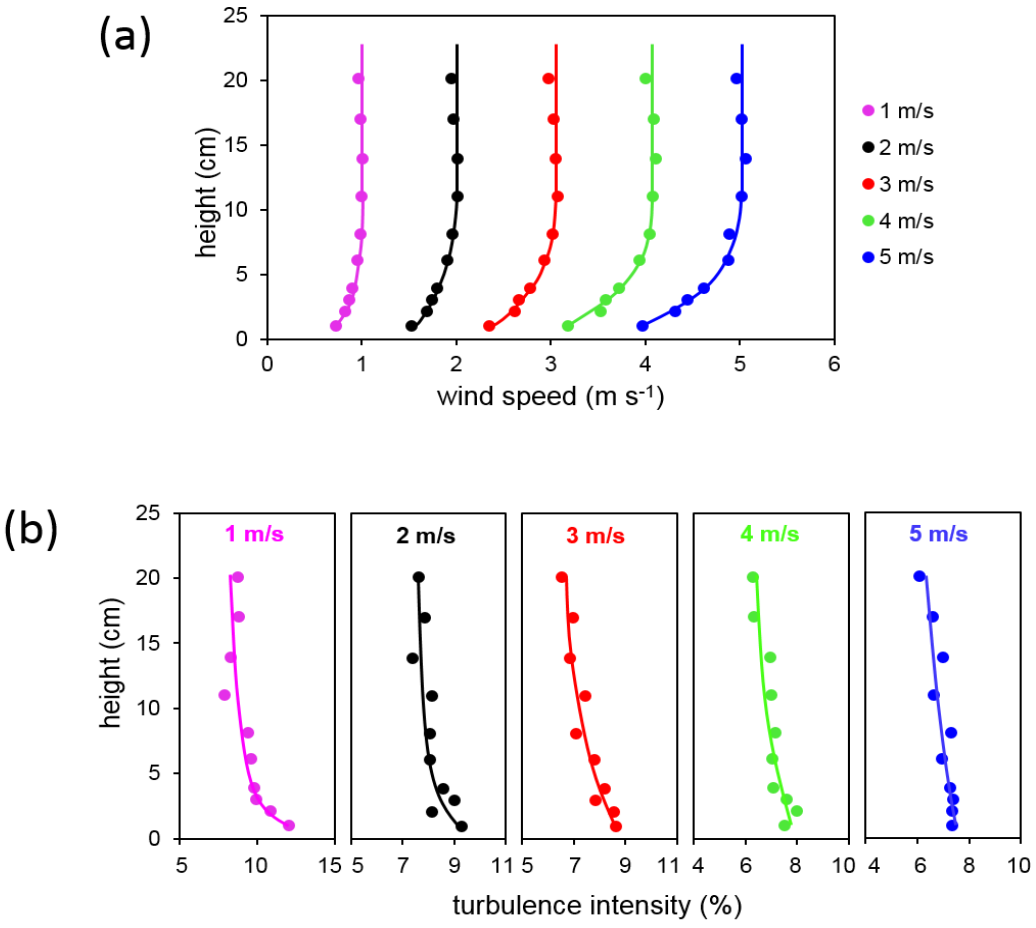

Figure 4-3: Inlet wind profile information. (a) Wind velocity profiles. Dots represent the experimental data; solid lines are the CFD profiles used in the calculations. (b) Turbulence intensity profiles.

4.4.3 Validation Metrics

Relative root-mean-square deviation (relative RMSE) and absolute root-mean-square deviation (absolute RMSE) were used to quantify the variance between the experimentally determined wind speeds and the CFD-simulated wind speeds. In addition, we also calculated the fractional bias (FB) and the correlation coefficient (R). These parameters were defined as:

$$Relative\ RMSE = \sqrt{\frac{\sum_{i=1}^{N}\left(\frac{M_i - S_i}{M_i}\right)^2}{N}} \tag{8}$$

$$Absolute\ RMSE = \sqrt{\frac{\sum_{i=1}^{N}(M_i - S_i)^2}{N}} \tag{9}$$

$$FB = \frac{\bar{M} - \bar{S}}{0.5(\bar{M} + \bar{S})} \tag{10}$$

$$R = \frac{\sum_{i=1}^{n}[(M_i - \bar{M})(S_i - \bar{S})}{[\sum_{i=1}^{n}(M_i - \bar{M})^2]^{\frac{1}{2}} \quad [\sum_{i=1}^{n}(S_i - \bar{S})^2]^{\frac{1}{2}}} \tag{11}$$

M_i and $\bar{M}$ are the experimentally measured individual and average wind speeds, S_i and $\bar{S}$ the CFD-calculated individual and average wind speeds, and N is the number of measurement points [92].

4.5 Results and Discussion

4.5.1 Comparison of Experimental and CFD Simulated Results

To validate the CFD model we compare the measured and simulated wind velocities over the top surface as well as those under the back surface of the module, for the 3.5 cm and 5.5 cm air gap setups (

Table 4-1: Statistical analysis of experimental and simulation data. RMSE = root-mean-square deviation; R = correlation coefficient; FB = fractional bias					
Statistical parameter	3.5 cm air gap			5.5 cm air gap	
	top surface	back surface		top surface	back surface
Relative RMSE	38.07 %	26.68 %		46.30 %	38.20 %
Absolute RMSE	0.58 m/s	0.51 m/s		1.13 m/s	1.16 m/s
R	0.94	0.97		0.99	0.98
FB	0.25	-0.15		0.25	-0.23

). Recall that the data refer to a distance of 1.5 mm above (or below) the module. The simulated and measured wind velocities match satisfactorily. For the 5.5 cm air gap setup the agreement is very good for the top surface except for the most upstream-located measuring point, but for the back surface, the CFD calculations slightly overestimate the measured wind velocities although the differences remain small enough for practical use. A similar slight overestimation on the back surface occurs for the 3.5 cm air gap whereas a slight underestimation is noticed on the top surface of the module.

Table 4-1: Statistical analysis of experimental and simulation data. RMSE = root-mean-square deviation; R = correlation coefficient; FB = fractional bias					
Statistical parameter	3.5 cm air gap			5.5 cm air gap	
	top surface	back surface		top surface	back surface
Relative RMSE	38.07 %	26.68 %		46.30 %	38.20 %

Absolute RMSE	0.58 m/s	0.51 m/s		1.13 m/s	1.16 m/s
R	0.94	0.97		0.99	0.98
FB	0.25	-0.15		0.25	-0.23

The

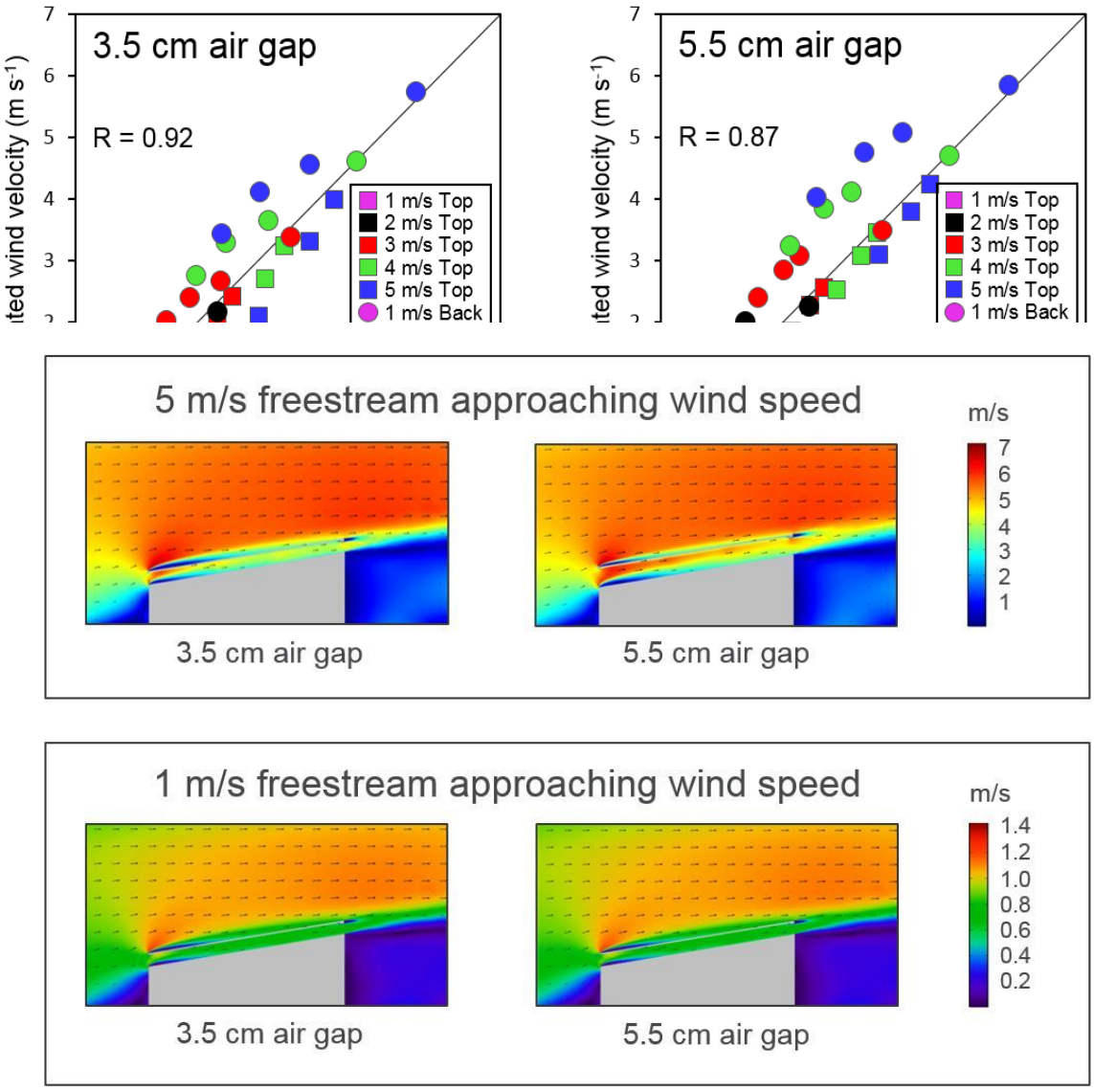

Figure 4-5: Air flow field along the central axis of the experimental setup. All data are for a 9.0 cm cavity, identical to the wind tunnel setup.

validation criteria in Table 4-1 confirm the visual observations in

Table 4-1: Statistical analysis of experimental and simulation data. RMSE = root-mean-square deviation; R = correlation coefficient; FB = fractional bias

Statistical parameter	3.5 cm air gap			5.5 cm air gap	
	top surface	back surface		top surface	back surface
Relative RMSE	38.07 %	26.68 %		46.30 %	38.20 %
Absolute RMSE	0.58 m/s	0.51 m/s		1.13 m/s	1.16 m/s
R	0.94	0.97		0.99	0.98
FB	0.25	-0.15		0.25	-0.23

. In general the CFD results correlate satisfactorily to the wind tunnel results (high values of R), but the slight overestimation in velocity of the former on the back surface and the slight underestimation on the front surface remain visible in the negative (back surface) and positive (top surface) values of the fractional bias FB.

The data indicate that the CFD simulations become less accurate as the air gap becomes thicker (higher RMSE for the 5.5 cm air gap compared to the 3.5 cm air gap, see Table 1) and as the wind speed increases (higher wind speeds result in more deviation from the line of perfect agreement in

Table 4-1: Statistical analysis of experimental and simulation data. RMSE = root-mean-square deviation; R = correlation coefficient; FB = fractional bias

Statistical parameter	3.5 cm air gap			5.5 cm air gap	
	top surface	back surface		top surface	back surface
Relative RMSE	38.07 %	26.68 %		46.30 %	38.20 %
Absolute RMSE	0.58 m/s	0.51 m/s		1.13 m/s	1.16 m/s
R	0.94	0.97		0.99	0.98
FB	0.25	-0.15		0.25	-0.23

). This might be due to the increased level of turbulence because high-turbulent flow is more difficult to accurately model than low-turbulent flow due to its

highly variable and random characteristics, which are only approximated in the currently available solvers. A narrow air gap reduces the maximum size of the eddies, thus decreasing the level of turbulence, and for evident reasons fluctuations in wind speed are larger for higher wind speeds. High turbulence can also explain why above the module the CFD results deviate from the wind tunnel data near the module's leading edge but become better more downwind. In Figure 4-5 the airflow field over the two air gap setups is shown for a high-velocity case (5 m s-1 freestream approaching velocity) and a low-velocity case (1 m s-1 freestream approaching velocity). At the leading edge, the flow separates from the upper part of the module, generating high turbulence near the position of the first measuring point (Figure 4-6), which is still located in the zone of return flow as was shown by the wind speed measurements at this location. More downwind the flow re-attaches to the module and becomes less turbulent (Figure 4-6). On the other side of the module, in the air gap, there is no flow separation near the module itself but a convergence of streamlines instead, resulting in high wind speeds in the most upstream part of the air gap. As the wind is blowing further through the air gap, a boundary layer develops near the bottom of the gap, resulting in a gradual decrease of the wind speed in the air gap. The convergence of streamlines results in lower turbulence (Figure 4-6), which explains the better CFD results for the most upstream measuring point on the back side of the module.

4.5.2 Effect of the Air Gap

Inspecting Figure 4-5 in detail, several differences in the airflow pattern appear between the 3.5 cm and 5.5 cm air gap setups: On top of the module, near-surface wind speed is lower for the 3.5 cm setup compared to the 5.5 cm setup. This can be observed over the entire length of the module. Flow separation is also more prominent: the separation zone is thicker, and it extends more downwind compared to the 5.5 cm setup.

Below the module, the higher wind speed in the upper part of the gap is prominent in the 5.5 cm setup but less so in the 3.5 cm setup. This is best seen in the 5 m s-1 simulation but also appears in the 1 m s-1 simulation.

The lower wind speeds in the air gap below the module and the limitations in maximum eddy size in the gap for the 3.5 cm setup result in lower turbulence near the module's back surface compared to the 5.5 cm setup. This results in better wind speed predictions by the CFD tool used in this study. It should also result in less evacuation of heat, and therefore in less performance of the PV system. For the module's top surface, the tool functions satisfactorily for both air gap setups (

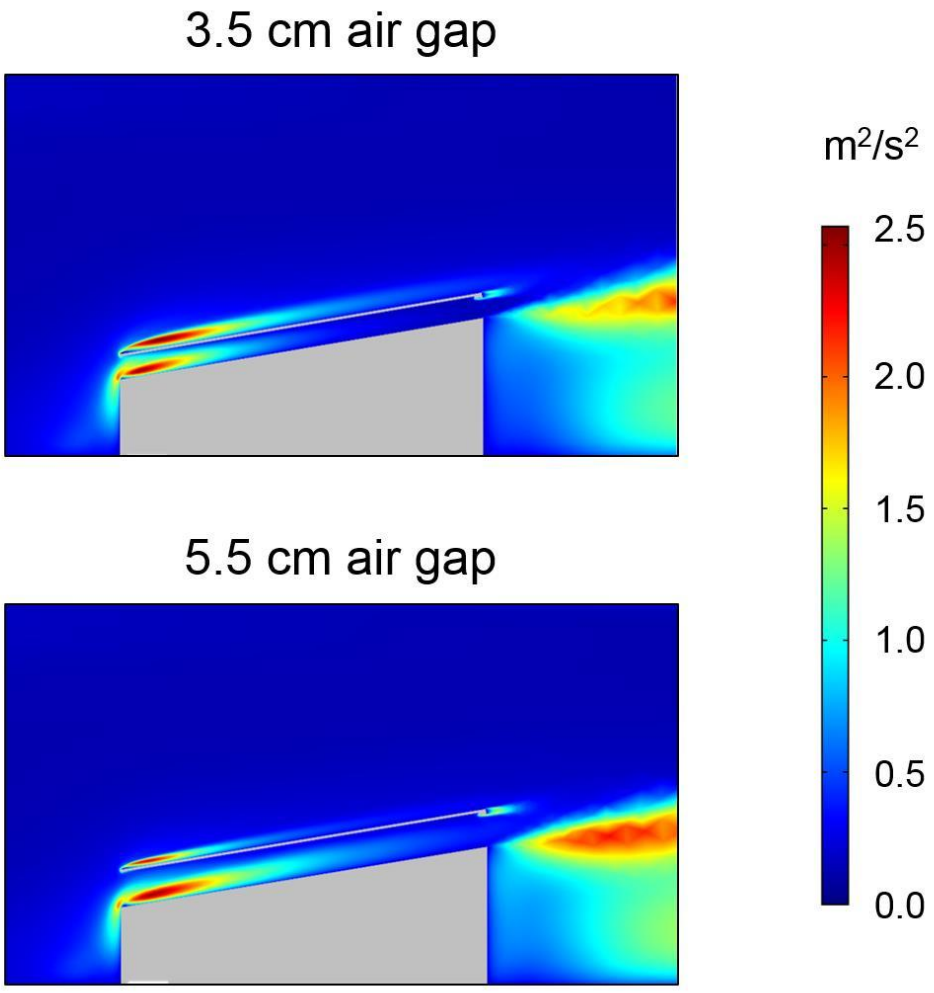

Figure 4-6: Turbulent kinetic energy for 5 m s-1 inlet wind velocity.

Table 4-1: Statistical analysis of experimental and simulation data. RMSE = root-mean-square deviation; R = correlation coefficient; FB = fractional bias					
Statistical parameter	3.5 cm air gap			5.5 cm air gap	
	top surface	back surface		top surface	back surface
Relative RMSE	38.07 %	26.68 %		46.30 %	38.20 %
Absolute RMSE	0.58 m/s	0.51 m/s		1.13 m/s	1.16 m/s
R	0.94	0.97		0.99	0.98
FB	0.25	-0.15		0.25	-0.23

), except for the most upstream-located measuring point on the module, which is located in a zone of return flow in the flow separation region (Figure 4-5).

4.5.3 Effect of the Wall Cavity

The experimental setup in the wind tunnel contained two identical wall cavities, one on each side of the setup (Figure 4-1(a,b)). To investigate the effects of such cavities on the wind velocity near the top and back surface of an inclined PV module, the CFD tool was used to calculate near-surface winds for three different cavity depths: 9 cm, 4.5 cm and 0 cm (no cavity). These cavities correspond to respectively 17.2 %, 8.6 % and 0 % of the width of the wind tunnel setup. Calculations were performed for the 3.5 cm air gap, with a 5 m s-1 freestream approaching wind speed.

To investigate how wall cavities affect the air flow we first calculated the wind speed at the top and back surface of the module, at the same positions where the wind speeds were measured in the wind tunnel (4.0 cm, 19.5 cm, 35.3 cm and 50.9 cm from the leading edge). This was done for 4 longitudinal sections, located at 0.0, 1.0, 4.0 and 26.3 cm from the side edge of the PV setup. No differences in wind speed were observed between the 3 cavities (Figure 4-7). The figure shows the data at 26.3 cm from the edge (central line of the module) as an example; the patterns for the other sections (not shown here) were identical.

Although the magnitude of the wind speed near the module was not affected, the cavities do have an important impact on the airflow pattern over the PV setup. Figure 4-8 shows the wind velocity vectors in a plane perpendicular to the setup, at the same 4 positions where the wind speeds were measured in the wind tunnel (4.0 cm, 19.5 cm, 35.3 cm and 50.9 cm from the leading edge). Because air pressure in the cavities is low (under-pressure zone) when the wind blows over the setup, clockwise and anti-clockwise eddies are formed on both sides of the setup. These eddies are only weakly developed near the onset of the cavity but become more apparent more downwind. The eddies do not only subtract energy

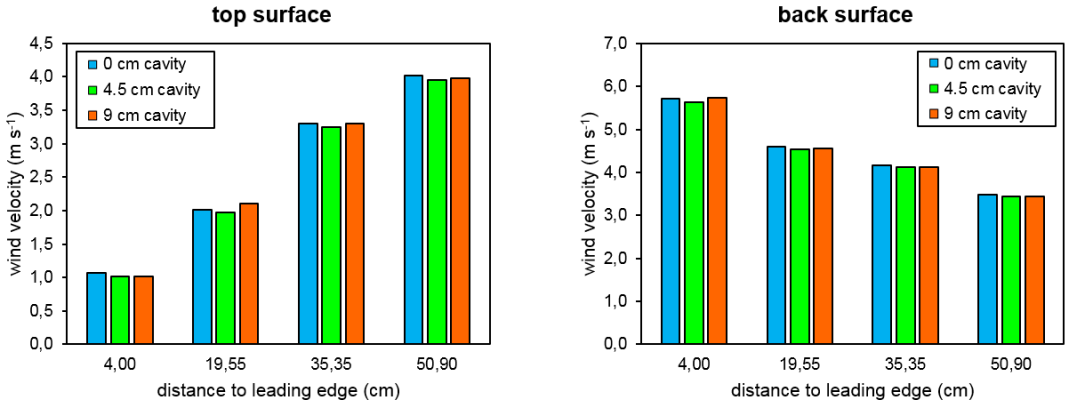

Figure 4-7: Average calculated wind velocity at 1.5 mm above the top surface (left) and below the back surface (right) of the module, for the 3 wall cavities investigated. Data are for the central line of the module and a freestream wind velocity of 5 m s-1.

from the flow due to the enhanced friction but also cause an increased deflection of the wind vector towards the lateral sides of the setup (Figure 4-8). The figure also shows that these effects become larger as the cavity becomes more deeply incised.

Although the magnitude of the near-surface wind speed was not affected, the cavities, therefore, do affect the airflow over the module. For correct CFD

simulations in PV applications, it is thus imperative that even small irregularities in the PV setup be included in the CFD model.

The CFD model allows predictions of the wind flow field over, around, and underneath inclined PV modules. The model also serves as a useful tool when the convection of heat from a PV module's surface has to be calculated. Previous studies [26], [27] have demonstrated that the heat transfer coefficient may strongly vary over a PV module due to variations in wind speed over the module. As a result of these variations, temperature differences occur over the front and back surface that affect the operating temperature of the individual solar cells in the module. As described in [26], these intra-module temperature variations

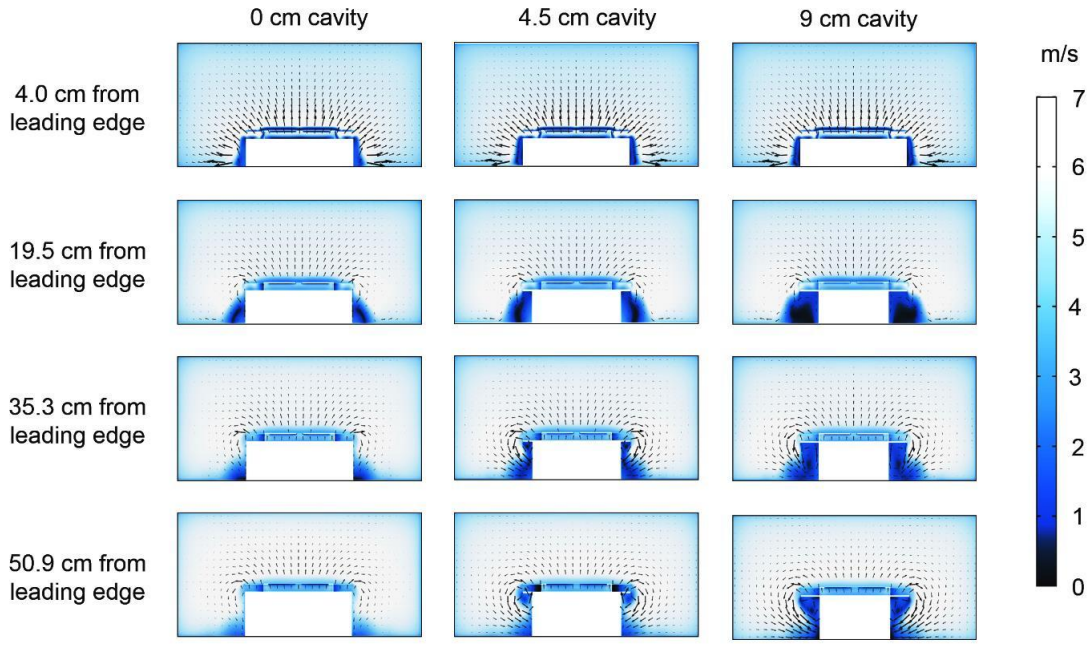

Figure 4-8: Average wind velocity vector field perpendicular to the module, for the 3 wall cavities investigated. The vector field is shown for the 4 positions where wind speeds were measured in the wind tunnel (4.0 cm, 19.5 cm, 35.3 cm and 50.9 cm from the leadin edge).

need to be taken into account for accurate energy yield predictions and evaluations. The CFD model used in this study can estimate the wind flow characteristics over and around a PV module, even when local wall cavities are present that need a special fine-grained grid in the simulation. It can serve as a useful alternative for delicate and time-consuming wind tunnel experiments or cumbersome and expensive field measurements.

4.6 Chapter Summary

The objective of this chapter was to examine how wind interacts with PV module geometry and mounting configuration, and how such interactions influence the spatial character of convective cooling. This was not pursued through analytical approximations or parametric assumptions but through a combination of controlled wind tunnel experiments and validated Computational Fluid Dynamics (CFD) simulations. The underlying rationale, as outlined at the beginning of the chapter, stems from a practical constraint: full-scale PV modules, typically 2 m by 1 m in size, cannot be readily accommodated in standard wind tunnels. Outdoor measurements, while valuable in capturing real operating conditions, introduce noise, uncertainty, and a lack of reproducibility. A miniaturized setup, though not thermally identical to commercial-scale installations, offered a controlled alternative for capturing the physical mechanisms that govern convective heat exchange.

Wind flow measurements were collected across both the top and underside of an inclined mini-module under varying freestream velocities (1–5 m/s). These data were used to calibrate a 3D CFD model, which in turn was applied to assess the effects of two air gap configurations (3.5 cm and 5.5 cm) and three cavity depths (0 cm, 6 cm, and 9 cm). The experiments revealed that narrowing the air gap restricts wind penetration, particularly at the underside of the module. This leads to a measurable reduction in local convective cooling potential and, by implication, an increase in operating temperature, especially in areas shielded from the main flow. Cavity structures did not significantly alter the magnitude of wind speed along the module surfaces. However, they produced secondary effects, and the formation of eddies and recirculation zones near the module boundaries. These localised features, although spatially confined, give rise to non trivial temperature differences across the module surface. This will be demonstrated in chapter 5.

The validated CFD model captures these effects with adequate spatial resolution and provides a useful platform for extending the analysis to configurations and scales beyond what can be physically tested. Its ability to resolve turbulence near wall boundaries, account for mounting-induced asymmetries, and incorporate geometrical irregularities makes it a flexible tool for thermal analysis. While its immediate application lies in reproducing the wind field measured in the wind tunnel setup, the broader utility of the model extends to scenarios where convective behaviour is difficult to approximate whether due to irregular terrain, rooftop structures, or complex mounting geometries. For such cases, the model

offers an alternative to the time consuming and equipment-intensive process of empirical testing.

What makes this framework particularly relevant is its capacity to support spatially resolved thermal simulations which will be demonstrated in chapter 5. These simulations pursued in Chapter 5 couple the CFD with thermal profiles and material-specific thermal conductivity. This chapter forms the foundation for chapter 6 as well. Outdoor experiments are costly and time consuming. It requires consistent long term efforts. Therefore, it is necessary to structure the design of experiments that would be provide optimum results. Fundamentally it supported the design of long outdoor experiments so that we can validate the modelling framework with outdoor operational datasets.

In Chapter 7, the model will be extended to floating PV systems, where wind interactions are further complicated by proximity to water surfaces and transient ambient conditions. In both cases, the spatial structure of the airflow, shaped by mounting geometry and environmental context, plays a decisive role in determining the thermal environment experienced by the PV cells.

In conclusion, this chapter establishes that the geometry of PV installations particularly air gaps and cavity structures exerts a strong influence on local wind behavior, and by extension, on convective heat loss. These effects are not peripheral. They alter the thermal operating point of the module in ways that affect energy yield, reliability, and long-term degradation. Any modelling effort that aims to predict PV performance with precision must incorporate these spatial interactions. The CFD approach developed here, once validated, provides that capability. It bridges the experimental and the computational, and offers a path forward for the more complex, coupled simulations explored in the subsequent chapters.

5 High Resolution Thermal Simulation of PV Modules

5.1 Motivation and Organisation

Building directly on the findings of the previous chapter, where wind-tunnel-calibrated CFD models revealed how detailed geometrical shapes like air gap size and cavity geometry influence convective flow near PV module surfaces, this chapter builds thermal layer physics on top of wind field characterisation. The core motivation remains unchanged: thermal behaviour is not uniform, and assumptions of homogeneity still common in energy yield models mask critical spatial and temporal variations that heavily affect PV performance.

While Chapter 4 emphasised how mounting geometry modulates external flow behaviour and surface shear, the next logical step is to understand how these flow regimes interact with the internal material structure of the PV module. In practice, the module acts as a thermally layered system: heat is generated volumetrically within the cell layer and dissipated through conduction, convection, and radiation across different material interfaces. These coupled processes, especially under non-uniform airflow conditions, give rise to temperature distributions that vary across the surface and depth of the module. Capturing this behaviour requires going beyond simplified surface boundary conditions and incorporating the physical 3D structure of the PV module into the CFD domain itself.

This chapter presents a three-dimensional, experimentally validated CFD-thermal model that integrates heat generation within the cell layer, spatially variable wind exposure, and material-specific conductivity. By embedding thin-

layer features within the computational mesh, the model resolves internal heat flow without an excessive computational burden. Simulations were conducted for modules mounted at a tilt, with freestream velocities ranging from 3 to 5 m/s and air gaps of 3.5 cm and 5.5 cm mirroring the wind tunnel scenarios introduced previously in chapter 4. Where the earlier model captured only the external velocity field, the current work includes spatial temperature fields within the module layers, allowing for direct comparison with cell-level experimental data.

Furthermore, this chapter introduces the role of wind direction, not merely wind speed, as a determinant of convective asymmetry. It was not possible to test these conditions within a wind tunnel. Therefore, a validated CFD thermal model was necessary. Unlike velocity magnitude, which is routinely included in empirical heat transfer models, directional dependence is never quantified or integrated into PV thermal simulations [refs]. Here, the directional component is treated explicitly, using angled inlet conditions to induce lateral pressure differences and boundary-layer disruptions. The resulting temperature differences across the module are non-trivial. In certain configurations, cells on the leeward side experienced temperatures more than 30 °C higher than those on the windward edge. These differences matter: they shift the maximum power point, and under real-world string conditions, introduce current mismatch losses.

5.2 Chapter Specific Introduction and State of the Art

Solar photovoltaic (PV) module energy yield depends on various ambient conditions and module components. The dependency on such dynamic ambient conditions makes it difficult to optimize non-flexible modelling approaches. Solar insolation, wind speed, wind direction, ambient temperature, the mounting structure, the building structure, and the local topography have a combined effect on energy yield. Before developing a method to describe all these environmental effects together, it is imperative to have a good understanding of these elements separately. In this paper, we focus on simulating the effect wind has on the surface temperature of a PV module mounted on an inclined surface with air gaps underneath.

Typically a commercial PV module converts 13-20% of the incident solar irradiation into electricity [93]. The remaining part is converted into heat. This heat increases the cell's temperature, which is transferred to the module surface both on the front and on the back. Depending on the technology, every increase

of one degree in temperature of a silicon solar cell results in a decrease of approximately 0.45% relative efficiency [94] [94]. Moreover, the surface temperature is not constant but varies over the module when the latter is subjected to wind [96] [95]. The temperature difference between the front and the back of a module can mount to 20°C [96].

Analytical models have been developed to correlate the wind speed and the heat transfer coefficient based on thermal boundary layer theory. These models usually consider smooth, horizontal, isothermal flat plates with parallel wind flow [97]. A growing body of literature recognizes that there are limitations in using such analytical formulations for PV applications [100] [98]. This chapter reports progress in the fine-grain analysis of coupled computational fluid dynamics (CFD) and heat transfer models to simulate the surface temperature of a PV module on an inclined surface with a 3.5 and 5.5 cm air gap underneath.

Extensive work has been done on module setups that go beyond the basic horizontal configuration. Wilson et al. studied the heat transfer inside air gaps under a PV module in which they considered average module temperature[99]. Xing et al. followed the assumptions of Wilson et al. and studied the effects of the tilt angle, mounting structure, and air gap size on module temperature and power output [100]. In their study, they considered the variation of solar irradiation due to changes in the tilt angle. They validated 2D simulations using experimental data from Trinuruk et al. [101]. Roeleveld et al. analyzed the heat transfer coefficient of a PV module, focusing on the air channel underneath the module. In their 2D simulation model, they specified the convective heat flux created by the wind and the natural convective heat flux as an input boundary condition [102]. Jubayer et al. and Karava et al. analyzed the forced convective heat transfer of PV modules in various setups of ground and roof-mounted systems in 3D. These studies focused on the array/system level, kept PV module surface temperature constant, and analyzed the convective heat transfer characteristics [106] [103].

Mirzaei et al. experimentally investigated the impact air gaps underneath a building integrated (BIPV) module have on cooling. They reported that air gaps and panel arrangements significantly change the air flow characteristics [104]. Zhang et al. used Mirzaei et al.'s experiments to validate a 3D CFD heat transfer model. Their model showed the highest deviation of 23.1% with measurement for a 0.5 m/s inlet wind speed. The overall average error was 9.7% for isothermal and 8.0% for non-isothermal cases. They observed large deviations on the top

surface's windward edge of the PV surface [105]. These papers are the closest related work to our approach today.

However, the assumption of constant heat transfer or an average temperature over a module's surface will translate into non-negligible overestimations of the power output. Overestimations of up to 4.3% have been reported [95]. Studying the spatial variations of the heat transfer coefficient through experiments is useful but has some limitations. This is because the number of measurement points on a module's surface is limited. Thermocouples surely cannot be placed on solar cells because they will create shading. One way to overcome this is to use infrared camera measurements. However, infrared images also capture unwanted reflections from the module surface. Another solution is to develop a validated model by placing thermocouples on the surface as near to the cell region as possible without interfering with the electricity output. This model can be used for fine-grain temperature variations. Such models were not considered in the literature so far. A validated model could further be used to explore different configurations of PV module setups for other novel applications of building applied PV

Here, we propose a feasible path towards the development of a bottom-up physical model. This model can simulate (1) the spatial temperature variations over an inclined PV module that (2) is subjected to different wind velocities and contains an air gap underneath it, and (3) considers a variable volumetric heat transfer from the cells. In this context, a coupled CFD and heat transfer model is the best option to simulate the temperature variations, caused by wind flow, in the thermal boundary layer near the PV surface. We wanted to integrate the front glass, encapsulant, cell, and black polythene back sheet and use these as heat generation sources. The primary challenge is to integrate the effects of the heat transfer from thin 0.2 mm solar cells and apply these to a 54.5×34.6×0.4 cm, six-cell module. We have worked to reduce complexities, memory requirements and the time required for convergence. In the simulation, we have used a resistive thin layer instead of resolving all thin layers as a 3D domain.

5.2.1 Experimental Wind Tunnel Setup

The tested setup is a 2×3 cell module of 54.5×34.6×0.4 cm mounted on an inclined roof surface (angle of inclination: 10˚). The roof rests on a building structure 54.5 by 52.7 cm. An air gap was left between the building and the roof. Wind speed and surface temperature were measured at four points along the centerline of the module, both on the front and the back surface, at 4.0, 19.6, 35.4, and 50.9 cm from the leading edge (Figure 5-1a). Wind speed was measured at 1.5 mm above the surface with a digital Furness FC016 manometer (precision: 0.01 ms-1). The surface temperature was measured using thermocouples (precision: 0.1˚C). Illumination was 300 Wm-2. A Keithley 2602A instrument was used to measure the electrical performance of 6 cells independently. Ambient temperatures for 3, 4 and 5 ms-1 freestream wind velocities were 21.7, 23.0 and 23.4˚C respectively, and atmospheric pressure, 1 atm.

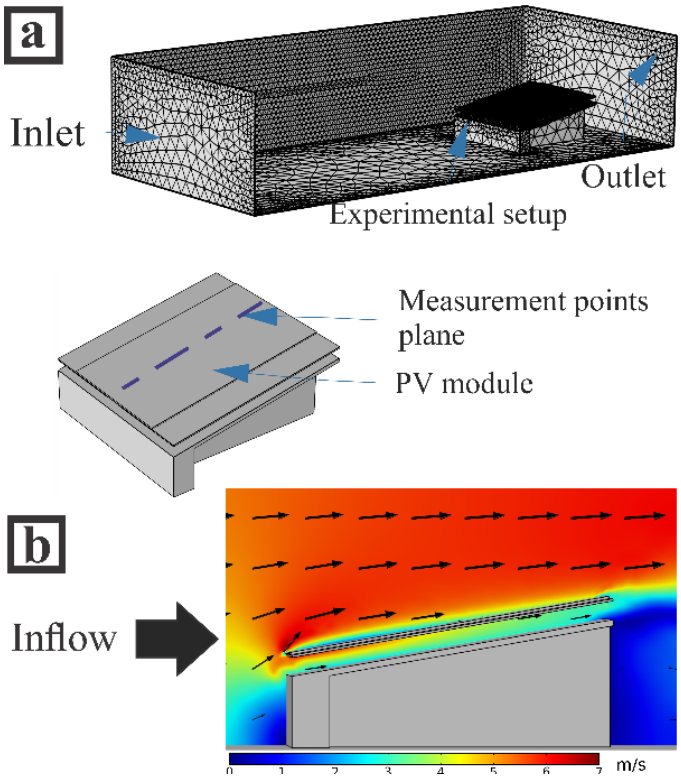

Figure 5-1: (a) 3D surface mesh of the wind tunnel test section (b) Wind velocity vector and magnitude for a 3.5 cm air gap and 5 ms-1 inlet wind speed.

Three aerodynamic conditions were simulated, with freestream wind speeds of 3, 4 and 5 ms-1. Figure 5-2 shows the local Richardson number (Ri), calculated from the experimental results. Ri is the ratio of a buoyancy term and a flow shear term [97]. For this calculation, we chose the third measuring point on the

module because it was located well downstream, where the boundary layer is well established. For the three wind velocities selected, Ri≤0.01. Natural convection could, therefore, be neglected [97] [106].

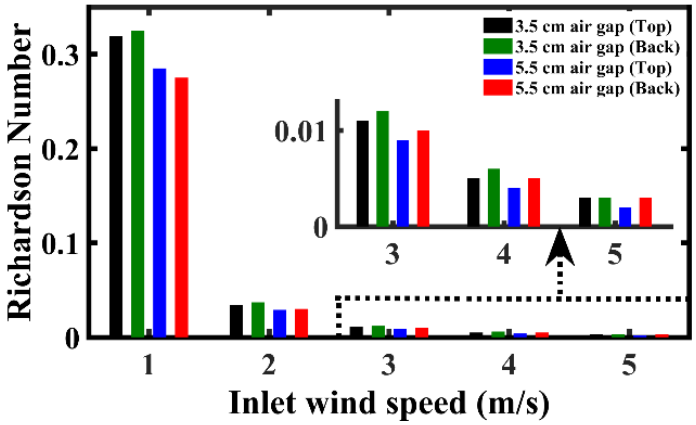

Figure 5-2: Richardson numbers for different inlet wind speed conditions, for 3.5 and 5.5 cm air gaps.

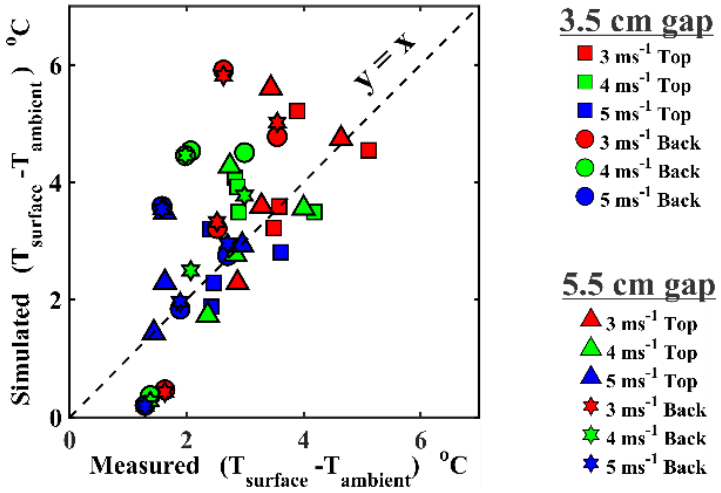

Figure 5-3: Simulated versus measured surface temperature, for a 3.5 and a 5.5 cm air gap

5.2.2 CFD Model Description

The CFD model is a 3D domain built in Comsol 5.3. The bulk domain of the fluid (air in this case) was an unstructured tetrahedral mesh to capture turbulence and vorticity properly. A dense mesh was applied near the PV module. For the gradual development of the fluid and thermal boundary layers in the near-wall region, prismatic cells were used. A total of 7.388×105 mesh elements were used. Wall function is used to approximate the boundary layer region. Fig 1(a) shows the surface mesh configuration for the bulk CFD domain with inlet and

outlet. Within the PV module, we considered glass (3.2 mm), EVA (0.6 mm) and a black back sheet (0.2 mm). The thin layer feature of Comsol 5.3 was used to simulate six full-sized cells within the EVA layer. The thickness of the cells was 0.2 mm. Heat generation from the cell was calculated from the short-circuit current of the cell separately. For the airflow, a standard $k - \epsilon$ model was used with wall functions on the wind tunnel floor and the module's front and back surfaces. CFD and heat transfer were coupled using the Kays-Crawford method. Heat transfer within the module took place via conduction, and from the module towards the surrounding area, via convection.

5.2.3 Experimental Validation

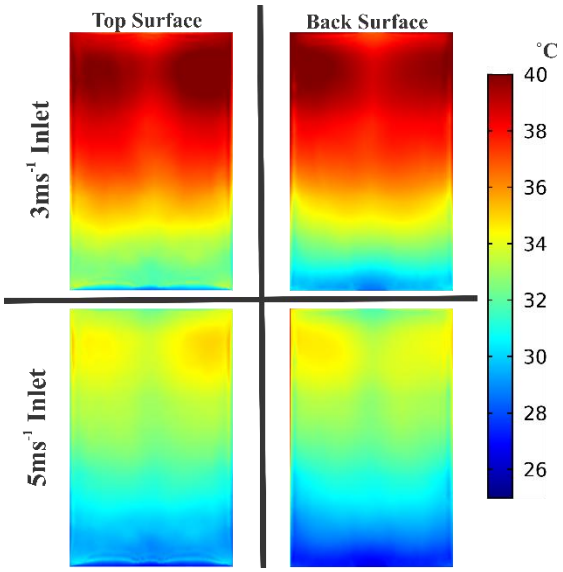

Figure 5-4: Surface temperature on the module's top surface, for a 5.5 cm air gap.

The patterns for the wind velocity vector and magnitude were very similar for the 3, 4 and 5 ms-1 freestream inlet wind conditions and resemble the pattern in Figure 5-1 (b). Hence only the case for a 3.5 cm air gap and a 5 ms-1 freestream inlet case is presented here.

To validate the model, wind tunnel experiments were performed in the environmental wind tunnel of the Geography and Tourism Division, KU Leuven, Belgium [86]. In Figure 5-3 the simulated result is compare to the experimentally measured result. Overall there is good agreement between the simulated and the measured result. Most of the discrepancies are because of overestimations of the simulated results, except for the first point on the front surface, where there is an underestimation. This underestimation can be explained by the flow separation that occurred near the module's surface. Zhang

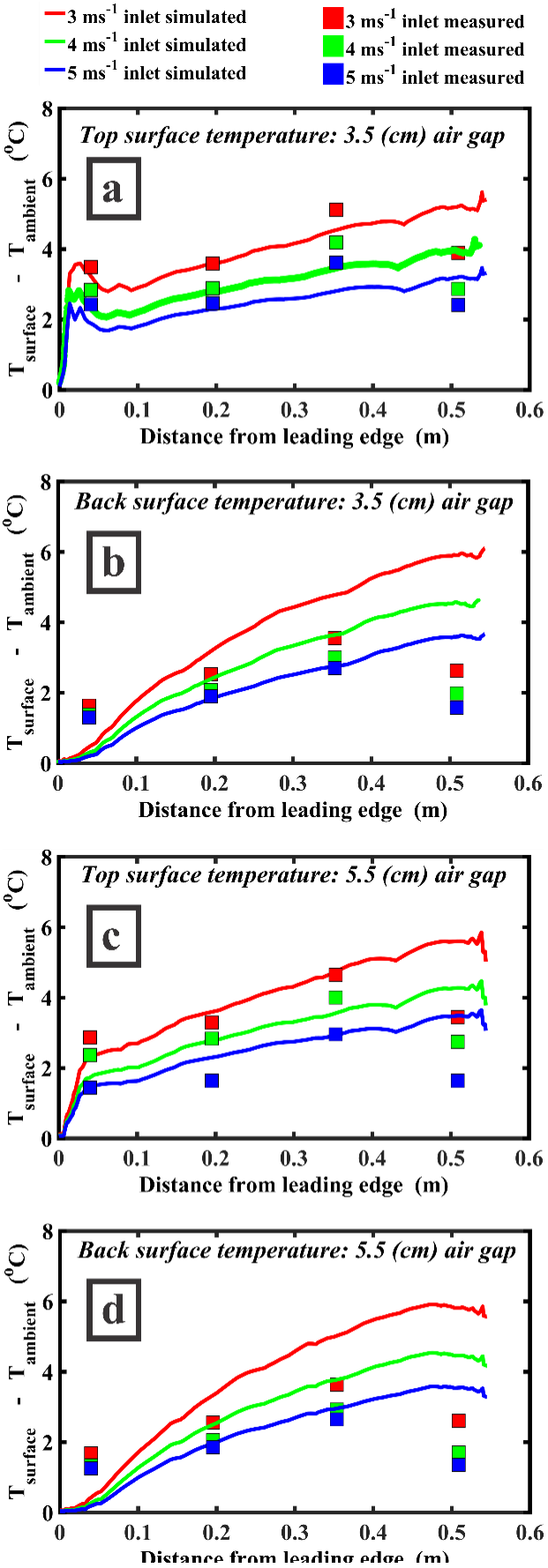

Figure 5-5: Temperature profile along the central line of the module

et al. reported a similar effect [105]. Less heat is carried away from the module because of the sudden drop in velocity. This suggests that the thermal boundary layer region should be improved in the CFD model.

From Figure 5-4 it can be seen that the upwind part of the module shows a fairly uniformly distributed temperature. The central region of the module shows a gradual change. Near the trailing edge high-temperature regions start to develop in the corners. As the air is already heated up, less heat is carried away from the module in these zones. Figure 5-5 shows the surface temperature from the leading edge towards the trailing edge of the module. The top surface is situated in the fully developed boundary layer, and therefore the temperature data show good agreement. The trend for the back surface is comparable, but there is a mismatch. This mismatch could have happened because of the region of transitional flow in the boundary layer, as explained in Chowdhury et al. [61]

5.2.4 Section Summary

In this chapter, we report on the progress in developing a bottom-up physical model to simulate the spatial temperature distribution over a PV module subjected to wind. The model includes the fine grain details of heat transfer from the cells towards the module surface. We proposed a feasible method to integrate all these fine details with a thin layer feature inside the module. The model allows a better understanding of the effect of air gaps underneath a module have on the module's temperature. These insights are necessary for accurate energy yield estimations. Another conclusion is that, for 3, 4 and 5 ms-1 free stream wind velocities, it sufficed to consider only forced convection in the coupled CFD-heat transfer model.

5.3 Simulation of Full Scale PV Module

In the second part of this chapter we expand the simulation capabilities. Validated CFD thermal model capacities will be expanded further to a full scale module. For this, detailed cell level finite element modelling will be presented. This would be a leap forward for state of art of PV finite element modelling. Impact of both wind speed and wind direction on PV's thermal response will be presented as well.

5.3.1 Physics Assumptions for Models

In order to assess the spatial temperature variations of a PV panel, cell level accuracy is required. In this part of the chapter, a single stand-alone silicon PV panel is studied. All the geometrical features of the PV module is illustrated on Figure 5-6. The aluminium frame and the supporting structure of the PV module were not modelled. The material properties of the PV module can be found in Figure 5-6. The PV panel has a tilt of 35°, which is typical for most solar farms in Belgium [107]. The default height of the lowest part of the module, h_0, was taken as 65 cm, being a typical height for ground mounted modules [34], [108].

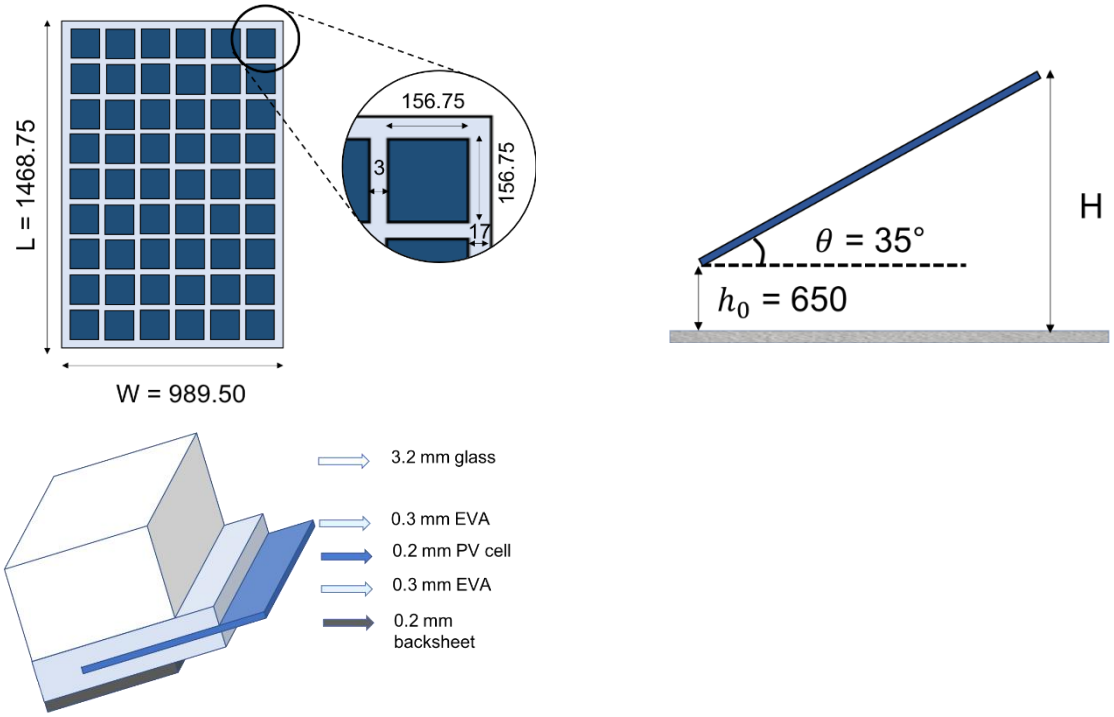

Components	Thickness (mm)	Thermal Conductivity (W/m·K)	Density (kg/m^3)	Heat capacity (J/kg·K)
Glass	3.2	1.8	3000	500
PV cell (Mono-Si)	0.2	148	2330	677
EVA	0.3	0.35	960	2090
Backsheet	0.2	0.2	1200	1250

Figure 5-6: PV module properties

When analyzing the temperature variations of a PV panel, two physics have to be considered: fluid flow and heat transfer. These physics are described by the Navier-Stokes equations. As the airflow over a PV panel is turbulent [29], [30], [34], [35], [61], [62], [77], those equations can be approximated by the Reynolds

Averaged Navier-Stokes (RANS) equations. These equations were simplified by considering air as incompressible and using the Boussinesq approximation in order to take buoyancy forces into account. Various studies have demonstrated good results by approximating the flow around a solar module as incompressible and using the Boussinesq approximation.

In order to compute the turbulent viscosity (μT) and the turbulence kinetic energy (k), additional transport equations have to be solved. Those equations are obtained out of a selected turbulence closure. The three most commonly used turbulence closures for industrial applications are two-equation closures: the k-ε, the k-ω and the Shear Stress Transport (SST) k-ω closures. The former does not resolve the viscous sublayer by using wall functions (y+ ≈ 30) and offers therefore a cheaper computational cost and limited accuracy compared to the two other models. The latter resolves the entire flow regime and requires the most computational resources. It is also well-known to exhibit the best performance in case of flow separation, which occurs significantly over a PV panel. As high accuracy is required to simulate local temperature variations and flow separation, the SST k-ω closure was chosen in this study. This closure showed a good agreement with experimental results in various studies for free-standing PV panels [34], [109], [110], [111].

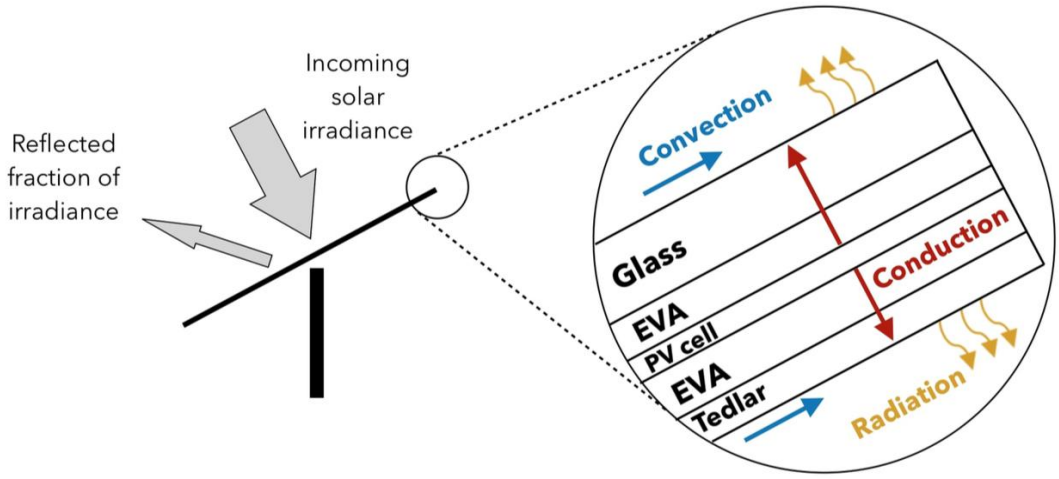

Figure 5-7: Energy balance over a ground-mounted PV module

When solar irradiance G hits a mono-facial PV module, a fraction (1-a) of it is directly reflected to the surroundings, a, representing the absorption coefficient of the module. The absorbed irradiance is transformed into electricity with a fraction η, being the module's efficiency. The rest is converted into heat. The total heat produced inside a PV module is therefore equal to $Q = (1 - \eta) \cdot a \cdot G$.

A with A the surface of the module. The PV module being almost always hotter than the ambient air, the heat transfer occurs from the module to the surroundings.

Heat transfer is described by the energy conservation equation and occurs in three mechanisms. The heat Q is first transferred by conduction from the inner PV cells to the module's outer surfaces through the different layers shown in Figure 5-7. This heat is next extracted by the surrounding air through radiative and convective heat transfer. The whole heat transfer mechanism is depicted on Figure 5-7. To a lesser extent, heat is also redistributed laterally by conduction within each layer, and next by convection and radiation through the edges of the module. Reflected radiation can be neglected as there is no specific reflection from the surface behind the module [112]. Conductive heat dissipation to the surroundings can also be neglected [78]. Radiative and convective heat transfer are more or less of the same order of magnitude [110] such that both have to be modelled in order to compute the heat extracted from the module.

Radiative heat transfer can be modelled by using a solar ray tracing model [39] or using a Discrete Ordinate radiation model [78]. As the aim of this chapter is to assess the impact of airflow on the temperature pattern of a PV module, the convective effect should be isolated with respect to the radiative effect. Various studies [110], [113], [114] suggest modelling the PV cells as a uniform equivalent heat source Q , avoiding to directly model radiation but only its effect on heat transfer. The magnitude of this equivalent heat source is defined by equation $Q = (1 - \eta) \cdot a \cdot G$. The results obtained from this modelling approach showed a good agreement with experimental results, while isolating the convective heat transfer and avoiding the difficulty to correctly model radiative heat transfer. For this reason, this approach was also used in this thesis.

In order to quantify the heat source magnitude Q for an incoming irradiance G, the absorption coefficient a and the PV cell efficiency η should be computed. The absorption coefficient of a solar module is, however, very difficult to estimate. First of all, a solar module is composed out of different layers (Figure 5-7) with different optical properties and absorption coefficients. Moreover, this coefficient depends on variable ambient parameters such as air humidity, the dust in the air and overcast [110]. The PV module efficiency on its side strongly depends on the temperature of the module. Introducing a heat source, which in turn is dependent on the module's operating temperature, would introduce a very high coupling. For the above-mentioned reasons, the efficiency and the absorption coefficient were considered as constant in this study. Therefore, it is

very important to highlight that the value of the equivalent heat source does not exactly correspond to the incoming irradiance. The value of the heat source is, however, able to represent the effect of increasing or decreasing irradiance and to provide a good order of magnitude of the cooling potential for a given irradiance. A higher degree model could be constructed in order to accurately model the sun radiation and the detailed heat transfer by modelling air dust, air humidity, the complete spectrum of sunlight and all the optical characteristics of each material of the PV module. This, however, goes beyond the scope of this PhD thesis which mainly focuses on the convective cooling effects.

Table 5-1: Optical properties used for the absorption coefficient.

Components	Reflectivity	Absorptivity	Transmissivity
Glass	0.018	0.032	0.950
PV cell (Mono-Si)	0.070	0.930	0
EVA	0.030	0	0.970

5.3.2 CFD Model Setup

The computational domain and the mesh were constructed following the COST [115]and ERCOFTAC [116] guidelines. The computational domain has an outlet clearance of 10Hb, an inlet clearance of 5Hb, a lateral clearance of 10Hb and a top clearance of 5Hb. The characteristic height was chosen as H - ho = L · sin(θ) (see conventions Figure 5-8). The domain is represented on Figure Figure 5-8 and is of total dimensions 4.68 m (Ltot) × 6.36 m (Wtot) × 2.41 m (Htot). Also, for a wind direction perpendicular to the solar module (α = 0° and 180°), symmetry was implemented.

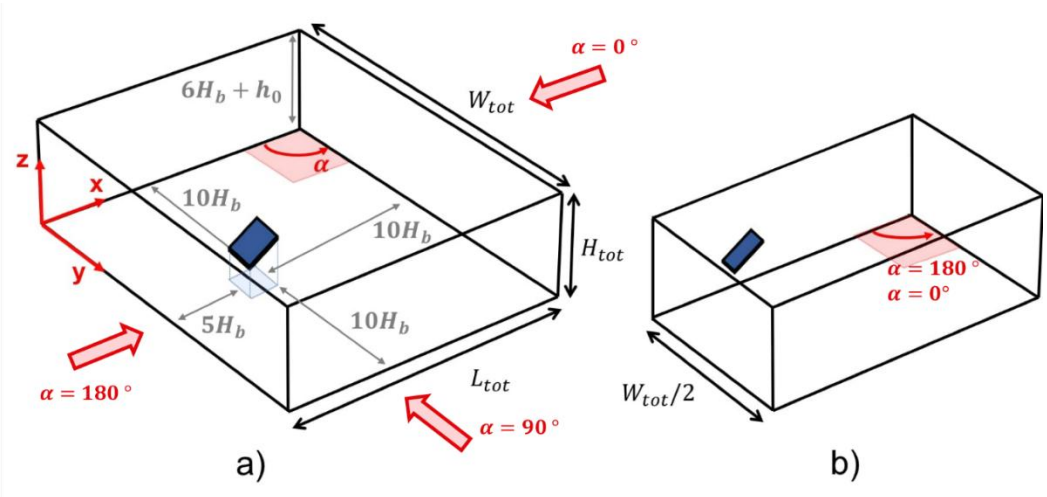

Figure 5-8: a) Computational domain, b) symmetry for wind direction $\alpha = 0°$.

A slip boundary condition was assigned to the lateral and top sides of the air domain while a no slip boundary condition was assigned to the ground and for the PV module boundaries. Zero gauge pressure was chosen as the domain outlet boundary condition. The inlet was assigned the velocity and turbulence profiles of a fully developed flow, obtained following the procedure described by Blocken, accurately simulating the atmospheric boundary layer [117], [118], [119]. The corresponding profiles for inlet wind velocities, U0, ranging from 0.5 m/s to 4 m/s and the related turbulence intensity profiles are displayed on Figure 5-9. U_0 is defined as the wind velocity at a height h0+Hb/2 = 0.8 m.

The equivalent heat source (W/m2) is defined as $Q = (1 - \eta) \cdot a \cdot G$

The absorption coefficient a and the efficiency η were considered as constant and need to be determined. In order to approximate the value of the absorption coefficient, the optical properties listed in Table 5-1.

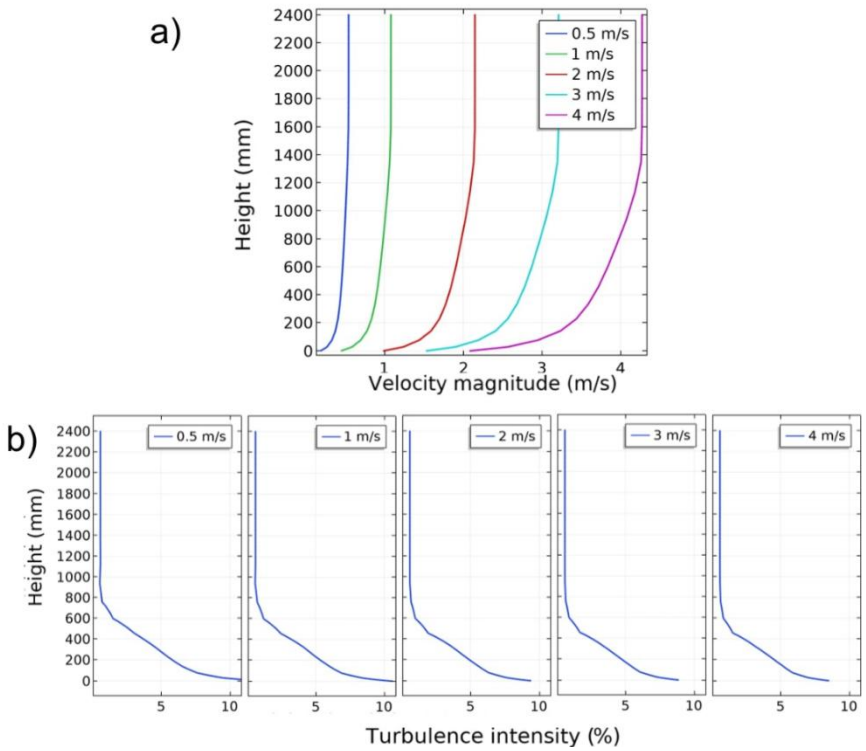

Figure 5-9: Inlet wind profiles: a) wind velocity magnitude; b) turbulence intensity.

In order to approximate the value of the absorption coefficient, the optical properties listed in Table 5-1 were used. Neglecting back radiation, the absorption coefficient can be computed as a = 0.95·0.97·0.93 ≈ 0.86. In order

to determine a constant value for η, the following elements were considered: the STC efficiency of a typical industrially available silicon PV cell is considered 21% and the power temperature coefficient is -0.38%/K. In Belgium, the mean wind speed amounts to 3 m/s while the irradiance contributing to the major part of the energy yield is ~800–900 W/m2. The latter information was collected from rooftop experimental measurements in EnergyVille 1, Genk (Belgium,) and is depicted on Figure 5-10 (where it contributes to 23% of the total yearly insolation). The average cell temperature for these conditions and an ambient temperature of 20◦ [109], [110]. Altogether, the average efficiency for these typical conditions can be approximated as $\eta = \eta STC \cdot (1 - 0.0038 \cdot (T - TSTC)) = 0.21 \cdot (1 - 0.0038 \cdot (42 - 25)) \approx 19.5\ \%$. Putting the constant values of η and a back, the relation between the equivalent heat source and irradiance is reduced to $Q = 0.69 \cdot G$. This value of 0.69 closely matches the ones used in previous studies [109], [110] where a good agreement between simulations and experiments was obtained.

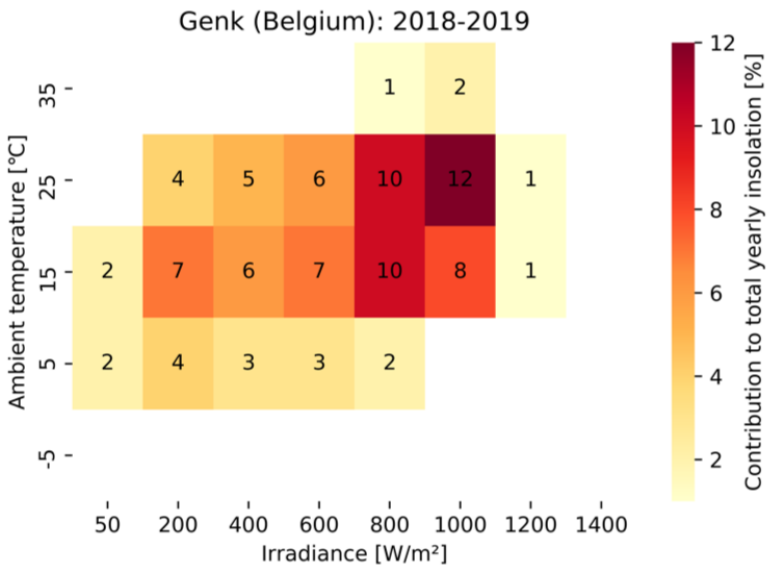

Figure 5-10: Contribution to the total yearly insolation (%) of different irradiance levels at different ambient temperatures, collected at Genk (Belgium).

5.3.2.1 Computational choices

The finite element CFD software COMSOL Multiphysics was employed for the simulation. The problem was modelled for steady-state coupled heat transfer and turbulent flow physics. Nižetić et al.[110] showed that the converged module temperature was the same for a steady-state and a transient simulation, such that a steady-state analysis can be used. The RANS equations for a steady-state

incompressible turbulent flow were solved with the Boussinesq approximation and an equivalent heat source, using the finite element method.

5.3.2.2 Mesh

For this domain, a high quality hybrid mesh consisting of hexahedral and tetrahedral elements was constructed (Figure 5-11). The inner block was used to reduce the number of tetrahedral elements as much as possible, giving a higher quality mesh [61], [120]. Pyramids formed the transition between hexahedral and tetrahedral elements (Figure 5-11). The PV cells and the surrounding EVA were meshed with hexahedra, which were swept over the whole solid module and over the boundary layer. The glass layer was meshed with eighth cell layers, the other material layers were meshed with one cell layer. The boundary layer consisted of twenty layers with an expansion ratio of 1.2. The first cell height for the was 0.05 mm, leading to a value of y+ ≈ 1 at every wall. Because the SST k-ω turbulence closure is used in this study (see later), the viscous sublayer has to be resolved without wall functions and a value of y+ ≈ 1 has to be chosen [61], [115], [116], [117], [119].

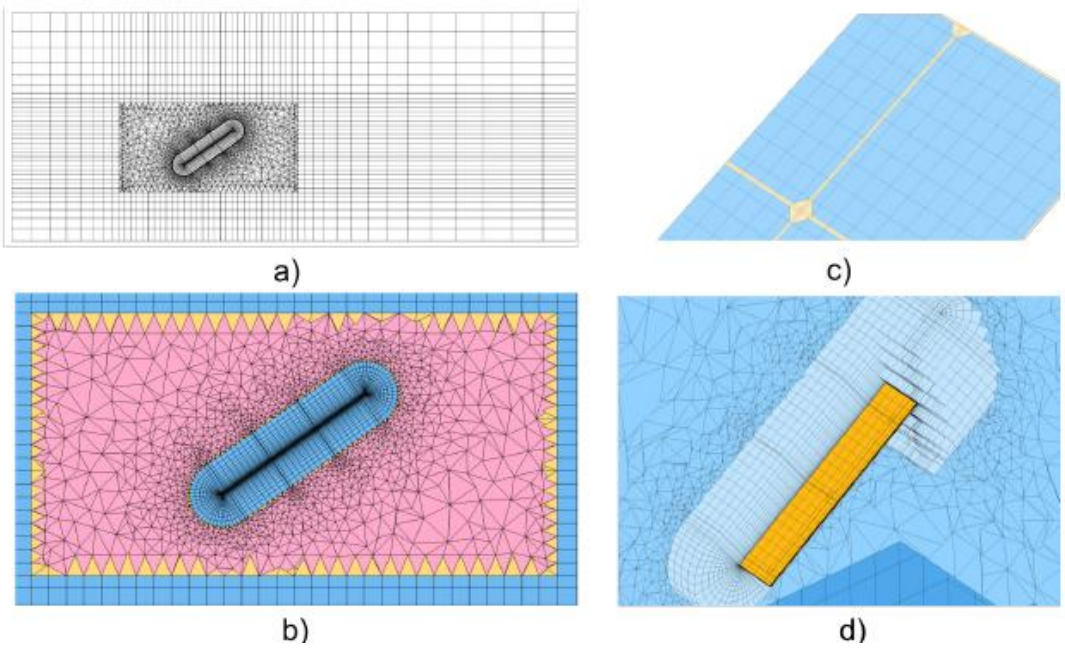

Figure 5-11: a) Hybrid Mesh. b) Zoom on inner block: different mesh element shapes: blue = hexahedra, yellow = pyramids, pink: tetrahedra. c) Meshing of the PV module: blue = PV cells, yellow = EVA. d) 3D view of the mesh: blue = air, orange= solid.

The mesh refinement study was performed with a mini module of 3x3 cells with the k-e turbulence closure in order to decrease the computational cost

significantly. The number of mesh elements was multiplied by a constant factor m everywhere in the domain (except from the number of layers in the boundary layer and some very thin geometries such as the EVA between the PV cells). The number of mesh elements for each grid is indicated in Table 5-2.

Table 5-2: Number of mesh elements for the different grids.

	G6	G5	G4	G3	G2	G1
m	1	1.5	2	2.5	3	4
Number of elements	$119{\cdot}10^3$	$213{\cdot}10^3$	$326{\cdot}10^3$	$499{\cdot}10^3$	$699{\cdot}10^3$	$1204{\cdot}10^3$

The mesh convergence plot for different temperatures is shown on Figure 5-12. G4 was chosen for the rest of the study as a trade-off between accuracy and computational time. The relative temperature difference between G4 and G3 is only 0.05 %, while the computational time doubled. For this reason, G4 was kept for the rest of this study and upscaled (keeping m = 2) to the full-scale module. The Grid Convergence Index (GCI) developed by Roache [90] is an indicator used to determine the level of convergence of a given mesh. The full theory behind this index can be found in [89], [121], [122], [123], [124]. The GCI was computed for G1, G4 and G6. The results are presented in Table 5-2. This represents the refinement ratio between mesh i and j, p represents the order of convergence and fh→0 is defined as the asymptotic solution and reports the best approximation for each quantity. It can be noted that the order of convergence p for this mesh, i.e. the speed at which the truncation error decreases with decreasing mesh size, is ~ 3. The grid convergence indices for the fine and the coarse grid are considerably low, which highlights the high quality of the mesh. Finally, the last column proves, together with Table 5-4 that mesh convergence was reached.

Table 5-3: Results for different discretization orders.

Dicretization order			
Temperature	**Velocity**	**Pressure**	**Results**
1	1	1	Default order
2	2	2	Exceedingly slow convergence
2	1	1	Maximum 0.1°C difference + slow convergence
2	2	1	Exceedingly slow convergence
1	2	2	Exceedingly slow convergence
1	2	1	Exceedingly slow convergence

Table 5-4: GCI computation for different physical quantities.

Physical quantity	Grid	r_{14}	r_{46}	T [K] p [Pa] v [m/s]	p	$f_{h\to 0}$	GCI_{14}[%]	GCI_{46}[%]	$\frac{GCI_{46}}{(r_{12}^{p}*GCI14)}$
Temperature	G1			308.17					
PV cell	G4	1.55	1.40	307.59	2.99	308.39	0.09	0.32	1.002
central point	G6			306.22					
Temperature	G1			306.38					
PV cell	G4	1.55	1.40	305.94	3.36	306.51	0.05	0.23	1.001
average	G6			304.75					
Temperature	G1			307.56					
backsheet	G4	1.55	1.40	306.96	2.99	307.78	0.09	0.36	1.002
central point	G6			305.54					
Temperature	G1			305.95					
backsheet	G4	1.55	1.40	305.49	3.35	306.09	0.06	0.25	1.002
average	G6			304.25					
Temperature	G1			307.46					
upper surface	G4	1.55	1.40	306.91	2.97	307.67	0.08	0.31	1.002
central point	G6			305.62					
Temperature	G1			305.75					
upper surface	G4	1.55	1.40	305.33	3.32	305.88	0.05	0.26	1.001
average	G6			304.21					
Pressure	G1			4.11					
1.5 mm above	G4	1.55	1.40	4.20	2.43	4.062	1.52	4.27	0.978
upper surface	G6			4.38					
Velocity	G1			2.72					
1.5 mm above	G4	1.55	1.40	2.70	3.10	2.73	0.31	1.21	1.007
upper surface	G6			2.66					

5.3.2.3 Element order refinement

Above results were computed for a first order discretization, which is the default order in COMSOL, for temperature, pressure and velocity. The results for increased orders can be found in Table 5-3. Very slow convergence was found for most of the all the increased discretization orders, except from second order for temperature and first order for velocity and pressure. For the latter, the simulation converged very slowly, with no substantial difference in results. For those reasons, first order discretization was chosen for all the variables.

The COST and ERCOFTAC guidelines recommend the use of second order (quadratic) discretization. First order (linear) discretization was, nevertheless, chosen and can be justified as follows. Due to the presence of very thin material layers in the PV module and thin EVA isolation between the PV cells, constructing the mesh with very small elements was unavoidable. For this reason the computational grid was by default very thin, leading to low Grid Convergence Indices Table 5-4. Even by increasing the number of mesh elements by almost 400% (G4 → G1), the temperature difference amounted to only 0.5◦C (Figure 5-12). This fine mesh resulted in a third order accurate scheme (Table 5-4), while linear and quadratic discretization usually result in second order and third order accurate schemes, respectively, for finite element modelling [125], [126]. It is often recommended combining a fine mesh and a

fine discretization order for accurate and fast converging finite element modelling [127]. In this case, due to the unavoidable very fine mesh, this combination was not feasible and third order accuracy was achieved through linear discretization and very fine mesh.

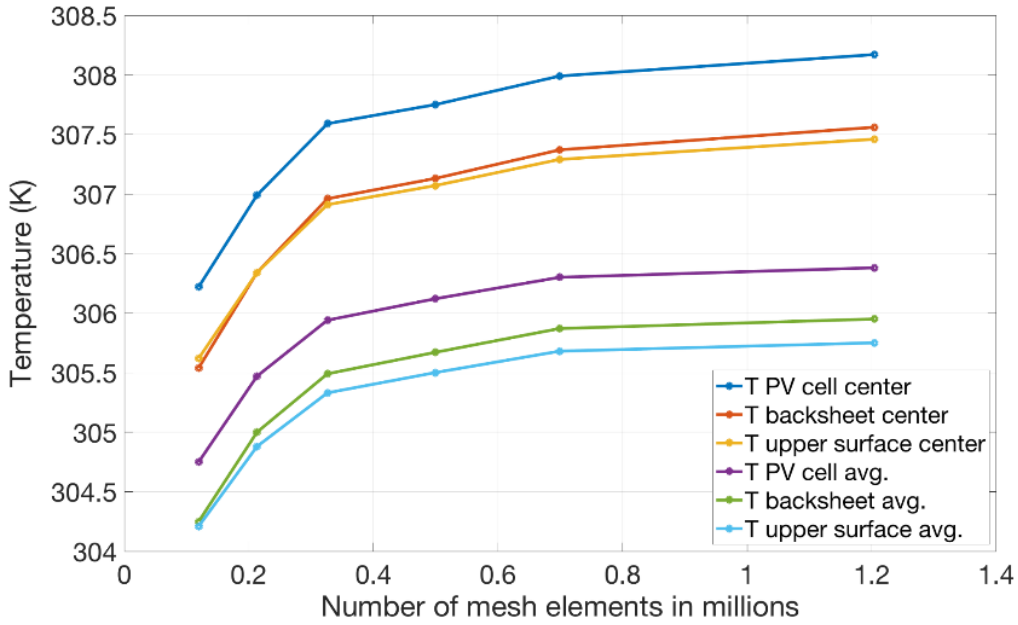

Figure 5-12: Mesh convergence plot.

5.3.2.4 Convergence criterion refinement

The default convergence criterion in COMSOL is 10−3 and was increased to 10−4 and 10−5. No difference between the different convergence criteria was assessed, while the computational time increased substantially. That is why the default convergence criterion was retained.

5.3.2.5 Summary of the CFD choices

Altogether, a stand-alone mini module consisting of 9 PV cells was modelled. A computational domain was constructed with a given wind profile at the inlet. The final computational model was meshed with a high quality hybrid mesh, using a multiplication factor m = 2 that was kept for any domain modification in this thesis. The steady-state incompressible Navier-Stokes equations were solved using the Boussinesq approximation and the SST k-ω turbulence closure. The first cell height was chosen as 0.05 mm leading to a value of y+ ≈ 1 at every wall. The incoming sun irradiance was modelled using an equivalent heat source. Linear discretization and a convergence criterion of 10−3 were finally chosen.

5.3.2.6 *Default parameters for the CFD simulation*

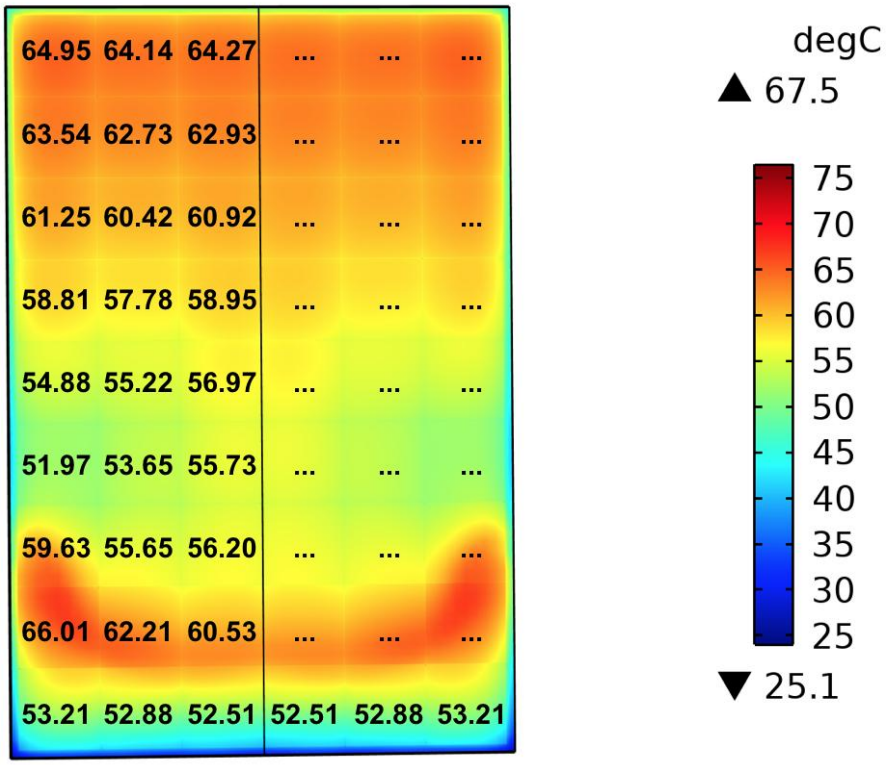

Figure 5-13: : Temperature of the centre point in the PV cell.

By default, the results presented in the next section are obtained for a wind velocity U0 = 1 m/s with a direction α = 180°. This wind speed is chosen for a purpose of accuracy. Chowdhury et al. show that for low wind speeds (up to 3m/s), the cell temperature is very sensitive to small changes in the heat transfer coefficient while for higher wind speeds, this sensitivity decreases significantly. Therefore, if high accuracy is reached for low wind speeds, it is also reached for higher wind speeds (while the opposite is not necessarily true). An ambient temperature 20°C and an equivalent heat source Q = 600 W/m2 were chosen. This heat source magnitude corresponds to an irradiance of 865 W/m2, which is within the irradiance range that contributes to the major energy production in Belgium. Temperature of the backboard in shows in Figure 5-13, measurement point located at the middle of each cell. Param: U0 = 1m/s, 180°, Irradiance 865 W/m2. This shows comparable magnitude of temperature deviation with outdoor tests presented in chapter 6 (Figure 6-4).

5.3.3 Results and Discussion

Figure 5-13 shows the temperature pattern of the full-scale PV panel for the default parameters. Its average temperature amounts to 58.68°C. It is clear from this figure that the temperature of a PV module is not uniform at all. The deviation in average cell temperature $\Delta T = T_{max} - T_{min}$ equals 11.88°C. The cause of this consequent deviations can be understood by analyzing the flow

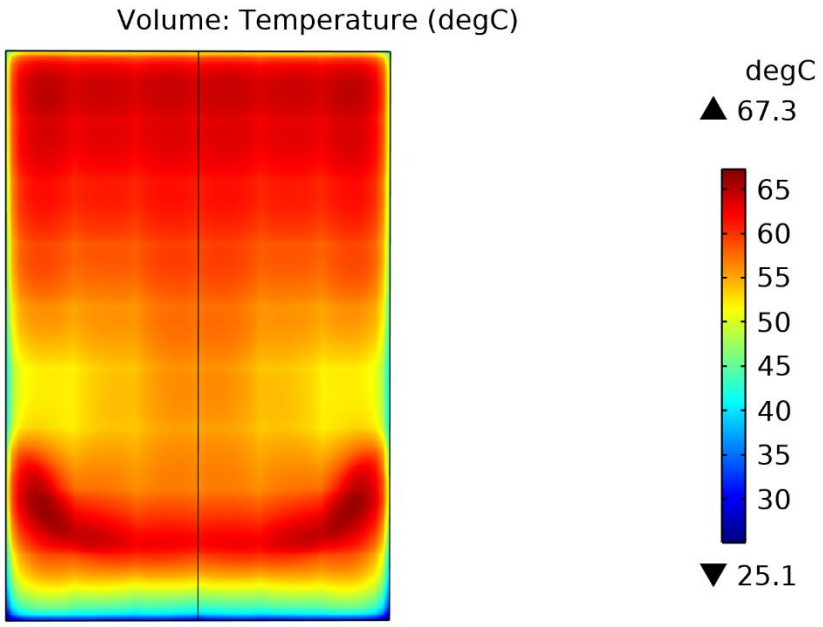

Figure 5-14: Temperature profile of full scale module under test condition.

patterns around such a PV panel.

Figure 5-14 illustrates the airflow around the PV module. From this figure, it can be seen that a flow separation bubble is created under the module. This bubble is the result of a high-pressure difference created by the flow hitting the sharp leading edge of the module. As a result, backflow occurs underneath the module: hot air from the middle of the module, comes back towards the leading edge, creating a bubble of hot stagnating air. Of course the air is not literally stagnating, it is 'backflowing' into a large eddy and no fresh high-speed air is directly adjacent to the module's back sheet. The separation bubble only covers the first half of the module. In the second half, the flow reattaches and a boundary layer is created seen in Figure 5-15.

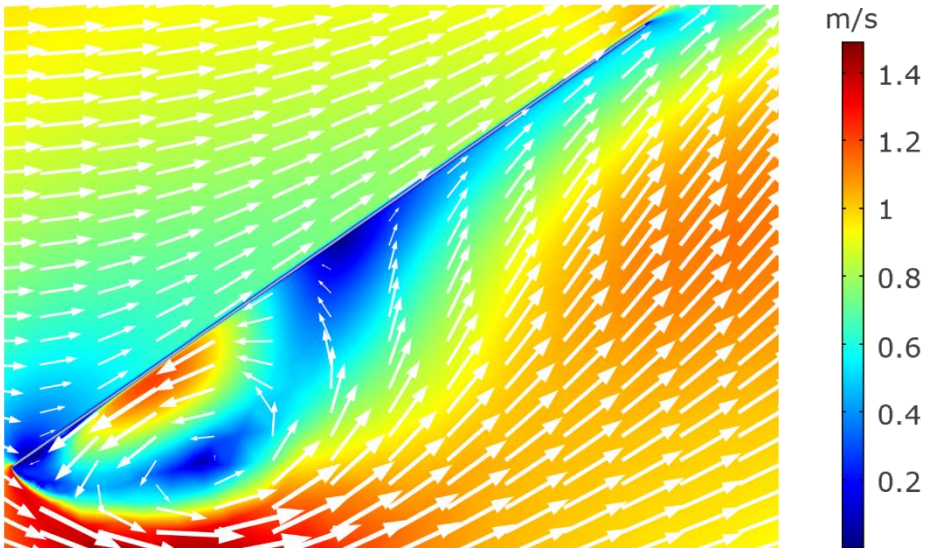

Figure 5-15: Airflow of the reference modules: cross-sectional profile view at the middle of the right windwise.

5.3.3.1 Spatial temperature distribution as function of wind direction

Flow separation is a complex flow mechanism leading to complex temperature patterns where it occurs. For this reason, the first half of the PV module is highlighted by a complex and flow pattern with a lot of spatial temperature variations. The second half of the module has a more uniform cooling. In this region, the flow reattaches and a more laminar boundary layer forms and develops. The air at this stage is hotter as it already has absorbed the heat from the first half of the module and therefore has less 'heat absorption capacity' than when hitting the module at its leading edge. Also, moving away from the leading edge, the boundary layer develops gradually and increasingly more heat is stored into it. Therefore, the cooling is gradually less effective for the second half of the module, resulting in hotter cells at the end of the module.

It is also interesting to study the effect of varying irradiance ,wind speed and direction on the deviation in average cell temperature ΔT. Figure 5-16 illustrates this effect. A few observations can be made from this Figure.

The average PV panel temperature T_{avg} and ΔT are correlated: if T_{avg} , ΔT decreases. Indeed, if the temperature decreases, it approaches the ambient temperature and the PV panel approaches uniformity. ΔT increases significantly for wind directions between 30° and 150° and is maximal for 90°. For these wind directions, its value is much higher than for any wind speed and irradiance variation (given for a wind direction of 180°) ΔT varies the most with

the wind direction (contrarily to the wind speed and the irradiance). The variation of ΔT with wind direction is asymmetrical which makes it not systematic and less predictable as well. It is asymmetrical because the PV panel is inclined. If the inclination is varied, ΔT would vary a lot as well.

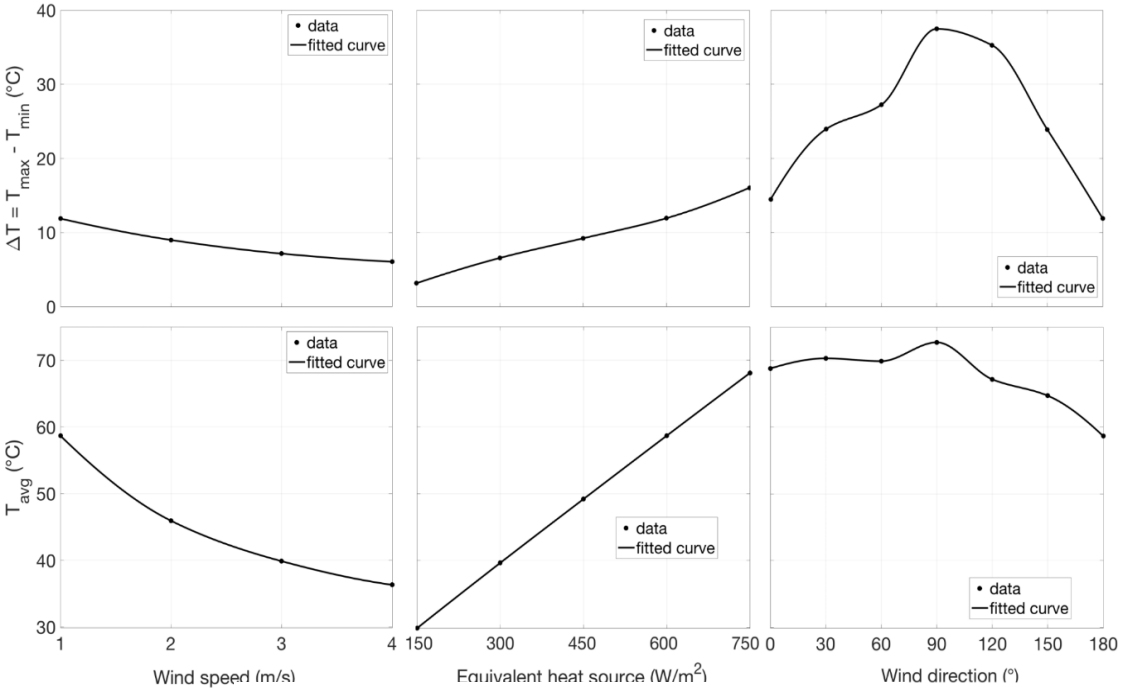

Figure 5-16: Simulation results from parametric studies.

From these observations, it is clear that wind direction is the parameter which has the biggest impact on the value of ΔT and its variations, leading to energy yield simulation mismatches that can be very consequent. As a solar farm is subject to varying wind directions, not taking these high variations in local cell temperature would lead to high energy yield mismatches. Also the energy yield is limited by the hottest cell. For the aforementioned reasons, a technique should be devised to reduce ΔT and subsequently the PV panel average temperature. This would decrease the mismatch for energy yield simulations and increase this energy yield.

5.4 Chapter Summary

This chapter has introduced a detailed thermal modelling framework that captures the spatial temperature distribution within full-size PV modules under convective airflow. While most existing yield models reduce thermal behaviour

to a single scalar value, the approach here explicitly resolves temperature differences across and within the module structure. The model integrates a 3D volumetric heat generation profile into thin-layer representations of the glass, EVA, silicon cells, and back sheet. Validated through wind tunnel experiments, the simulations reproduce temperature patterns under different air gaps, tilt angles, and wind velocities with considerable accuracy.

What distinguishes this work is not only its resolution but its computational feasibility at real module scale. A meshing strategy was developed that allows the inclusion of 0.2 mm thick solar cells in a 2 m by 1 m module, representing a geometric scale ratio of 1:10,000. This is significant step and one of a kind in the state of art. Achieving convergence for such high aspect ratio domains typically results in prohibitive computational demands or instability. Through months of targeted refinement optimizing turbulence models, grid structures, and solver routines we arrived at a stable, efficient formulation. This enabled cell-level resolution of temperature differences for the first time at this scale, forming a foundation upon which more complex environmental interactions could be explored.

The results confirm that wind flow, particularly its direction and interaction with module geometry, governs much of the spatial thermal behaviour. Direct exposure at the leading edge facilitates cooling, while downstream regions especially where recirculation and boundary layer development occur experience significant heat accumulation. This specific knowledge contributed to a product patent later onwards [128]. These asymmetries are not just theoretical; they reflect measurable differences of up to 30 °C between cells under realistic boundary conditions. Attempts to mitigate these differences through design interventions such as introducing spacing between module sections demonstrated clear, though non-linear, thermal benefits. Wind direction again proved decisive, with oblique flows enhancing the convective efficiency of modified layouts.

This chapter marks a turning point in the thesis. It closes the loop on controlled, simulation-based understanding of PV module thermal dynamics and opens two distinct avenues of inquiry that will be pursued in the next chapters.

The first path, developed in Chapter 6, extends the insights from controlled wind tunnel tests and simulation models into real-world operating conditions. While the CFD framework provides a detailed picture under repeatable lab conditions, the question remains whether those patterns especially the directional and spatial effects is persist under outdoor environments where variability,

turbulence, and mounting diversity introduce noise. Chapter 6 builds upon this by analysing long-term high-frequency outdoor measurements across geographically separate sites. It asks whether the spatial deviations of different PV setups shows similar magnitude of thermal response. It also seeks to construct a simplified, calibratable model that embeds directional wind effects into temperature.

The second path, taken up in Chapter 7, uses the modelling capacity developed in this chapter to explore hypothetical and less accessible domains specifically, the debated cooling effects in floating PV (FPV) systems. Chapter 5 has provided the physical and numerical foundation; Chapter 7 takes that framework and applies it to investigate open questions in "What if" simulation style. In literature, where empirical claims often exceed the explanatory power of current models, we wanted to verify on the validity of those claims. Here, the emphasis shifts from direct validation to scenario testing. The same meshing fidelity and thermal-fluid coupling are used to simulate "what-if" cases: how much cooling, if any, is attributable to close proximity to water bodies, and under what conditions wind remains the dominant driver. In that sense, Chapter 7 grows from Chapter 5 not as a linear continuation but as a lateral application adapting a known, validated model to interrogate less understood contexts.

In conclusion, the work presented in this chapter forms a dual bridge: it consolidates the methodological progress made so far while enabling two parallel strands of application one rooted in outdoor long term operational datasets, the other in theoretical scenario analysis. Both directions derive their credibility from the same core achievement: a CFD thermal framework that sees the PV module not as a flat surface, but as a thermally active, spatially complex system shaped by its environment.

6 A Calibratable PV Temperature Model that Integrates Wind Direction

6.1 Motivation and Organization

PV module temperature is not a uniform scalar, but a dynamic, spatially and temporally variable field shaped by environmental and geometric factors. Earlier chapters particularly Chapters 3 through 5 laid the groundwork. Those analyses showed how simulation models respond to changes in temporal resolution (Chapter 3), how airflow interacts with mounting geometry to create surface-level temperature differences (Chapter 4), and how even subtle 3D structural modifications to the module can shift the thermal distribution significantly (Chapter 5). What remains now is to move from controlled and computational domains into the operational domain.

This chapter focuses on experimental data collected over long periods in outdoor installations. The objective is twofold. First, to quantify intra-module temperature variability under realistic operating conditions. Second, to evaluate whether that variability follows patterns that can be understood, modeled, and eventually predicted.

The method does not rely on guesswork or proxy measurements. Usually in state of art, often you will find one or few thermocouples attached to the back of the module. If you have conducted outdoor experimentation you are aware how difficult it can be to collect good reading. We took a step beyond. A dense matrix of thermocouples is embedded directly within the module encapsulation. Sensor positions were chosen to capture not only centerline values but edge conditions, hotspots, and zones exposed to recurrent airflow anomalies. Data collection

span multiple seasons and included both high-irradiance and diffuse light conditions. The temporal resolution is kept high on the order of seconds not to chase noise, but to isolate transients that would be averaged out in hourly data. Earlier work has shown that the smallest thermal time constants are in the order of seconds indeed [24], [25], [26], [27], [28], [45], [46], [62]

What emerges from this dataset is not a single conclusion but a pattern. Certain weather conditions clear skies with directional wind, for example lead to sharp differences across the same module surface. Others, such as overcast days with turbulent or low-speed wind, suppress that variability. In some cases, edge cells showed mean operating temperatures up to 12°C cooler than adjacent interior cells. These are not anomalies. They are fundamental structural features of the system's thermal response.

Rather than forcing these variations into the mold of a single average value, this chapter proposes an alternate route. A model is developed to account for wind direction explicitly not just as a boundary condition in CFD, but as a corrector in empirical field-based temperature estimation. The proposed model is simple enough to be implemented in standard PV simulation workflows, yet precise enough to reflect observed variability. Its calibration is discussed in detail, including a cross-site validation where parameters derived from one installation are successfully applied to another location, separated by more than 100 kilometres.

The implications are immediate and practical. In multi-megawatt installations, a few degrees Celsius of thermal misestimation if applied uniformly can distort lifetime energy yield forecasts, impact degradation models, and misguide inverter sizing. But more than that, this chapter demonstrates that site-specific, directional wind patterns are not noise. They are the signal.

The following sections will walk through the instrumentation, the calibration protocol, the temperature field analyses, and the resulting model. Unlike earlier chapters grounded in simulation, this one leans heavily on what the modules themselves recorded: the kind of evidence that resists speculation and requires no extrapolation.

6.2 Chapter Specific Introduction and State of the Art

For a long time, most PV temperature prediction is built upon this hypothesis and predicts one temperature output for a single set of G_{poa}, T_{amb}, W_s input as presented in chapter 3. Some prediction models came up with a better solution

to address PV temperature prediction models with thermal capacitance in mind. Such transient or dynamic models averaged out highly variable weather inputs contribution to the thermal state of PV [71], [129]. However, even after implementing those models, there was a significant PV temperature prediction mismatch in stable or highly fluctuating days, especially in the high insolation periods already presented in chapter 3. Therefore, we wanted to test the modelling results seen in chapter 5 in real life outdoor conditions. If the PV module temperature is not uniform, what is the range of non-uniformity that can be observed in real life operation. Moreover, it also investigates methods to predict such non-uniformity.

The first part of the study systematically investigates the hypothesis of non-uniformity with extensive experimental procedures over two different test sites. From that exercise, we see that PV module does have spatial temperature. There are days with lower insolation and higher wind speed where PV temperature can be considered uniform. However, days with higher insolation and lower wind sped the spatial non-uniformity is significant. This means that the models which predict one single output for PV temperature would have inherent errors.

In the second part, we explained where this non-uniformity came from and provided a pathway to model that. The chapter will conclude with experimental validation of such a model. The learning from chapter 3, 4,5 is used to correlate the temperature signals with environmental conditions. The empirical model was built with measurement from one experiment and validated with a separate independent experiment in another geo-location with PV module built and installed differently. This will test the robustness of the proposed method.

6.3 Indoor Experimental Result

First, it is necessary to conduct a controlled experiment to analyse PV module spatial temperature with a variable such as irradiance and wind speed. Wind tunnel experiment results from chapter 5 and other published literature shows clear results [22], [24], [27], [61]. To summarize, there is a significant temperature difference both in mini and full-scale modules. The difference can be from 6-12 ℃. This is mainly due to the spatial differences of wind velocity on the module resulted from tilt angles and installation design explained in chapter 4, 5. This difference of cell temperature resulted in the different performance levels of each cell. First, wind tunnel experiments offer insight with steady-state analysis while real-life PV modules are subjected to a transient state. Secondly, physical constraints don't fully permit to experiment with a full-scale module

with practical tilt angle and wind directions, which is only possible in an outdoor experiment. However, outdoor experiments required a long period of data collection for a realistic conclusion. Therefore, both indoor and outdoor experiments should provide a complementary set of knowledge.

6.4 Experimental Set Ups

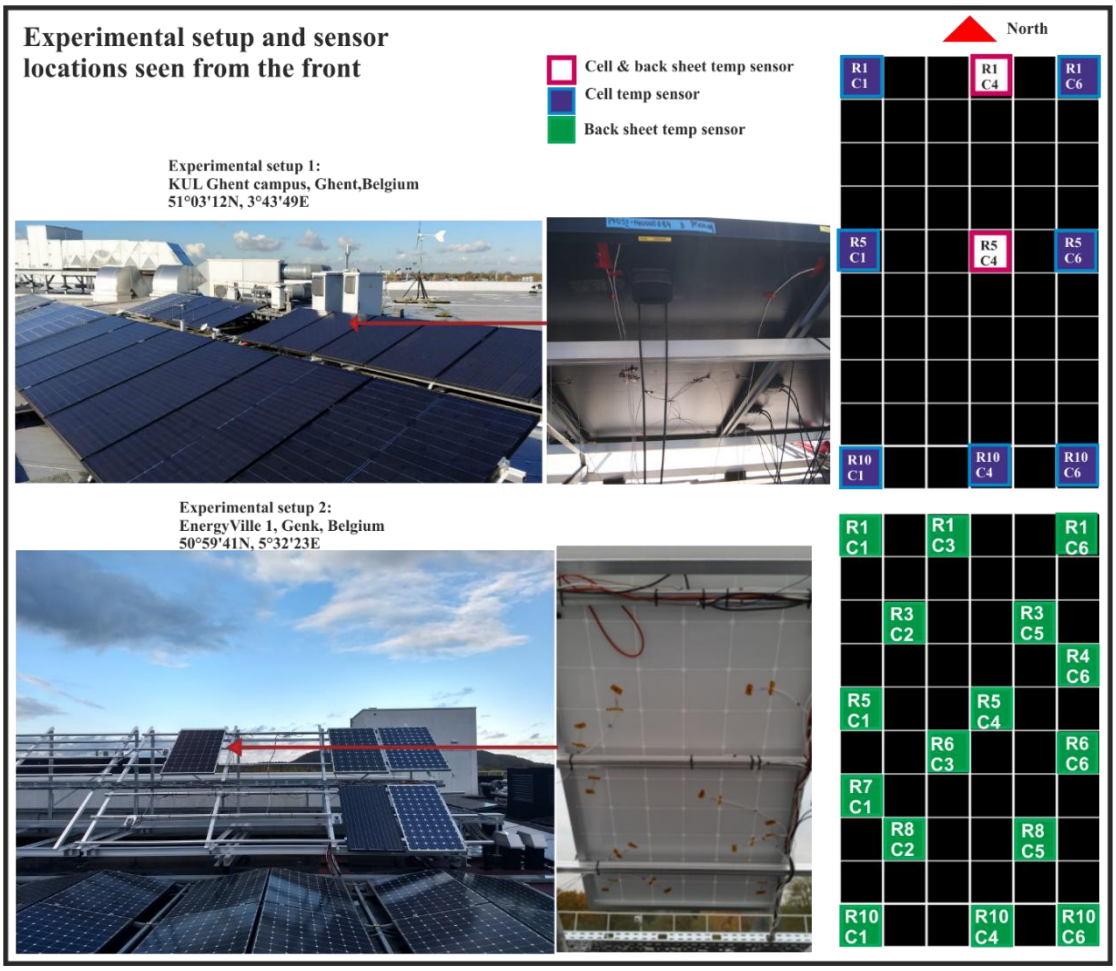

Figure 6-1: Experimental setup description

For this study two experimental set-up was installed with in-house PV module for this special purpose. Experimental set-up one was installed and managed by the KU Leuven Ghent campus in Ghent, Belgium. Experimental set-up two were installed in Energyville 1 Campus, Genk, in collaboration with imec and KU Leuven. The geo-location and experimental set-up images are given in Figure 1. For both of the experiments, 60 monocrystalline cell cells are made in-house in a standard configuration. Both are glass back sheet modules where one back sheet is black, and the other is white. This can be seen in the graph (Figure 6-1).

The key differences are the design of the experiment and the measurement apparatus.

Experiment-1 was conducted with a special PV module where nine pt-100 sensors were laminated inside the PV module. It was placed right underneath the centre of the cell. Two extra sensors were placed on the back sheet of the module also. The choices of location and number of sensors were made with respect to provide the highest visibility on the intra module temperature and technical feasibility of laminating such sensors inside. The irradiance was measured on the plane of the array at 18°. All the measured values Gpoa, Tamb, WS, WD, PV temperature sensors, power data was measured with 1Hz resolution. Moreover, there are two datasets available for this set-up one from May-Dec 2015 and another from Feb-July 2021. The critical difference is the wind vector measurement apparatus. For 2015, wind speed data is acquired by a first-class advanced anemometer from Theis Clima. Ekopower wind vane is used to measure wind direction. They were installed 4 meters north of the PV module. Whereas for the 2021 dataset, Young Model 81000 ultrasonic anemometer is used where it was installed 0.8 m south of the module. It was installed closer to measure the local wind vector experienced by the module. Most importantly, it was placed in the middle of the long array to restricting the free airflow access from East and West. The azimuth of the installation is South (180°).

Experiment-2 was conducted with a module that is relatively free from any wind flow obstructions from any direction. Azimuth angle was South (180°) with a tilt of 35°. The primary difference with experiment-1 is that there were 16 pt-100 sensors on the back sheet. However, special care was taken while installing those sensors on the back sheet to ensure a thin layer of thermal paste between the sensor and back sheet. This reduced the uncertainty of environmental degradation over time. Moreover, the 16 sensors are distributed over the module to provide maximum visibility on spatial temperature distribution. Gpoa was measured just beside the module at 35° tilt. WS and WD were measured with a Young Model 81000 ultrasonic anemometer installed 5-meter West of the module. Gpoa, Tamb, WS, WD, and all the temperature sensors were measured with a minimum 1Hz resolution. The dataset is from Nov 2019- June 2020.

For both experimental set-ups, all the measured values were in high resolution. The two key differences: firstly, the placement of sensors laminated inside the module and on the back sheet. Secondly, one module was right in the middle of the array, and one module was with no modules installed in close proximity.

Moreover, while interpreting the temperature data and providing quantitative and qualitative aspects, it was necessary to interpolate spatially. It was a linear interpolation. For experiment 1, there were 9 data points, and experiment two has 16 data points spread with the design of experiments to support that process.

6.5 Data Analysis

In **Error! Reference source not found.** the results from both experimental site is presented. It is clear that the spatial temperature difference deviation ranges between 0-8 m/s wind speed. What is interesting to observe is that even with same wind speed and same irradiance condition you can see a wide range of spatial temperature within PV module. Our modelling results from chapter 5 supports this observation that it is driven by wind direction. However, we don't stop here and conclude. We go ahead and verify this claim which fine grain analysis presented in the upcoming sections.

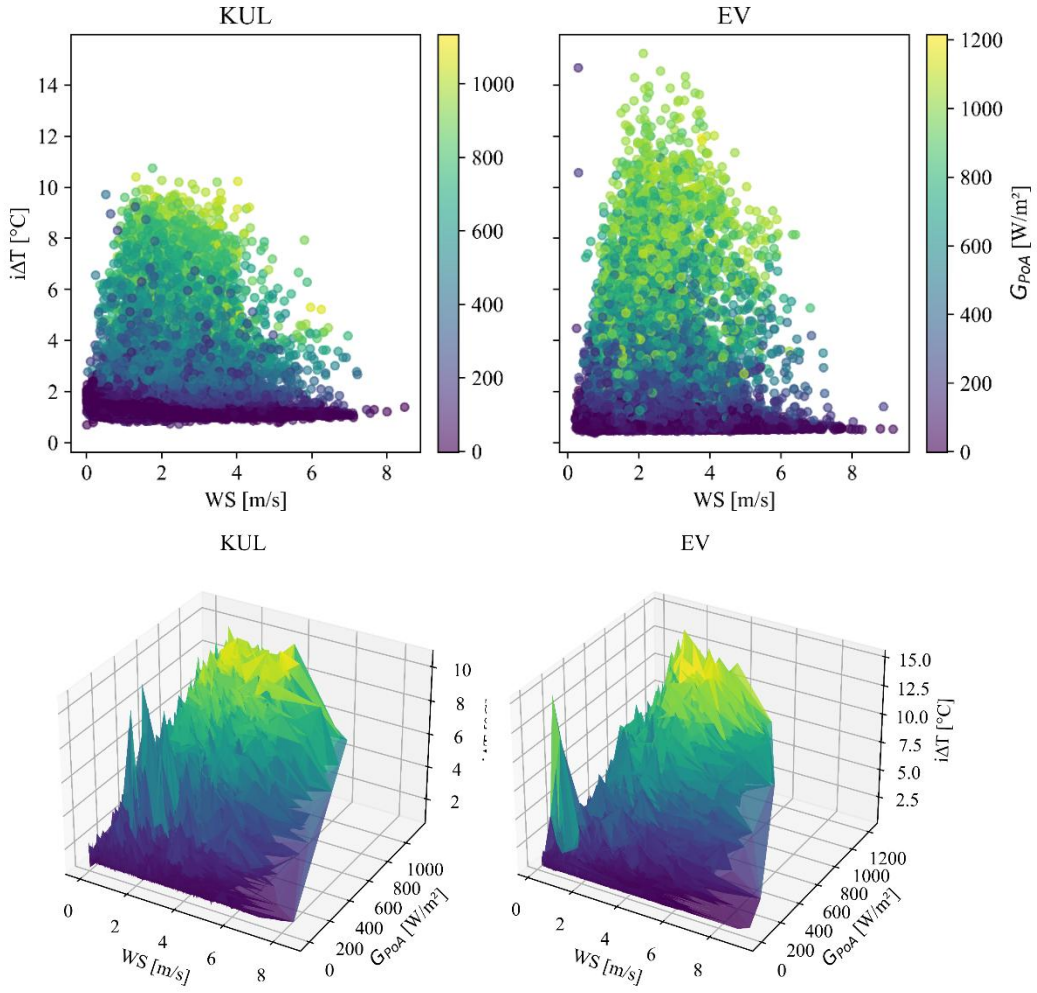

Figure 6-2: PV spatial temperature as function of both G_{poa} and W_s

In a controlled wind tunnel experiment, it is possible to simulate specific conditions. However, replicating a stable global plane of array irradiance (Gpoa) or wind speed (WS) in outdoor analyses is not feasible. Such stable conditions are rarely, if ever, present outdoors. Therefore, the only viable approach is to analyze results over an extended period and identify specific intervals that can be compared to indoor experiments. The thermal capacity response, influenced by transient Gpoa and WS, does not occur with a 1 Hz resolution. Hence, conclusions drawn from instantaneous data may be misleading. **Error! Reference source not found.** illustrates the maximum intra-module spatial temperature difference as a function of WS and Gpoa. The experiments reveal a temperature deviation of 0–15°C with 30-second averaging. These absolute values align with those observed in controlled wind tunnel tests. However, unlike in the wind tunnel experiments, the wind direction in the outdoor experiments was not restricted to 180° azimuth (South) but varied across several directions.

Importantly, the data show that within the same WS and Gpoa domains, there can be a different range of spatial temperatures. Additionally, as Gpoa increases, the deviation range also expands. This variation is likely influenced by other meteorological factors, such as wind direction (WD). The following paragraph will explore this hypothesis further.

Figure 6-3 and Figure 6-4 present the spatial temperature distribution from selected days with a dominant wind direction. Analyzing days with a predominant wind direction helps assess the impact of WD on spatial temperature. These plots reveal that WD significantly affects the spatial thermal characteristics of the PV module. The dominant WD dictates the intra-module heat flow direction. The possibility of temperature sensor bias consistently showing cooler or hotter readings is also nullified here. Therefore, two conclusions can be drawn from this part of the investigation. Firstly, both wind direction and wind speed regulate intra-module spatial temperature. Secondly, this relationship is not static as traditionally accepted. Understanding the heat flow direction within the module requires considering the thermal capacitance.

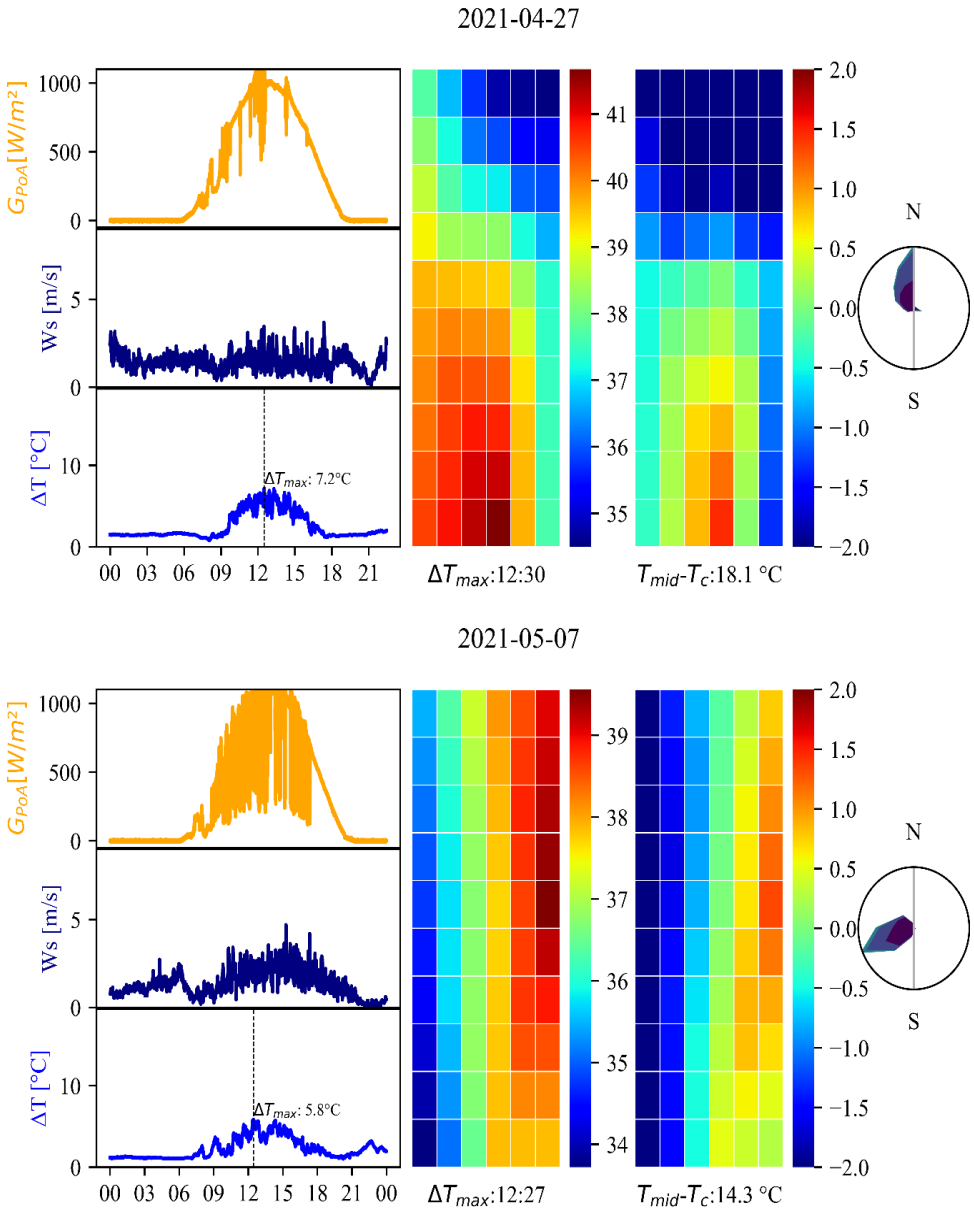

Figure 6-3: Spatial temperature distribution and cooling analysis from

6.5.1 The Influence of G_{poa} On iΔT and Its Relationship With Wind Direction

The preceding section established a robust correlation between wind direction and intra-module spatial temperature. Given the high frequency of wind direction changes and the non-instantaneous effects of wind direction and wind speed, it is crucial to explore how these fluctuating meteorological parameters relate to the thermal capacity of PV modules. This exploration forms the foundation for developing an accurate predictive model.

Over temperature (OT) is defined as the difference between the PV module temperature (Tpv) and the ambient temperature (Tamb). This approach serves two purposes: first, it mitigates the inherent uncertainties associated with temperature sensors by focusing on relative rather than absolute values; second, it provides a more stable variable for analysis since Gpoa and Tamb are proportionate, yet Tamb changes are more consistent over time. Therefore, over temperature offers a reliable starting point for this analysis. For a detailed discussion on this formulation, refer to relevant studies [8], [9].

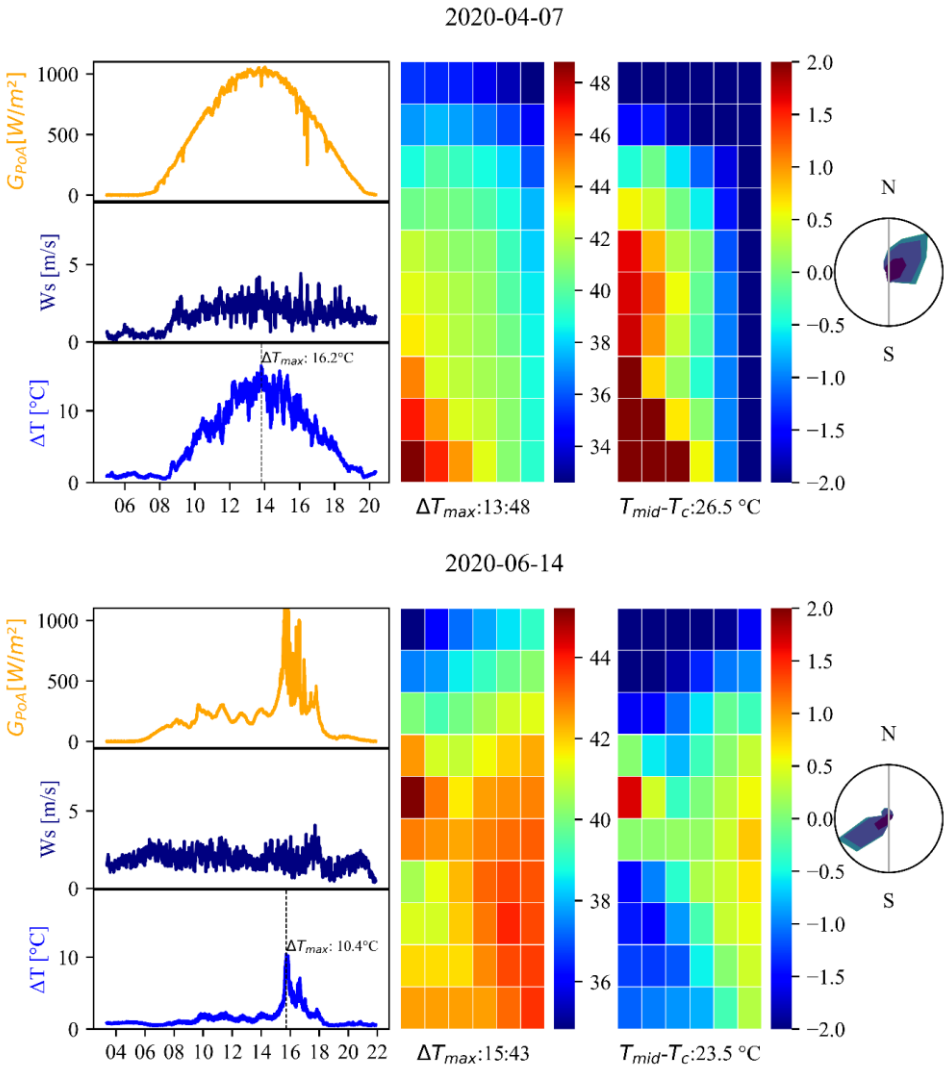

Figure 6-4: Spatial temperature distribution and cooling analysis from

As shown in Figure 6-5, over temperature exhibits a trend similar to that of Gpoa. Notably, intra-module temperature difference (iΔT) correlates strongly with OT, with a Pearson correlation coefficient of 0.88. This correlation exists

because the accumulated heat within the PV module is regulated by the bulk ambient temperature. The iΔT does not track Gpoa with the same frequency due to the thermal capacity of the PV module, which slows its response. Consequently, iΔT and OT can be used to calculate wind direction coefficients by expressing over temperature as Tpv–Tamb.

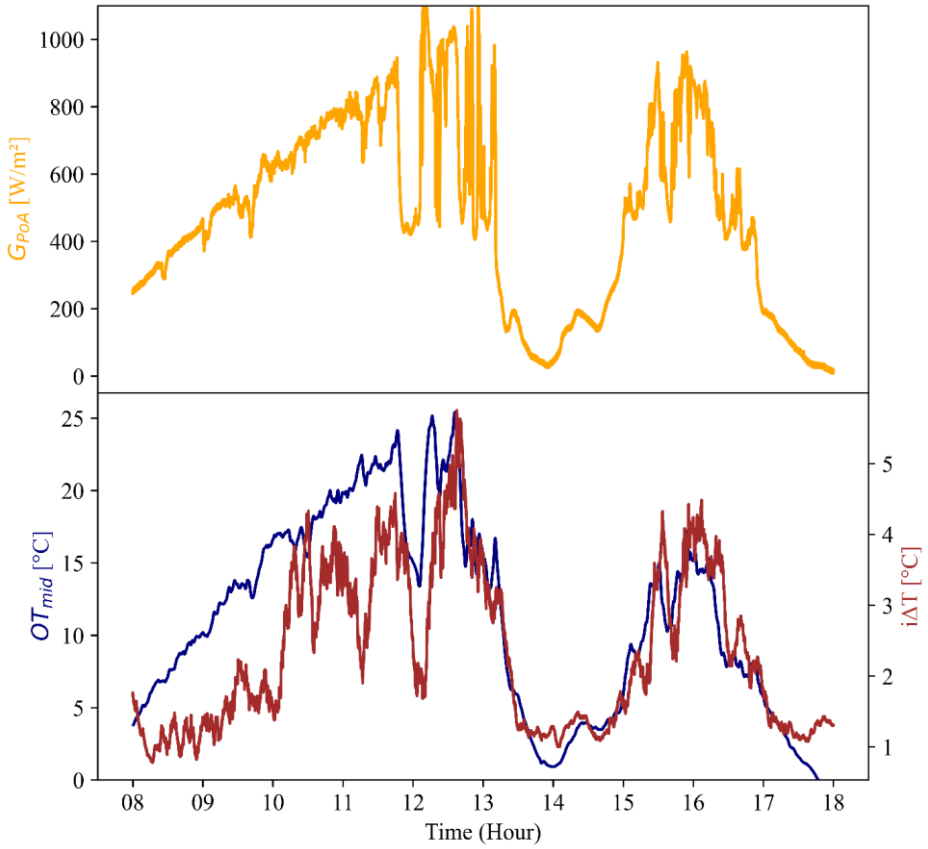

Figure 6-5: This figure demonstrates the correlation between PoA, over temperature and ΔTintra-module. The plots are from 07/06/2021 with one second resolution.

6.5.2 Analysis Between iΔT and OT Relative to Wind Direction

The subsequent step involves identifying trends in broad segments of wind direction, focusing on north and south winds as these represent the most asymmetrical conditions for inclined PV module installations. When the wind originates from the South, it impacts the experimental PV module directly from the front, and vice versa when coming from the North. The thermal impacts observed in these contexts differ significantly. In Experiment 1, most data points pertain to wind from the North-West or South-West.

Figure 6-6 reveals distinct patterns depending on wind direction. The rate of change in iΔT varies between north and south cases, with northward winds inducing a higher rate of change. Consequently, the module can develop more extreme spatial temperature differences under northward winds than under southward winds. To further investigate this phenomenon, a smoke generator was employed to visualize the wind flow field from the North side, and a slow-motion video sample is provided in the annex. Air Accumulation and Velocity Difference: When wind impacts the backside of the module, some air accumulates there, creating a velocity difference between the backside and the topside of the module. This phenomenon aligns with findings from previous wind tunnel experiments [61].

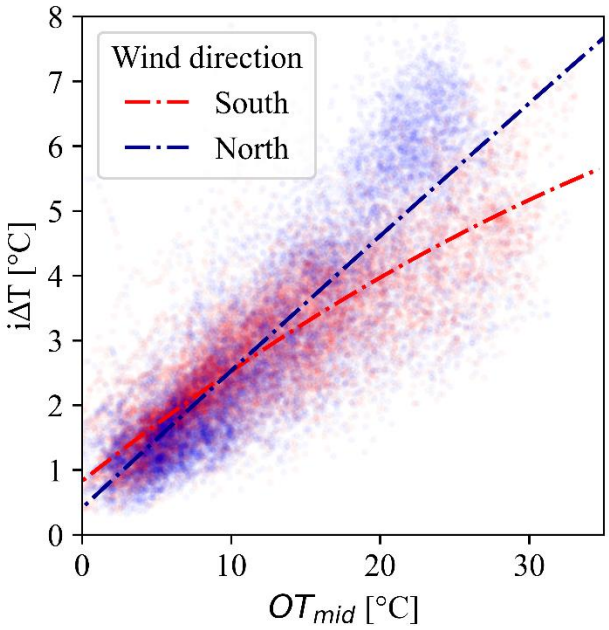

Figure 6-6: Scatter plot between the $\Delta T_{intra\text{-}module}$ and over temperature. The data used for this graph are from April 2021-June 2021 in five-minute resolution.

Vortex Formation and Heat Transfer: Wind hitting the top edge of the module from the North creates a vortex, which enhances heat transfer in the module's top corners. This vortex effect facilitates faster heat removal, leading to a more significant intra-module temperature difference compared to wind impacting from the South side. Quantification of Wind Direction Coefficients: These differences in the rate of temperature change can be quantified as wind direction coefficients, offering insights into the dynamic relationship between wind direction and the thermal behavior of PV modules. By understanding these dynamics, we can better model and predict the spatial temperature variations within PV modules under varying wind conditions, contributing to more accurate and reliable performance assessments.

6.5.3 Method Development

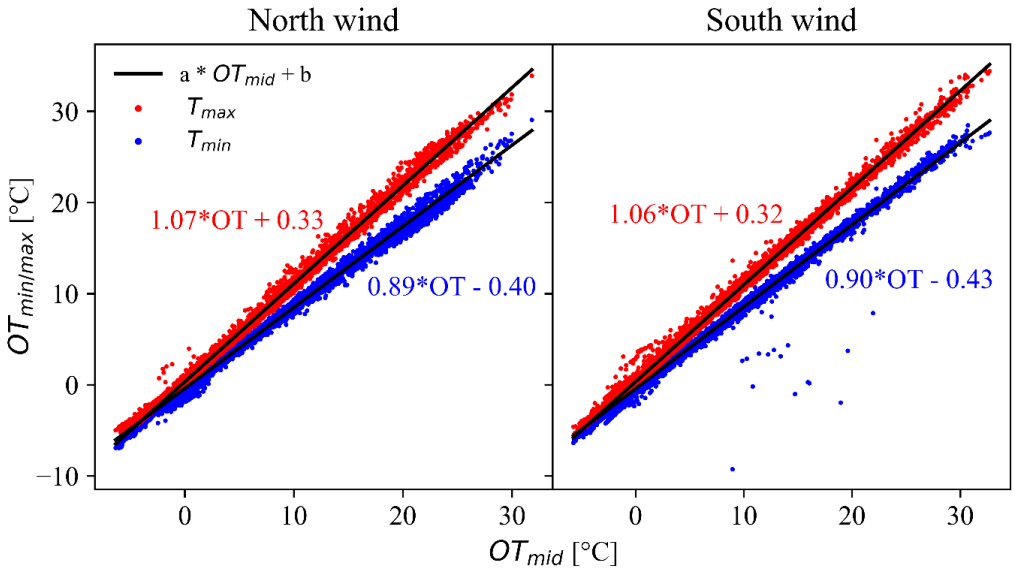

Figure 6-7: This figure demonstrates the linear relationship between the extreme over temperatures and the middle cell's over temperature. The data used for this graph are from April 2021-June 2021 in five-minute resolution.

Now that it is clear that wind direction motivates different rates of heat transfer within the module, it is necessary to determine how many segments of wind direction are required to determine Tmax and Tmin within a module as a function of Tmid. First, the analysis would contain two general directions of North and South. Second, would be 12 equal segments of 30°. The third would be 24 unequal segments. This part of the analysis would be conducted with five minutes resolution for avoiding the transient states. The dataset is from April 2021-June 2021.

$$[\![\text{Over Temperature}]\!]\_(\text{max/min}) = \text{a} * \text{OverTemperature\_midlle} + \text{b} \quad (2)$$

$$\text{T\_(max/min)} - \text{T\_amb} = \text{a} * (\text{T\_middle} - \text{T\_amb}) + \text{b} \quad (3)$$

$$\text{T\_(max/min)} = \text{a} * \text{T\_middle} + (1 - \text{a}) * \text{T\_amb} + \text{b} \quad (4)$$

$$\text{a, b} = \text{wind direction coefficient}$$

Schematic of Over Temperature Model represent the analysis of two broad segments (North and South). It is visible that there are clear linear relationships between T_(max/min) over temperatures and T_mid over temperature. Taking

benefit of it, linear regressions T_(max/min) as a function of T_mid. The formulation of the equation is as follows:

$$\llbracket \text{Over Temperature} \rrbracket\_(\text{max/min}) = a * \text{OverTemperature\_midlle} + b \quad (2)$$

$$\text{T\_(max/min)} - \text{T\_amb} = a * (\text{T\_middle} - \text{T\_amb}) + b \quad (3)$$

$$\text{T\_(max/min)} = a * \text{T\_middle} + (1 - a) * \text{T\_amb} + b \quad (4)$$

$$a, b = \text{wind direction coefficient}$$

6.6 Schematic of Over Temperature Model

As from my previous segment, it is seen that how the spatial temperature of the module is primarily motivated by the wind direction. Therefore, in this part of the chapter, we would report on a method to model this in a realistic way. In

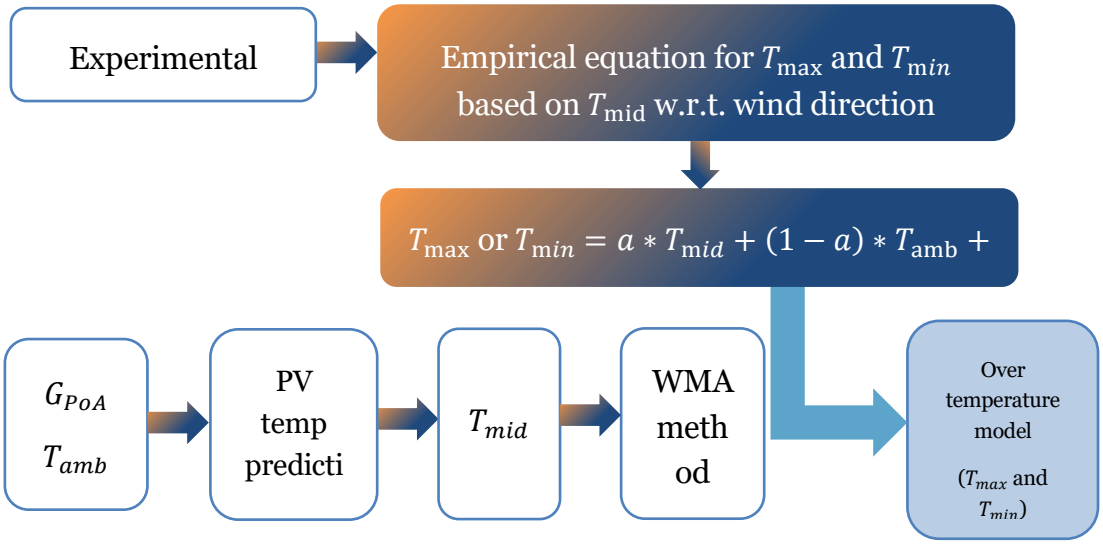

Figure 6-8: Schematic of over temperature model

Figure 6-8, the high-level schematic of the method to find intra module T_{max} and T_{min} is shown. This would be named as the "over temperature" model throughout this chapter. In essence, it is a bootstrapping concept, where the over temperature model is dependent on T_{mid} and weighted mean average (WMA) method. The crucial aspect is to determine T_{mid} through any steady-state model first. There are different choices in state of art to choose such a model. However, as all the model has the underlying hypothesis of PV intra module temperature

uniformity, taking a single reading in the middle or averaging few sensors is considered a negligible difference. Therefore very few of them actually report on the location of the temperature sensors. For the over temperature model, we choose to propose a model with T_{mid} as it is easily accessible compared to T_{avg}.

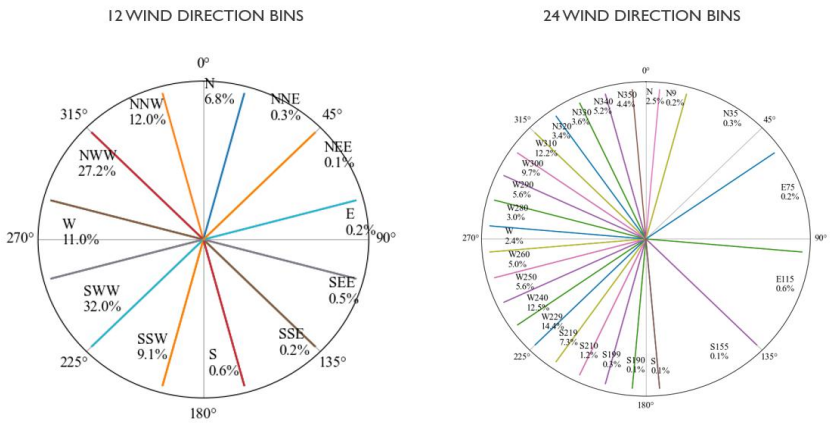

Figure 6-9: Demonstration of the wind direction bins used for coefficient calculation. Below the bin title, the percentage of the data coming from that direction is visible. Below the direction title in each polar plot, the percentage of data that this bin contain

Therefore for the proposed over temperature model, T_{mid} would be used.

WMA method is implemented on the derived T_{mid} to consider the thermal capacitance. This can be independently implemented on any model. Therefore the accuracy of T_{max} and T_{min} depends on the accuracy of T_{mid} first. As we have access to T_{mid} from measurement, we would use it as an input to the model to evaluate the robustness of the proposed over temperature model. The empirical equation of the over temperature model is derived from long term experimental data analysis. The key input to this model comes from wind direction, namely a and b coefficients. In this chapter, they would be defined as wind direction coefficients. The method to derive these coefficients and values would be described in the following segment of the report.

However, there are wind direction data points that don't fully belong to either the North or South bin. Therefore to provide a range of wind direction, the whole spectrum was segmented further. The number of wind direction bins that have been selected are 12 (equal) and 24 (unequal), as shown in Figure 6-9. The rationale behind the higher number of unequal bins was to test the limit of the

over temperature model. 24 bins were selected based on data point availability. The approach for the multiple bins calculation is following:

- Resampling the dataset in 30 seconds resolution, using the mean values of each interval.
- Split the dataset into different wind direction bins.
- Perform linear regression for minimum and maximum temperature equations.
- Make a new dataset with the calculated coefficients.
- Split the above dataset into two, which contain the coefficients from South to North, clockwise and counter-clockwise respectively, so the one dataset contains the coefficients from East and the other from West, as shown in Figure 6-11.
- Perform cubic interpolation between each dataset's coefficients to connect the dots harmonically and end up having 360 pairs of coefficients or one every degree.

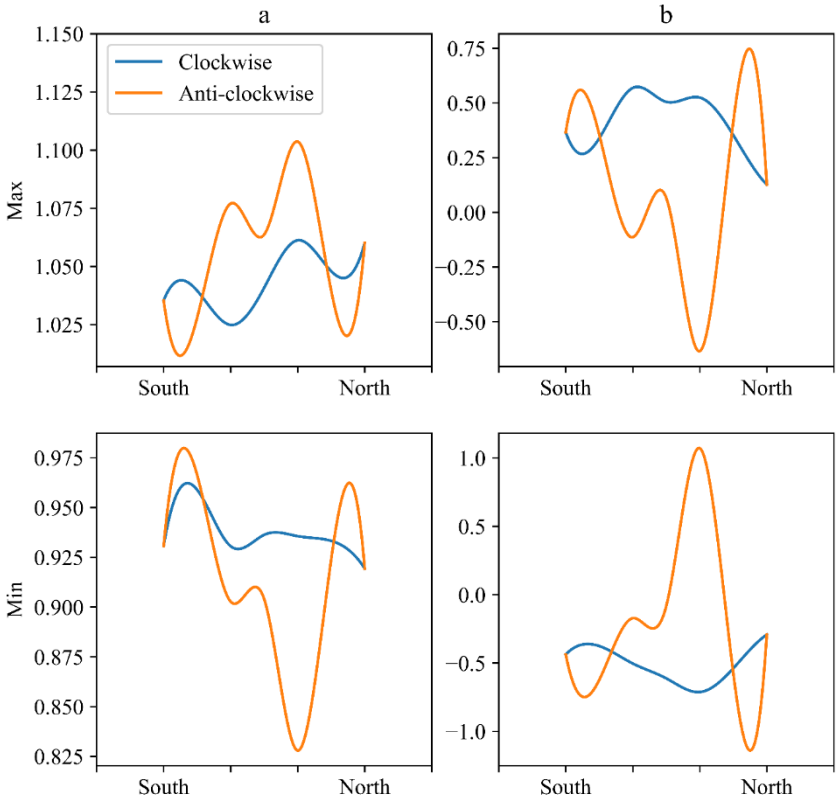

Figure 6-10: Wind direction coefficients from 12 bin method: The counter clock-wise stands from West wind direction coefficients and the clock-wise for East.

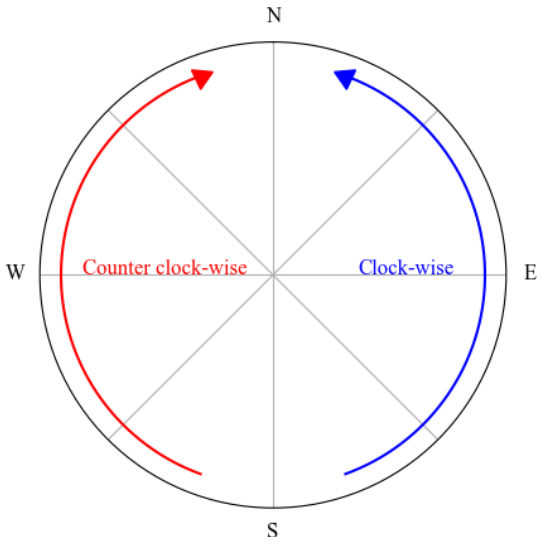

Figure 6-11: Demonstration of the approach behind the coefficient dataset splitting. The counter clock-wise stands from West wind direction coefficients and the clock-wise for East.

Table 6-1: I ance with 2, 12, and 24 segmen

Absolute R		Cloudy	
		in	T_{max}
2			0.38
24	0.52	0.54	0.32	0.37

Now, 2, 12, and 24 direction performance were tested with respect to measurement. For this, three clear skies and semi-cloudy day was chosen. The average absolute RMSE from these three directions is shown in Table 6-1. For all the cases, the best performance can be seen from the 12 directions. Therefore, all following analyses in this paper would be done with wind direction coefficient from 12 direction segmentation. Now the coefficient from this 12 direction segmentation is plotted in Figure 6-10. The coefficients curves for clock and counter-clockwise would be expected to be symmetrical, but Figure 6-10 do not give such a conclusion. Several factors introduce this, such as equal data points and the experimental array where the PV is installed are not symmetrical. As the wind flow field from east and west is not symmetrical for the PV, the wind direction coefficient is not symmetrical either. Repeated experiments on an indoor controlled environment coupled with finite element analysis are encouraged to find more reliable coefficients for those models.

6.7 Experimental Validation

In this segment, we would analyse the over temperature model performance. In the experimental set-up description, it is described that there are three distinct datasets available from two experiments: experiment 1(2015), experiment 1(2021), and experiment 2(2020). The over temperature model was developed on measurements from April- June Experiment 1(2021). Therefore this model

would be implemented on Experiment 1(2015) and Experiment 2(2020). As our motivation is to test the over temperature model's performance, we would not implement the common pathway of predicting Tmid first because then it will introduce errors into the over temperature model, which is not inherently there. Therefore, to independently verify the current over temperature model, we assume we already have Tmid acquired from measurements. In Figure 6-12 for

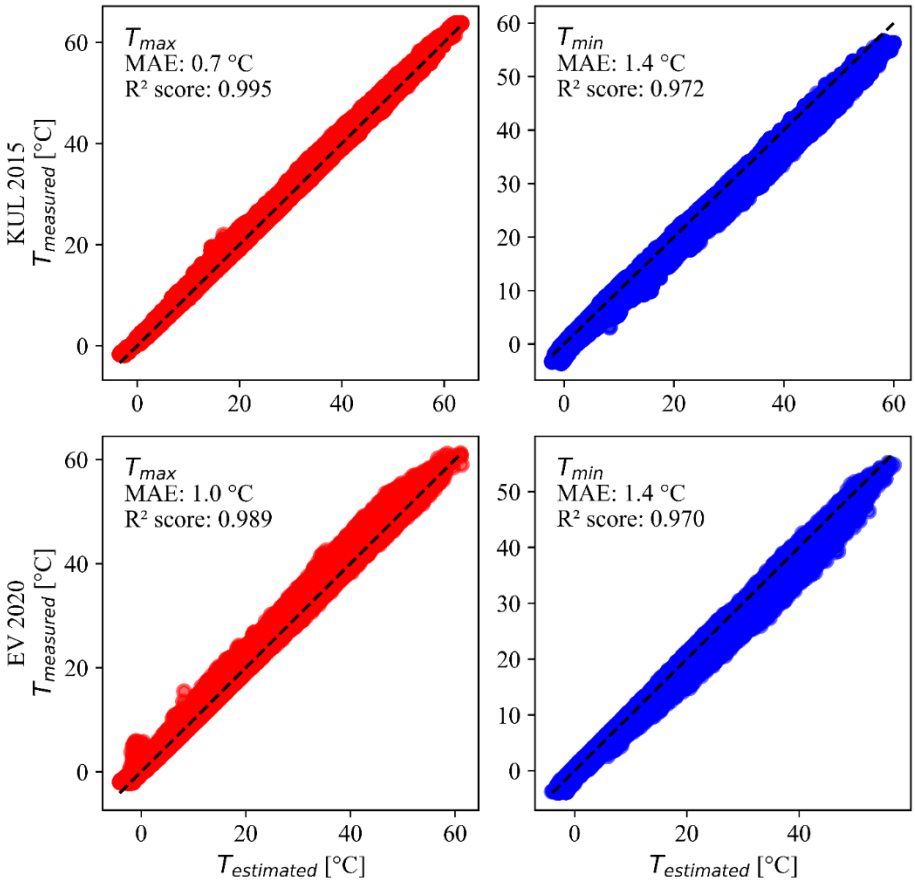

Figure 6-12: T measured vs T predicted comparison

Experiment 1(2015) and Experiment 2(2020), it can be seen that both for Tmax and Tmin, there is an excellent match. There is a difference in MAE for Tmax than Tmin; for both the experiments. However, the overall absolute MAE is low.

As shown earlier in **Error! Reference source not found.** is that intra module spatial temperature increase with higher Gpoa. Therefore, the over temperature model would now be tested with both semi-cloudy and clear sky days in days with high Gpoa with a dominant wind direction. There are two sets of experiments available. Measurement results from Experiment 1 were used to develop wind direction coefficients. So first, we would test it two days from Experiment 1, and then the model would be implemented in experiment 2. This would be an independent validation dataset.

In Figure 6-13 for experiment 1 in both clear sky and semi-cloudy day, of course, the model performs well. This is expected as the over temperature model was derived from the analysis from this set-up. Interestingly, on semi-cloudy days, both Tmax and Tmin prediction errors are close to zero even with high fluctuations on Gpoa. Whereas in a clear sky day, the absolute error is higher, but even then, the maximum error is below 2.5°C. For the days chosen from independent experiment 2, the errors are lower than clear sky day on the semi-cloudy day. But even in clear sky day, Tmax and Tmin absolute error is below 5°C. There are three general observations from these plots. First, Tmax tends to be underestimated, and Tmin is overestimated in all the cases. It indicates that the wind direction coefficient for the over temperature model has to be calibrated further to remove this consistent bias. Second, all the cells' daily median wind affected cooling and intra module heat flow remain consistent with dominant wind direction. Finally, even with an independent experiment 2, which had a different configuration of installations and back sheet temperature measurements, the over temperature model performs quite well.

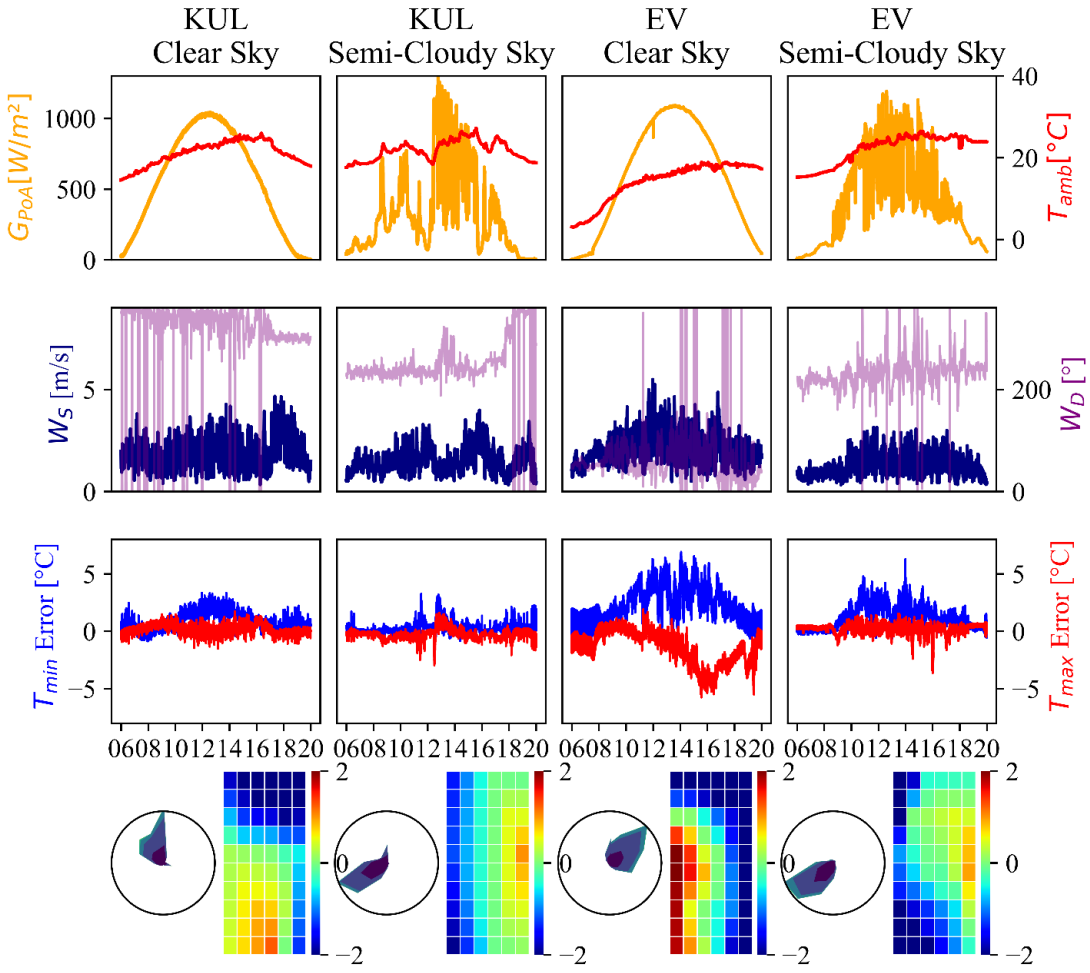

Figure 6-13: Over temperature model performance on clear sky and semi cloudy day from experiment 1 and 2

6.8 Result Discussion

The purpose of this study was to address two elements. The first was to test the validity of the assumption of PV intra module temperature uniformity. Second, if PV intra module temperature is not uniform, what are the dominant meteorological parameters regulating this effect. Based on that if a method can be proposed to model these thermal characteristics.

For the first argument, the PV intra module temperature assumption can be considered uniform in lower Gpoa. With the increase of wind speed from 0-2.5 ms-1, the intra module spatial temperature proportionally increase but becomes inversely proportional after 2.5 ms-1. But this weight of this relation is dependent on Gpoa too. What is clear is that in high Gpoa conditions, even a PV installed in the middle of an array bordered by other PV can have a spatial temperature difference of up to 10℃. Whereas for experiment 2, where other PV modules did not surround it in close proximity, experiences spatial temperature difference up to 15 ℃. The impact is that any model that assumes a uniform temperature would overestimate PV energy yield, especially in the high Gpoa domain, and that is the condition when PV produces the highest energy yield. Such a mismatch will introduce inherent inaccuracies. A controlled lab test result analysis proved such overestimation earlier in a limited context. Therefore, it is essential to have a clear understanding of such non-uniformity. The energy yield differences with uniform and spatially variable PV temperature versus real-life measurement is an interesting research avenue for the future. But it is out of the scope of the current studies.

For the second argument, both from controlled indoor experiments and long term outdoor measurements in multiple locations, this is conclusive that both wind speed and wind direction regulates the intra module spatial temperature. However, the state of the art of PV temperature prediction models have only implemented wind speed as an input variable but did not include the impact of wind direction in an explicit form. Through the proposed over temperature model, we provide a method to calibrate wind direction into PV temperature analysis. It is not a finalised model yet; instead, it is a pathway that can be used. The choice is either the base wind direction coefficients reported in this paper or the coefficients that can be calibrated for your set-up. In any case, if you use the base coefficients for your configuration, we have demonstrated that it will work well to some level of accuracy. However, for better performance, calibration is recommended. Even if calibration is needed, as we have shown,

the methods don't require a year-long calibration, but few months of high-resolution measurements can already provide acceptable accuracy.

It is important to highlight that, as illustrated in Figure 6-10 (12-bin wind-direction coefficients), an ideal symmetric distribution of coefficients is not observed. This asymmetry arises because local geography, array geometry, mounting details, and exposure shape the wind field and therefore the directional coefficients. In short, site and installation characteristics govern these coefficients. The calibrated wind-direction model developed for one site should not be reused at another site without re-calibration. The principal contribution of this chapter is the methodology to derive site-specific directional coefficients, not any particular coefficient set. This site-specific limitation will be made more explicit in the chapter's conclusion to avoid any impression of generalizability beyond the calibration context.

6.9 Chapter Summary

This chapter has addressed a recurring shortfall in PV thermal modelling: the absence of directional wind effects in empirical temperature estimation. While wind speed is routinely included in many models as a scalar input or embedded in a fixed convective coefficient wind direction remains largely ignored, both in commercial software and academic formulations. This omission is not a trivial detail. The measurements presented here make that point unambiguously clear. Across multiple test sites, directional airflow introduced persistent and structured thermal differences across module surfaces, with significant consequences for both yield estimation, forecasting and thermal degradation.

In response, this chapter proposed and validated a new model that introduces wind direction as a calibratable input into PV module temperature prediction alongside wind speed. The model's structure is deliberately simple. It does not require complex CFD input or proprietary software. Instead, it builds on well-established temperature estimation frameworks by embedding a directionally sensitive correction factor. That factor can be derived from short-term, high-resolution field data or from CFD informed parameter sets. Once calibrated, the model shows strong generalization when applied to similar wind regimes elsewhere.

It is essential to emphasize that this model is not a finalized universal solution. The calibration coefficients are inherently site specific, governed by the local geography, array geometry, mounting, and exposure. Applying the calibrated model from one location to another without recalibration could lead to

inaccuracies. Hence, the chapter stresses the need for site specific calibration procedures as a central outcome. This site specific limitation is now made explicit to avoid any misunderstanding of generalizability beyond the calibration context.

This model is not positioned as a final answer. Rather, it opens up a path forward: a bridge between detailed physical simulation and field-operational estimation. Its merit lies not only in improved accuracy, but in accessibility. It lowers the threshold for integrating spatial thermal realism into large-scale PV performance forecasting. The work here reaffirms a theme running through earlier chapters: temperature cannot be reduced to a background parameter. It has structure, direction, and consequence. Models that fail to capture that structure risk misrepresenting the performance of PV systems.

What follows in chapter 7 is an exploration of how such thermal asymmetries play out in yet another emerging PV context floating PV where assumptions of enhanced cooling are widespread, but rarely scrutinized.

7 How Cool is Floating PV?

7.1 Motivation and Organization

Floating photovoltaic (FPV) systems, despite their growing commercial footprint, continue to attract scrutiny over one core claim: that proximity to water inherently cools PV modules and thus improves their energy yield. The literature surrounding this assertion is both expansive and contradictory. Reported performance gains span from marginal fractions to double-digit percentages. Proposed explanations ranging from evaporative cooling and enhanced convective flows to the thermal inertia of water bodies are rarely isolated or tested with a consistent methodology. This chapter seeks to unpack and investigate those claims using a physically grounded, simulation-based approach.

The preceding chapters laid out the rationale for this investigation. In Chapter 5, a high-fidelity thermal model was introduced to capture spatial temperature differences in ground-mounted PV modules, accounting for airflow dynamics, mounting geometry, and material stratification. That work established not only the role of convective asymmetry but also the practical feasibility of resolving such effects at full-module scale. Chapter 6 then extended these insights to realistic indoor and outdoor environments, where long-term high-resolution measurements revealed that wind direction and not just wind speed plays a decisive role in shaping intra-module temperature patterns. A direction-sensitive calibration model was proposed to bridge simulation and field conditions, providing a pathway for more robust operational yield predictions.

Building on this foundation, Chapter 7 applies the same coupled CFD–thermal modelling framework to a different context. The goal here is not to reiterate or extend the same validations, but to shift the focus: from confirming known spatial effects in standard installations to probing the underlying physics of FPV systems. Unlike earlier chapters, which leaned on either controlled experiments or sensor-based field data, the emphasis here lies in scenario analysis. The question is not whether FPVs are cooler, but why under what boundary conditions, and to what extent the cooling is attributable to specific mechanisms.

To that end, the chapter begins by dissecting existing literature. A broad range of FPV studies is reviewed not for their reported gains, but for the explanatory frameworks they rely on. Four main hypotheses emerge: evaporative cooling due to proximity to water, modified ambient microclimate, water as a passive heat sink, and improved airflow due to unobstructed terrain. The next sections present a parametric modelling campaign designed to test these variables individually and in combination. The PV module is modeled using the same multilayer thin-film structure validated in Chapter 5, now placed over a water domain and subjected to controlled environmental inputs wind velocity, direction, ambient and water temperature, humidity, and tilt.

What follows is not an endorsement or rejection of FPV cooling claims, but a systematic evaluation of their plausibility under controlled physics. Early results indicate that the commonly cited "water effect" is spatially limited: evaporative cooling creates a narrow vapor envelope, insufficient to affect module-level temperatures unless aided by wind. It is wind, once again, that emerges as the dominant factor. The simulations show that thermal advantage only materializes under conditions of sufficient clearance and unobstructed air flow paths conditions often absent in dense or sheltered FPV layouts.

In essence, this chapter repurposes the methodological scaffolding built across Chapters 5 and 6 to interrogate a topic long mired in empirical generalizations. Where past claims often drew from correlation, the aim here is causal explanation. The intention is not to dismiss the potential of FPV, but to recenter its performance modelling on the thermodynamic processes that actually govern its behaviour. If such systems are to scale meaningfully, it is not enough to know that they are cooler. We must understand how, and under what constraints, that cooling occurs.

7.2 Chapter Specific Introduction and State of the Art

According to projections, the global total installed PV power will reach 19 TWp in 2050. To cope up with this level of growth, the dual-usage PV concept is gaining traction to reduce land usage. In that line of argument, FPV has emerged in the last decade, avoiding the land occupancy issue with potential energy yield gain due to positive thermal improvement. The presented paper will address the potential thermal impact of FPV. To provide the context of the positive thermal impact, it is established that PV modules have a lower energy output in the field than measured under Standard Test Conditions, mainly attributed to increased cell temperature [24], [26], [62], [72]. Due to their adverse impact on lifespan and power output, it is now apparent that thermal losses are the most significant factor in silicon crystalline PV technology [22], [24], [26], [62], [63], [72], [130]. The decrease in operating temperature would increase efficiency. Therefore, state-of-the-art agrees on the potential energy yield gain due to positive thermal performance. A PV module's efficiency is known to be highly influenced by the temperature of the cells [62], [131], [132]. PV crystalline silicon cells' efficiency is inversely related to their temperature. Many correlations have been proposed for calculating the efficiency decline, ranging from 0.40 to 0.65 rel%/°C [24], [63], [72]. The temperature coefficient is the name for this property of PV cells, and it is always negative for crystalline silicon cells. A commercial PV module's efficiency is generally between 15% and 20%. As a result, even a 1% reduction in efficiency significantly impacts total performance. Due to higher operating temperatures, PV panels might lose up to 10% to 15% of their power on hot days[133]. Kim et al. demonstrated that the modules' temperature had the second most significant impact on the output after solar radiation [130]. Therefore, the claim that FPV systems may experience a cooling effect and perform more efficiently than Ground-mounted Photovoltaic (GPV) systems is of utmost importance. The critical issue is this cooling benefit is heavily disputed. Some claim that FPV modules have temperatures 10◦C lower than their GPV counterparts, while others claim much lower cooling values. Making matters worse, even the physical phenomena behind the cooling effect are debated! According to different developers, the gains in energy yield coming from the unknown origin cooling effect range from 0.11 to 70% [131]. However, if you consider FPV with no other modifications, the potential gains are reported from 0.11-31.29%. Hence, it is highly vital to the floating PV industry to estimate the potential energy yield gain to assess long-term operational feasibility. However, there are various claims about the actual thermal performance

improvement of floating PV. Hence, this chapter extensively reviews published literature on the claim of positive gain of FPV and its root cause. According to different developers, the gains in energy yield from the unknown origin cooling effect range from 0.11% to 31.29%. These last points lead to the presented research. The cooling of FPV modules has been widely claimed yet poorly documented and justified. There is currently a significant degree of disagreement regarding the cooling effect of FPV. Thus comes the paper's aim to study the thermal dynamics of FPV systems. This paper will systematically investigate the root causes behind such disagreement about FPV's effectiveness. Such an extensive set of experiments are time-consuming and expensive. Therefore, this study uses validated finite element modelling to investigate FPV's superior thermal performance from a global perspective. Firstly, confirm if FPV modules have better thermal performance than GPV modules. Secondly, sensitivity analysis of the impact on FPV modules with exogenous parameters such as wind velocity, water temperature, relative humidity, etc. Lastly, to provide a physics-based explanation from finite element modelling of why FPVs are better cooled than GPVs. This way, the presented research aspires to bridge the ambiguity gap regarding FPV cooling quantification and justification through physics-based modelling. The model will be built based on information collected from the literature. Various simulations stressing different parameters will be performed then, followed by a review of the obtained results.

Many theories have come forward trying to explain the cooling of FPV systems. The following lists are several variations and combinations of the most common views.

- First Theory: Evaporative Cooling [132], [134], [135], [136], [137]
- Second Theory: The Water Cycle [133], [138], [139], [140], [141], [142], [143]
- Third Theory: Wind Speeds [131], [141], [144], [145], [146], [147], [148], [149]
- Fourth Theory: Water as Heat Sink [137], [150], [151], [152], [153], [154], [155]

7.3 Chapter Specific Introduction of FPV

FPV systems operate at lower temperatures, supposedly due to one or more of the four theories described earlier. The theories have been explained, and a summary of FPV gains reported in the literature was given. The most obvious for FPVs is the operating temperature of a FPV module compared to an identical

GPV one. It is common in the literature to state that FPV modules are cooler than GPV ones. The temperature difference can be vast, around 10◦C, or minor, around 1°C [149], [156]. The average difference in cooling, in favor of the FPV module, is around a mere 2°C [149] but reaches nearly 10°C in [156]. The large majority of the work proving this cooling effect is done experimentally. Choi et al. [157] show that a FPV system's annual PV module temperature averages 21°C, 4°C cooler than land or rooftop temperatures.

Some papers align themselves on the opposite side of the spectrum, claiming that FPV modules are not always cooler than their GPV counterparts. Such observations are plotted [148], [158]. A warming of the FPV module has been reported by Kumar and Kumar [158] at a 2°C higher FPV temperature; hence, the gain dropped by 1.5%. Their reasoning is attributed to warmer ambient conditions [158]. Another study by Peters and Nobre [148] compared an FPV system with a PV on the roof installed a few meters away from each other in Cambodia. An astounding 10°C module temperature difference was reported against the FPV module, shown in [148].

One key issue that FPV faces is the realistic range of quantification of the cooling and the expected gain. Despite the lower operating temperatures of FPV modules, some modifications or heat exchangers are used to increase FPV systems' performance even further. A few installations use extra functions like tracking, cooling, and concentration [159]. Solar tracking is a strategy for increasing solar energy harvesting and, as a result, increasing the amount of electricity the system generates. One and dual-axis tracking systems are the two types of tracking systems categorized based on the number of degrees of freedom [160]. The cost increase of 7–8% for the tracking system is compensated for by a gain in energy harvesting of 15–20% [159]. Reflectors are used in concentrating FPVs to focus light and enhance the radiation intensity on the PV cells [159]. However, there are two disadvantages to consider. First, the focused radiation boosts the temperature of the cell. Second, the concentration system necessitates a very accurate dual-axis monitoring device, which raises the structure's cost. A guaranteed technique to reduce FPV operational temperature is water veil cooling (WVC). Performed by spraying water on the module with a set of irrigators located at the upper part [161]. Although it lowers the temperature at which FPVs operate, this approach necessitates using external energy, such as pumps. Even though water is a powerful light absorber, the impact of water absorption is negligible for a few millimetres of water veil

[162]. The downside is the difficulty of utilizing such a cooling system in salty or filthy water. A filtering method is required in the latter situation.

After collecting the available information in the literature regarding FPVs and GPVs temperature differences, a table is created which presents the reported gains arising from using an FPV system compared to a GPV one. Before reading the table, the reader must be aware of three points. First, if the author(s) do not provide an explicit justification for why the FPV module performed better than the GPV one, their "supported theory" will be non-applicable (NA). The "cooling effect of water" is also considered NA as the statement is too vague and can't be sorted whether it belongs to theory 1 or 2. Second, authors that report temperature differences only between FPV and GPV and do not report power/energy/efficiency gains are not included so as not to over/underestimate their findings. Only authors that explicitly extrapolate the temperature difference into gain or those that monitored yield improvements are included. Third, parties that stand to gain financial benefit from claiming high FPV efficiency will have their reportings omitted. Thus, this table excludes gains reported by companies installing FPV systems, market reports, or websites. Table 1 contains an exhaustive literature review regarding FPV cooling.

Even though, according to various recent experiments and publications, the cooling advantage on ordinary pontoon-based floaters is small (< 3%) [166] [163] [162], the expectation of extraordinary cooling for FPV continues to be repeated, even though many FPV technologies may indeed have a performance superior to GPV for various reasons. Nevertheless, an obvious observation can be seen from Table 1 that the conclusions on the increase in the energy efficiency of FPVs compared to GPVs are incredibly diverse. Speaking in average terms, FPV has enhanced efficiency by about 7%. The vast disagreement in the literature undoubtedly proves one point: there is a need to understand whether the association of FPV with cooling is true, how much the cooling effect impacts temperature, and where it originates from. In this paper, both systems will be placed in the same simulation environment, shown in the following segments, where we demonstrate a finite element model built upon knowledge explained here. A simulation-based approach enables a fair comparison, more flexibility, and a precise understanding of the thermal performance FPVs.

7.4 CFD Model Description

7.4.1 Geometry and Finite Element Model Assumptions

The industry standard was followed for the presented research to design the optimal coupled CFD domain. Details of the design assumptions will follow in a future revision. Figure 7-1 shows the schematic of the FPV design along with the dimensions. Because the width of ethyl-vinyl acetate (EVA) between cells 2mm is significantly lower than that of the PV surface, the gap between cells is insignificant. As a result, the module is regarded as a five-layer setup. This simplification has been used by Du et al. to assess temperature distribution for a PV module [164]. Furthermore, the vast majority of today's PV modules are made using a glass-back sheet [164]. Thus, the FPV panel model comprises five layers: Glass, EVA, polycrystalline silicon, EVA, and back sheet.

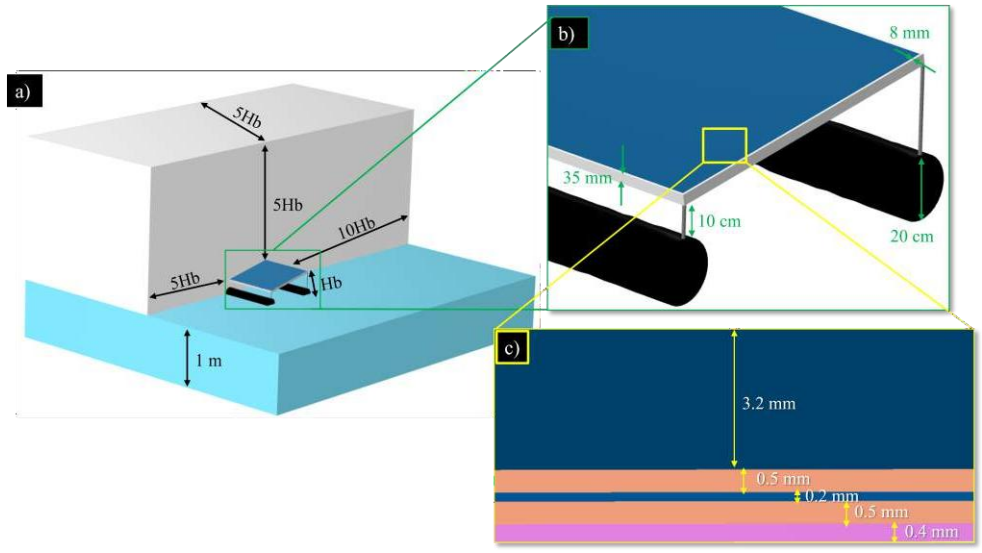

Figure 7-1: a) Wind tunnel (shown only half) and the water domain of the model. b) FPV system, showing the frame and floating structure dimensions. c) The PV module's layers.

Since one of the theories regarding FPV cooling is through conduction, the geometry must include the supporting metal frame as well as the floating structure. Aluminum is used for the PV module's frame. The frame dimensions were obtained from the solar frame website [165]. Horizontal struts/rods extend out of the frame to support the panels [166]. The struts are not in direct contact with water; instead, the water is through HDPE supports or floats [167]. These floats are placed and connected under the panels to keep the system afloat. The optimal tilt angle (θ) for a PV installation in Belgium is 35◦ [107]. But for FPVs, a tilt angle of 10◦ is more common to get high-density arrangements [168].

Table 7-1: The thermal properties of the materials used throughout the paper (∗ Indicates values obtained from COMSOL material library)			
Material	Density ρ (kg/m3)	Thermal Conductivity k (W/m · K)	Heat Capacity Cp (J/kg · K)
Tempered Glass	3000 [74]	1.8 [74]	500 [74]
EVA	948 [169]	0.34 [170]	2090 [169]
Silicon	2330 [169]	148 [169]	677 [169]
Back sheet	1200 [169]	0.18 [169]	1250 [169]
Aluminum	2700 [146]	237 [169]	900 [146]
HDPE	960 [171]	0.48 [172]	2250 [173]
Air ∗	1.18	1.7	1014
Water ∗	998	0.6	4185
Soil	1700 [174]	0.98 [175]	1419 [174]

Usually, 65 cm is a typical height for GPV off the ground [57]. But this value is lower for FPV systems. The initial height chosen for the system is 20 cm away from water, which is close to the usual clearing of 40 cm [166]. This height is measured from the closest point of the aluminum frame at the tilted side to the water.

7.4.2 Air and Water Domains

The air mass flowing over the FPV system is infinitely large in real life. It is impossible to represent such an air mass for modelling purposes. As a result, it's critical to create a limited air domain surrounding the FPV system that's as tiny as feasible while nevertheless simulating the limitless air mass found in real life. To generate the air domain, Franke et al. [176] COST recommendations for CFD modelling in an urban context are used. The recommendations suggest utilizing a cuboid volume whose dimensions are determined by the characteristic height

Hb, which is the highest obstacle's height. The top, sides, and inflow boundaries of the computational domain should be at least 5Hb away [176]. A value of 10Hb is necessary for the outflow boundaries to ensure the influence of the target building is negligible [177]. Stated differently, the region behind the built area should be far enough away from the wake region to allow for flow redevelopment. The water dimensions in upstream, downstream, and lateral directions are set the same as the air domain. The water areas where FPV systems are installed tend to be shallow (1-4 m) [155]. Therefore, the water depth is chosen as 1 m to reduce computational time. This constitutes the geometry of the reference FPV system, and it is illustrated in Figure 7-1, along with the dimensions used.

7.4.3 Multiphysics Settings

Aluminum is used for both the frame and the supporting attachments extending out of the frame. HDPE is used for the floating structure. The physical characteristics of the various materials are used to determine thermal resistances and capacitances. When an absolute value for the material property could not be obtained, the average between the values reported in the literature was taken instead. Table 2 lists the thermal properties of the materials used in the model. For radiative heat transfer, The emissivity of a substance is a measurement of how effectively it radiates heat. The emittance of PV glass and the back sheet is set to 0.9[178].

Computational Fluid Dynamics was used to study wind flow over PV modules. CFD can resolve the RANS equations. Furthermore, by utilizing a verified CFD model, it is feasible to predict and enhance the thermal performance of a particular PV module design, considerably decreasing the time and money spent on testing. It is important to solve the viscous sublayer for accurate temperature profiling. The standard k ω and SST k ω– models can resolve such layer, but they differ in one aspect. A reverse pressure difference arises when the fluid contacts a sharp edge, such as a module, and the fluid is reversed. Menter's [179] SST–k ω model correctly predicts unfavorable pressure differences and separation compared to Wilcox's [83] conventional k– ω model. Shademan et al. [180] demonstrated how the SST model performed well for flow around an inclined plate. This makes SST the model of choice employed in this paper. In a FPV environment, the air density will change with temperature. Thus, the air is approximated as weakly compressible, indicating that density is a function of just the temperature and does not vary with pressure. Furthermore, the gravity force is accounted for in this model.

Table 7-2: The reference parameter values used in the simulations.	
Parameter	Value
Tilt Angle (θ)	10°
Angle of Attack (α)	0°
Distance from Water	20 cm
Ambient Temperature (Ta)	25°
Water Temperature (Tw)	22°
Solar Irradiance (G)	600 W/m²
Wind Speed (U)	4 m/s
Relative humidity (φ)	50%
Diffusion Coefficient (D)	2.6 m²/s
Evaporation Rate (K)	100 m/s

The ground and every solid wall must have a no-slip boundary condition, with no slip meaning zero normal velocity. The lateral sides and top domain boundaries are treated as slip walls. An inlet wall with a boundary condition of velocity was chosen. At the outlet, zero gauge pressure is specified. A wet surface node for the modelling of evaporation and condensation was employed as well. Lastly, the symmetry plane cuts down the geometry to one-half and accelerates simulations. The simulations omitted two kinds of physics that occur in real life. The first is water movement and wave characteristics physics. Most FPV systems are installed in calm waters (lakes, lagoons, reservoirs, rivers, canals, etc.). Second, the solar radiation will be modeled as a heat source inside the module. The value of which is decided in the next section.

In this paper, we assumed the PV module's efficiency as constant at 18.4%. Also, the cell absorbs only some of the irradiance falling on the panel. Nizetic et al. [110] used an absorption coefficient of 0.86, which is used in this paper as well. Combining the last two values, this model converts approximately 70% of the irradiance into heat. Empirical (regression-based) or deterministic (physical-based) models can be used to forecast and measure water temperature.

Empirical models rely on statistical regression to create less sophisticated models. Harvey et al. [181] suggest an equation that makes use of ambient temperature (Ta) to deduce a value for water temperature (Tw). However, placing water temperate under user control will be easier to better isolate the impact of water temperature alone quantitatively. Thus the water temperature will be independent of the ambient temperature in this paper. The water was set at 3°C cooler than the ambient in the reference scenario. Table 3 summarizes the default geometry-based values and the physics-based ones used in the paper.

The angle of attack α signifies the wind direction and a value of 0° indicates the wind's first impact is on the tilted front surface of the module. The default wind velocity of 4 m/s is chosen as the median wind speed in Belgium. The same goes for the irradiance of 600 W/m2. The diffusion coefficient of water into the air at 25°C is around 2.6 m2/s [182], and the evaporation rate is kept at its COMSOL default of 100 m/s. The RH was set at a neutral start of 50%. For a steady-state problem, the quantities do not change with time. Stationary simulations indicate that all quantities have reached equilibrium. The heat flux exchanged media via

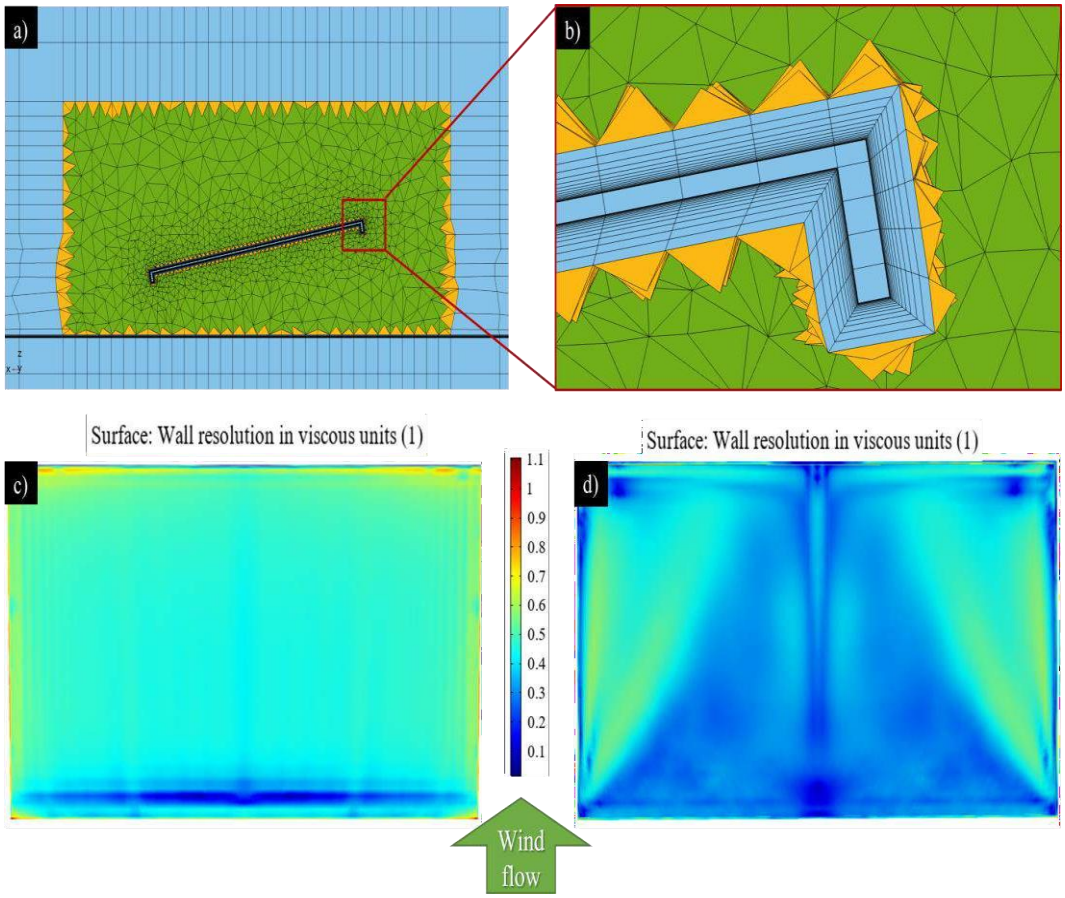

Figure 7-2: a) Elements used to construct mesh, blue=hexahedrons, orange = pyramids and green = tetrahedrons. b) Zoom in demonstrating boundary layer meshing. c) and d) Results of y+ on top and bottom module faces respectively.

conduction, convection, and radiation processes balance the heat created within. For both steady-state and transient simulations, Nizetic et al. [110] proved that the converged panel temperature remained unchanged, allowing for a steady-state analysis, which is the case employed in the paper.

7.4.4 Mesh Creation and Grid Independency Test

Because a domain has an unlimited number of points, there are an endless number of equations to solve. The computing domain is discretized to a finite number of elements N to address this problem. For 3D geometries, the mesh generator discretizes the domains into a tetrahedron, hexahedron with a quadrilateral base, prism with a triangular base, or pyramid mesh elements.

Table 7-3: GCI computation across three grids for different physical quantities. Temperature measurements are averages.

Quantity	Grid	Result	p	fo	GCI13	GCI36	$(GCI\_36)/(r_{13}^{P} \times GCI_{13})$
Module temperature	G1 G3 G5	34.31◦C 34.6◦C 35.5◦C	3.52	34.13◦C	0.65%	1.7%	0.992
Frame temperature	G1 G3 G5	28.39◦C 28.46◦C 28.81◦C	4.88	28.36◦C	0.12%	0.45%	0.997
Velocity 1.5 mm above module	G1 G3 G5	2.51m/s 2.46m/s 2.36m/s	1.83	2.59 m/s	3.9%	6.57%	1.02
Pressure 1.5mm above module	G1 G3 G5	-1.75 Pa -1.64 Pa -1.27 Pa	4.03	-1.8 Pa	3.71%	11.92%	1.06

The geometry is partitioned into multiple subdomains to facilitate the meshing. An inner air box of dimensions Hb is created inside the larger wind tunnel, which surrounds the FPV system. Because a combination of hexahedron and tetrahedron cells offers better results than a strict tetrahedron grid, the inner air block is used to decrease the number of tetrahedron meshes as much as feasible [176]. Arrangements of the elements are: hexahedron cells on the surface interior of the FPV system, tetrahedron cells in the interior air block encompassing the FPV system, then hexahedrons again for the remainder of the large air tunnel. The model is meshed using the "swept mesh" structured mesh type. Sweeping a source face to an opposing destination face is how the swept mesh works, and in the sweep direction, a swept mesh is built.

For solar modules, the velocity field changes quite rapidly in the normal direction. This observation motivates the use of a boundary layer mesh, a unique meshing approach. A mesh with dense element distribution in the normal direction along certain boundaries is known as a boundary layer mesh [183]. To make a boundary layer mesh, three values are needed. First, the height of the first layer of cells. Through trial and error, it was found that a value of 0.08 mm was adequate. Smaller values take longer to converge without large deviation in outcomes. On the other hand, larger values do affect the solution and are considered an example of under-meshing. Second, the boundary layer stretching factor is used to express the thickness increase between two successive layers; for example, entering 1.3 indicates a 30% increase in thickness from one layer to the next. Third is the number of boundary layers. It was decided to link the last two values together to obtain a boundary layer with total thickness of 10 mm. Hence, a stretching factor of 1.27 with 15 boundary layers was used. Figure 7-2 demonstrates the created mesh.

It can be seen in Figure 7-2(b) that the unstructured tetrahedron mesh shares an interaction with the topmost layer of the stack of boundary layer components, and the connection is made through a pyramid element. More importantly, the created mesh obtains a $y+ < 1$ on all the module's surfaces, shown in Figure 7-2 (c&d), indicating the turbulent boundary layer, including the viscous sub-layer area, is resolved to the panel surface. Thus the application of wall functions, which overestimates the convective heat transfer by 60% [119], is eliminated.

7.4.5 Finite Element Model Grid Independence Test

COMSOL uses the finite element method (FEM) to compute simulations. When using FEM, the accuracy of the solution is linked to the mesh size. As mesh size

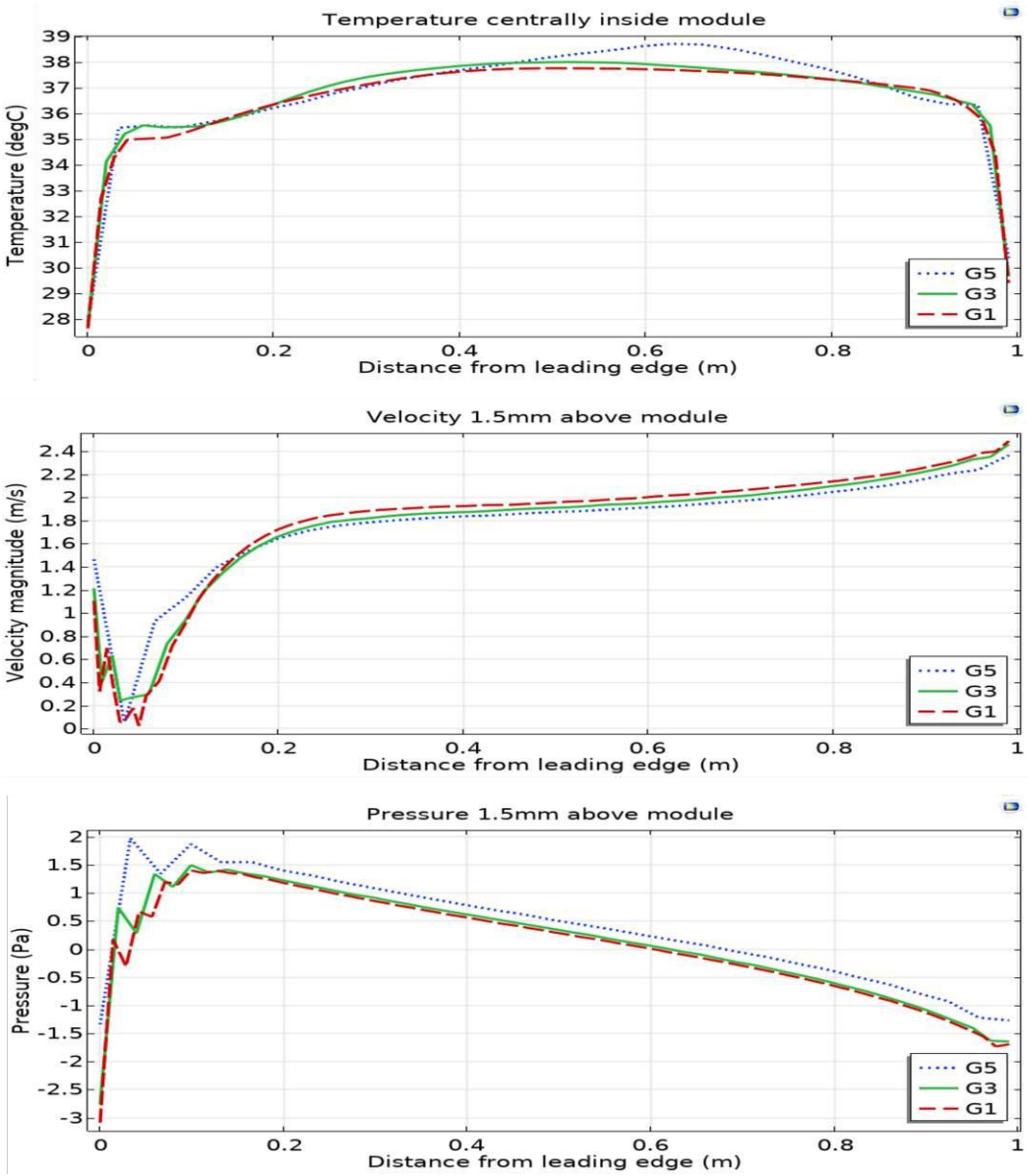

Figure 7-3: Plots of temperature, velocity and pressure from left to right respectively.

decreases towards zero, solutions tend to be the exact solution. However, an approximation of the solution will suffice due to limited computational resources and time. A grid convergence index (GCI) analysis, which estimates grid uncertainty and is derived from the generalized Richardson extrapolation, is used to report uncertainty owing to discretization in CFD applications [90]. It involves comparisons of discrete solutions at different grid spacings. A GCI study has two primary purposes: to establish convergence and to determine the rate of convergence p. To check grid independence, a set of five meshes with a different number of elements were created. Namely, the meshes are ranked from coarsest to finest based on the number of elements. G5 with 150·103, G3 with 374·103 and G1 with 853·103 elements. The grids contain these specific number

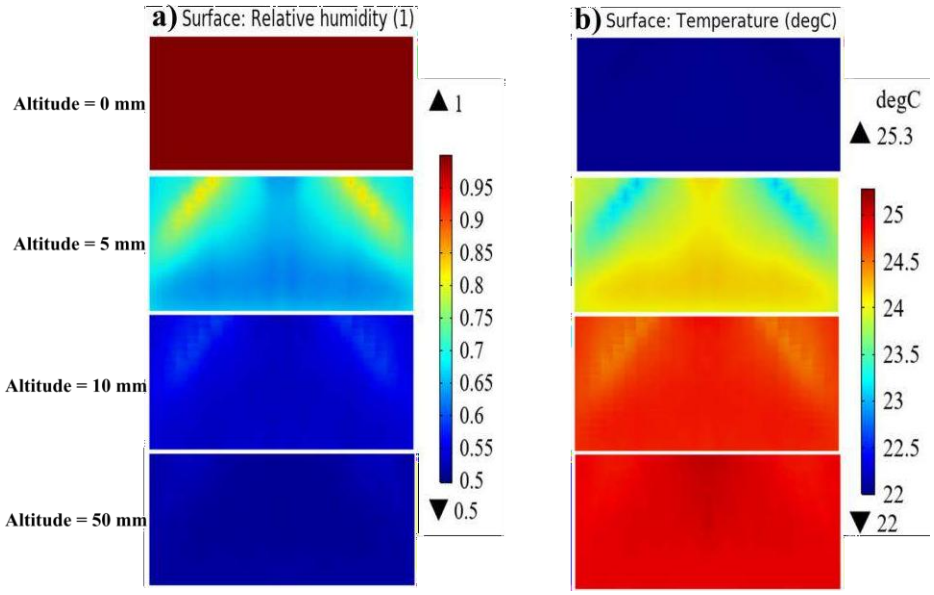

Figure 7-4: Plots of a) Relative Humidity and b) Air temperature directly underneath the module at various altitudes from water level.

of elements such that the grid refinement ratio r between grids is set to 1.3 in accordance with Roache's guidelines [90]. First-order discretization schemes are used for all unknowns: pressure, velocity, temperature, and humidity of their respective governing equations. Table 7-4 confirms that the solution does not change by monitoring the temperature, velocity, and pressure. This indicates that the numerical simulation's reliance on the grid has been lessened.

For a grid refinement ratio of r = 1.3 and the first order of the used numerical method, the GCI should be around 10% or less, as reported by Roache [90] which is achieved as reported in Table 4. Another metric of convergence is that the results approach the extrapolated solution f0. The apparent order of accuracy ‘p’ and the corresponding GCIxy matches with what was reported in literature [90][77]. Moreover, the consistency of the computed apparent order with the formal order is a good indicator that the grids are in the asymptotic range. From the table it can be seen that for the tested cases, asymptotic range where GCI36/(r13p.GCI13) ≈ 1 is ensured [90]. Another way of proving mesh convergence is through temperature, velocity, and pressure plots across the different grids. The mesh convergence plots are shown in Figure 7-3. Based on the previous, the average grid G3 and fine grid G1 gave almost co-incident results, indicating mesh convergence. Given the computing resources available, G3 is chosen as the final grid for simulation.

7.4.6 Model Validation With Experimental Results From The Literature

The simulation work of Nizetic et al. [110] was replicated; if both results were close to each other, then the model was verified. First, their simulation was for a standard GPV system. Hence the water domain was removed. Then the same settings of wind speed and irradiance were applied. Their results showed that the average temperature for G = 800W/m2 and U = 3m/s was 43℃. In the constructed model, the average temperature reading was 44.8℃. A relative error value of 4%. The most probable explanation is that in the Nizetic simulation, the module was assumed to have an efficiency of 19.5%, while in this paper, the efficiency was considered to be 18.4%. Lower efficiency indicates a larger heat source and, thus, a larger temperature reading. Nonetheless, the model was validated to be accurate enough to proceed.

7.5 Results and Discussion

After each simulation, the results are post-processed and analyzed to minimize ambiguity and maximize understanding. Whenever possible, the results obtained are compared with literature results, whether they agree or disagree. Lastly, a conclusion is made regarding which theory is the most probable for FPV cooling.

7.5.1 Comparing FPV with GPV

The first simulation compares FPVs against GPVs since that seems to be the industry standard. It must be noted that the systems were simulated in the exact same environment. The default parameters listed in Table 7-2 were used for both simulations. Meaning, both systems experience the same wind speed, RH, ambient temperature, etc,. The only difference is that water is swapped out for soil when simulating for GPVs. This essentially states that the only differentiating factor between the FPV and GPV simulations is the existence of water. With that being said, the simulated module temperature in both scenarios came out to be identical at 34.71℃. This is obviously the exact opposite of what was expected which was a minor or major cooling for the FPV module. Concluding that water has proved ineffective in cooling but further analysis is needed to know why.

Figure 7-4 shows how water changes the surrounding air. What is shown is the portion of air directly underneath the module. It is demonstrated in Figure 7-4 (a) that at the water surface (altitude=0 mm), the air is completely saturated with water vapor molecules. This is clearly indicated by having air at 100% RH.

It can be described as water-like air and this translates into air temperature as well as shown in Figure 7-4 (b). The water temperature was set to 22°C and the air directly at the water level has the same temperature reading. Up till now, the theory of evaporative cooling is working just as intended. The water is providing an extremely valuable benefit of cooling the surrounding air. Unfortunately, this cooling effect hardly continues any further away from the water level. Once only 5 mm away from the water, the water properties that were given to the air dramatically dissipate to the environment. The air no longer becomes saturated with water vapor, and, consequently, has a temperature that is much higher than water temperature. The further away the air is from the water, the less water-like the air becomes. At an altitude of just a mere 1 cm, the air that used to carry some water properties has now become very similar to ambient air. At around 5 cm and beyond, the air becomes indistinguishable from the ambient air already present. Meaning the portion of air actually nearby the FPV system has a RH of 50% and a temperature of 25°C. Both of these are the exact same settings used in the GPV simulation, making the air around the FPV module identical to the one surrounding the GPV module. This explains why both FPV and GPV modules had the same temperature.

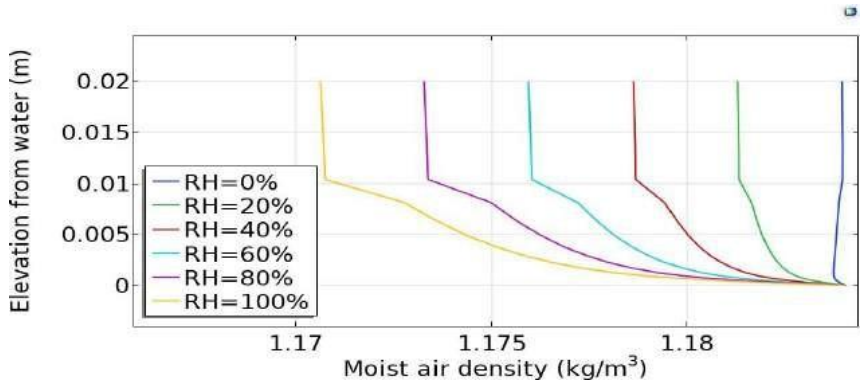

Figure 7-5: Plots of air density at different humidity levels.

In short, while evaporative cooling of air is proven to take effect for FPV systems, the effect is extremely lackluster and is only clearly present in the first cm away from the water. The evaporative cooling process changes air properties for the better but only at a small domain that will be termed a 'Vapor Blanket'∗. This vapor blanket is a maximum 2 cm thick, and all air above said blanket retains very little to no features of the water body. Stated differently, the water is unable to induce a change that can reach the module level. So it can be said that the mere existence of water is not enough to induce any cooling to the panel. With all other parameters being equal, placing a PV system on top of water or soil will

have no difference in operating temperature. In conclusion, the cooling process for FPVs is in need of a stimulus that does not originate from water. Thus more simulations are needed to see which parameter is most prominent for FPV

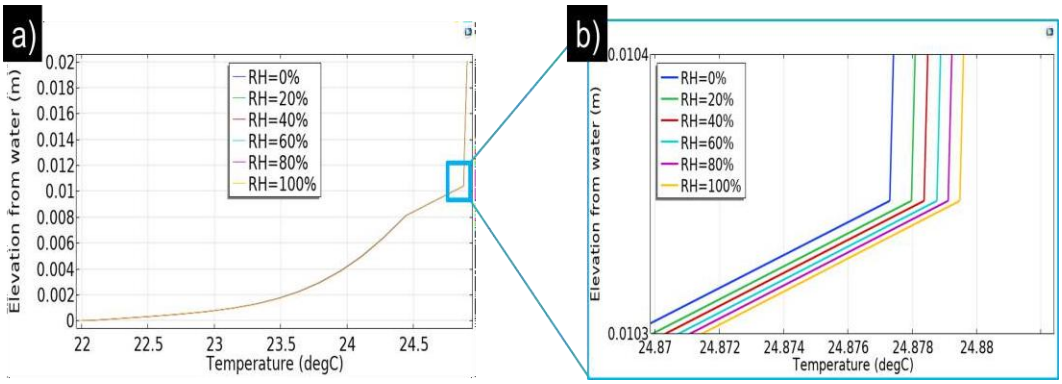

Figure 7-6: a) Air temperature at different humidity levels. b) Close up plot.

temperature.

7.5.2 Relative Humidity Impact

Since RH is one of the key components of the evaporative cooling process [184], in the sense that evaporative cooling efficiency is inversely proportional to RH level. One could expect that the lower the ambient RH level, the larger the vapor blanket will become. This is explained by the psychometric fact that humid air is lighter than dry. So the larger the disparity in RH levels, between the ambient air and the cooler air entrapped inside the blanket, the larger the blanket should be, ideally reaching the module and cooling it. A number of simulations were run with all parameters fixed except the ambient RH which varied from 0% to 100%.

As per the theory, the higher the humidity, the less dense the air became. This is clear in Figure 7-5. When the air is free of water vapor and completely dry, the density was around 1.184 kg/m3. On the opposing end when the air is saturated with vapor and humidity, the density dropped to nearly 1.171 kg/m3. A relative density drop of around 1%. More interestingly, the density change is more apparent inside the blanket. Once the blanket has expired, the remaining portion of the air still maintains the density of the air that was inside the blanket. In other terms, the air inside the blanket changes the density of the ambient air and not vice versa like in the previous section where the ambient changed the RH levels of the air inside the blanket. What remains to be seen however is if this density disparity had an effect on air temperature and consequently FPV temperature. Figure 7-6 holds the answer.

On the upside, when the ambient is dry, this gives more room for the blanket to rise since now there is a bigger density disparity. This can be better seen in Figure 7-6 (b). At a given altitude from the water depicted on the y-axis, the blanket is holding slightly cooler air if the ambient was dry. As the cooler air gradually rises, it can be stated that the effective thickness of the blanket has increased slightly or that the blanket remains the same thickness but is holding colder air, increasing efficacy. Also as expected, the higher the humidity, the worse the evaporative cooling operation performs. Because now both the ambient air and the air inside the blanket have similar humidity levels. This essentially acts as a barrier for the cold air inside the blanket to rise upwards towards the module. Hence, the blanket is now characterized by an even smaller effective thickness. The changes that RH prompts in air density and temperature are in line with expectations. On the downside, however, the density difference is not significant enough to induce large cooling. When the ambient was dry with 0% RH -which is the ideal scenario for the evaporative cooling process-, the module's temperature was 34.7℃. Just 0.01℃ lower than the reference case with 50% RH. On the other hand, when the ambient is saturated with 100% RH, the module's reading was 34.72℃. Symmetrically the opposite result, where here a heating of 0.01◦C is noted. The results obtained agree with the literature. Choi et al. [93] showed that the module temperature increases with humidity. A decrement of the air's RH is always desired as RH shortens module lifespan and has an impact on PV power output in a similar way to dust collection. Increased water content in the air increases solar radiation scattering and lowers solar intensity received [200]. As a result, the solar cell suffers a loss in incoming energy.

In any case, these outcomes essentially refute the potential of evaporative cooling entirely. Simply put, the first theory of evaporative cooling is way too constrictive and does not stimulate a cooling that is large enough to match or even come close to the lower end of the cooling numbers reported in the literature of around 1-2 ℃.

Table 7-4: Change in module temperature with ambient temperature setting.

T_a (℃)	20	22	24	25	26	28	30
T_{mod} (℃)	30.4	32.1	33.9	34.71	35.6	37.3	39

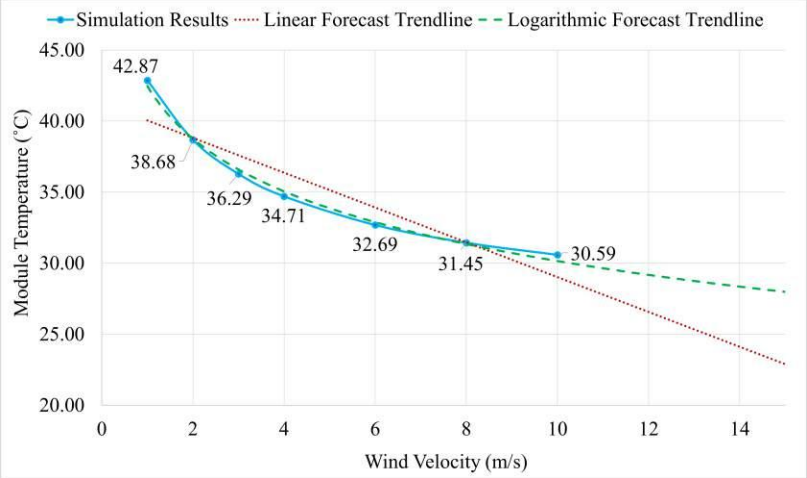

Figure 7-7: Module operating temperature versus wind velocity. Dotted lines are linear and logarithmic forecasts.

7.5.3 Ambient Temperature Impact

Ambient temperature is without a doubt one of the most important elements influencing PV module operating temperature (Tmod). Because heat convection is dependent upon the temperature differential between the surface and the air itself. The warmer the air is, the less heat is transferred from the module to the ambient air resulting in a warmer module. The opposite effect shall occur as the ambient becomes cooler, carrying more heat out of the module resulting in a lower temperature. The results of the simulations are written in Table 7-5 and they follow expectations.

When the ambient is cool (20°C), there exists a larger temperature difference between PV and ambient, this facilitates heat transfer. The temperature differential between the module and the ambient reduces as the ambient temperature rises, reducing the rate of heat loss from the module to the environment [185]. Additionally, the relationship between ambient and FPV temperature is of linear nature, with a change of 0.85°C for every 1°C change in ambient.

No difference was found in the temperature distribution along the module. The hottest spot was always in the middle, especially downwind. The coolest spots were near the frame and at the upwind edge. In conclusion, the findings show that a lower ambient temperature aids heat dissipation and, as a result, improves the electrical efficiency of FPV modules like the findings of Charles Lawrence Kamuyu et al. and Zhou et al. [24], [80].

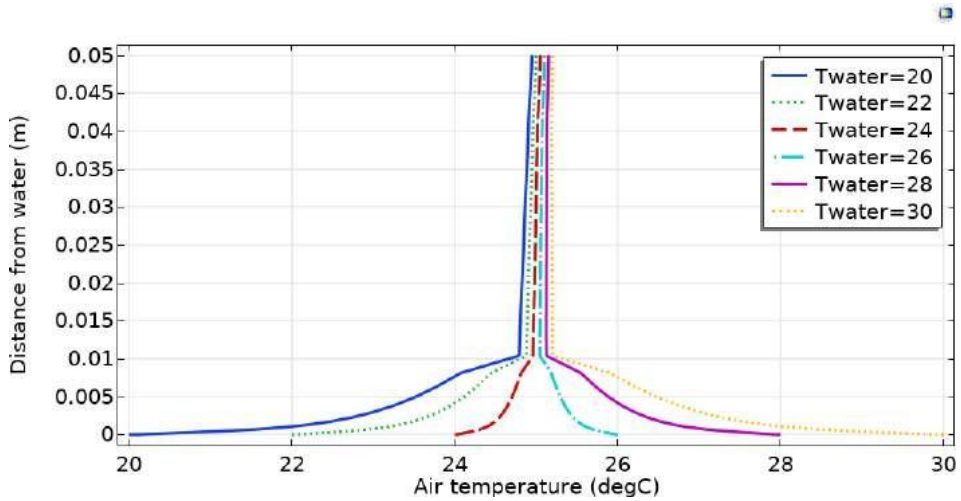

Figure 7-8: Evolution of air temperature with elevation from water for different water body temperatures.

This subsection validates the second theory in justifying FPV cooling since the simulations show that the ambient environment affects FPV temperature by a significant margin. However, to know with certainty whether the second theory is the sole, or partial, contributor to FPV cooling requires further investigations carried out in the following sections.

7.5.4 Wind Speed Impact

The third theory of FPV cooling was through wind velocity enhancement. Lower wind speeds result in less turbulence and hence, less evacuation of heat. Most literature agrees that module temperature changes linearly with wind speed [186]. However, the obtained results deviate slightly from this norm as shown in Figure 7-7. The obtained curve for module cooling shows a square-root dependency on the wind velocity, the same as the findings of Goverde et al. [26]. When wind speed is low (≤2 m/s), natural convection dominates, this results in a large jump in module temperature. As the wind speed increases, more heat is extracted from the panel, decreasing its temperature. This is attributed to the more turbulent nature of the airflow which improves heat transfer as compared to laminar flows [26]. Nevertheless, the cooling rate slows down as wind speed gets larger similar to the findings of Zhou et al. [187]. More than likely due to the better cooling performance which shrinks the temperature difference leading to smaller cooling for every 1 m/s increment in wind speed. Hence it can be concluded that FPV temperature is sensitive to wind speed, and more so at the lower end. It is a valid theory that higher wind speeds experienced by FPV systems will aid in cooling, leading to a better efficiency rating than GPVs. Yet, the parametric sweeps performed so far do not show the full picture yet. At this

point, it is inconclusive to say which of the two theories, ambient temperature or wind speed, is the one responsible for FPV cooling. For these reasons, the following sections explore every other aspect regarding FPV operation. This will provide further understanding regarding the thermal workings of FPVs and a more decisive conclusion.

7.5.5 Water Temperature Impact

One key feature of FPV is water presence. It has already been explored that the positive effects of water on the surrounding air disappear quickly into the environment. This section investigates how the temperature of the water changes the vapor blanket and how major are these changes in the blanket to the module temperature. In order to keep the simulations compatible with real-life environments, the maximum difference between water temperature and ambient temperature was set to ± 5℃ [188]. This determines the water temperature span for this section's simulations.

The simulation outcomes show a significant correlation between water and module temperature. While the correlation is significant, the resulting cooling or heating is not. When the water temperature is at 20℃, the module cools down to 34.46℃, 0.25℃ lower than the reference. When the water temperature is set to 30℃, the module heats up to just 35.7℃, 0.99℃ warmer than the reference case. So there is a definite correlation but with small changes. A valid estimate is that the average FPV module temperature changes by 0.125◦C for every ℃ change in water temperature.

The reason for the correlation is the direct impact of water temperature on the air temperature inside the vapor blanket. This is demonstrated in the bottom portion of Figure 7-8. This creates a more favorable temperature difference that cools down the module the colder the water is. The opposite effect is true the hotter the water. This explains why module temperature changes but the reason why the change is small is better demonstrated using the top portion of Figure 7-8. where it becomes clear that regardless of water temperature, the air temperature will converge close to the ambient temperature (25℃). Once the vapor blanket blends with the environment (occurs around 1 cm away from water), there is an extremely small difference in the temperature of the air that reaches the FPV panel, hence the small change.

Conclusively, the water temperature does indeed impact FPV temperature both positively and negatively. This is a key consideration as that would indicate worse performance for FPVs in the winter as during winters, the water becomes warmer than ambient. This observation was also evident in the work of Golroodbari and Sark [138]. The outcomes of the paper's simulations disagree with Hwang et al. [189] and Peters and Nobre [148] which state water temperature has no impact on FPVs. The outcomes agree more with Jeong's et

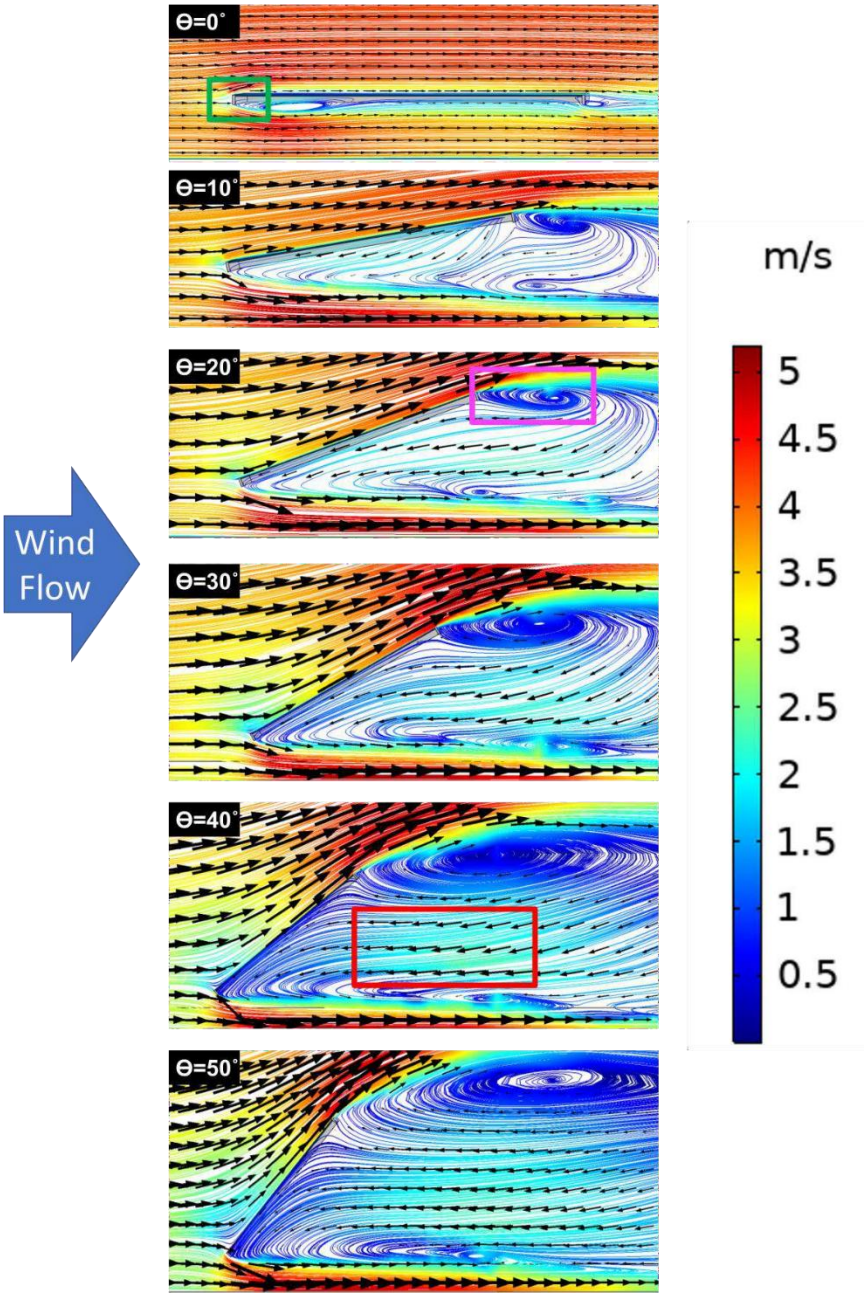

Figure 7-9: Streamlines of wind velocity for different module tilt angles.

al. study [149] with a moderately strong correlation between water and module temperatures.

7.5.6 Tilt Angle Impact

The tilt angle of panels that corresponds to local latitude is better for increasing annual power generation. Low tilt angles, on the other hand, are favored in FPVs [190] [168] because they allow for a smaller space between rows, allowing for more area to be used and a reduction of wind forces on the structure. Furthermore, it was found that the flatter the panel, the less water was evaporated due to the reduction of water exposure to solar radiation [205]. Since the common practise is low tilt angles, the simulations span from θ = 0° till 50°, in increments of 10. Higher tilt angles were not encountered in practise nor in literature experimentation.

The results of the simulations were as follows, for a flat panel, the average temperature was 34.75°C. Slightly higher than the reference (θ=10°) which sat at 34.71°C. As the angle increased to 20° and 30°, so did the temperature, reaching 34.95°C and 35°C respectively. But with a further increase in tilt, the opposite observation is noted. For the angles of 40° and 50°, the module temperature reduced to 34.8°C and 34.7°C. To better explain this unsteady trend, a closer look into wind behaviour is required. Figure 7-9 illustrates the wind streamlines for the simulated tilts.

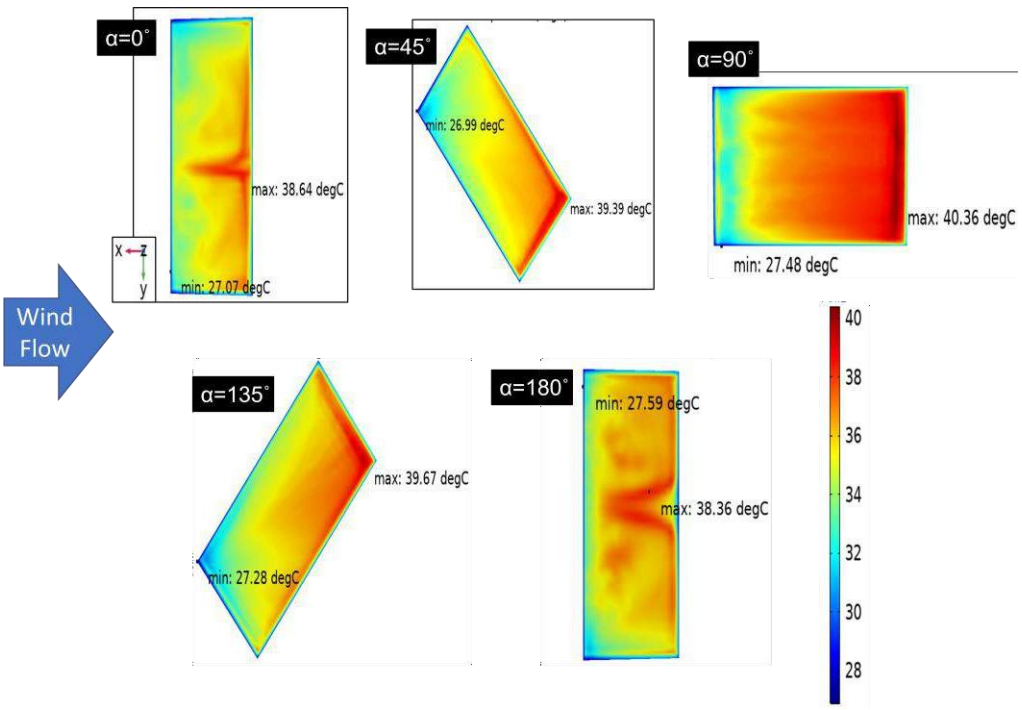

Figure 7-10: Top view of FPV temperature profiles for various values of the wind direction (α).

Three phenomenons occur to the wind profile. The first, is flow detachment (green box in θ=0° in Figure 7-9). This occurs as the wind strikes the leading edge of the module. The detachment divides the wind flow into two parts, the major part will go and glide over the front side of the module all the way to the trailing end, the second part will flow down and around the aluminum frame and converge with the streamlines coming from the inlet. The second phenomena is the recirculation bubbles/zones (pink box in θ=20° in Figure 7-9). Close to obstructions, the wind deviates from its normal course, resulting in intricate recirculating patterns known as vortices. Winds spread outwards away from high high pressure to low pressure places. Since the entire backside of the module sits at low pressure, the wind will aim to go towards this low-pressure region instead of continuing towards the outlet. This leads to the third phenomena which is return flow (red box in θ=40° Figure 7-9). This is more prevalent in higher tilt angles as now the pressure imbalance becomes larger, this will encourage more wind to flow back towards the backside of the module. The flat panel heated up because the inclination makes it that less panel area is impacted by wind, the flow detaches and then reattaches at a much later point because of the lack of any inclination. By increasing the tilt, more panel area is coming into contact with the wind. So one expects better cooling with an increment of the tilt angle which is true for θ=10° but not for larger angles. As tilt angle increases, both the vortex and return flow get larger. But for the case of 20° and 30◦, the module experienced a heating because the return flow was not as strong as the one for the 40° and 50° tilts. The latter two cases experience a higher wind speed contact at their back side resulting in lower temperature than in the earlier two cases of 20° and 30°.

To conclude, the paper outcomes would disagree with the literature which supports the general finding of better convection with increments in tilt angle [78], [191], [192]. The finding of the paper are more case specific but they prove that the low tilt angles common for FPVs will not hinder performance by a large degree. The optimum angle was found to be 10° like the findings of Ueda's et al. [193] FPV project where the angle was changed from 1.3° to 10° to enhance air cooling.

7.5.7 Wind Direction Impact

So far the module was placed such that the incident wind's first point of impact was on the front side of the panel. Indicating that wind was perpendicular on the module's front surface. Wind direction is often characterised by the angle of attack α. The default has been 0° so far. This section sweeps over the possible

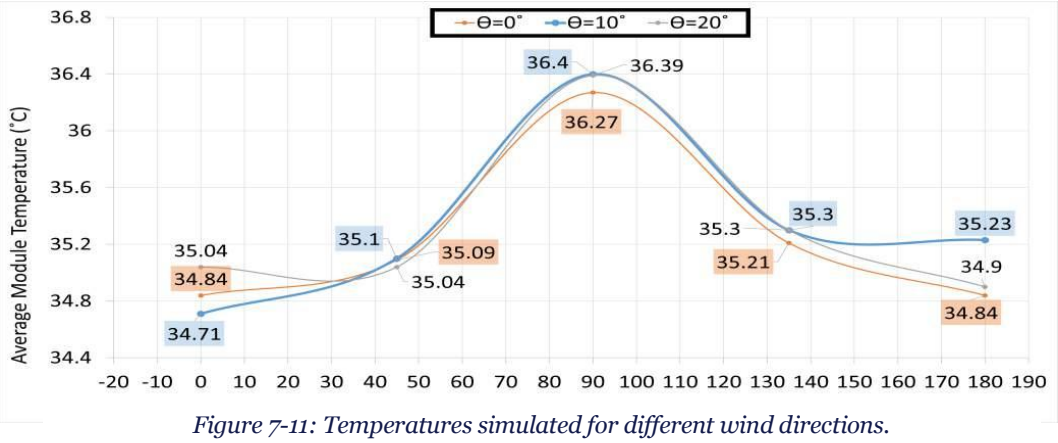

Figure 7-11: Temperatures simulated for different wind directions.

directions where wind can originate from. The results of the simulations are illustrated in Figure 7-10. It can be noted that in all scenarios, the coldest region of the module is also the region that is closest to the wind inlet. On the other hand the hottest spots are at the opposite end of the panel, at the downwind located regions. This is best shown for the case of α=90°. This phenomena is explained by the air's boundary layer. At initial impact, the wind is at ambient temperature and is characterised by high velocity. Both of these characteristics provide a cold spot at the leading edge. Further down, the wind separates and then reattaches at a later point. A boundary layer forms after reattachment. This barrier layer stores heat [83] , resulting in a reduction in heat transport. Hence why temperature of the downwind-located portion is highest [24].

Moving from hot and cold spots to averages, one notices the following trend plotted in Figure 7-11 for not only the default θ = 10° but for a flat panel and a pane tilted 20°. As α increases, the heat transfer rate decreases similar to the outcomes of Turgut and Oner [194] and Wu et al. [81]. The effect persists till and including α=90° which carries the highest module temperature. With further

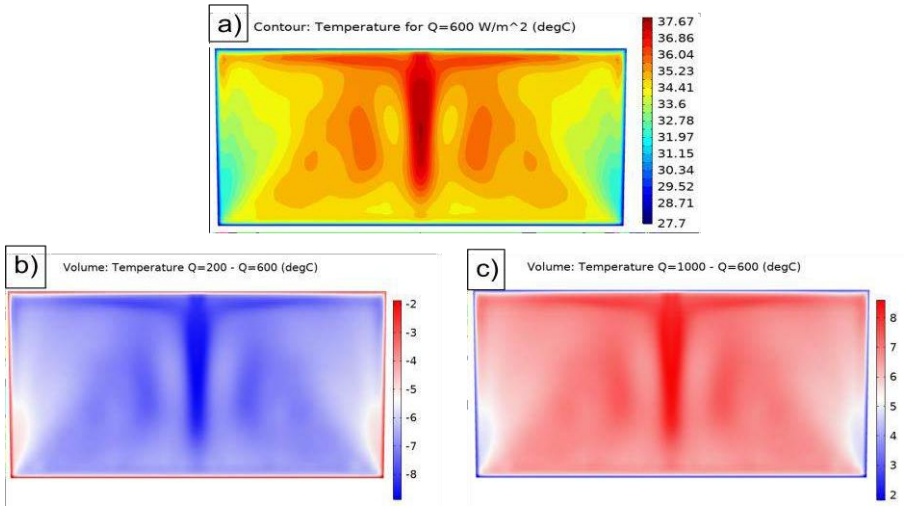

Figure 7-12: Wind flow from bottom to top. a) Temperature contours for the reference panel. b) Temperature difference between Q = 200W/m² and Q = 600W/m². c) Temperature difference between Q = 1000W/m2 and Q = 600W/m2.

increase of α, we return back to oblique winds (α=45° and α=135°) which are characterised by a higher temperature than the reference case of α=0°. Lastly, the scenario when the wind makes first contact with the back-side of the module showed a higher temperature than the oblique winds even though more panel area is in contact with the inlet wind. This is attributed to the unfavorable inclination and the aluminum frame both of which make the flow separation more severe. The previous explanation also applies to the other two tilt angles tested. One note to make is that the flat panel is the least sensitive to deviations in α. It still conforms to the bell shape but to a lesser extent as θ=10° or 20°.

To sum, the convection by wind is at its maximum when the wind is falling perpendicularly on the panel. Moreover, this section demonstrates that wind direction has a considerable impact of the operating temperature of FPVs. The fact that manipulating wind direction alone had a more significant impact on FPV temperature compared to water temperature, is already an indication that the third theory which supports cooling of FPVs due to convection is definite contender to justify better FPV performance. However, even more analysis is still needed which follows next.

Table 7-5: Average panel temperature for different amounts of irradiance. Bold indicates reference FPV settings.

Irradiance G (W/m2)	200	400	600	800	1000
Panel Temperature (°C)	28	31.3	34.71	38	41.3

7.5.8 Solar Irradiance Impact

The amount of radiation absorbed by the module largely dictates its temperature. The irradiance intensity is by far one of the most impactful parameters. As a reminder, the user inputs the solar irradiance (G) and not the heat source (Q). The heat source is what is left from the irradiance after factoring in the efficiency and the absorption coefficients for the different layers. Table 6 documents the consequences of the simulations.

As expected, by increasing heat flux, the operational temperature of PV panel increases. It is observed that the module temperature is linearly proportional to

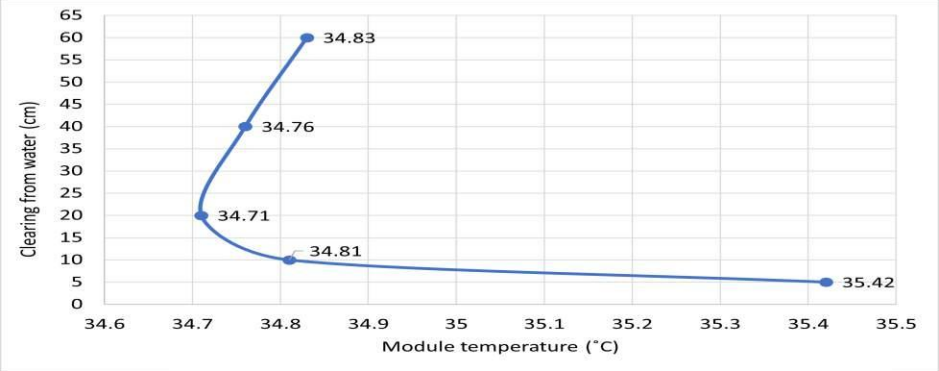

Figure 7-13: FPV temperature vs clearing distance.

irradiance like in [195]. The change in FPV temperature is around 1.6°C for every 100 W/m2 change in irradiance. The temperature patterns and distributions for the reference irradiance case are shown in Figure 7-12 (a).

The temperature distribution throughout the surface of the module reaches its highest in the middle and its lowest near the edge, a similar pattern as the results by Zhou et al. [187]. With a specific notice that the downwind zone is slightly hotter due to heat entrapment in the boundary layer. To see where exactly on the module will a change in irradiance change the temperature, Figure 7-12 (b&c) show the cases for cooling and heating. In the cooling case, the irradiance is dropped from the default 600 W/m2 to 200 W/m2. The area that experienced the largest cooling was down the center. A similar observation is noted for the heating case when the irradiance increased from the default to 1000 W/m2. Majority of the acquired heat was concentrated down the middle. This is because the underlying heat transfer method remains the same. In other words, both convection and conduction are still present and contributing. However, their

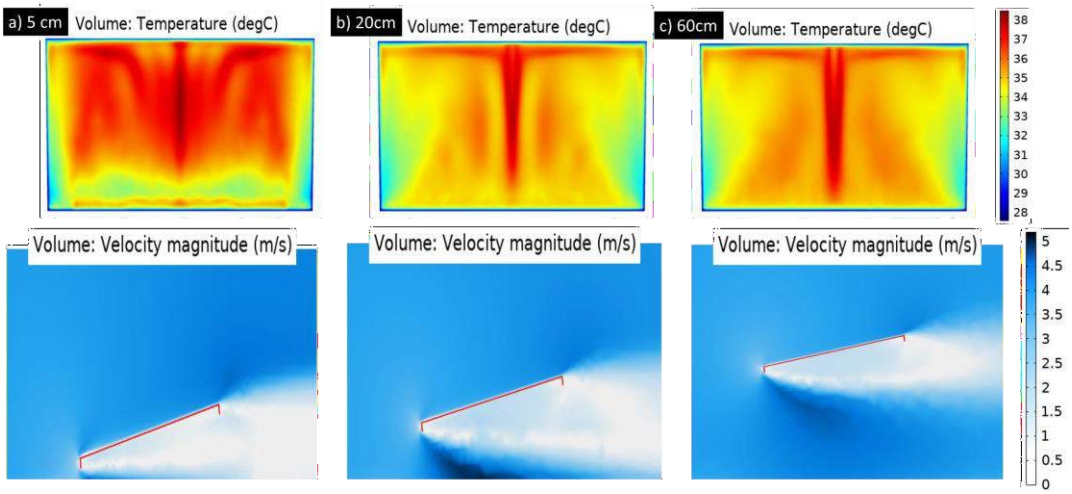

Figure 7-14: Temperature distributions and wind flow for three different clearings (height from the water level is changed)

contributions are low during low irradiance, as the module's temperature approaches ambient. The opposite is true where high solar irradiance helps dissipate heat out of the module because of the larger temperature difference between PV and ambient. However, the increased solar irradiation results in a larger input energy than the heat transported out, resulting in a higher panel temperature [187].

7.5.9 Water Proximity Impact

By now it is an established fact that near the water surface, the air becomes cooler since it picks up water vapor and gains some of the water's characteristics. This was especially evident in the vapor blanket where the air characteristic dramatically change to become similar to that of the water's. Thus one would logically assume that installing the FPV module closer to the water shall yield a benefit in cooling. Simply, since the module is now closer to a cold surface, the operating temperature should decrease as well. This section investigates how FPVs are affected by the clearing distance left between the bottom edge of the aluminum frame and the water surface. The simulation results are presented in Figure 7-13.

Quite the opposite to expectations, the closer the module was placed to the water, the warmer it became. This is by far the most debatable result obtained across all parametric sweeps. Vega Orrego [196] , Desai et al. [197], Rodrigues et al. [198] and Hayibo et al. [199] all state better cooling and performance the closer the modules' are placed to water, as then the modules' take better advantage of water cooling. Despite all this evidence supporting better cooling with closer water proximity, the opposite effect found in this paper is perfectly explainable.

Velocity magnitude changes with elevation in the sense that the closer the module is to the water, the lower the wind velocity striking the module. The further away the system is from the water, the higher the exposure of the panel to the open air and hence, the lower the temperature. This all goes back to how wind interacts with walls. In this case, the wall (water), is reducing wind speed due to friction. The reduction in velocity is outweighed by any other benefit that the FPV enjoys, for example, a cooler surrounding environment coming from the vapor blanket. The temperature and wind velocity plots that show such an effect for the FPV at three elevation scenarios are shown in Figure 7-14. Another observation noted in both Figure 7-13 and Figure 7-14 is that the FPV temperature increased slightly with an increment of the clearing distance above

the default of 20 cm. This can no longer be attributed to a change in wind velocity since at such a large clearing, the wall (water) has no influence on velocity. The larger clearing allows the air coming out of the blanket more distance for recovery. During this recovery distance, the air will start to revert back to its ambient character. Slowly gaining temperature till equalisation with ambient air. By the time the air reaches the module, the surrounding environment is no longer cooler than ambient. This is the more than likely explanation why placing the module further than 20 cm away results in a slightly higher operating temperature.

To sum, there exists a specific distance away from the water where the FPV will benefit from both the fully developed wind flow and the temperature difference from the blanket that creates a cooler environment. This is an optimization problem by nature that is out of the scope of the paper but from the results, it seemed that the default of 20 cm was most optimal to benefit from both water and wind. In any case, close FPV proximity to water is ill-advised in practise, the high RH and chloride accelerate PID and corrosion [151].

The results are another piece of strong evidence that FPV cooling is through wind. FPVs are highly dependent on good air ventilation. The experimental work of Liu et al. [145] indicated due to efficient air circulation, the free-standing kind offers great cooling efficacy. Cooling was reduced in the other variants, which had modules located close to water. When module is very close to water, wind has smaller role and water has larger role. Since a warming of the module was noted, it would highly encourage the theory of convective FPV cooling, and that water serves minor influence.

7.5.10 Evaporation Rate Impact

One of the parameter input of the simulations was the evaporation rate constant

K. It is an indication of how much water is being evaporated per unit time. From the outcomes of the paper so far, water has been lacklustre in cooling the FPV module. It could be possible that evaporating more water in a shorter time span will make the blanket thicker leading to more heat extraction. However, due to the stationary nature of the performed simulations, seeing the effect of evaporating water on the air as time passes is not possible. Such a result would require a time-dependent simulation which is computationally too prohibitive. Regardless, a simulation set spanning a range of K values was performed in a time-independent manner.

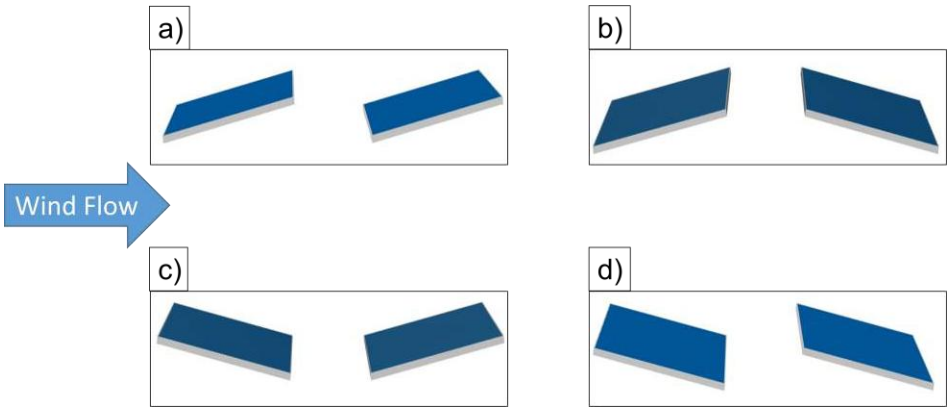

Figure 7-16: The four studied power plant configurations. a) Both modules facing wind inlet.

The simulations showed no effect on FPV temperature. This is because the simulations are in steady-state, where the end solution is displayed which is not affected by the evaporation rate. This corresponds to assuming that vapor is in equilibrium with the liquid. Hence, K has no effect on end temperature or RH indices. In practice, it is expected that the quicker the rate of evaporation, the greater the cooling [184]. But even then, this is only applicable inside the vapor blanket, the remaining air domain remains indifferent and experiences little to no cooling.

7.5.11 Water Depth

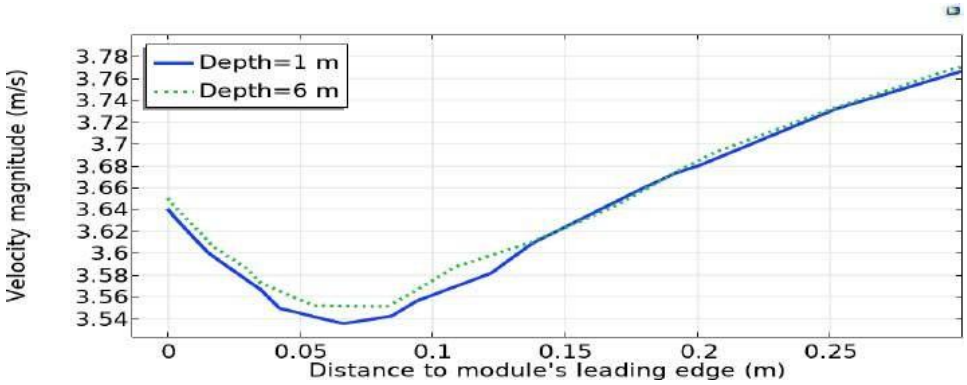

Figure 7-15: Approaching wind velocity for 1 m and 6 m deep waters. Movement to the left on x-axis means approaching module.

The water depth employed so far was 1 m. This value is not the most reflective of the water depth of real-life FPV installations which might be deployed in deeper waters. A positive correlation was obtained between deeper water and cooler modules. However, the significance is in the range of just 0.04°C between 1 m and 6 m deep water. It is not known with certainty why shallow water would

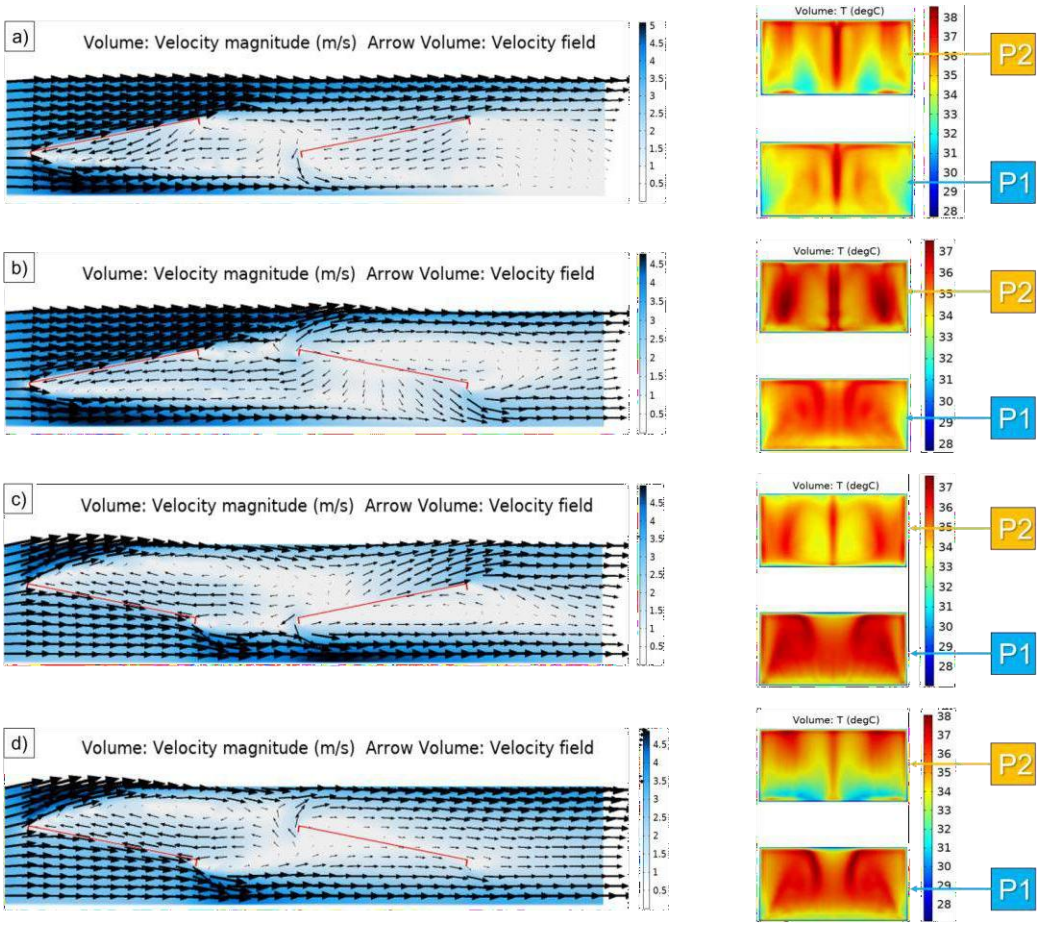

Figure 7-17: Wind and temperature profiles for all configurations. Modules and frame are colored red for clarity. In the velocity temperature plots, P1 is on the left.

lower FPV temperature. Nothing was found in the literature that presents the same correlation. One possible explanation is the following. Water depth is found to have almost a one-to-one correlation with distance from the shore. In other words, the further offshore, the more likely that the water is deeper. It is also known that further offshore, wind speed is larger due to having fewer obstacles and enjoying a longer fetch. Deeper water can be associated with more open space to build up wind speed or less surface roughness to restrict wind speed. In either case this leads to an increase in wind speed near the module as shown in Figure 7-15. Whereas the deeper water scenario sees a slightly faster wind speed close to the module's leading edge. This would explain the lower operating temperature. Further experimentation is needed to confirm the positive minor correlation between water depth and FPV performance.

7.5.12 Power Plant Characteristics

Just like their GPV counterparts, FPVs are built on large scales as power plants supplying MW s of power. Hence, from both an engineering and economic standpoint, one desire to know which power plant configuration will lead to the lowest average PV temperatures and hence the best power output and return on investment. There are four possible combinations encountered in practice, they are shown in Figure 7-16. The simulations will still maintain the default parameter values listed in Table 3. The distance between the two panels is set to a fixed value of 60 cm. For simplicity, the panel closest to the inlet is given the name 'P1', and the other is named 'P2'. Furthermore, the configurations will be given a letter instead of a description similar to as displayed in Figure 7-16. The temperature outcomes of simulating the four installations are shown in Figure 7-18. The PV panel's average temperature was calculated by summing up all the PV surface temperature nodes and dividing by the number of nodes. It can be seen that configuration 'A' shows a similar average temperature for both panels. In configuration 'B', both panels experience fair heating. While in installations 'C' and 'D', only 'P1' sees remarkable heating while an opposite effect is observed for 'P2' which cools down marginally. The results are best explained through observations of the wind and temperature profiles illustrated in Figure 7-17.

For configuration A, P1 sees the incoming developed wind and hence cools down as expected. Conversely, P2 sees slightly weaker wind flow due to the blockage of P1, hence heating P2 up slightly. For configuration B, one would assume that P1 would have the same temperature as P1 in configuration A since they both experience the same wind and orientation. Instead, P1 heats up to 34.95℃, this is explained by the lack of wind on the back side of P1. In configuration A, the

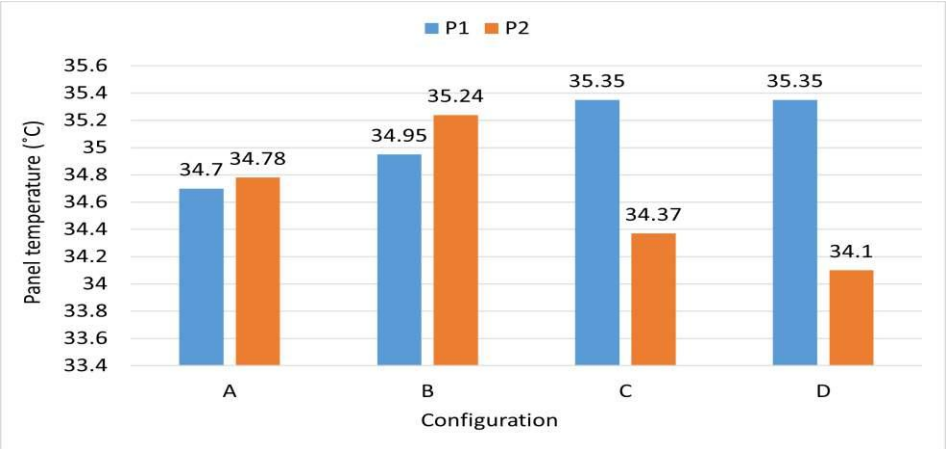

Figure 7-18: Average PV temperature per panel for the four power plant installation types.

recirculating wind successfully flows to the back side of P1 while in configuration B, the wind is unable to flow back towards P1 because of the orientation of P2. Admittedly, P2 acts as a wall that prevents P1 from cooling down further. It is worth to note that an increase in the spacing between the panels will likely fix such an issue. Unfortunately, simulations varying the spacing could not be performed due to time constraints. Further, the larger the spacing, the more costly the power plant commissioning will be. More than likely, the advantage of operating the modules at slightly lower temperatures will not compensate for the additional financing needed for the added water area. P2 in configuration B sees large heating because of its inclination and orientation both opposing the wind inlet. Hence experiencing poor wind flow. P1 in both configurations C and D had the largest recorded temperature. The explanation for both is the same, the orientation of P1 doesn't allow its front side to get any cooling whatsoever. The flow detaches at the leading edge but it does not circulate back to P1. Yet it continues onward toward P2. Couple with that the strong wind coming from the ground level because of streamlined convergence. Both of the previous observations allow P2 to be cooled significantly. The streamline convergence is more apparent in configuration D than C, this is why P2 shows a lower temperature at the bottom portion for installation D.

One key point that has to be made here is the following. Those supporting FPV cooling through water or ambient temperature would have a valid argument if and only if both panels in any configuration showed similar temperature readings. For the reason that both water and ambient temperature are not spatially variant in the simulation environment while the air is. Unquestionably their effects would be felt by all panels in all configurations in generally speaking equal magnitude. The difference in temperatures between P1 and P2 across all installations signifies undoubtedly the importance of wind in the thermal operation of FPV plants.

7.5.13 Summary of the finite element modelling results

This section will nail down why exactly are FPVs reported to be cooler than GPVs. The simulation sets performed earlier can be split into two categories; one is water-related parameters, and the other is ambient or wind-related parameters. For the earlier, the simulations included studying RH, water temperature, evaporation rate, diffusion coefficient, and water depth. The latter group included studying ambient temperature, wind speed, tilt angle, wind direction, solar irradiance, turbulence intensity, and power plant behavior. The water-related parameters exhibited minimal to insignificant variations in

response to the FPV temperature. In contrast, the ambient or wind-related parameters displayed minor to noteworthy influences on the FPV temperature. Based on the aforementioned observations, it can be inferred that water has a limited to negligible contribution to the performance of FPV modules.

The visual aspect may be the primary reason why individuals commonly associate water with the cooling of FPV panels. On an eye-to-eye basis between a low-efficiency GPV and a higher-efficiency FPV, people are quick to point out the key difference: the existence of water. Hence they associate high efficiency with water. However, this study presents a different finding. It establishes that whenever the FPV outperforms the GPV, the improved performance can be attributed to one of the following factors: either a decrease in ambient temperature (referred to as Theory 2) or an increase in wind speed (referred to as Theory 3) as stated in this paper.

Table 7-6: Sensitivity analysis of ambient temperature and wind speed variations on FPV module temperature.

Ta (°C)	Wind Speed (m/s)	Tmod (°C)	ΔT (°C)	Efficiency Gain (%)
25	4	34.71	0	0
24	4	33.85	-0.86	0.39
25	5	33.7	-1.01	0.45
23	4	32.99	-1.72	0.77
25	6	32.69	-2.02	0.91

Since both theories 2 and 3 hold the most truth when it comes to claiming FPV cooling, a demand to know the sole reason for cooling exists. To isolate which is more dominant, a sensitivity analysis was performed and compared to the reference FPV system. This will help see the deviation in module temperature against a 1-2 m/s wind speed difference or against a 1-2°C ambient temperature difference. The temperature difference is then converted to expected efficiency gain from the use of the heat coefficient value of 0.0045 %/°C. The outcomes of the sensitivity study are presented in Table 7. It turns out that a 1 or even a 2 unit change in ambient temperature is less impactful to the module compared

to wind speed. In other words, for a step size of 1 or 2 units, wind dominates ambient temperature when it comes to affecting FPV temperature. Therefore, it is evident that wind speed bears greater significance in cooling the FPV module. Furthermore, if ambient temperature conditions were solely responsible for FPV cooling, it would be expected that the literature would consistently report poorer FPV performance during winter seasons. However, such observations are rarely encountered, indicating that ambient temperature is less likely to be the primary factor in FPV cooling. Considering the evidence presented thus far, this paper concludes that the improved cooling of FPVs can be attributed to the enhancement in wind speed.

As for the extremely high gains reported in the literature, the only possible explanation is a lack of understanding and over-advertising. The same flaws that encircle any new technology. Moreover, experimentation, where FPV is compared to another case, has to abide by a key rule; otherwise, you risk location bias. As a recommendation for future experiments, the FPV and the comparison case must be located as close to each other as possible. The further the distance, the more exogenous parameters take effect, which hinders the findings of an irrefutable conclusion. The simulated energy increase in output using FPV technologies is less than the literature's predicted values, which are equal to or greater than 10%. A more realistic, conservative and recently-supported-in-literature value is around 0.5-3% depending on the FPV environment's parameters.

7.5.14 Modelling summary

Along with the land savings of FPVs, came a belief that FPV modules have superior thermal performance than GPVs. The cooling claim was ill-understood and quantified. This paper was written to understand the thermal dynamics of FPVs. This cooling can be attributed to one of four theories. Evaporative cooling, ambient temperature, wind speed, and heat transfer by conduction. To decide upon the true reason behind FPV cooling, a simulation model was created. A number of parametric sweep simulations were performed to measure the impact of each parameter on the thermal workings of FPVs. The simulations' most important outcomes can be stated as follows: Decreasing the RH of the ambient air increases the efficiency of the evaporative cooling process. But the improvement is minor in the range of 0.01℃. Debunking the theory that FPVs can be cooled through water evaporation. Ambient temperature heavily affects FPV temperature. The relation is linear with a difference of 0.85℃ per degree change in ambient temperature.

Wind velocity contributes to cooling the FPV module. However, the sensitivity of module temperature to wind speed is large at low speeds and decreases with increments in wind velocities. Presenting a non-linear relationship.

A correlation between water and FPV temperatures was found. Despite this, the quantity of the correlation is small. The module's temperature changes by 0.125℃ for every degree change in water temperature. The tilt angle did not make a major difference in a single-array simulation. No large disadvantage of laying the panel flat or at a high tilt was found. The recommendation to keep FPVs at low tilt angles will not hinder FPV performance. FPVs are sensitive to wind direction. Parallel winds show the largest cooling. Oblique wind and backward wind result in slight warming. The hottest module was obtained when the wind was 90◦ incident on the system.

Laying the FPV system closer to the water was found detrimental to performance. This is attributed to worse incoming wind flow. The wind near the water experiences more friction which slows it down. Placing FPVs away from the water allows for better ventilation. Expanding the model to simulate power plant behavior for different configurations showed varying panel temperatures for all configurations. This stipulates the heavy dependency of FPV operational temperature on wind flow and the smaller dependency on water or ambient temperature. The fourth theory of cooling through conduction is disproven based on three factors: the small temperature difference, a limited contact area between the PV module and floating structure, and extremely low thermal conductivity values. These factors restrict heat transfer through conduction, resulting in a mere 0.5℃ temperature difference in FPVs. Out of the two most probable explanations for FPV cooling, the sensitivity analysis showed higher reliance on wind speed than ambient temperature.

Ultimately, all evidence presented in the paper points towards the cooling of FPVs through higher wind speed on open water bodies. Generally, the findings show once more that one should be wary of generalizations. Further, while it is possible that FPVs have higher proficiencies, the expectations should be more conservative at a maximal 3% gain. Despite that, the outlook for FPV is positive and is set to break free of its niche status. For future work, the development of a model that accounts for different designs, power plant sizes, and energy calculations is needed. Further, more experimental work is encouraged to concur with the results obtained in this paper and the literature. A recommendation for future study is to experiment with FPV and GPV in the exact location to eliminate uncontrollable variables.

7.6 Chapter Summary

Floating photovoltaic (FPV) systems have often been promoted with the assumption that their positioning over water inherently confers a thermal advantage. This claim, while intuitively appealing and frequently cited, has not been consistently backed by mechanistic understanding. In this chapter, the question is approached not as a matter of belief or trend, but as a problem of fluid and thermal interaction. The aim was to separate what is observable from what is explainable.

Using the modelling framework developed earlier in this thesis, a series of controlled simulations are conducted to probe the thermal dynamics of FPV installations. Variables such as wind velocity, direction, panel height, water temperature, and ambient humidity are systematically varied. The intention is not to produce a universal performance estimate, but to examine how each parameter contributes to, or limits, thermal regulation at the module surface.

The simulations make clear that the presence of water does not, in itself, deliver substantial cooling. While evaporative effects are detected, their influence is highly localized confined to a shallow layer immediately above the water surface, rarely reaching the active PV area in a meaningful way. By contrast, convective cooling driven by wind exposure consistently plays a dominant role. This holds true across different module geometries and environmental conditions. Where airflow is unobstructed and surface exchange is strong, lower module temperatures follow whether the system is floating or not.

This finding carries implications beyond the immediate case of FPV. It highlights, once again, the centrality of airflow in determining the thermal behaviour of PV modules. In this study, FPV acts less as a special category and more as a test and demonstration case a configuration that reveals, through its variation, the broader air flow and thermal principles at work. Wind direction, clearance, and array spacing matter more than the medium beneath the structure.

Importantly, this chapter did not seek to generalize FPV outcomes across all contexts. Instead, it provides a way to evaluate competing claims through reproducible, physics-based analysis. The methodology grounded in validated CFD and thermal coupling offers not just estimates, but insight into causal mechanisms. It allows for testing "what if" questions under boundary conditions that are difficult to control in the field.

In doing so, this final study rounds off a larger argument developed throughout the thesis: that temperature behaviour in PV systems is neither uniform nor incidental. It is shaped by the interaction between environmental forces and structural design and those interactions can, and must, be resolved with precision. As the industry continues to diversify its deployment configurations, including over water, the tools to evaluate thermal performance must be equally adaptive. FPV, when stripped of its generalizations, becomes one more demonstrative example of why PV systems should be modelled not as thermally passive entities, but as surfaces embedded within moving air.

8 Conclusion

8.1 Summary of PhD contributions

This thesis began with some of the foundational assumptions in PV modelling that have long been accepted without sufficient scrutiny. It was important to verify and challenge these widely used assumptions particularly regarding how temperature is treated in PV system modelling. While irradiance is well accounted for with high precision, thermal behaviour though known to impact efficiency is typically simplified, and its influence in real-world operation is often underestimated. These simplifications may be acceptable in limited contexts, but for systems operating in demanding environments or at a large scale, they risk introducing persistent bias in performance estimation.

Through a series of steps, this work sought to unpack what actually happens to PV module temperatures under several such conditions. Chapter 2 focused on how different cell technologies respond to heat, and how even small differences in thermal assumptions can shift the ranking of one technology over another. One interesting implication is that the generally high tolerance for modelling error in thermal estimation will actually lead PV plant developers to select sub-optimal technologies. A secondary insight was that we may not always need the most expensive low-temperature-coefficient cell technologies in every context. Instead, a Pareto-type analysis could be performed to determine the most suitable technology for a given climate, provided we have high confidence in the thermal modelling itself. That premise guided the deeper investigations in the chapters that followed.

The next step was to examine the models themselves. Chapter 3 addressed this in depth, and is partly published (*Chowdhury, G., Goverde, H., Manganiello, P., Voroshazi, E., Poortmans, J., & Catthoor, F. (2019). Sensitivity analysis of the effect of forced convection on photovoltaic module temperature and energy yield. 2019 IEEE 46th Photovoltaic Specialists Conference (PVSC), 1237–1241. https://doi.org/10.1109/PVSC40753.2019.8980517*), (*Shirazi, E., Lemmens, J., Gofran Chowdhury, M., Tuomiranta, A., Catthoor, F., Voroshazi, E., & Gordon, I. (2021). Cloud Detection for PV Power Forecast based on Colour Components of Sky Images. 2021 IEEE 48th Photovoltaic Specialists Conference (PVSC), 2389–2391. https://doi.org/10.1109/PVSC43889.2021.9518667*), (*Chowdhury, G., Kladas, A., Herteleer, B., Cappelle, J., & Catthoor, F., "Performance Analysis of Highly Cited Silicon Photovoltaic Module Temperature Estimation Methods: A Critical Review," SSRN: https://ssrn.com/abstract=4212108 " (Currently in review in Solar RRL*)).: In chapter 3 the purpose was to test all the highly used PV temperature models, their assumptions, performance, and where they tend to break down. It became clear early on that many of the most highly cited models behave unpredictably once time resolution is increased or when applied under conditions with heavily fluctuating irradiance. One major takeaway was that outdoor experimental validations in literature are typically conducted under clear-sky, summer-like, dry conditions often chosen for ease of testing. Rarely are these models validated under rapidly changing conditions. Our recommendation is that future model validation must consider different climatic settings and stress conditions, including unstable irradiance profiles and humid or mixed climates. To explore this further, we conducted an extensive comparison of both steady-state and transient temperature models using long-term outdoor datasets and high-frequency field measurements. The results were mixed. Some models performed well on average but failed on specific days; others were more sensitive to wind and irradiance variability than expected. This points to a broader conclusion: temperature modelling accuracy is not solely about model formulation, but about how well the model reflects physical processes under variable conditions. Going forward, a mixed approach may be needed adapting models dynamically rather than relying on a single set of assumptions.

This led to the second major part of the thesis in chapter 4,5, and 6. Chapter 3 closes by introducing the direction for Chapter 4. Having demonstrated the limitations of existing approaches, the next step is not to tinker with coefficients, but to explore a modelling method that resolves the physics directly.

Computational Fluid Dynamics (CFD), although computationally demanding, offers a way to examine how wind actually interacts with a module surface, how flow detaches at the frame, how cooling varies across cells, and how temperature fields emerge over time. Chapter 4 takes up that task.

While real-life outdoor testing remains the benchmark, jumping directly to it is not always feasible due to physical constraints. Even a standard commercial PV module measures roughly 2 meters by 1 meter, and it's extremely rare to find wind tunnels capable of accommodating modules at that scale. The logical next step was to consider reduced-scale testing. For irradiance, downscaling is manageable due to proportionality. But thermal behaviour doesn't scale the same way, especially where convection and material properties are concerned. We therefore adopted a pragmatic approach: custom mini-PV modules were built and tested in wind tunnel conditions. The resulting data was used to validate CFD models, which were then scaled up in simulation to assess full-size modules under realistic conditions.

This work forms the basis for the simulations presented in Chapters 5 and 7 where thermal models are coupled with CFD models to see PV's thermal interaction in several use cases. While the modules used here are not thermally identical to full-scale systems, the CFD framework, once validated can be reliably extended to larger geometries. The goal is not replication at scale but extrapolate from experimentally observed flow mechanisms to spatially resolved temperature fields in full scale PV modules. In this way, this chapter establishes a validated link between physical structure and convective behaviour, which will underpin the subsequent analysis of thermal differences, investigated and used in Chapter 5,6, and 7.

The CFD work focused on convective cooling, particularly wind-driven effects and the spatial variability of temperature across PV module surfaces. These models, validated against both wind tunnel and outdoor data, confirmed that temperature is often unevenly distributed. Details such as frame design, air gap, and tilt angle significantly affect the local thermal profile. These variations, though often dismissed as minor, can impact degradation patterns, inverter loading, and yield prediction especially during high production hours. This part of the work is already published in *Gofran Chowdhury, Dirk Goossens, Hans Goverde, Francky Catthoor, Experimentally validated CFD simulations predicting wind effects on photovoltaic modules mounted on inclined surfaces, Sustainable Energy Technologies and Assessments, Volume 30, 2018, Pages 201-208, ISSN 2213-1388, https://doi.org/10.1016/j.seta.2018.10.005.*

One of the central finding from this thesis is that module temperature is not uniform, neither across individual modules nor across larger systems. While this has been acknowledged anecdotally, it is rarely quantified or validated in field studies. This part of the work has been published in conference and under review in peer reviewed journal publication (*Chowdhury, G., Somma, L., Goossens, D., Goverde, H., Horvath, I., Voroshazi, E., Poortmans, J., Catthoor, F. (2018). Novel computational fluid dynamics modelling of spatial convective heat transfer over PV-modules mounted on an inclined surface with an underlying air gap. 35th European Photovoltaic Solar Energy Conference and Exhibition - EUPVSEC, 1182–1185. https://doi.org/10.4229/35thEUPVSEC20182018-5CV.1.15*), and (*Chowdhury Gofran, Du Boullay Gauthier, & Poortmans Jef., "Investigating the temperature distribution of a PV module under various environmental factors and exploring novel module geometries for the reduction of thermal losses". " (Currently in review in Solar RRL*))" .

Chapter 6 directly addressed this by collecting long-term sensor-based temperature data from two distinct test sites. The results showed that intra-module temperature differences can reach 10–15°C under certain conditions, particularly in high irradiance with low or directional wind. These differences are not just thermal anomalies; they influence system-level performance and durability. To respond to this, the thesis introduced a calibratable over temperature model that explicitly incorporates wind direction into temperature estimation. While wind speed is often included in modelling frameworks, direction has rarely been handled in a calibrated or structured way. The proposed model uses directional correction factors that can be applied from empirical datasets or calibrated using short-term high-resolution measurements. Remarkably, the model trained at one site performed accurately when applied to another location 137 km away, provided wind regimes were similar. This supports its potential for broader regional or utility-scale implementation, offering a low-barrier method to improve the accuracy of PV yield simulations. This part of the work has been selected by EUPVSEC as one of the top article for peer reviewed publication (*Chowdhury, G., Kladas, A., Herteleer, B., Cappelle, J., & Catthoor, F., "A calibratable PV temperature model that integrates Wind Direction in a realistic way: Insights from Long-Term Outdoor Measurements" (Currently in review in Progress in Photovoltaic Journal*)), (*Herteleer, B., Kladas, A., Chowdhury, G., Catthoor, F., & Cappelle, J. (2023). Investigating methods to improve photovoltaic thermal models at second-to-minute timescales. Solar Energy, 263, 111889.*

https://doi.org/10.1016/j.solener.2023.111889), and (*Manganiello, P., Govaerts, J., Horvath, I. T., Chowdhury, M. G., Yordanov, G. H., Goverde, H., Aldalali, B., Beausoleil-Morrison, I., Valkealahti, S., Lappalainen, K., & Poortmans, J. (2020). Tuning electricity generation throughout the year with PV module technology. Renewable Energy, 160, 418–427. https://doi.org/10.1016/j.renene.2020.06.106*). This modelling insight ties back to the CFD results: both lines of investigation reinforce that forced convection and particularly wind direction is the dominant mechanism driving thermal variability. The evidence suggests that wind should not be treated merely as a scalar quantity; its directional component has meaningful impact on module-level performance.

Floating PV was explored in chapter 7, both for its emerging relevance and as a case to test thermal modelling under different boundary conditions. Here too, the results showed that proximity to water does not inherently guarantee lower operating temperatures. Rather, wind exposure speed and direction again emerged as the critical factor. This reinforces the thesis's central argument: that thermal behaviour in PV systems is driven by site-specific airflow and must be modelled accordingly. Major part of this work has been selected as one of the top paper in WCPEC-8 conference for peer reviewed publication (*Chowdhury Gofran, Haggag Mohamed, & Poortmans Jef. (2023). How cool is floating PV? A state-of-the-art review of floating PV's potential gain and computational fluid dynamics modelling to find its root cause. EPJ Photovolt., 14, 24. https://doi.org/10.1051/epjpv/2023015*). Moreover this work in broader collaboration with Kuwait University also resulted in patent application. The patent has been already approved in EU and USA both, *Bourisli, R., Aldalali, B. S. H. M., Tuomiranta, A., Chowdhury, G., & Poortmans, J. (2025). System comprising photovoltaic modules with multiple vanes and corresponding arranging method. (US2025023503A1, EP4199120A1).*

This work does not claim to offer a universal solution. Instead, it illustrates where current assumptions in PV thermal modelling fall short and demonstrates practical ways to reduce error. Better thermal modelling enables more accurate yield predictions. While not every system requires high-resolution modelling, the increasing scale and density of PV deployments make these refinements more relevant than ever.

Looking ahead, several areas offer scope for continuation: integrating spatial temperature profiles into standard yield prediction tools. More than anything, this work makes the case that temperature is not a background parameter in PV

performance it is part of the active system. No single modelling approach will be optimal for every scenario. Taking a pragmatic, context-driven view is key.

8.2 Future Work

The work presented in this thesis focused on improving the understanding and representation of PV module temperature under varying environmental and installation conditions. While several new insights and modelling approaches were introduced, the scope of the study was necessarily constrained. A number of directions emerge from this research that can be pursued in future work. These can be grouped into three general thematic directions. First is the CFD based modelling framework, second is the how to make PV thermal model adapted to operational efficiency and location specific condition, lastly going beyond the scope of the thesis on how learning from this can be extrapolated into topics like degradation and climate specific cell technology R&D.

8.2.1 Theme 1: CFD Based Modelling Framework

Practical Use of CFD in System Design And Monitoring

While CFD was used in this work to explore detailed convective effects, its computational requirements limit its use in everyday system design or monitoring. One possible direction is to extract simplified relationships from validated CFD runs that can be used to adjust standard temperature models for certain array configurations or wind exposure categories. These could take the form of empirical modifiers or correction factors tied to module geometry or mounting height. Another path is to use CFD selectively for sites where wind exposure is known to vary significantly due to terrain, built environment, or nearby obstructions.

Knowledge Library Creation for Typical Geometries

The CFD work in this thesis showed that mounting details such as tilt angle, air gap, and frame design significantly influence the thermal profile of modules. However, only a limited number of configurations were studied. A future direction is to build a systematic database of CFD-derived thermal responses for a wide range of mounting parameters. This could inform both simulation tools and early-stage design decisions. Such a library would allow users to quickly assess whether their chosen mounting strategy is likely to introduce thermal hotspots or impede cooling.

8.2.2 Theme 2: Adapting PV Thermal Models for Operational Efficiency

PV Thermal Models Tested Under More Typical Transient Weather Conditions

Most PV temperature models have been tested under stable sky conditions, particularly clear days with gradual irradiance variation. However, semi-cloudy days with frequent transitions tend to produce the highest model errors, as demonstrated in Chapter 3. There is a need to systematically test both steady-state and transient models under such mixed conditions. This would require a curated dataset of high-frequency outdoor measurements from multiple sites, each annotated by sky condition. The goal would be to understand not only average performance, but also under what specific scenarios each model fails.

Integration of PV Spatial Temperature Models Into Yield Estimation and Forecasting

One of the recurring findings in this study is the presence of spatial temperature differences within individual modules. These differences, although modest in absolute terms, can affect degradation patterns, inverter sizing, PV energy forecasting, and real-time control for grid flexibility. Current commercial yield prediction tools and forecasting models typically use a single temperature value per module. It would be valuable to explore how spatial temperature distributions can be approximated and integrated into these tools without significantly increasing computational cost. Simplified spatial weighting functions or lookup tables derived from CFD simulations might offer a practical path forward. Validation against plant-level data from systems with distributed thermal sensors would be needed to support this extension.

Library of General Wind Directions and its Effects Validated by Outdoor Measurements

In Chapter 6, a directional correction approach was developed to account for the effect of wind direction on PV module temperature. While the model performed well across two sites with broadly similar wind patterns, it remains an open question how transferable the method is to other locations and climates. Future studies should focus on generalising this model using long-term wind data from multiple regions. It would also be useful to test whether representative wind-directional coefficients can be established for specific climates or installation geometries, reducing the need for site-specific calibration.

8.2.3 Theme 3: Going beyond the thermal topic

PV degradation induced by thermal differences

While this thesis focused on temperature as it relates to short-term performance, there is a strong rationale to explore how the observed temperature differences influence long-term degradation. For example, consistent over temperature at the downwind edge of modules may accelerate localised stress or delamination. Future work could link field measurements of thermal differences to long-term monitoring of electrical performance, electroluminescence imaging, or hotspot formation. This would help establish whether the spatial variability in temperature plays a measurable role in performance decline or failure modes.

Detailed thermal characterisation of Floating PV under seasonal and climatic variation

Chapter 7 showed that floating PV does not always provide the cooling benefit often claimed in the literature. However, the analysis focused on a limited set of scenarios. Further work should explore FPV thermal behaviour under different seasonal cycles and climatic regimes. Of particular interest are regions with high humidity, low wind speeds, or where water temperatures remain close to ambient air. Additional CFD simulations or controlled outdoor measurements would help clarify when, and under what conditions, FPV offers a thermal advantage. The role of mounting height above water, as well as potential fouling or corrosion at low elevations, should also be assessed.

Supporting technology choice through climate specific PV modelling

The comparative study of cell technologies in Chapter 2 illustrated that minor variations in thermal assumptions can change the preferred technology for a given site. This suggests the potential value of a simulation framework that allows for climate-specific technology selection. Such a tool would require combining irradiance, temperature, and wind datasets with thermal and electrical models of different cell types. A larger study could explore how technology choice shifts when more accurate temperature models are used, especially in hot or low-wind locations where the performance gap is likely to widen.

Each of these directions builds on the foundation laid by this thesis, but addresses questions that go beyond its original scope. As PV continues to evolve into a mature and central part of the energy system, the importance of accurate

and context-aware modelling will only grow. The refinement of thermal models, particularly those that account for spatial variation and environmental interaction, remains an open and relevant field of study.

9 References

[1] IEA, “IEA (2024), Renewables 2024, IEA, Paris (https://www.iea.org/reports/renewables-2024, Licence: CC BY 4.0),” 2025.

[2] F. J. M. M. Nijsse *et al.*, “The momentum of the solar energy transition,” *Nat Commun*, vol. 14, no. 1, p. 6542, 2023, doi: 10.1038/s41467-023-41971-7.

[3] I. Kaaya, J. Ascencio-Vásquez, K.-A. Weiss, and M. Topič, “Assessment of uncertainties and variations in PV modules degradation rates and lifetime predictions using physical models,” *Solar Energy*, vol. 218, pp. 354–367, 2021, doi: https://doi.org/10.1016/j.solener.2021.01.071.

[4] D. L. King, W. E. Boyson, and J. A. Kratochvil, “Photovoltaic array performance model,” *Sandia Report No. 2004-3535*, vol. 8, no. December, pp. 1–19, 2004, doi: 10.2172/919131.

[5] D. Faiman, “Assessing the Outdoor Operating Temperature of Photovoltaic Modules,” *Progress in Photovoltaics: Research and Applications*, vol. 16, no. 4, pp. 307–315, Jun. 2008, doi: 10.1002/pip.813.

[6] “Front Matter,” in *Solar Engineering of Thermal Processes, Photovoltaics and Wind*, John Wiley & Sons, Ltd, 2020, pp. i–xxi. doi: https://doi.org/10.1002/9781119540328.fmatter.

[7] R. Ross, “Interface design considerations for terrestrial solar cell modules,” 1976, pp. 801–806.

[8] D. L. King, “Photovoltaic module and array performance characterization methods for all system operating conditions,” *AIP Conf Proc*, vol. 394, no. 1, pp. 347–368, Feb. 1997, doi: 10.1063/1.52852.

[9] G. M. Tina, C. Ventura, S. Ferlito, and S. De Vito, “A state-of-art-review on machine-learning based methods for PV,” *applied sciences*, vol. 11, no. 16, p. 7550, 2021.

[10] M. Massaoudi, I. Chihi, H. Abu-Rub, S. S. Refaat, and F. S. Oueslati, "Convergence of photovoltaic power forecasting and deep learning: State-of-art review," *Ieee Access*, vol. 9, pp. 136593–136615, 2021.

[11] J. F. Gaviria, G. Narváez, C. Guillen, L. F. Giraldo, and M. Bressan, "Machine learning in photovoltaic systems: A review," *Renew Energy*, vol. 196, pp. 298–318, 2022.

[12] J. Gaboitaolelwe, A. M. Zungeru, A. Yahya, C. K. Lebekwe, D. N. Vinod, and A. O. Salau, "Machine learning based solar photovoltaic power forecasting: A review and comparison," *IEEe Access*, vol. 11, pp. 40820–40845, 2023.

[13] B. Huang and J. Wang, "Applications of physics-informed neural networks in power systems-a review," *IEEE Transactions on Power Systems*, vol. 38, no. 1, pp. 572–588, 2022.

[14] S. Cuomo, V. S. Di Cola, F. Giampaolo, G. Rozza, M. Raissi, and F. Piccialli, "Scientific machine learning through physics–informed neural networks: Where we are and what's next," *J Sci Comput*, vol. 92, no. 3, p. 88, 2022.

[15] L. Deville, M. Theristis, B. H. King, T. L. Chambers, and J. S. Stein, "Comparison of Open-Source Photovoltaic Performance Models Against Multi-Year Field Data," in *2023 IEEE 50th Photovoltaic Specialists Conference (PVSC)*, IEEE, Jun. 2023, pp. 1–3. doi: 10.1109/PVSC48320.2023.10359971.

[16] L. Deville, M. Theristis, B. H. King, T. L. Chambers, and J. S. Stein, "Open-source photovoltaic model pipeline validation against well-characterized system data," *Progress in Photovoltaics: Research and Applications*, vol. 32, no. 5, pp. 291–303, May 2024, doi: 10.1002/pip.3763.

[17] M. Theristis *et al.*, "Blind photovoltaic modeling intercomparison: A multidimensional data analysis and lessons learned," *Progress in Photovoltaics: Research and Applications*, vol. 31, no. 11, pp. 1144–1157, Nov. 2023, doi: 10.1002/pip.3729.

[18] W. F. Holmgren, C. W. Hansen, and M. A. Mikofski, "pvlib python: a python package for modeling solar energy systems," *J Open Source Softw*, vol. 3, no. 29, p. 884, Sep. 2018, doi: 10.21105/joss.00884.

[19] K. S. Anderson, C. W. Hansen, W. F. Holmgren, A. R. Jensen, M. A. Mikofski, and A. Driesse, "pvlib python: 2023 project update," *J Open Source Softw*, vol. 8, no. 92, p. 5994, Dec. 2023, doi: 10.21105/joss.05994.

[20] A. R. Jensen *et al.*, "pvlib iotools—Open-source Python functions for seamless access to solar irradiance data," *Solar Energy*, vol. 266, p. 112092, Dec. 2023, doi: 10.1016/j.solener.2023.112092.

[21] M. Kivambe *et al.*, "Comprehensive assessment of performance and reliability of PERC, TOPCon and SHJ modules in desert climates," *Solar Energy*, vol. 295, p. 113555, Jul. 2025, doi: 10.1016/j.solener.2025.113555.

[22] I. T. Horváth *et al.*, "Photovoltaic energy yield modelling under desert and moderate climates: What-if exploration of different cell technologies," *Solar Energy*, vol. 173, pp. 728–739, 2018, doi: https://doi.org/10.1016/j.solener.2018.07.079.

[23] P. Manganiello *et al.*, "Tuning electricity generation throughout the year with PV module technology," *Renew Energy*, vol. 160, pp. 418–427, Nov. 2020, doi: 10.1016/j.renene.2020.06.106.

[24] D. Goossens, H. Goverde, and F. Catthoor, "Effect of wind on temperature patterns, electrical characteristics, and performance of building-integrated and building-applied inclined photovoltaic modules," *Solar Energy*, vol. 170, no. April, pp. 64–75, Aug. 2018, doi: 10.1016/j.solener.2018.05.043.

[25] H. Goverde, J. Govaerts, K. Baert, F. Catthoor, J. Driesen, and J. Poortmans, "Optical-thermal-electrical model for a single cell PV module in non-steady-state and non-uniform conditions build in SPICE," in *28th European Photovoltaic Solar Energy Conference and Exhibition - EUPVSEC*, 2013, pp. 3291–3295.

[26] H. Goverde *et al.*, "Spatial and temporal analysis of wind effects on PV modules: Consequences for electrical power evaluation," *Solar Energy*, vol. 147, pp. 292–299, May 2017, doi: 10.1016/j.solener.2016.12.002.

[27] H. Goverde *et al.*, "Spatial and temporal analysis of wind effects on PV module temperature and performance," *Sustainable Energy Technologies and Assessments*, vol. 11, pp. 36–41, Sep. 2015, doi: http://dx.doi.org/10.1016/j.seta.2015.05.003.

[28] H. Goverde *et al.*, "Model requirements for accurate shot term energy yield predictions during fast-varying weather conditions," *31st European Photovoltaic Solar Energy Conference and Exhibition - EUPVSEC*, pp. 1556–1559, 2015.

[29] P. Karava, C. Mohammad Jubayer, E. Savory, and S. Li, "Effect of incident flow conditions on convective heat transfer from the inclined windward roof of a low-rise building with application to photovoltaic-thermal systems," *Journal of Wind Engineering and Industrial Aerodynamics*, vol. 104–106, pp. 428–438, 2012, doi: http://dx.doi.org/10.1016/j.jweia.2012.03.026.

[30] P. Karava, C. M. Jubayer, and E. Savory, "Numerical modelling of forced convective heat transfer from the inclined windward roof of an isolated low-rise building with application to photovoltaic/thermal systems," *Appl Therm Eng*, vol. 31, no. 11–12, pp. 1950–1963, Aug. 2011, doi: http://dx.doi.org/10.1016/j.applthermaleng.2011.02.042.

[31] F. Toja-Silva, C. Peralta, O. Lopez-Garcia, J. Navarro, and I. Cruz, "Effect of roof-mounted solar panels on the wind energy exploitation on high-rise buildings," *Journal of Wind Engineering and Industrial Aerodynamics*, vol. 145, pp. 123–138, 2015, doi: http://dx.doi.org/10.1016/j.jweia.2015.06.010.

[32] W. P. Warsido, G. T. Bitsuamlak, J. Barata, and A. Gan Chowdhury, "Influence of spacing parameters on the wind loading of solar array," *J Fluids Struct*, vol. 48, pp. 295–315, 2014, doi: http://dx.doi.org/10.1016/j.jfluidstructs.2014.03.005.

[33] A. Radu, E. Axinte, and C. Theohari, "Steady wind pressures on solar collectors on flat-roofed buildings," *Journal of Wind Engineering and Industrial Aerodynamics*, vol. 23, pp. 249–258, 1986, doi: http://dx.doi.org/10.1016/0167-6105(86)90046-2.

[34] C. M. Jubayer, K. Siddiqui, and H. Hangan, "CFD analysis of convective heat transfer from ground mounted solar panels," *Solar Energy*, vol. 133, pp. 556–566, Aug. 2016, doi: http://dx.doi.org/10.1016/j.solener.2016.04.027.

[35] C. M. Jubayer and H. Hangan, "Numerical simulation of wind effects on a stand-alone ground mounted Photovoltaic (PV) system," *Journal of Wind Engineering and Industrial Aerodynamics*, vol. 134, pp. 1–37, Nov. 2015, doi: 10.1016/j.jweia.2014.08.008.

[36] A. Abiola-Ogedengbe, H. Hangan, and K. Siddiqui, "Experimental investigation of wind effects on a standalone photovoltaic (PV) module," *Renew Energy*, vol. 78, pp. 657–665, 2015, doi: http://dx.doi.org/10.1016/j.renene.2015.01.037.

[37] T. Stathopoulos, I. Zisis, and E. Xypnitou, "Local and overall wind pressure and force coefficients for solar panels," *Journal of Wind Engineering and Industrial Aerodynamics*, vol. 125, pp. 195–206, 2014, doi: http://dx.doi.org/10.1016/j.jweia.2013.12.007.

[38] P. A. Mirzaei and R. Zhang, "Validation of a Climatic CFD Model to Predict the Surface Temperature of Building Integrated Photovoltaics," *Energy Procedia*, vol. 78, pp. 1865–1870, 2015, doi: http://dx.doi.org/10.1016/j.egypro.2015.11.348.

[39] R. Zhang, P. A. Mirzaei, and J. Carmeliet, "Prediction of the surface temperature of building-integrated photovoltaics: Development of a high accuracy correlation using computational fluid dynamics," *Solar Energy*, vol. 147, pp. 151–163, 2017, doi: 10.1016/j.solener.2017.03.023.

[40] C. Misiopecki, A. Gustavsen, and B. Time, *Cooling of PV panels by natural convection*. SINTEF Academic Press, 2012.

[41] D. Goossens, H. Goverde, and F. Catthoor, "Effect of wind on temperature patterns, electrical characteristics, and performance of building-integrated and building-applied inclined photovoltaic modules," *Solar Energy*, vol. 170, no. April, pp. 64–75, 2018, doi: 10.1016/j.solener.2018.05.043.

[42] "Global Energy Review 2020," *Global Energy Review 2020*, 2020, doi: 10.1787/a60abbf2-en.

[43] P. Manganiello *et al.*, "Tuning electricity generation throughout the year with PV module technology," *Renew Energy*, 2020, doi: 10.1016/j.renene.2020.06.106.

[44] I. T. Horváth *et al.*, "Photovoltaic energy yield modelling under desert and moderate climates: What-if exploration of different cell technologies," *Solar Energy*, vol. 173, pp. 728–739, 2018, doi: https://doi.org/10.1016/j.solener.2018.07.079.

[45] A. Dimitrios *et al.*, "Demonstration and validation of an energy yield prediction model suitable for non-steady state non-uniform conditions," 2014.

[46] H. Goverde *et al.*, *Energy Yield Prediction Model for PV Modules Including Spatial and Temporal Effects*. WIP, 2014, pp. 3292–3296. doi: 10.4229/EUPVSEC20142014-5CV.2.28.

[47] J. Haschke *et al.*, "The impact of silicon solar cell architecture and cell interconnection on energy yield in hot & sunny climates," *Energy Environ Sci*, vol. 10, no. 5, pp. 1196–1206, 2017, doi: 10.1039/C7EE00286F.

[48] and E. M. H. Sakata, Y. Tsunomura, H. Inoue, S. Taira, T. Baba, H. Kanno, T. Kinoshita, M. Taguchi, "R&D PROGRESS OF NEXT-GENERATION VERY THIN HIT TM SOLAR CELLS," Valencia, Spain: 25th European Photovoltaic Solar Energy Conference and Exhibition, 2010, pp. 6–10. doi: 10.4229/25thEUPVSEC2010-2DP.2.4.

[49] D. D. Smith, G. Reich, M. Baldrias, M. Reich, N. Boitnott, and G. Bunea, "Silicon solar cells with total area efficiency above 25 %," in *2016 IEEE 43rd Photovoltaic Specialists Conference (PVSC)*, 2016, pp. 3351–3355. doi: 10.1109/PVSC.2016.7750287.

[50] K. Yoshikawa *et al.*, "Silicon heterojunction solar cell with interdigitated back contacts for a photoconversion efficiency over 26%," *Nat Energy*, vol. 2, no. 5, p. 17032, 2017, doi: 10.1038/nenergy.2017.32.

[51] W. Wu *et al.*, "22\% efficient dopant-free interdigitated back contact silicon solar cells," *AIP Conf Proc*, vol. 1999, no. 1, p. 40025, 2018, doi: 10.1063/1.5049288.

[52] H. E. Beck, N. E. Zimmermann, T. R. Mcvicar, N. Vergopolan, A. Berg, and E. F. Wood, "Data Descriptor: Present and future Köppen-Geiger climate classification maps at 1-km resolution Background & Summary," *Nature Publishing Group*, vol. 5, pp. 0–12, 2018, doi: 10.1038/sdata.2018.214.

[53] H. Goverde *et al.*, "Model requirements for accurate shot term energy yield predictions during fast-varying weather conditions," *31st European Photovoltaic Solar Energy Conference and Exhibition - EUPVSEC*, pp. 1556–1559, 2015.

[54] M. Z. Jacobson and V. Jadhav, “World estimates of PV optimal tilt angles and ratios of sunlight incident upon tilted and tracked PV panels relative to horizontal panels,” *Solar Energy*, vol. 169, no. April, pp. 55–66, 2018, doi: 10.1016/j.solener.2018.04.030.

[55] H. E. Beck, N. E. Zimmermann, T. R. Mcvicar, N. Vergopolan, A. Berg, and E. F. Wood, “Data Descriptor: Present and future Köppen-Geiger climate classification maps at 1-km resolution Background & Summary,” *Nature Publishing Group*, vol. 5, pp. 0–12, 2018, doi: 10.1038/sdata.2018.214.

[56] I. Beausoleil-morrison, B. Kemery, A. D. Wills, and C. Meister, “Design and simulated performance of a solar-thermal system employing seasonal storage for providing the majority of space heating and domestic hot water heating needs to a single-family house in a cold climate,” *Solar Energy*, vol. 191, no. August, pp. 57–69, 2019, doi: 10.1016/j.solener.2019.08.034.

[57] H. Goverde *et al.*, “Energy Yield Prediction Model for PV Modules Including Spatial and Temporal Effects,” 2014.

[58] D. Goossens, R. Lundholm, H. Goverde, and J. Govaerts, “Effect of soiling on wind-induced cooling of photovoltaic modules and consequences for electrical performance,” *Sustainable Energy Technologies and Assessments*, vol. 34, no. May, pp. 116–125, 2019, doi: 10.1016/j.seta.2019.05.007.

[59] Solargis s.r.o, “Solargis.” Accessed: Oct. 01, 2021. [Online]. Available: https://globalsolaratlas.info/download/world

[60] M. G. Chowdhury, H. Goverde, P. Manganiello, E. Voroshazi, J. Poortmans, and F. Catthoor, “Sensitivity analysis of the effect of forced convection on photovoltaic module temperature and energy yield,” in *2019 IEEE 46th Photovoltaic Specialists Conference (PVSC)*, Jun. 2019, pp. 1237–1241. doi: 10.1109/PVSC40753.2019.8980517.

[61] M. G. M. G. Chowdhury *et al.*, “Experimentally validated CFD simulations predicting wind e ff ects on photovoltaic modules mounted on inclined surfaces,” *Sustainable Energy Technologies and Assessments*, vol. 30, no. March 2017, pp. 201–208, Dec. 2018, doi: 10.1016/j.seta.2018.10.005.

[62] G. Chowdhury *et al.*, “Novel computational fluid dynamics modeling of spatial convective heat transfer over PV-modules mounted on an inclined surface with an underlying air gap,” in *35th European Photovoltaic Solar Energy Conference and Exhibition - EUPVSEC*, BE: Wip Renewable Energies, Nov. 2018, pp. 1182–1185. doi: 10.4229/35thEUPVSEC20182018-5CV.1.15.

[63] P. Manganiello *et al.*, “Tuning electricity generation throughout the year with PV module technology,” *Renew Energy*, 2020, doi: 10.1016/j.renene.2020.06.106.

[64] D. Torres Lobera and S. Valkealahti, “Dynamic thermal model of solar PV systems under varying climatic conditions,” *Solar Energy*, vol. 93, pp. 183–194, 2013, doi: https://doi.org/10.1016/j.solener.2013.03.028.

[65] G. Tamizhmani, L. Ji, Y. Tang, L. Petacci, and C. Osterwald, “Photovoltaic Module Thermal/Wind Performance : Long-Term Monitoring and Model Development For Energy Rating,” *NCPV and Solar Program Review Meeting*, pp. 936–939, 2003.

[66] M. Mattei, G. Notton, C. Cristofari, M. Muselli, and P. Poggi, “Calculation of the polycrystalline PV module temperature using a simple method of energy balance,” *Renew Energy*, vol. 31, no. 4, pp. 553–567, 2006, doi: https://doi.org/10.1016/j.renene.2005.03.010.

[67] E. Skoplaki, A. G. Boudouvis, and J. A. Palyvos, “A simple correlation for the operating temperature of photovoltaic modules of arbitrary mounting,” *Solar Energy Materials and Solar Cells*, vol. 92, no. 11, pp. 1393–1402, 2008, doi: https://doi.org/10.1016/j.solmat.2008.05.016.

[68] S. Tselepis and Y. Tripanagnostopoulos, “Economic analysis of hybrid photovoltaic/thermal solar systems and comparison with standard PV modules,” Jan. 2002.

[69] R. Chenni, M. Makhlouf, T. Kerbache, and A. Bouzid, “A detailed modeling method for photovoltaic cells,” *Energy*, vol. 32, no. 9, pp. 1724–1730, 2007, doi: https://doi.org/10.1016/j.energy.2006.12.006.

[70] J. D. Mondol, Y. G. Yohanis, and B. Norton, “Comparison of measured and predicted long term performance of grid a connected photovoltaic system,” *Energy Convers Manag*, vol. 48, no. 4, pp. 1065–1080, 2007, doi: https://doi.org/10.1016/j.enconman.2006.10.021.

[71] M. Prilliman, J. S. Stein, D. Riley, and G. Tamizhmani, “Transient Weighted Moving-Average Model of Photovoltaic Module Back-Surface Temperature,” *IEEE J Photovolt*, vol. 10, no. 4, pp. 1053–1060, Jul. 2020, doi: 10.1109/JPHOTOV.2020.2992351.

[72] M. G. Chowdhury, A. Kladas, B. Herteleer, J. Cappelle, and F. Catthoor, “Sensitivity analysis of the state of the art silicon photovoltaic temperature estimation methods over different time resolution,” in *2021 IEEE 48th Photovoltaic Specialists Conference (PVSC)*, 2021, pp. 1340–1343. doi: 10.1109/PVSC43889.2021.9519068.

[73] A. Oliveira *et al.*, “Comparative Analysis of Module Temperature Measurements and Estimation Methods for Various Climate Zones across the Globe,” in *37th European Photovoltaic Solar Energy Conference and Exhibition*, 2020, pp. 1345–1351. doi: 10.4229/EUPVSEC20202020-5DO.2.2.

[74] S. Armstrong and W. G. Hurley, “A thermal model for photovoltaic panels under varying atmospheric conditions,” *Appl Therm Eng*, vol. 30, no. 11–12, pp. 1488–1495, Aug. 2010, doi: http://dx.doi.org/10.1016/j.applthermaleng.2010.03.012.

[75] Y.-B. Assoa, T. Guiot, L. Gaillard, B. Boillot, C. Ménézo, and A. Jay, “A validated model to predict the thermal and electrical performance of residential rooftop BIPV systems,” in *27th European Photovoltaic Solar Energy Conference (EU PVSEC)*,

[76] D. Kuzmin, O. Mierka, and S. Turek, *On the Implementation of the K-epsilon Turbulence Model in Incompressible Flow Solvers Based on a Finite Element Discretization*. Univ. Dortmund, 2007. [Online]. Available: https://books.google.be/books?id=h-McYAAACAAJ

[77] C. M. Jubayer and H. Hangan, “A numerical approach to the investigation of wind loading on an array of ground mounted solar photovoltaic (PV) panels,” *Journal of Wind Engineering and Industrial Aerodynamics*, vol. 153, pp. 60–70, Jun. 2016, doi: 10.1016/j.jweia.2016.03.009.

[78] M. J. Wilson and M. C. Paul, “Effect of mounting geometry on convection occurring under a photovoltaic panel and the corresponding efficiency using CFD,” *Solar Energy*, vol. 85, no. 10, pp. 2540–2550, Oct. 2011, doi: http://dx.doi.org/10.1016/j.solener.2011.07.013.

[79] W. Xing, J. Zhou, and Z. Feng, “Effects of mounting geometries on photovoltaic module performance using CFD and single-diode model,” *Solar Energy*, vol. 103, pp. 541–549, May 2014, doi: http://dx.doi.org/10.1016/j.solener.2014.02.032.

[80] P. Trinuruk, C. Sorapipatana, and D. Janwitthaya, “Electricity generation and heat gain on photovoltaic roofs in Thailand,” *Academic thesis of The Joint Graduated School of Energy and Environmental, King Mongkut’s University of Technology Thonburi, Thailand*, 2006.

[81] Y.-Y. Wu, S.-Y. Wu, and L. Xiao, “Numerical study on convection heat transfer from inclined PV panel under windy environment,” *Solar Energy*, vol. 149, pp. 1–12, Jun. 2017, doi: 10.1016/j.solener.2017.03.084.

[82] D. Roeleveld, G. Hailu, A. S. Fung, D. Naylor, T. Yang, and A. K. Athienitis, “Validation of Computational Fluid Dynamics (CFD) Model of a Building Integrated Photovoltaic/Thermal (BIPV/T) System,” *Energy Procedia*, vol. 78, pp. 1901–1906, 2015, doi: http://dx.doi.org/10.1016/j.egypro.2015.11.359.

[83] P. A. Mirzaei, E. Paterna, and J. Carmeliet, “Investigation of the role of cavity airflow on the performance of building-integrated photovoltaic panels,” *Solar Energy*, vol. 107, pp. 510–522, Sep. 2014, doi: http://dx.doi.org/10.1016/j.solener.2014.05.003.

[84] D. A. Kaminski and M. K. Jensen, *Introduction to Thermal and Fluids Engineering*. John Wiley & Sons, 2017.

[85] H. K. Versteeg and W. Malalasekera, *An Introduction to Computational Fluid Dynamics. The Finite Volume Method*. Longman Group Ltd., 1995. doi: citeulike-article-id:352986.

[86] D. Goossens, “Height distortion and the sedimentation of dust on topographic scale models: considerations and simulations,” *Earth Surf Process Landf*, vol. 14, no. 6, pp. 655–667, 1989.

[87] Climate-Charts. World Climate Maps: Wind Speed., “http://www.climate-charts.com/World-Climate-Maps.html#wind-speed; 2007 .”

[88] Wind Atlas - WaSP, “http://www.wasp.dk/dataandtools#wind-atlas__world,” Wind Atlas - WaSP.

[89] J. Franke, A. Hellsten, K. H. Schlünzen, and B. Carissimo, “Best practice guideline for the CFD simulation of flows in the urban environment-a summary,” in *11th Conference on Harmonisation within Atmospheric Dispersion Modelling for Regulatory Purposes, Cambridge, UK, July 2007*, Cambridge Environmental Research Consultants, 2007. Accessed: Jul. 10, 2023. [Online]. Available: https://research.aalto.fi/en/publications/best-practice-guideline-for-the-cfd-simulation-of-flows-in-the-ur

[90] P. J. Roache, “Perspective: A Method for Uniform Reporting of Grid Refinement Studies,” *J Fluids Eng*, vol. 116, no. 3, p. 405, Sep. 1994, doi: 10.1115/1.2910291.

[91] H. Grotjans and F. Menter, “Wall functions for general application {CFD} codes,” in *ECCOMAS 98*, Papailou, Ed., pp. 1112–1117. doi: citeulike-article-id:4016872.

[92] J. L. Santiago, A. Martilli, and F. Martín, “CFD simulation of airflow over a regular array of cubes. Part I: Three-dimensional simulation of the flow and validation with wind-tunnel measurements,” *Boundary Layer Meteorol*, vol. 122, no. 3, pp. 609–634, 2007, doi: 10.1007/s10546-006-9123-z.

[93] J. K. Tonui and Y. Tripanagnostopoulos, “Air-cooled PV/T solar collectors with low cost performance improvements,” *Solar Energy*, vol. 81, no. 4, pp. 498–511, 2007, doi: https://doi.org/10.1016/j.solener.2006.08.002.

[94] T. Hahn, K. Dornich, J. R. Niklas, and F. I. Gmbh, “25th European Photovoltaic Solar Energy Conference and Exhibition / 5th World Conference on Photovoltaic Energy Conversion, 6-10 September 2010, Valencia, Spain,” *25th European Photovoltaic Solar Energy Conference and Exhibition / 5th World Conference on Photovoltaic Energy Conversion , 6-10 September 2010 , Valencia , Spain*, no. September, pp. 343–346, 2010.

[95] H. Goverde *et al.*, “Spatial and temporal analysis of wind effects on PV modules: Consequences for electrical power evaluation,” *Solar Energy*, vol. 147, pp. 292–299, 2017, doi: 10.1016/j.solener.2016.12.002.

[96] H. Goverde *et al.*, “Spatial and temporal analysis of wind effects on PV module temperature and performance,” *Sustainable Energy Technologies and Assessments*, vol. 11, pp. 36–41, 2015, doi: http://dx.doi.org/10.1016/j.seta.2015.05.003.

[97] T. L. Bergman *et al.*, *Fundamentals of Heat and Mass Transfer, 7th Edition*, 6th ed. John Wiley & Sons, Incorporated, 2011.

[98] S. Armstrong and W. G. Hurley, "A thermal model for photovoltaic panels under varying atmospheric conditions," *Appl Therm Eng*, vol. 30, no. 11–12, pp. 1488–1495, 2010, doi: http://dx.doi.org/10.1016/j.applthermaleng.2010.03.012.

[99] M. J. Wilson and M. C. Paul, "Effect of mounting geometry on convection occurring under a photovoltaic panel and the corresponding efficiency using CFD," *Solar Energy*, vol. 85, no. 10, pp. 2540–2550, 2011, doi: http://dx.doi.org/10.1016/j.solener.2011.07.013.

[100] W. Xing, J. Zhou, and Z. Feng, "Effects of mounting geometries on photovoltaic module performance using CFD and single-diode model," *Solar Energy*, vol. 103, pp. 541–549, 2014, doi: http://dx.doi.org/10.1016/j.solener.2014.02.032.

[101] P. Trinuruk and C. Sorapipatana, "Effect of Air Gaps on Photovoltaic Operating Temperature and Heat Gain Penetration into Buildings," *Thammasat Int. J. Sc. Tech.*, vol. 14, no. 2, 2009.

[102] D. Roeleveld, G. Hailu, A. S. Fung, D. Naylor, T. Yang, and A. K. Athienitis, "Validation of Computational Fluid Dynamics (CFD) Model of a Building Integrated Photovoltaic/Thermal (BIPV/T) System," *Energy Procedia*, vol. 78, pp. 1901–1906, 2015, doi: http://dx.doi.org/10.1016/j.egypro.2015.11.359.

[103] P. Karava, C. M. Jubayer, and E. Savory, "Numerical modelling of forced convective heat transfer from the inclined windward roof of an isolated low-rise building with application to photovoltaic/thermal systems," *Appl Therm Eng*, vol. 31, no. 11–12, pp. 1950–1963, 2011, doi: http://dx.doi.org/10.1016/j.applthermaleng.2011.02.042.

[104] P. A. Mirzaei, E. Paterna, and J. Carmeliet, "Investigation of the role of cavity airflow on the performance of building-integrated photovoltaic panels," *Solar Energy*, vol. 107, pp. 510–522, 2014, doi: http://dx.doi.org/10.1016/j.solener.2014.05.003.

[105] R. Zhang, P. A. Mirzaei, and J. Carmeliet, "Prediction of the surface temperature of building-integrated photovoltaics: Development of a high accuracy correlation using computational fluid dynamics," *Solar Energy*, vol. 147, pp. 151–163, 2017, doi: 10.1016/j.solener.2017.03.023.

[106] R. B. Bird, W. E. Stewart, and E. N. Lightfoot, *Transport Phenomena, Revised 2nd Edition*, 2nd ed. John Wiley & Sons, Inc., 2006.

[107] M. Z. Jacobson and V. Jadhav, "World estimates of PV optimal tilt angles and ratios of sunlight incident upon tilted and tracked PV panels relative to horizontal panels," *Solar Energy*, vol. 169, no. April, pp. 55–66, Jul. 2018, doi: 10.1016/j.solener.2018.04.030.

[108] Zimmermann Pv-Stahlbau, “Catalogue for Ground Mount Solar Mounting Systems. Technical report,” 2015.

[109] I. Marinić-Kragić, S. Nižetić, F. Grubišić-Čabo, and A. M. Papadopoulos, “Analysis of flow separation effect in the case of the free-standing photovoltaic panel exposed to various operating conditions,” *J Clean Prod*, vol. 174, pp. 53–64, 2018.

[110] S. Nižetić, F. Grubišić- Čabo, I. Marinić-Kragić, and A. M. Papadopoulos, “Experimental and numerical investigation of a backside convective cooling mechanism on photovoltaic panels,” *Energy*, vol. 111, pp. 211–225, Sep. 2016, doi: 10.1016/j.energy.2016.05.103.

[111] C. Verona CROITORU, F. Ioan BODE, A. Meslem, and I. NASTASE, “Innovative Ventilated Envelope Elements For Solar Heat Recovery In Low Energy Buildings,” in *Building Simulation 2013*, IBPSA, 2013, pp. 1210–1215.

[112] F. Grubišić-Čabo, S. Nižetić, I. Marinić Kragić, and D. Čoko, “Further progress in the research of fin-based passive cooling technique for the free-standing silicon photovoltaic panels,” *Int J Energy Res*, vol. 43, no. 8, pp. 3475–3495, 2019.

[113] S. Nižetić, I. Marinić Kragić, F. Grubišić Čabo, A. Papadopoulos, and G. Xie, “Analysis of novel passive cooling strategies for free-standing silicon photovoltaic panels,” *J Therm Anal Calorim*, vol. 161, no. 1, pp. 163–175, 2020, doi: 10.1007/s10973-020-09410-7.

[114] L. Liu, Q. Wang, H. Lin, H. Li, Q. Sun, and R. wennersten, “Power Generation Efficiency and Prospects of Floating Photovoltaic Systems,” *Energy Procedia*, vol. 105, pp. 1136–1142, May 2017, doi: 10.1016/j.egypro.2017.03.483.

[115] J. Franke *et al.*, “Recommendations on the Use of CFD in Wind Engineering,” *Cost Action C*, no. January, pp. 1–11, 2004, [Online]. Available: http://s3.amazonaws.com/academia.edu.documents/33100785/Recommendations_for_CFD_in_wind_engineering.pdf?AWSAccessKeyId=AKIAIWOWYYGZ2Y53UL3A&Expires=1486455232&Signature=vJRCxb1YOFG9Vb2eSeBepZisLGM%3D&response-content-disposition=inline%3B filename%3DRECOM

[116] M. V Casey and T. Wintergerste, *ERCOFTAC Best Practice Guidelines for Industrial CFD*. ERCOFTAC, Brussels, Belgium, 2000.

[117] B. Blocken, T. Stathopoulos, and J. Carmeliet, “CFD simulation of the atmospheric boundary layer: wall function problems,” *Atmos Environ*, vol. 41, no. 2, pp. 238–252, Jan. 2007, doi: 10.1016/j.atmosenv.2006.08.019.

[118] T. Defraeye, B. Blocken, and J. Carmeliet, “CFD analysis of convective heat transfer at the surfaces of a cube immersed in a turbulent boundary layer,” *Int J Heat Mass Transf*, vol. 53, no. 1–3, pp. 297–308, 2010, doi: 10.1016/j.ijheatmasstransfer.2009.09.029.

[119] B. Blocken, T. Defraeye, D. Derome, and J. Carmeliet, “High-resolution CFD simulations for forced convective heat transfer coefficients at the facade of a low-rise building,” *Build Environ*, vol. 44, no. 12, pp. 2396–2412, Dec. 2009, doi: http://dx.doi.org/10.1016/j.buildenv.2009.04.004.

[120] Chowdhury Gofran, Haggag Mohamed, and Poortmans Jef, “How cool is floating PV? A state-of-the-art review of floating PV’s potential gain and computational fluid dynamics modeling to find its root cause,” *EPJ Photovolt.*, vol. 14, p. 24, 2023, doi: 10.1051/epjpv/2023015.

[121] P. J. Roache, “Quantification of Uncertainty in Computational Fluid Dynamics,” *Annu Rev Fluid Mech*, vol. 29, no. 1, pp. 123–160, Jan. 1997, doi: 10.1146/annurev.fluid.29.1.123.

[122] F. Stern, R. V Wilson, H. W. Coleman, and E. G. Paterson, “Verification and validation of CFD simulations,” *Iowa Institute of Hydraulic Research IIHR*, vol. 407, 1999.

[123] F. E. Division *et al.*, “Procedure for Estimation and Reporting of Uncertainty Due to Discretization in CFD Applications,” *J Fluids Eng*, vol. 130, no. 7, p. 078001, Jul. 2008, doi: 10.1115/1.2960953.

[124] L. Kwaśniewski, “Application of grid convergence index in FE computation,” *Bulletin of the Polish Academy of Sciences. Technical Sciences*, vol. Vol. 61, no. nr 1, pp. 123–128, 2013, [Online]. Available: http://yadda.icm.edu.pl/baztech/element/bwmeta1.element.baztech-article-BPG8-0098-0017

[125] A. Hutton and M. Casey, “Quality and trust in industrial CFD - A European initiative,” in *39th Aerospace Sciences Meeting and Exhibit*, American Institute of Aeronautics and Astronautics, 2001. doi: 10.2514/6.2001-656.

[126] Ed Fontes. FEM vs. FVM., “https://www.comsol.com/blogs/fem-vs-fvm/.”

[127] M. G. Kittur and R. L. Huston, “Mesh refinement in finite element analysis by minimization of the stiffness matrix trace,” 1989.

[128] Bourisli, R., Aldalali, B. S. H. M., Tuomiranta, A., Chowdhury, G., & Poortmans, J. (2025). System comprising photovoltaic modules with multiple vanes and corresponding arranging method, US2025023503A1. Mar. 26, 2025

[129] S. Kaplanis and E. Kaplani, “A new dynamic model to predict transient and steady state pv temperatures taking into account the environmental conditions,” *Energies (Basel)*, vol. 12, no. 1, 2019, doi: 10.3390/en12010002.

[130] G. G. Kim *et al.*, “Prediction Model for PV Performance With Correlation Analysis of Environmental Variables,” *IEEE J Photovolt*, vol. 9, no. 3, pp. 832–841, May 2019, doi: 10.1109/JPHOTOV.2019.2898521.

[131] K. Trapani, M. R. Santafé, and M. Redón Santafé, “A review of floating photovoltaic installations: 2007–2013,” *Progress in Photovoltaics: Research and Applications*, vol. 23, no. 4, pp. 524–532, 2015, doi: https://doi.org/10.1002/pip.2466.

[132] J. O. Hirschfelder Curtiss Charles F. Bird R. Byron University of Wisconsin. Naval Research Laboratory., *Molecular theory of gases and liquids*. New York: Wiley, 1954.

[133] M. Gouldrick, “Why Is It Cooler By the Lake?,” 2019. [Online]. Available: https://spectrumlocalnews.com/nys/rochester/blog/2019/04/11/cooler-by-the-lake

[134] Y.-G. Lee, H.-J. Joo, and S.-J. Yoon, “Design and installation of floating type photovoltaic energy generation system using FRP members,” *Solar Energy*, vol. 108, pp. 13–27, Oct. 2014, [Online]. Available: https://www.sciencedirect.com/science/article/pii/S0038092X14003326

[135] B. Sutanto and Y. S. Indartono, “Computational fluid dynamic (CFD) modelling of floating photovoltaic cooling system with loop thermosiphon,” *AIP Conf Proc*, vol. 2062, no. 1, p. 20011, Jan. 2019, doi: 10.1063/1.5086558.

[136] M. Rosa-Clot, G. M. Tina, and S. Nizetic, “Floating photovoltaic plants and wastewater basins: an Australian project,” *Energy Procedia*, vol. 134, pp. 664–674, Oct. 2017, [Online]. Available: https://linkinghub.elsevier.com/retrieve/pii/S1876610217347197

[137] N. Dang Anh Thi, *The global evolution of floating solar PV*. Working paper, IFC, 2017.

[138] S. Z. Golroodbari, W. van Sark, W. van Sark, and W. van Sark, “Simulation of performance differences between offshore and land-based photovoltaic systems,” *Progress in Photovoltaics: Research and Applications*, vol. 28, no. 9, pp. 873–886, 2020, doi: https://doi.org/10.1002/pip.3276.

[139] V. Durković, Ž. Đurišić, V. Durkovíc, Ž. Durišíc, V. Durković, and Ž. Đurišić, “Analysis of the potential for use of floating PV power plant on the skadar lake for electricity supply of aluminium plant in montenegro,” *Energies (Basel)*, vol. 10, no. 10, p. 1505, Oct. 2017, doi: 10.3390/en10101505.

[140] G. M. Tina, F. Bontempo Scavo, L. Merlo, and F. Bizzarri, “Comparative analysis of monofacial and bifacial photovoltaic modules for floating power plants,” *Appl Energy*, vol. 281, p. 116084, Jan. 2021, [Online]. Available: https://www.sciencedirect.com/science/article/pii/S0306261920315117

[141] W. Luo *et al.*, “Performance loss rates of floating photovoltaic installations in the tropics,” *Solar Energy*, vol. 219, pp. 58–64, 2021, Accessed: Jun. 30, 2022. [Online]. Available: https://www.sciencedirect.com/science/article/pii/S0038092X20312706

[142] G. Blengini, “Floating photovoltaic systems: state of art, feasibility study in Florida and computational fluid dynamic analysis on hurricane resistance,” Politecnico di Torino, 2020. [Online]. Available: https://webthesis.biblio.polito.it/16339/

[143] E. M. do Sacramento, P. C. M. Carvalho, J. C. de Araújo, D. B. Riffel, R. M. da C. Corrêa, and J. S. P. Neto, “Scenarios for use of floating photovoltaic plants in Brazilian reservoirs,” *IET Renewable Power Generation*, vol. 9, no. 8, pp. 1019–1024, Nov. 2015, doi: 10.1049/iet-rpg.2015.0120.

[144] R. Oblack, “Why Is Wind Speed Slower Over Land than Over Ocean?,” 2019. [Online]. Available: https://www.thoughtco.com/wind-speed-slower-over-land-3444038

[145] H. Liu, V. Krishna, J. L. Leung, T. Reindl, and L. Zhao, “Field experience and performance analysis of floating PV technologies in the tropics,” *Progress in Photovoltaics: Research and Applications*, vol. 26, no. 12, pp. 957–967, 2018, doi: https://doi.org/10.1002/pip.3039.

[146] H. Ziar *et al.*, “Innovative floating bifacial photovoltaic solutions for inland water areas,” *Progress in Photovoltaics: Research and Applications*, 2020, doi: https://doi.org/10.1002/pip.3367.

[147] W. Charles Lawrence Kamuyu *et al.*, “Prediction model of photovoltaic module temperature for power performance of floating PVs,” *Energies (Basel)*, vol. 11, no. 2, p. 447, Feb. 2018, doi: 10.3390/en11020447.

[148] I. M. Peters and A. M. Nobre, “On Module Temperature in Floating PV Systems,” in *2020 47th IEEE Photovoltaic Specialists Conference (PVSC)*, Calgary, AB, Canada: IEEE, Jun. 2020, pp. 238–241. doi: 10.1109/PVSC45281.2020.9300426.

[149] H. S. Jeong, J. Choi, H. H. Lee, and H. S. Jo, “A Study on the Power Generation Prediction Model Considering Environmental Characteristics of Floating Photovoltaic System,” *Applied Sciences*, vol. 10, no. 13, p. 4526, Jan. 2020, doi: 10.3390/app10134526.

[150] S. Gorjian, H. Sharon, H. Ebadi, K. Kant, F. B. Scavo, and G. M. Tina, “Recent technical advancements, economics and environmental impacts of floating photovoltaic solar energy conversion systems,” *J Clean Prod*, vol. 278, p. 124285, Jan. 2021, doi: 10.1016/j.jclepro.2020.124285.

[151] P. Rosa-Clot, “Chapter 9 - FPV and Environmental Compatibility,” in *Floating PV Plants*, M. Rosa-Clot and G. Marco Tina, Eds., Academic Press, 2020, pp. 101–118. doi: 10.1016/B978-0-12-817061-8.00009-9.

[152] N. Yadav, M. Gupta, and K. Sudhakar, “Energy assessment of floating photovoltaic system,” in *2016 International Conference on Electrical Power and Energy Systems (ICEPES)*, Dec. 2016, pp. 264–269. doi: 10.1109/ICEPES.2016.7915941.

[153] Z. A. A. Majid, M. H. Ruslan, K. Sopian, M. Y. Othman, and M. S. M. Azmi, "Study on Performance of 80 Watt Floating Photovoltaic Panel," *Journal of Mechanical Engineering and Sciences*, vol. 7, pp. 1150–1156, Dec. 2014, doi: 10.15282/jmes.7.2014.14.0112.

[154] O. Levenspiel, "The Three Mechanisms of Heat Transfer: Conduction, Convection, and Radiation," *Engineering Flow and Heat Exchange*, pp. 179–210, 2014, doi: 10.1007/978-1-4899-7454-9_9.

[155] J. Garro Etxebarria, "Toolbox for the design and simulation of a floating bifacial PV plant with reflectors," 2018, [Online]. Available: https://repository.tudelft.nl/islandora/object/uuid%3Aa86fd44c-379c-48f8-a737-2c0b01086384

[156] A. Goswami, P. Sadhu, U. Goswami, and P. K. Sadhu, "Floating solar power plant for sustainable development: A techno-economic analysis," *Environ Prog Sustain Energy*, vol. 38, no. 6, p. e13268, 2019, doi: https://doi.org/10.1002/ep.13268.

[157] Y. K. Choi, W. S. Choi, and J. H. Lee, "Empirical Research on the Efficiency of Floating PV Systems," *Sci Adv Mater*, vol. 8, no. 3, pp. 681–685, Mar. 2016, doi: 10.1166/sam.2016.2529.

[158] M. Kumar and A. Kumar, "Experimental validation of performance and degradation study of canal-top photovoltaic system," *Appl Energy*, vol. 243, pp. 102–118, Jun. 2019, doi: 10.1016/j.apenergy.2019.03.168.

[159] R. Cazzaniga, M. Cicu, M. Rosa-Clot, P. Rosa-Clot, G. M. Tina, and C. Ventura, "Floating photovoltaic plants: Performance analysis and design solutions," *Renewable and Sustainable Energy Reviews*, vol. 81, no. September 2016, pp. 1730–1741, Jan. 2018, doi: 10.1016/j.rser.2017.05.269.

[160] A. Awasthi *et al.*, "Review on sun tracking technology in solar PV system," *Energy Reports*, vol. 6, pp. 392–405, Nov. 2020, doi: 10.1016/j.egyr.2020.02.004.

[161] R. Cazzaniga, M. Rosa-Clot, P. Rosa-Clot, and G. M. Tina, "Floating tracking cooling concentrating (FTCC) systems," in *2012 38th IEEE Photovoltaic Specialists Conference*, Jun. 2012, pp. 514–519. doi: 10.1109/PVSC.2012.6317668.

[162] M. Rosa-Clot and G. M. Tina, "Chapter 6 - Cooling Systems," in *Floating PV Plants*, M. Rosa-Clot and G. Marco Tina, Eds., Academic Press, 2020, pp. 67–77. doi: 10.1016/B978-0-12-817061-8.00006-3.

[163] D. Mittal, B. K. Saxena, and K. V. S. Rao, "Comparison of floating photovoltaic plant with solar photovoltaic plant for energy generation at Jodhpur in India," in *2017 International Conference on Technological Advancements in Power and Energy (TAP Energy)*, Dec. 2017, pp. 1–6. doi: 10.1109/TAPENERGY.2017.8397348.

[164] Y. Du, W. Tao, Y. Liu, J. Jiang, and H. Huang, “Heat transfer modeling and temperature experiments of crystalline silicon photovoltaic modules,” *Solar Energy*, vol. 146, pp. 257–263, Apr. 2017, doi: 10.1016/j.solener.2017.02.049.

[165] “Solar Panel Frame , PV Frame , Aluminium Frame Profile - Solar Panel Frame , PV Frame , Anodized Aluminum Frame.” [Online]. Available: http://www.alu-solarframe.com/html_products/Solar-Panel-Frame-with-Corner-Key-114.html

[166] C. Ferrer-Gisbert, J. J. Ferrán-Gozálvez, M. Redón-Santafé, P. Ferrer-Gisbert, F. J. Sánchez-Romero, and J. B. Torregrosa-Soler, “A new photovoltaic floating cover system for water reservoirs,” *Renew Energy*, vol. 60, pp. 63–70, Dec. 2013, doi: 10.1016/j.renene.2013.04.007.

[167] M. Rosa-Clot and G. M. Tina, “Chapter 3 - Geographic Potential,” in *Floating PV Plants*, M. Rosa-Clot and G. Marco Tina, Eds., Academic Press, 2020, pp. 19–32. doi: 10.1016/B978-0-12-817061-8.00003-8.

[168] M. Redón Santafé, J. B. Torregrosa Soler, F. J. Sánchez Romero, P. S. Ferrer Gisbert, J. J. Ferrán Gozálvez, and C. M. Ferrer Gisbert, “Theoretical and experimental analysis of a floating photovoltaic cover for water irrigation reservoirs,” *Energy*, vol. 67, pp. 246–255, Apr. 2014, doi: 10.1016/j.energy.2014.01.083.

[169] J. Kim, S. Bae, Y. Yu, and Y. Nam, “Experimental and Numerical Study on the Cooling Performance of Fins and Metal Mesh Attached on a Photovoltaic Module,” *Energies (Basel)*, vol. 13, no. 1, p. 85, Jan. 2020, doi: 10.3390/en13010085.

[170] P. Nyanor, O. Kabu, K. Stephen, and D. Anthony, “3D finite element method modelling and simulation of the temperature of crystalline photovoltaic module,” pp. 2321–7308, Dec. 2018.

[171] J.-Y. Wang and Q.-B. Yang, “Experimental Study on Mechanical Properties of Concrete Confined with Plastic Pipe,” *ACI Mater J*, vol. 107, p. 132, Mar. 2010.

[172] “Thermoplastic High Density Polyethylene (HDPE),” 2013. [Online]. Available: https://www.substech.com/dokuwiki/doku.php?id=thermoplastic_high_density_polyethylene_hdpe

[173] M. W. Woo *et al.*, “Melting behavior and thermal properties of high density polythylene,” *Polym Eng Sci*, vol. 35, no. 2, pp. 151–156, 1995, doi: https://doi.org/10.1002/pen.760350205.

[174] H. Oosterbaan, M. Janiszewski, L. Uotinen, T. Siren, and M. Rinne, “Numerical Thermal Back-calculation of the Kerava Solar Village Underground Thermal Energy Storage,” *Procedia Eng*, vol. 191, pp. 352–360, Dec. 2017, doi: 10.1016/j.proeng.2017.05.191.

[175] T. Instruments, “Testing the Thermal Conductivity Of Soil using TLS-100.” [Online]. Available: https://thermtest.com/applications/soil-thermal-conductivity-tls

[176] J. J. Franke, A. Hellsten, H. Schlünzen, and B. Carissimo, *Best practice guideline for the CFD simulation of flows in the urban environment*, vol. 44, no. May. Meteorological Inst., 2007. [Online]. Available: http://cat.inist.fr/?aModele=afficheN&cpsidt=23892111%5Cnhttp://scholar.google.com/scholar?hl=en&btnG=Search&q=intitle:Best+practice+guideline+for+the+CFD+simulation+of+flows+in+the+urban+environment#0

[177] Y. Tominaga *et al.*, "AIJ guidelines for practical applications of CFD to pedestrian wind environment around buildings," *Journal of Wind Engineering and Industrial Aerodynamics*, vol. 96, no. 10, pp. 1749–1761, Oct. 2008, doi: 10.1016/j.jweia.2008.02.058.

[178] G. Notton, C. Cristofari, M. Mattei, and P. Poggi, "Modelling of a double-glass photovoltaic module using finite differences," *Appl Therm Eng*, vol. 25, no. 17–18, pp. 2854–2877, Dec. 2005, doi: 10.1016/j.applthermaleng.2005.02.008.

[179] F. R. Menter, "Two-equation eddy-viscosity turbulence models for engineering applications," *AIAA Journal*, May 2012, doi: 10.2514/3.12149.

[180] M. Shademan, R. M. Barron, R. Balachandar, and H. Hangan, "Numerical simulation of wind loading on ground-mounted solar panels at different flow configurations," *Canadian Journal of Civil Engineering*, vol. 41, no. 8, pp. 728–738, Aug. 2014, doi: 10.1139/cjce-2013-0537.

[181] R. Harvey, L. Lye, A. Khan, and R. Paterson, "The Influence of Air Temperature on Water Temperature and the Concentration of Dissolved Oxygen in Newfoundland Rivers," *Canadian Water Resources Journal / Revue canadienne des ressources hydriques*, vol. 36, no. 2, pp. 171–192, Jan. 2011, doi: 10.4296/cwrj3602849.

[182] E. L. Cussler and E. L. Cussler, *Diffusion: Mass Transfer in Fluid Systems*. Cambridge University Press, 2009.

[183] R. Jain and T. J. Tautges, "PostBL: Post-mesh Boundary Layer Mesh Generation Tool," *Proceedings of the 22nd International Meshing Roundtable*, pp. 331–348, 2014, doi: 10.1007/978-3-319-02335-9_19.

[184] A. lal Basediya, D. V. K. Samuel, and V. Beera, "Evaporative cooling system for storage of fruits and vegetables - a review," *J Food Sci Technol*, vol. 50, no. 3, pp. 429–442, Jun. 2013, doi: 10.1007/s13197-011-0311-6.

[185] A. K. Abdulrazzaq, B. Plesz, and G. Bognár, "A Novel Method for Thermal Modelling of Photovoltaic Modules/Cells under Varying Environmental Conditions," *Energies (Basel)*, vol. 13, no. 13, p. 3318, Jan. 2020, doi: 10.3390/en13133318.

[186] E. Skoplaki and J. A. Palyvos, "On the temperature dependence of photovoltaic module electrical performance: A review of efficiency/power correlations," *Solar Energy*, vol. 83, no. 5, pp. 614–624, 2009, doi: http://dx.doi.org/10.1016/j.solener.2008.10.008.

[187] J. Zhou, Q. Yi, Y. Wang, and Z. Ye, "Temperature distribution of photovoltaic module based on finite element simulation," *Solar Energy*, vol. 111, pp. 97–103, Jan. 2015, doi: 10.1016/j.solener.2014.10.040.

[188] F. B. Scavo, G. M. Tina, A. Gagliano, and S. Nižetić, "An assessment study of evaporation rate models on a water basin with floating photovoltaic plants," *Int J Energy Res*, 2020, [Online]. Available: https://www.bib.irb.hr/1038721?rad=1038721

[189] S. H. Hwang, D. Y. Lee, O. geuk Kwon, and J. H. Lee, "The Electrical Characteristics of The Modules According to The Environment of The Floating Photovoltaic System," *Journal of the Korean Institute of Electrical and Electronic Material Engineers*, vol. 31, no. 5, pp. 283–289, 2018, doi: 10.4313/JKEM.2018.31.5.283.

[190] S. Oliveira-Pinto and J. Stokkermans, "Assessment of the potential of different floating solar technologies – Overview and analysis of different case studies," *Energy Convers Manag*, vol. 211, p. 112747, May 2020, doi: 10.1016/j.enconman.2020.112747.

[191] F. Arpino, G. Cortellessa, and A. Frattolillo, "Experimental and numerical assessment of photovoltaic collectors performance dependence on frame size and installation technique," *Solar Energy*, vol. 118, pp. 7–19, Aug. 2015, doi: 10.1016/j.solener.2015.05.006.

[192] A. Glick *et al.*, "Influence of flow direction and turbulence intensity on heat transfer of utility-scale photovoltaic solar farms," *Solar Energy*, vol. 207, pp. 173–182, Sep. 2020, doi: 10.1016/j.solener.2020.05.061.

[193] Y. Ueda, K. Kurokawa, M. Konagai, S. Takahashi, A. Terazawa, and H. Ayaki, "Five Years Demonstration Results of Floating PV Systems with Water Spray Cooling," *27th European Photovoltaic Solar Energy Conference and Exhibition; 3926-3928*, pp. 3 pages, 1647 kb, 2012, doi: 10.4229/27THEUPVSEC2012-5AV.1.15.

[194] O. Turgut and N. Onur, "Three dimensional numerical and experimental study of forced convection heat transfer on solar collector surface," *International Communications in Heat and Mass Transfer*, vol. 36, no. 3, pp. 274–279, Mar. 2009, doi: 10.1016/j.icheatmasstransfer.2008.10.017.

[195] H. Bahaidarah, A. Subhan, P. Gandhidasan, and S. Rehman, "Performance evaluation of a PV (photovoltaic) module by back surface water cooling for hot climatic conditions," *Energy*, vol. 59, pp. 445–453, Sep. 2013, doi: 10.1016/j.energy.2013.07.050.

[196] M. Vega Orrego, "Evaluación experimental y numérica de módulos fotovoltaicos bifaciales flotantes en comparación con sistemas monofaciales y terrestres," *Repositorio Institucional Universidad EIA*, 2019, [Online]. Available: https://repository.eia.edu.co/handle/11190/2497

[197] S. Desai, M. Wagh, and N. Shinde, "A Review on Floating Solar Photovoltaic Power Plants," *Int J Sci Eng Res*, vol. 6, pp. 789–794, Jun. 2017.

[198] I. S. Rodrigues, G. L. B. Ramalho, and P. H. A. Medeiros, “Potential of floating photovoltaic plant in a tropical reservoir in Brazil,” *Journal of Environmental Planning and Management*, vol. 63, no. 13, pp. 2334–2356, Nov. 2020, doi: 10.1080/09640568.2020.1719824.

[199] K. S. Hayibo, P. Mayville, R. K. Kailey, and J. M. Pearce, “Water Conservation Potential of Self-Funded Foam-Based Flexible Surface-Mounted Floatovoltaics,” *Energies (Basel)*, vol. 13, no. 23, p. 6285, Jan. 2020, doi: 10.3390/en13236285.